

REPORT DOCUMENTATION PAGE

The public reporting burden for this collection of information is estimated to average 1 hour per response, including the time for reviewing instructions, searching existing data sources, gathering and maintaining the data needed, and completing and reviewing the collection of information. Send comments regarding this burden estimate or any other aspect of this collection of information, including suggestions for reducing the burden, to the Department of Defense, Executive Services and Communications Directorate (0704-0188). Respondents should be aware that notwithstanding any other provision of law, no person shall be subject to any penalty for failing to comply with a collection of information if it does not display a currently valid OMB control number.

PLEASE DO NOT RETURN YOUR FORM TO THE ABOVE ORGANIZATION.

1. REPORT DATE (DD-MM-YYYY) 11 DEC 2008		2. REPORT TYPE Final		3. DATES COVERED (From - To) 01 JUN 2005 - 31 MAY 2008	
4. TITLE AND SUBTITLE THE SPRING NANOENERGETICS HUB AT UTD				5a. CONTRACT NUMBER	
				5b. GRANT NUMBER FA9550-05-1-0393	
				5c. PROGRAM ELEMENT NUMBER	
6. AUTHOR(S) DR. JOHN FERRARIS				5d. PROJECT NUMBER	
				5e. TASK NUMBER	
				5f. WORK UNIT NUMBER	
7. PERFORMING ORGANIZATION NAME(S) AND ADDRESS(ES) UNIVERSITY OF TEXAS AT DALLAS DEPARTMENT OF CHEMISTRY 2601 N. FLOYD ROAD, RICHARDSON, TX 75080				B. PERFORMING ORGANIZATION REPORT NUMBER	
9. SPONSORING/MONITORING AGENCY NAME(S) AND ADDRESS(ES) AF OFFICE OF SCIENTIFIC RESEARCH / <i>ME</i> 875 NORTH RANDOLPH STREET ROOM 3112 ARLINGTON VA 22203 <i>Dr Harold Weinstein</i>				10. SPONSOR/MONITOR'S ACRONYM(S)	
				11. SPONSOR/MONITOR'S REPORT NUMBER(S)	
12. DISTRIBUTION/AVAILABILITY STATEMENT UNLIMITED					
13. SUPPLEMENTARY NOTES					
14. ABSTRACT The objective of this proposed research, to be carried out as part of the Strategic Partnership for Research in Nanotechnology, or SPRING (in collaboration with AFRL/MLMT, Rice University, the University of Texas, Arlington and the University of Texas, Austin), is the synthesis and processing of advanced nanostructured materials, the structure and property characterization needed for materials optimization, the fabrication of sophisticated structures, and device testing in the areas of energy harvesting, storage, transmission and conversion. Research will be pursued in solar cells, thermo-electromechanical cells, thermionics, thermoelectrics, fuel cells, actuators, batteries, supercapacitors and energy transmission lines.					
15. SUBJECT TERMS <h1 style="text-align: center;">20090319181</h1>					
16. SECURITY CLASSIFICATION OF:			17. LIMITATION OF ABSTRACT	18. NUMBER OF PAGES	19a. NAME OF RESPONSIBLE PERSON JOHN FERRARIS
a. REPORT	b. ABSTRACT	c. THIS PAGE			19b. TELEPHONE NUMBER (Include area code) 972-883-2905

SPRING III Final Report

Research Objective

The research emphasis of the SPRING NanoEnergetics facility at the University of Texas at Dallas is the synthesis and processing of advanced nanostructured materials, the structure and property characterization needed for materials optimization, the fabrication of sophisticated structures, and device testing in the areas of energy harvesting, storage, transmission, and conversion. SPRING III funds were used to support five \$150K (for two years) seed grants. Remaining funds were used to continue support for four technical staff members and two graduate students. Summaries of SPRING III seed grants are given below.

Synthesis, Characterization and Energy Transfer Studies in Donor-Acceptor PPV Diblock Copolymers for Solar Cell Applications (John Ferraris)

Block copolymers are known to phase separate into ordered micro-phases (10-100 nm) due to the chemical composition and connectivity between the block segments and is on the scale as the macromolecules' radii of gyration. The shape and size of these micro-phases can be tailored by changing the block composition, ratio and molecular weight. This type of self-structuring has an attractive application in nanotechnologies such as plastic solar cells designed with a bulk heterojunction (BHJ). The desired nano-structured donor/acceptor (D/A) domains can in principle be reached using block copolymers containing electron donor and acceptor conjugated polymer segments.⁵ We report here further characterization of D/A PPV block copolymers: poly-p-[bis-2,5-(2'-ethyl-hexyloxy)]-block-[bis-2,5-(N,N',N''-di-methylhexylammonium)]-1,4-phenylenevinylene (BEH-block-QBAMH PPV); poly-p-[bis-2,5-(2'-ethylhexyloxy)]-block-[bis-2,5-(2'-ethylhexylsulfanyl)]-1,4-phenylenevinylene (BEH-block-BEHSO PPV).

The homopolymers of BAMH PPV, BEH PPV, and BEHM PPV were synthesized using the modified Gilch route displaying molecular weights that are higher than 105 kDa with moderately molecular weight distributions ($PDI \leq 1.8$). This modified polymerization route has also been used to synthesize different polymer architectures (diblock, triblock, and star copolymers) with high molecular weights ($>10^5$ kDa) and narrow molecular weight distributions. The block copolymers presented here were also synthesized through the modified Gilch route. For the block copolymerizations, aliquots were taken after the first PPV monomer addition and compared to the final product. An increase in molecular weight from the intermediate product (193 kDa) to the final block (BEH-b-BAMH PPV, 323 kDa) was observed. For BEH-b-BEHM PPV, we observed a smaller increase from the intermediate product (217 kDa) to the final block (BEH-b-BEHM PPV, 273 kDa).

Poly-p-[1,4-bis-2-ethylhexyloxy]-block-[1,4-bisN,N',N''-dimethyl hexyl ammonium]-2,5-phenylenevinylene (BEH-b-QBAMH PPV). The N-methylation of the tertiary amine moiety on the block polymer backbone was carried out with the use of methyl trifluoromethanesulfonate in chloroform. The N-methylation was confirmed by FT-IR analysis where the characteristic peaks of the triflate counter-ion appeared at 1258, 1033, and 644 cm^{-1} .

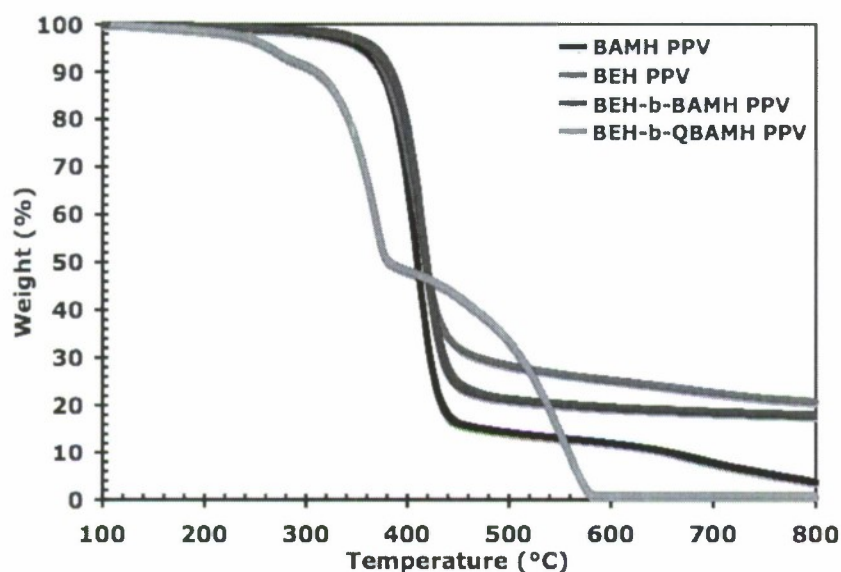


Figure 1. TGA of BAMH PPV (black), BEH PPV (green), BEH-b-BAMH PPV (blue), and BEH-b-QBAMH PPV (red), at a heating of 10 °C/min in nitrogen atmosphere.

Figure 1 shows a comparison of the thermal stability of the PPV homopolymers, pristine block copolymer (BEH-b-BAMH PPV) and the treated block copolymer (BEH-b-QBAMH PPV). The thermal stability of the PPV homopolymers (BAMH PPV and BEH PPV) and the pristine block copolymer are similar with onset points of weight loss at 368 and 374 °C, respectively. The thermal stability of the treated block copolymer is greatly reduced. An early weight loss (5%) occurs at 240 °C, attributed to the loss of the triflate counter-ion, with subsequent losses of the functionalities at 322 and 422 °C. DSC analysis (Table 1) shows the glass-temperatures (T_g) of the PPV homopolymers, the pristine and treated block copolymers that are higher compared to reported values for this type of PPVs.

	T_D (°C)	T_g (°C)
BAMH	364	110
BEH	368	106
BEH- <i>block</i> -BAMH	374	98
BEH- <i>block</i> -QBAMH	274	105

Table 1. TGA (T_D) and DSC (T_g) values of BAMH PPV, BEH PPV, BEH-b-BAMH PPV, and BEH-b-QBAMH PPV. Decomposition temperature (T_D) at 5% weight loss. T_g : glass-transition temperature.

Figure 2 shows atomic force microscopy images of thin films composed of a BAMH/BEH PPV blend, the pristine material, and the treated material. The fine and high degree of phase separation in the blend's micrograph indicates that the polymers are not miscible with respect to each other. No observable phase separation in the BEH-b-BAMH PPV film indicates micro-

phase separation (< 20 nm) and confirms the formation of the block copolymer. The formation of the bulky quaternary ammonium moiety on BEH-b-QBAMH PPV disrupts the planarity observed in the BEH-b-BAMH PPV film that is manifested as large aggregates.

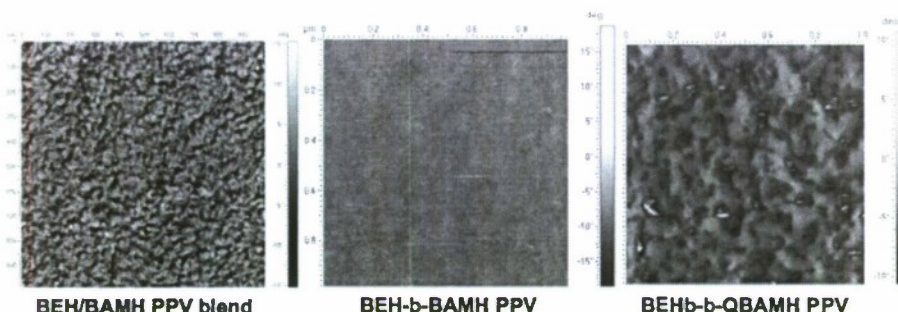


Figure 2. AFM images of BEH/BAMH blend (left), BEH-b-BAMH PPV (middle) and BEH-b-QBAMH PPV (right).

Thin films of BEH PPV, BAMH PPV, and the block copolymers BEH-b-BAMH and BEH-b-QBAMH PPV were analyzed by emission spectroscopy (Figure 3). BAMH PPV (green) shows a broad emission with a maximum of 574 nm possibly due to its bulkier side groups, leading the chains to be farther away from each other. BEH PPV (blue) shows its characteristic emission maximum at 580 nm with a shoulder at 620 nm. This shoulder (620 nm) can be attributed to inter-chain aggregations. The pristine block copolymer of BEH and BAMH PPV (black) showed a broad emission with a maximum of 584 nm and a higher shoulder emission also at 620 nm, similar to BEH PPV. BEH-b-QBAMH PPV (red) has the same emission maximum as its parent polymer, but with a more intense inter-chain aggregation emission at 620 nm, attributed to the even bulkier quaternary amine side chains. These groups occupy more space and thus pack the BEH components closer to enhance such aggregation. It also is the indication of photoluminescence quenching of the BEH segment emission due to the electron withdrawing quaternary amine PPV segment.

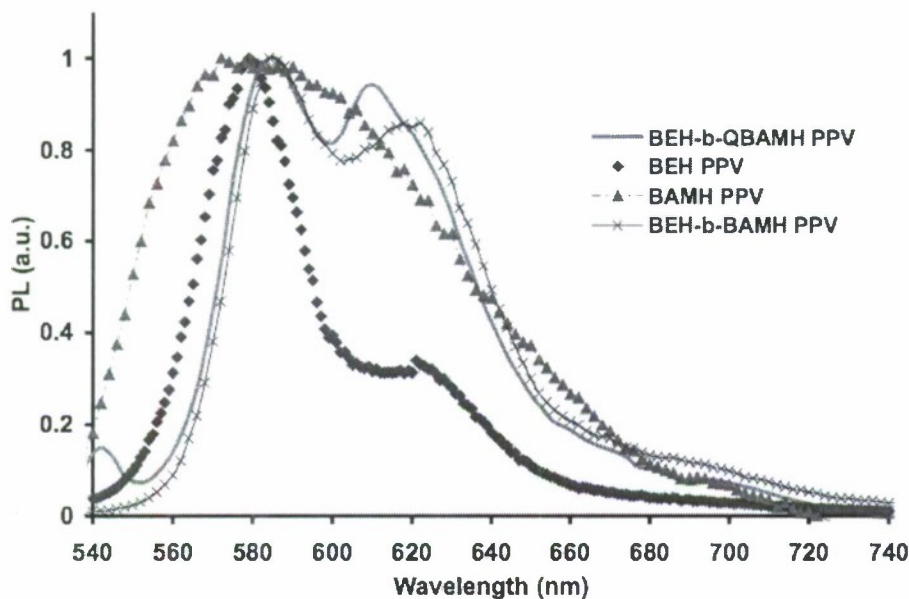


Figure 3. Photoluminescence spectra of BEH PPV (diamonds), BAMH PPV (triangles) and BEH-b-BAMH PPV (x's) and BEH-b-QBAMH PPV (solid line) block copolymer films.

Poly-p-[2,5-bis-(2-ethylhexyloxy)]-block-[2,5-bis-(2-ethylhexylsul-fanyl)]-1,4-phenylenevinylene (BEH-b-BEHSO PPV). The oxidation of the thioether functionality on the BEHM PPV segment of the block copolymer was oxidized to the sulfoxide moiety using excess hydrogen peroxide in the presence of glacial acetic acid. The oxidation of the sulfur was confirmed by FT-IR, where the sulfoxide peak appeared at 1040 cm^{-1} corresponding to the sulfoxide stretch. The intensity of this peak increases in the BEH-b-BEHSO PPV block copolymer relative to the intensity ratio of the peak in BEH-b-BEHM PPV.

Figure 4 also shows a comparison of the thermal stability of the PPV homopolymers, pristine block copolymer (BEH-b-BEHM PPV) and the treated block copolymer (BEH-b-BEHSO PPV). The thermal stability of the PPV homopolymers BEH PPV and BEHM PPV are observed to be the most stable with onset points of weight loss at 368 and 335 °C, respectively. The thermal stability of the BEH-b-BEHM is reduced with an early weight loss occurring at 270 °C attributed to the loss of the thioether functionalities. The treated block copolymer's thermal stability is further reduced. An early weight loss (5%) occurs at 170 °C, attributed to the loss of the sulfoxide functionalities. The steady weight loss is observed from 220-360 °C with a final loss at 370 °C due to the loss of the alkoxy functionalities.

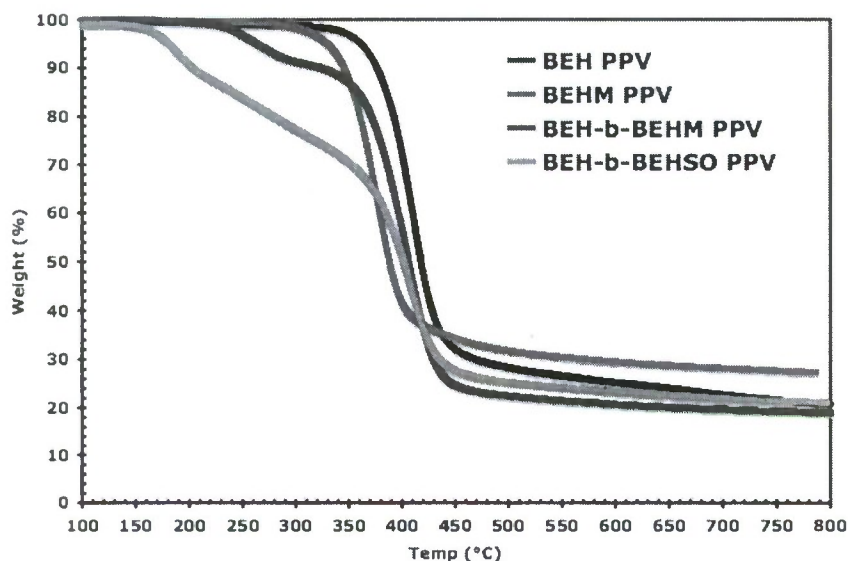


Figure 4. TGA of BEH PPV (black), BEHM PPV (green), BEH-b-BEHM PPV (blue), and BEH-b-BEHSO PPV (red), at a heating of 10 °C/min in nitrogen atmosphere.

Atomic force microscopy images (Figure 5) shows the morphology of thin films composed of a BEH/BEHM PPV blend, the pristine material, and the treated material. The bulky phase separation in the blend's micrograph indicates that the polymers are somewhat miscible with respect to each other. Observable of lesser degree of phase separation in the BEH-b-BEHM PPV film confirms the formation of the block copolymer. The formation of the bulky sulfoxide moiety in BEH-b-BEHSO PPV does not show expected aggregates. More investigation is being done to reconcile the observed results.

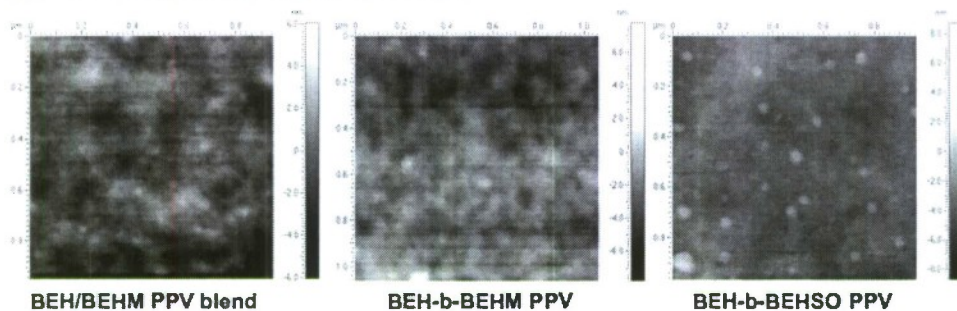


Figure 5. AFM images of BEH/BEHM blend (left), BEH-b-BEHM PPV (middle) and BEH-b-BEHSO PPV (right).

DSC analysis (Table 2) shows the glass-temperatures (T_g) of the PPV homopolymers, the pristine and treated block copolymers that are higher compared to reported values for alkoxy PPV derivatives.

Thin films of BEH PPV, BEHM PPV, and the block copolymers BEH-b-BEHM and BEH-b-BEHSO PPV were analyzed by emission spectroscopy (Figure 6) also. BEHM PPV (yellow) shows an emission maximum of 574 nm without any shoulder. This is probably also due to alkylthio-bulkier side group causing the chains to be farther away from each other. BEH PPV

(blue) shows its characteristic emission maximum at 580 nm with a shoulder at 620 nm. This shoulder (620 nm) can be attributed to inter-chain aggregations. The blend (1:1 w/w) of the two homopolymers shows a broad emission profile with a maximum at 620 nm. This is a 40-50 nm shift when compare to their individual emission profiles and at the moment it is not well understood. However, the pristine block copolymer of BEH and BEHM PPV (green) showed also shows a broad emission with a maximum at 620 nm and with a slight shoulder emission at 700 nm, similar to the blend film.

	T_D (°C)	T_g (°C)
BEH	368	102
BEHM	335	94
BEH- <i>block</i> -BEHM	290	105
BEH- <i>block</i> -BEHSO	200	---

Table 2. TGA (T_D) and DSC (T_g) values for BEH PPV, BEHM PPV, BEH-b-BEHM PPV, and BEH-b-BEHSO PPVs. Decomposition temperature (T_D) at 5% weight loss. T_g : glass-transition temperature.

BEH-b-BEHSO PPV (red), on the other hand, has an emission maximum at 620 nm with a slight shoulder at 580 nm. This phenomena is attributed to the photoluminescence quenching of the BEH PPV segment (580 nm). The peak observed at 620 nm can also be attributed to the aggregation of BEH PPV segments issuing in inter-chain emissions. A small aggregation emission also occurs at 700 nm, attributed to excimers.

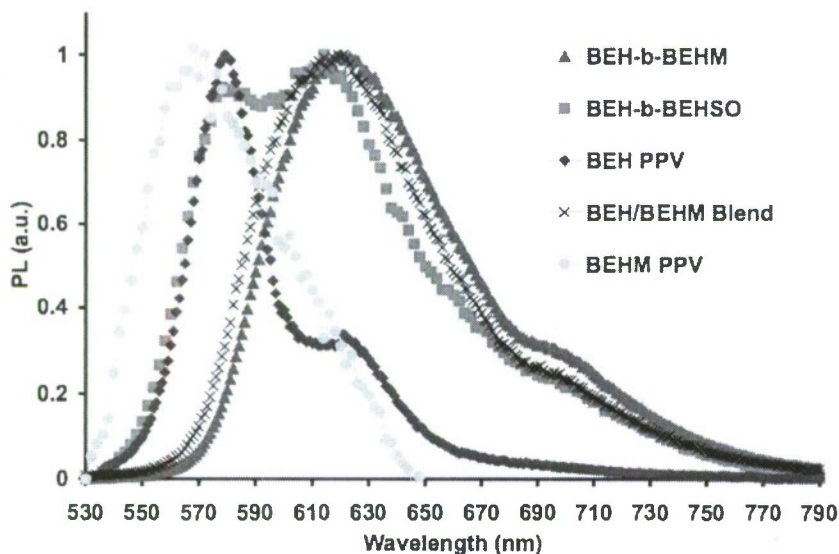


Figure 6. Photoluminescence spectra of BEH PPV (diamonds), BEHM PPV (circles), blend (x's), BEH-b-BEHM PPV (triangles) and BEH-b-BEHSO PPV (squares) block copolymer films.

Collaborations: Plastic Solar Cells.

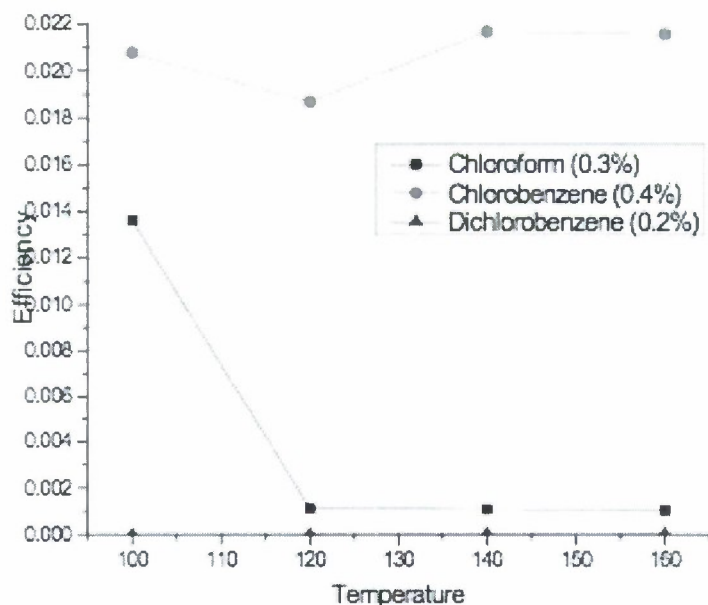


Figure 7. BEH-b-QBAMH PPV photovoltaic performance.

BEH-b-QBAMH PPV was used as the active material in a plastic solar cell fabricated in collaboration with Kamil (NanoTech). Kamil encountered solubility issues, but nevertheless he managed to analyze the performance of the devices. The efficiency of the device was poor at 0.022% (red circles) using chlorobenzene (solvent) and PCBM (4 equiv/w). The polymer was purified using chloroform in a Soxhlet apparatus and will be used again.

Conclusions. The PPV block copolymers comprising BEH PPV, BAMH PPV and BEHM PPV segments were synthesized following the PPV block polymerization synthetic strategy. The chemical modifications were made on the block copolymers of BEH-co-BAMH PPV and BEH-co-BEHM PPV and obtained BEH-co-QBAMH PPV and BEH-co-BEHSO PPV. These were confirmed by FT-IR, TGA, atomic force microscopy and emission spectroscopy (films). Its photovoltaic power conversion was low but optimization is ongoing. Collaboration with Raquel Ovalle using our PPVs in PLEDs, show high luminescence at low threshold voltages. Our efforts are ongoing to include other PPV derivatives having sulfur moieties. Collaboration with Harvey A. Liu with the Kenneth J. Balkus Jr. group, yielded BEH PPV electro-spun fibers and composite fibers with PCBM. Both collaborative works will be submitted for publication

Quantum Dot Sensitized Nanostructured Solar Cells with Charge Multiplication (Anvar Zakhidov)

Most existing semiconducting nanocrystal/conjugated polymer composites are photosensitive only in the visible spectral region, while such composites do not exist for the near infrared spectral range. Therefore, the fundamental problem of further increase of solar light harvesting in artificial photosynthetic systems requires more effective collection of photons from the infrared portion of the solar spectrum as well as more effective utilization of the ultraviolet. The objective is to demonstrate a substantial increase of the efficiency of inexpensive plastic solar cells (SC)

by the use of charge multiplication (CM) in infrared quantum dots-sensitized solar cell and bulk heterojunction hybrid SC. The key idea for achieving this goal is to use the phenomena of charge multiplication (CM) by impact ionization in PbSe quantum dots (QDs) discovered recently by Victor Klimov's team in Los Alamos.

Synthesis of polymers with attached quantum dots. We have developed several new synthetic methods for functionalization of the chains of polyhexylthiophenes (PHTs) and enabled more effective attachment to PbS QDs. Device made with the composite of functionalized P3HT and PbS showed several folds of increase in photocurrent due to better dispersion of QDs within the polymer matrix [1,2]. Carrier multiplication-enhanced photocurrent and photovoltaic response at wavelengths as far to the red as 2 microns were observed. Also we have modified QDs by various ligands exchange (by pyridine, butylamine and octylamine) and found significant increase of photocurrent due to more efficient charge separation due to smaller ligands. In addition, we have successfully prepared PO group functionalized P3HTs (POP3HTs). The POP3HT was then successfully employed in the direct synthesis of PbS nanocrystals without the aid of additional ligands to form the nanocomposites. The devices made of POP3HT-50/PbS are several times more efficient than reported P3HT/PbS device [5]. The improvement of power conversion efficiency is attributed to the better affinity between functionalized polymer and QDs.

IR sensitive PHT/PbS solar cells. We have created new type of PHT/PbSe solar cells and investigated the photovoltaic response of nanocomposites comprised of colloidal, infrared-sensitive, PbSe nanocrystals (NCs) and conjugated polymers of either regioregular poly (3-hexylthiophene) (RR-P3HT) or poly (2-methoxy-5-(2-ethylhexoxy)-1,4-phenylene vinylene (MEH-PPV). The conduction and valence energy levels of PbSe NCs were determined by cyclic voltametry and reveal type II alignment with respect to energy levels in RR-P3HT. Devices composed of NCs and RR-P3HT show good diode characteristics and sizable photovoltaic response in a spectral range from the ultraviolet to the infrared. Using these materials, we have observed photovoltaic response at wavelengths as far to the infrared as 2 microns (0.6 eV), which is desirable due to potential benefits of carrier multiplication (or multiexciton generation) from a single junction photovoltaic. Under bias, the devices also exhibit good photodiode responses over the same spectral region.

CNTs in solar cells. We further developed the concept of 3-D charge collection in polymeric solar cells by a network of carbon nanotubes used as transparent hole collector. A twice increased charge collection efficiency was achieved, and this work, presented at the MRS Spring meeting in San Francisco was awarded the Top 5 Talks/Cool Papers award. If optimized P3HT/PCBM OPV is used, even more dramatic performance enhancement can be expected with a hybrid t-CNT/ITO anode for devices with QDs. The matrices for IR sensitive solar cells, based on chalcogenide opals have been synthesized, for future use with QD/PHT hybrids for the infrared pigments

We have also developed the new concept of cooperative resonance energy transfer in nano-assemblies of CdSe/ZnS quantum dots and polymers and organic dyes, such as porphyrin molecules and have studied experimentally the quenching of photoluminescence in a system of QDs attached to porphyrins. In addition we developed a statistical theory of multiple exciton generation in QDs based on the Fermi approach to the problem of generation of elementary

particles at nucleon-nucleon collision. Our calculations show that the quantum efficiencies of multiple excitons generation in PbSe QDs-CP system at absorption of single photon are in a good agreement with experimental data for dots of different sizes. We also have studied a new type of a promising nanomaterial (ZnO nanotetrapods and their composites with CNTs) for solar cells. It was found that ZnO nanotetrapods show interesting lasing properties, and that a nanocomposite of ZnO/CNT can be a better 3-dimensional charge collector for hybrid solar cells with quantum dots.

Template Derived Semiconductor Nanoparticles for Solar Cells (Ken Balkus)

The research objectives were to develop strategies for the synthesis of semiconductor nanoparticles for solar cells. Specific goals include the synthesis of high aspect ratio, crystalline titanium oxide nanoparticles as well as the configure the titania nanoparticles as core shell structures, fibers, films, nanotubes and highly dispersed composites. Additionally, the semiconductor fibers, nanotubes and single nanocrystals were decorated with metal and semiconductor quantum dots on preferred crystalline faces. Molecular sieves have been employed as templates for the growth of TiO₂ nanofibers < 10nm in diameter. We found that doping the nanofibers with tin oxide enhances the photocatalytic properties. We have also employed block copolymers to template the growth of metal oxide nanofiber sheets. For example, we have prepared partially reduced vanadium oxide and silver nanoparticle decorated nanofibers. These nanofiber sheets were employed as the active layer in an electrochromic device. Lithium ion diffusion rates were measured that me the fastest ever reported. Other applications under investigation include supercapacitors and bolometers. We have also prepared TiO₂ nanotubes (TNTs), typically 10nm in diameter with pores 3nm in size. We have developed a method to support quantum dots (QDs) such as PbS on both the inside and outside the nanotubes. This involves treating the TNTs with a thiolactic acid linker (TLA) followed by dip coating with Pb²⁺ ions and Na₂S. By controlling the concentration of linker the size of the resulting PbS quantum dots can be controlled. This is important since the band gap and multiple exciton generation depend on size. By wrapping the TNT with a surfactant, we have functionalized the TNT with QDs only on the inside and not on the outside. Interestingly, heating these TNT composites results in stable TNTs with PbS nanorods inside the pores. Normally the TNT would collapse and PbS nanorods with controlled size are difficult to make. We can also cover the outside surface only by using a pulsed laser ablation technique. This involves vibrating the TNTs in a laser generated plume of semiconductor material. This was demonstrated using titanium silicide which has been shown to be an effective catalyst for splitting water. Other metal oxide and phosphate materials with interesting optical properties have been synthesized using conventional hydrothermal techniques as well as microwave heating. Significant changes in purity, morphology and emission properties were found with microwave based syntheses.

Development of Nanostructures for Negative Refraction at IR and Visible: Opal/Inverse Opal Infiltrated with Quantum Dots and Gain Media (Ali Aliev)

The goal of research was to demonstrate the negative phase velocity in 3D photonic crystal on the basis of direct silica opal. Our previous study (2005-2007) of negative refraction in 3D photonic crystals ended by demonstration of "wrong bended" laser beam propagating in medium with negative group velocity. For the first time the negative refraction in bulk 3D Photonic Crystals is demonstrated experimentally in visible, particularly at 405 and 488 nm. Using a prism of SiO₂ opal filled with various high refractive index liquids we demonstrated a "wrong way" bended beam observed at incident light energies and angles corresponding to a group velocity

directed opposite to k -vector in a second Brillouin zone. The bended beam has wide distributed cone due to a diffractive nature of phenomena. On the last stage we confirmed that the phase of light with energy corresponding to the second Brillouin zone has opposite sign to the group velocity and opposite to the phase in air.

Pulsed Plasma Synthesis of New Nanostructured Inorganic/Organic Composite Materials (Larry Overzet)

This research was a collaboration between UTD (Overzet and Goeckner) and UTA (Timmons). A new approach to the synthesis of flexible, nanostructured organic/inorganic composite films is being explored. It involves spraying micro-droplets of liquid into low pressure plasma. This new technology will permit systematic and controlled variations in film compositions with respect to an incorporating organic matrix. In particular, it will allow one to control the extent of loading of metal containing (i.e. ceramic like) nanoparticles. While the well known Plasma Enhanced Chemical Vapor Deposition (PECVD) technique is used to synthesize the films; several innovative experimental factors distinguish our work and are being developed as part of this research. The key innovation is: *The introduction mode of an organic / inorganic liquid mixture into the plasma reactor*. For this purpose, we chose to directly inject the liquid mixture that consists of metal(s) or mixed metal organometallic compound(s) dissolved in a volatile organic solvent (e.g. ethanol, benzene or hexane). This liquid mixture is injected directly into the reactor as micron sized droplets upstream of the plasma discharge zone via an atomizer on a fuel injector. A second innovation will be: *The use of variable duty cycle pulsed plasmas in lieu of the conventional CW approach*. Variations in the pulsed plasma duty cycle employed to generate the composite films will be utilized to provide further control of film compositions. Our research centers on proof of concept of these innovations and requires development of the tools and fundamental techniques.

Initially, the UT Arlington group was to grow films using a Benzene-Ferrocene liquid mixture. Unfortunately they immediately ran into trouble with the Ferrocene solidifying at the port of their (long) glass injection nozzle. The evaporating Benzene, left behind the Ferrocene in the nozzle both clogging the nozzle and causing the nozzle to freeze. (The latent heat of vaporization of the Benzene caused the nozzle temperature to drop.) They tried heating the nozzle and controlling the fluid flow more precisely, but to no avail. Consequently, we jointly decided that both the UTA and UTD groups would begin looking into other means for fluid injection into the low pressure plasma reactor. This took precedence over our first goals in the proposal (diagnosing the plasma state and electrical measurements of the resulting films.)

In this we have now made good progress, although we still have significant work to do. We decided to try incorporating a fuel injector as the liquid injection port rather than the long glass micro-tube initially employed at UTA. The glass tube limited liquid flow (and injection) by the low conductance of its' micro-sized bore, but the fuel injector limits liquid flow by sealing itself shut using it's fast acting mechanical valve. We have been able to characterize the fuel injector performance into vacuum using various solvent liquids (ethanol for example) and have proven that: (1) the injection into vacuum can result in complete vaporization of the liquid injected, (2) we can control the vapor pressure in the plasma region well while performing liquid injection, and (3) we can produce stable and well confined plasma during liquid injection and use that plasma to grow films.

A schematic diagram of our prototype reactor is shown in Fig. 1. The reactor is approximately 18 inches long with a Toyota fuel injector attached at the top flange. The fuel injector is found to hold vacuum well (when closed) with an absolute leak rate of approximately 1.7×10^{-9} Torr l/s (1.3×10^{-7} sccm) with roughly 10 psi of helium behind it. The injector has 12 ports, so that the liquid flowing through it is divided into 12 streams that are nominally equal. The 12 ports are shown in Fig. 2 for the fuel injector inserted into its' 2.75" conflat vacuum flange. Each port is approximately $150 \mu\text{m}$ in diameter and the entire fuel injector is approximately 0.36" (9 mm) in diameter.

The reactor consists of a 4" conflat cross attached to a 4" 6-way cross below. The bottom-most port of the 6-way cross has a capacitively coupled driven electrode inserted into it. The electrode acts as the wafer chuck and plasma source so that plasma is generated in the lower chamber. It has a door on it for loading wafers onto the wafer chuck. The reactor also has heater elements surrounding it to allow the chamber temperature to be controlled as well as the liquid temperature at the input to the fuel injector.



Fig. 2. The 12 fuel injector ports for our prototype reactor. The fuel injector is inserted into a specially modified 2.75 inch conflate flange.

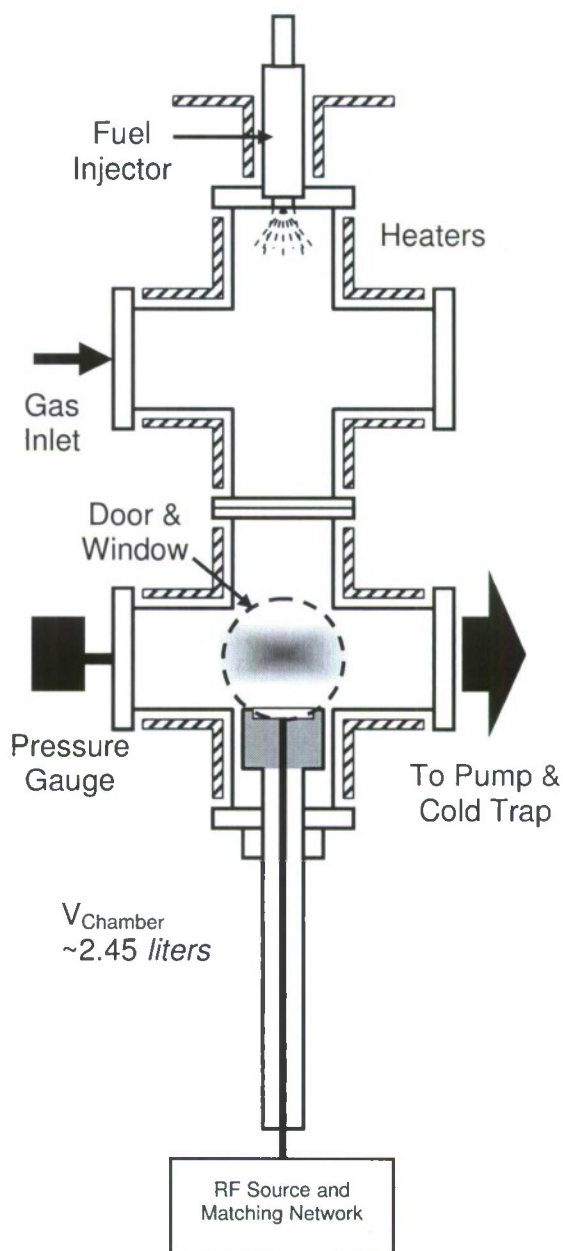
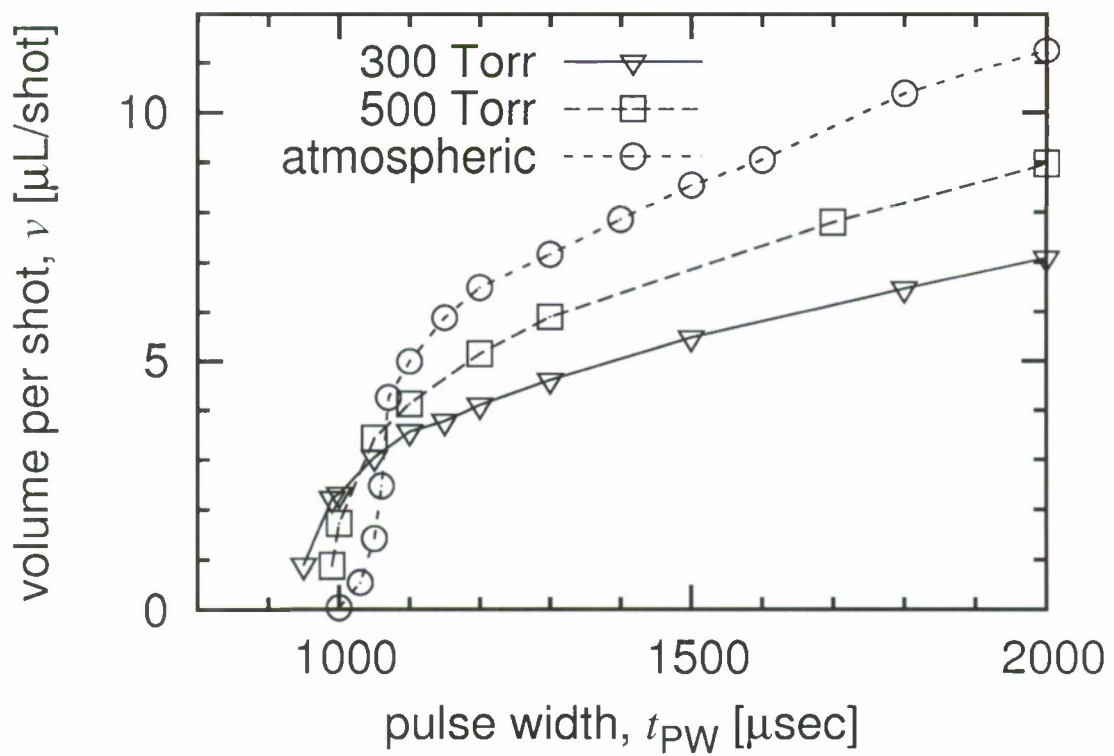


Fig. 1. A schematic of the prototype reactor. The fuel injector sits at the top and injects liquid into the reactor where it evaporates and is ignited into plasma by the rf voltage on the electrode at the bottom. Heaters on the chamber walls help to set the evaporation rate for various liquids.



(a)



(b)

Fig. 3. (a) ICCD camera picture of the droplet spray from the fuel injector showing the atomization of the liquid. (b) The amount of liquid injected into the reactor per pulse as a function of the pulse duration and input side pressure.

Liquid injection through the fuel injector into both atmosphere and vacuum have been studied and example results are shown in Fig. 3. In figure 3 (a) we injected ethanol into the atmosphere by putting excess gas pressure on the input side of the fuel injector. The resulting spray was measured as a function of time using forward scattering of a HeNe laser beam. This was used to find the average droplet speed. It was found that droplets exit the fuel injector with approximately 9 to 16 m/s velocities. Consequently, they can traverse our entire reactor in several 10's of milliseconds. This is fast compared to the expected evaporation times.

Figure 3(b) shows the amount of liquid volume injected through the fuel injector into vacuum as a function of the pulse width applied and the gas pressure behind the liquid. It is evident that we have the ability to inject small quantities of liquid (less than 1 micro-liter per shot) using this fuel injector. Further, the amount of liquid injected is controllable using the input side pressure. Finally, the pressure differential across the fuel injector does affect the time required to open. At large input side pressures the time to open increases; while at lower pressures the valve is able to open more quickly.

Using this system we have deposited a variety of films. Example pictures of two films are shown in Fig. 4. By controlling the plasma conditions and the liquid injection conditions, it is possible to produce films having very smooth morphology as shown in the top picture. The film there was produced by injecting hexane into argon plasma. The Argon plasma cracks the hexane to form reactive radicals which then deposit the film. Clearly the droplets have been evaporated in the plasma before impacting the growing film; otherwise we would see evidence of such impacts. The lower film was grown by injecting hexane having Fe nano-particles dispersed in it. The iron nanoparticles clearly have agglomerated into circles in the resulting film. This agglomeration of iron into rings can be greatly reduced (so that such rings are no longer visible) however; the visibility of the iron in this micrograph demonstrates the ability to form metal particle rich films by the technique. We have been able to measure up to 4.3% iron by volume in the films deposited to date. This is well beyond the iron in ferrocene for example (3.6%) The sizes of the iron circles in this lower film are comparable to the expected droplet size and likely indicates

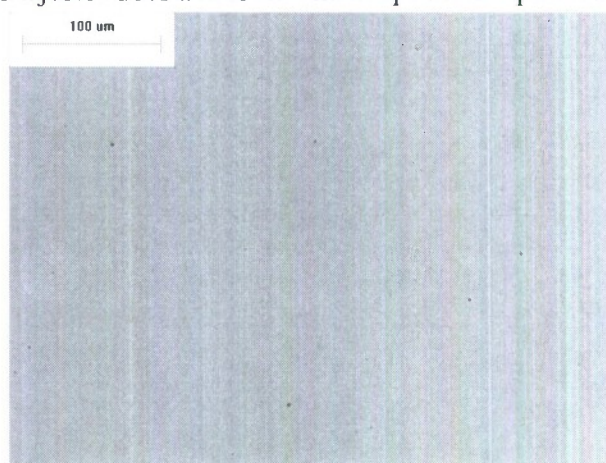
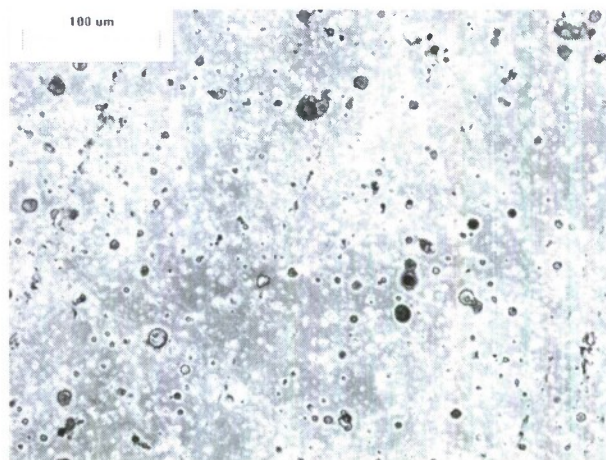


Fig. 4. Microscope images of two films produced by direct liquid injection. (Top) A film produced using pure hexane injection to argon plasma. (Bottom) A film produced by injecting hexane containing iron nano-particles into argon plasma.



that the droplets did not fully evaporate under those growth conditions.

Figure 5 shows the film growth rates for ethanol and hexane injection. As expected the growth rate is unaffected by the injection period, but does depend upon the precursor (ethanol or hexane). It is interesting to note that the deposition rate when injecting hexane is much larger than when injecting ethanol, but it would take significant effort beyond what was accomplished using this seed funding to determine the causes for this difference.

We have also modeled the droplet evaporation process. We have made estimates of the droplet evaporation time as a function of initial droplet size and temperature, as well as the presence of plasma. The various processes included in this model are shown in Fig. 6. They include: Gas heating (energy brought to the droplet by gas molecules), vapor heating (energy brought to the droplet by vapor molecules), radiation heating or cooling, evaporation (energy and mass lost from the droplet) and condensation as well as heating caused by the surface recombination of electrons and ions.

In a vacuum environment, the initial flux of evaporating solvent from the droplet will greatly exceed the flux of gas phase molecules impinging on the droplet. As a consequence, the temperature of the droplet decreases as molecules evaporate off it. This decrease in droplet temperature reduces the evaporation rate and extends the evaporation time. At some point, the temperature of the droplet becomes low enough and the evaporation rate becomes slow enough that energy brought to the droplet balances energy taken from it in evaporation events. When this is the case, the temperature of the droplet reaches a steady state and the evaporation rate becomes essentially constant in time.

This is shown in the model results of Fig. 7. The model was for 25 micron radius droplets of various solvents injected into a low pressure environment (100 mTorr) at an initial temperature

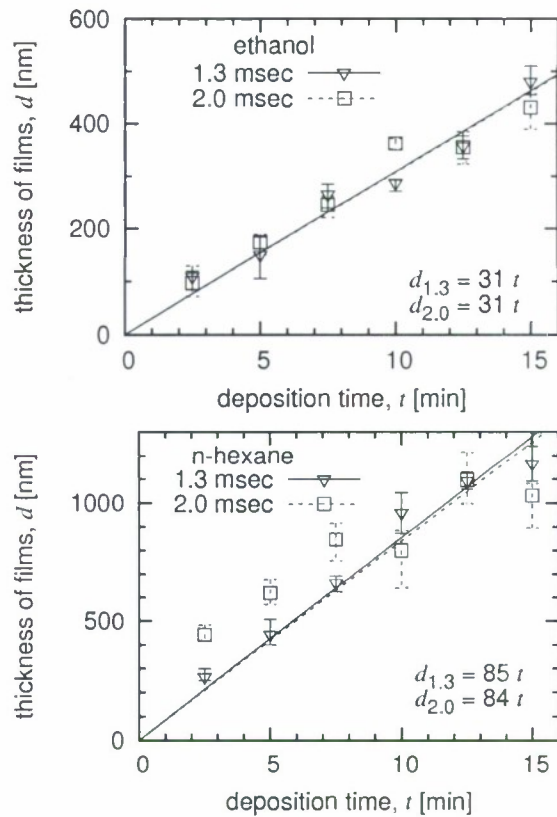


Fig. 5. Deposition rates for (Top) ethanol and (Bottom) hexane injections into an argon plasma.

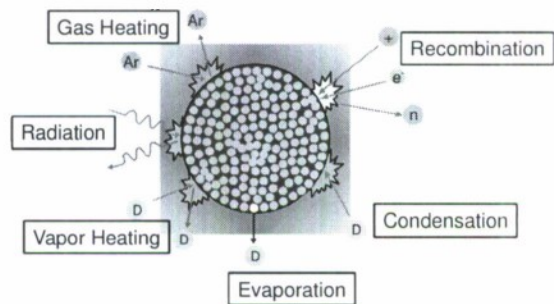
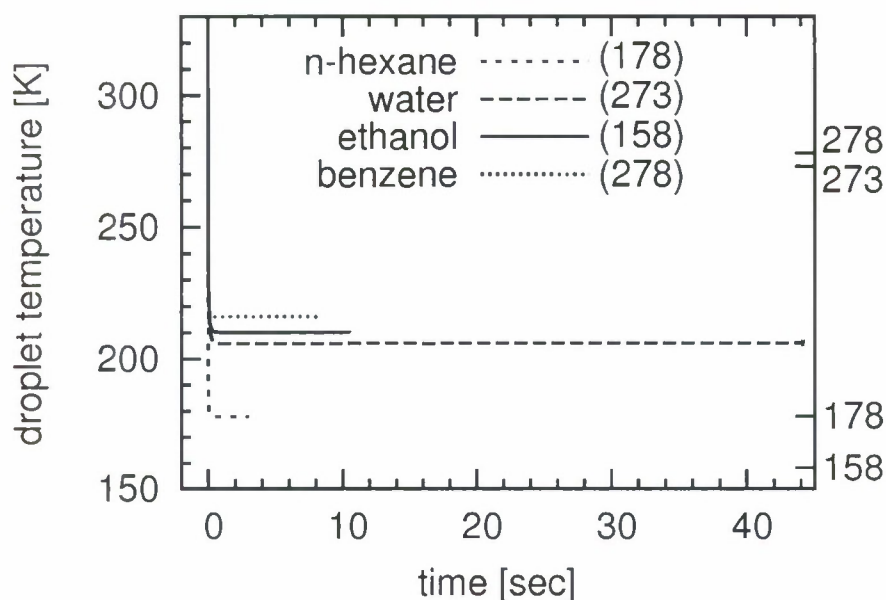


Fig. 6. The processes occurring on the surface of a liquid droplet which either bring heat and/or mass to the droplet or take them away.



of 325 Kelvin. The droplets immediately begin to evaporate and cool. As one can see in Fig. 7, the cooling is very fast compared to the total evaporation time for all the solvents modeled. In fact, the evaporation times were found to be of order of seconds (as much as 45 seconds for water) while this cooling time was of the order of milliseconds. In Fig. 7, one can also see that both water and benzene cool to well below the freezing temperature, while water and ethanol remain slightly above freezing. (The freezing temperatures are listed for each solvent in the legend and their locations on the right axis.)

Incorporating plasmas does two things. First it brings additional energy to the surface of the droplet in the form of recombining electrons and ions. Second, it brings net charge to the surface (since free electrons can flow to the surface faster than positive ions). As a consequence, the droplet interacts with the plasma in two fashions and evaporation is influenced by both the additional energy brought and by the surface stresses caused by the net surface charge. We have been able to estimate how the additional energy brought to the droplet by surface recombination affects evaporation; but we have not yet dealt with the charging to our satisfaction. The latter will require a much more extensive model. We see that the additional energy brought by plasma can dramatically reduce the evaporation times of droplets in a controllable fashion. This is shown in Fig. 8. The evaporation time can be reduced from seconds to 10's of milliseconds simply by controlling the plasma density around the evaporating droplets.

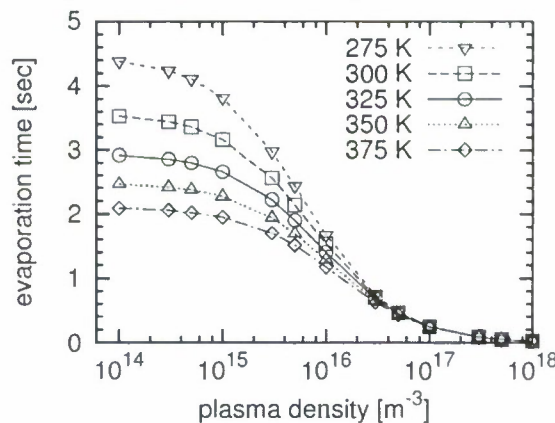


Fig.8. The time to complete evaporation of 25 micron radius hexane droplets as a function of the initial droplet temperature and the density of plasma.

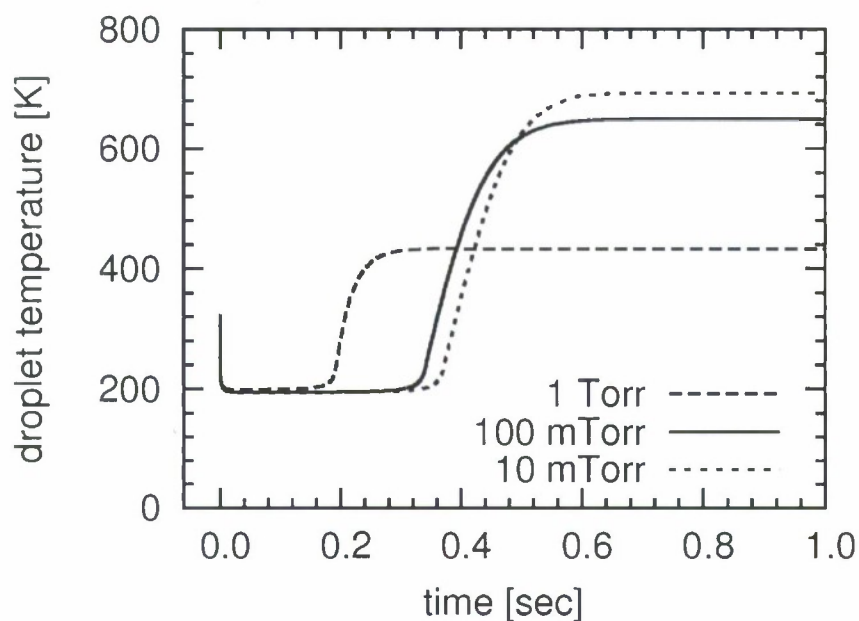


Fig. 9. The figure shows the temperature as a function of time for an evaporating droplet having a solute that does not evaporate. The temperature initially decreases due to solvent evaporation, but after the solvent has fully evaporated, the temperature of the remaining solute can rise by over 500 Kelvin. This can all occur in less than 1 second.

Related to this, we have incorporated non-evaporable solutes (for examples: Fe nano-particles and ferrocene) into the modeled solvent and simulated the evaporation. This is analogous to what we have shown in Fig. 5. There, we incorporated Fe nano-particles into hexane solvent a deposited films. Here we are modeling that processes to see how the droplet evaporation progresses in time. What we find is that the solvent evaporation does not change dramatically, but the solute can be made to undergo a somewhat interesting temperature fluctuation. This is shown in Fig. 9. The temperature of the droplet initially decreases as seen previously because of solvent evaporation. But after the solvent has fully evaporated, the remaining solute is heated by the plasma and can reach large temperatures (~500 to 700 Kelvin). All this can occur in the space of less than one second.

PDF files of publications resulting from SPRING supported efforts that have not been previously submitted follow.

Donor-Acceptor Functionalized PPV Di-Block Copolymers for Plastic Solar Cells

Danny Zapeda, Josa J. Gutierrez and John P. Farraris

Department of Chemistry, University of Texas at Dallas, P.O. Box 830688, Richardson, Texas 75083-0688

INTRODUCTION

Plastic solar cells (PSCs), consisting of PPV derivatives and 1-(3-methoxycarbonyl)propyl-1-phenyl [6.6] C61 (PCBM) block heterojunction have demonstrated a power conversion efficiency of up to 2.5%.¹⁻² The performance of these solar cells can be attributed to the photo-induced electron generation in the PPV derivative and the efficient electron transfer to the PCBM. Although a high efficiency is exhibited at the donor/acceptor interface, the charge carrier mobility is still limited by the phase separation of the PPV and the PCBM due to their incompatibility. The PCBM aggregation reduces the donor/acceptor interfaces by creating numerous donor/acceptor domain sizes that are greater than the required exciton diffusion length (10-20 nm).¹⁻³

The ideal bulk heterojunction for photovoltaic devices requires the morphology of the donor/acceptor system to be two continuous phases where each phase has a size on the order of the average exciton diffusion length (10-20 nm scale).¹ The desired nano-structured donor/acceptor domains may not be obtained through blends, but can in principle be reached using diblock copolymers.⁴ Diblock copolymers are known to phase separate into ordered micro-phases on the same scale as the macromolecules' radii of gyration (10-50 nm).⁴⁻⁶

We have designed and synthesized PPV diblock copolymers consisting electron donor and electron acceptor segments (D-A). The synthesis of the PPV block copolymers: poly[1,4-bis-2-ethylhexyloxy]-block-[1,4-bis-N,N',N''dimethylhexylammonium]-2,5-phenylenevinylene (BEH-b-QBAMH PPV) and, poly[1,4-bis-2-ethylhexyloxy]-block-[1,4-bis-2-ethylhexyl-sulfinyl]-2,5-phenylene vinylene (BEH-b-BEHSO PPV) present potential donor/acceptor block systems due to the electron donating effects of the tertiary amine and alkoxy groups and the electron withdrawing effects of the sulfinyl and the quaternary ammonium moieties.

EXPERIMENTAL

All reagents were commercially available and used as received unless otherwise stated. THF was dried prior to use. BAMH PPV precursor monomer was provided by Dr. Pete Zarras of the U.S. Naval Airfare Center.

Block Copolymer Synthesis. (BEH-b-BAMH PPV 3:1): BEH PPV monomer (0.75g, 1.5 mmol) dissolved in 20 ml dry THF was injected at 1 ml/hr using a KDS (series 200) syringe-pump into a basic solution containing potassium tert-butoxide (3.0 g, 27 mmol) and p-methoxyphenol (4.6 mg, 2.5 mole % to monomer) and stirred at 250 rpm (IKA EuroStar Dissolver Stirrer), at 0 °C, under nitrogen atmosphere. After monomer addition, the reaction mixture was left to stir for one hour. At the end of the aging process, an aliquot (15 ml) was taken and injected into rapidly stirred methanol (400 ml). The red polymer was collected and dried under vacuum. A sample of this polymer was subjected to molecular weight analysis using a Viscotek TDA 302 equipped with two Viscotek TSK GMHR-H (7.8 mm x 30.0 cm) columns with THF elution (193 ± 9% kDa).

BAMH PPV monomer (3.0 g, 7.5 mmol) dissolved in 20 ml dry THF was then injected to the already formed BEH PPV at 1 ml/hr using the syringe-pump. The reaction was aged for three hours, and then injected into rapidly stirred methanol (1L). A red-orange polymer was collected on a Millipore Durapore® 0.45 µm membrane filter and dried under vacuum at 50 °C. The polymerization yield was 73%. The polymer was purified through Soxhlet extraction using hexanes. Molecular weight analysis: 323 kDa ± 40%) 1H-NMR (CDCl₃, 270 MHz): δ 7.84-7.35 (q, 4H Arom), 4.06-3.75 (d, 1H Ph-O-CH₂-CH-), 3.08 -2.60 (d, 12H Ph-N-CH₃-CH₂-), 1.90-1.75 (s, 1H Ph-O-CH₂-CH-

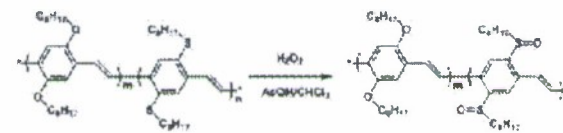
CH₂), 1.70-0.65 (m, 50H, -N(O)-CH₂-CH-(CH₂)_x-(CH₃)_x). UV-Vis absorption λ_{max}: 481 nm. Emission λ_{max}: 551 nm. FT-IR (KBr, cm⁻¹): 3060, 2930, 2860, 1630, 1510, 1470, 1420, 1380, 1360, 1260, 1200, 1090, 1040, 966, 860, 773, 729.

BEH-b-BEHM PPV (12:1 ratio) was synthesized and characterized in the same manner as described above.



Scheme 1 N-methylation of BEH-b-BAMH PPV

Chemical Modifications of Block Copolymers. (Scheme 1: N-methylation) BEH-b-BAMH PPV (0.1 g) was dissolved in dichloromethane (75 ml) and purged with nitrogen. Methyl triflate (10 equiv) was added and the reaction was left stirring for 24 hours. The solvent was then removed in vacuum. The polymer was then dissolved in THF (100 ml) and the solvent was removed in vacuum. Recovered amount: 0.09 g. Spectroscopic analysis showed a slight change in the absorption maxima from 497 nm relative to the starting material (496 nm). ¹H-NMR (CDCl₃, 270 MHz): δ 7.7-7.4 (s, Arom), 4.2-3.6 (s, Ph-O-CH₂-CH-; Ph-N⁺-(CH₃)₂-CH₂-), 1.90-1.75 (s, Ph-O-CH₂-CH-CH₂), 1.70-0.65 (m, 50). UV-Vis absorption λ_{max}: 497 nm. Emission λ_{max}: 556 nm.



Scheme 2. Oxidation of BEH-b-BEHM PPV

(Scheme 2: Oxidation) BEH-co-BEHM PPV (0.10 g) was dissolved in 100 ml dichloromethane at room temperature. Acetic acid (1 ml) and hydrogen peroxide (35%, 2 ml) were then added. The solution was left stirring for two hours where a red colored solution (previously clear orange-red) was observed. An aliquot was taken and absorption/emission spectroscopy showed no change in absorption or emission maxima. To prevent any oxidation of the vinyl groups, the reaction was then quenched with 50 ml 5% sodium bicarbonate solution after eight hours. The organic layer was washed with 50 ml of 5% sodium bicarbonate solution, collected, and dried over magnesium sulfate. The solvent was removed under reduced pressure and a dark red polymer was obtained. It was dried in vacuum at 40 °C for 5 hours. The collected polymer amounted to 0.095 g. ¹H-NMR (CDCl₃, 270 MHz): δ 7.75-7.40 (s, Arom), 4.10-3.70 (s, Ph-O-CH₂-CH-; Ph-S=O-CH₂-CH-), 1.90-1.75 (s, Ph-O-CH₂-CH-CH₂), 1.70-0.50 (m, -S(O)₂-CH₂-CH-(CH₂)_x-(CH₃)_x). UV-Vis absorption λ_{max}: 501 nm Emission λ_{max}: 560 nm. FT-IR (KBr, cm⁻¹): 1040 (S=O).

RESULTS AND DISCUSSION

Block copolymers comprising BEH PPV, BAMH PPV and BEHM PPV were synthesized as intermediates to the target acceptor-donor block copolymers. BEH-b-BAMH PPV and BEH-b-BEHM PPV with 3:1 and 12:1 block ratios were synthesized following the modified Gilch route.⁷⁻⁶ Various analytical techniques (GPC, ¹H-NMR, UV-Vis, PL) were used to characterize the block copolymers synthesized.

Table 1. PPV DI-Block Copolymer Data Table

PPV	Block Ratio	Yield (%)	MW (kDa)	UV-Vis
BEH-b-BAMH (BEHM)	2.5	73	323 ± 40 (193 ± 9)	481/551
BEH-b-BEHM (BEHM)	1.75	21	273 ± 30 (217 ± 26)	500/562

¹ First monomer injected
² p-methoxyphenol

From Table 1 we observed that the BEH-b-BAMH PPV diblock copolymer shows an increase in molecular weight from the intermediate product (BEH PPV, 193 kDa), to the final block (BEH-b-BAMH PPV, 323 kDa). As for BEH-b-BEHM PPV, we observed a smaller increase from the intermediate product (BEH PPV, 217 kDa) to the final block (BEH-b-BEHM PPV, 273 kDa). Figure 1 shows the UV-Visible absorption and photoluminescence spectra of BEH-b-BAMH PPV (green) and BEH-b-BEHM PPV (red). The spectra were

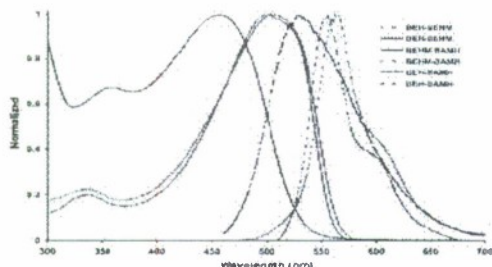


Figure 1. UV-Visible absorption (solid) and photoluminescence (dotted) spectra of the PPV block copolymers

obtained from 10^{-5} M solutions in THF. The BEH-b-BAMH PPV block copolymer has an absorption maximum of 481 nm and emission maximum 551 nm. BEH-b-BEHM PPV has an absorption maximum of 500 nm and emission maximum 562 nm. The block copolymers have characteristics of BEH PPV, BAMH PPV and BEHM PPV homopolymers, respectively, that indicate the incorporation of both segments into a block copolymer.

Chemical Modifications on PPV Di-Block Copolymers. The N-methylation of the tertiary amine moiety on the BAMH segment of the block copolymer BEH-b-BAMH PPV was done using methyl triflate. From Figure 2 the methyl protons adjacent of the tertiary

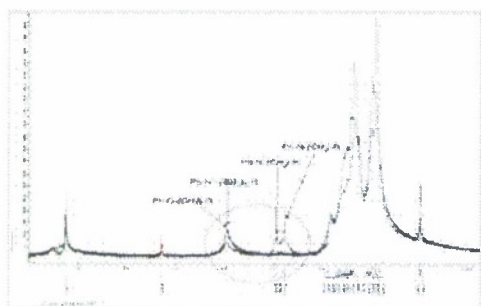


Figure 2. Proton NMR comparison of BEH-b-BAMH PPV (dotted line) and BEH-b-QBAMH PPV (solid line).

amine moiety (2.9 ppm) in the BAMH segment have shifted and overlap with the methylene protons of the ether moiety in the BEH segment. Although there is no significant change in the absorption and emission maxima from the pristine block copolymer (red) to the treated block copolymer (blue), photoluminescence quenching is observed in the following figure (Figure 3).

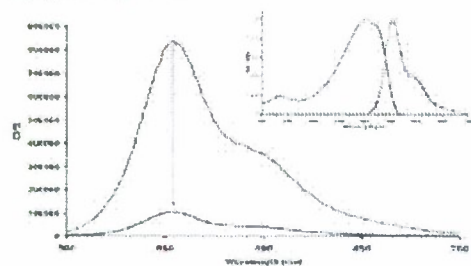


Figure 3. Photoluminescence analysis of BEH-b-BAMH PPV (red) and BEH-b-QBAMH PPV (blue).

The oxidation of the thioether moiety on the BEHM segment of the block copolymer BEH-b-BEHM was done using hydrogen peroxide and glacial acetic acid. In Figure 4 the absorption of methylene

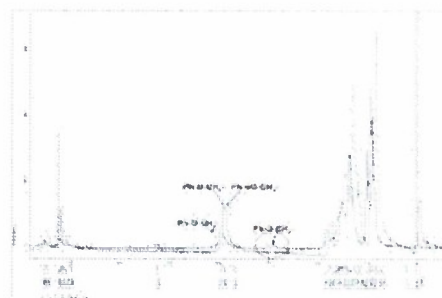


Figure 4. Proton NMR comparison of BEH-b-BEHM PPV (solid line) and BEH-b-BEHSO PPV (dotted line).

protons of the thioether moiety (2.95 ppm) shifts as a result of the oxidation of the sulfur to a sulfoxide (3.9 ppm). There is no significant change in the absorption and emission maxima from the pristine block copolymer to the treated block copolymer, but a small shoulder is observed at 500 nm in the emission of the treated block due to the low amount of BEHSO block segment within the block copolymer (inset spectra). Photoluminescence quenching is also observed in this block copolymer following figure (Figure 5).

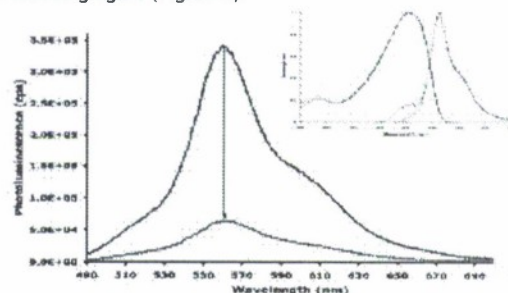


Figure 5. Photoluminescence analysis of BEH-b-BEHM PPV (blue) and BEH-b-BEHSO PPV (red).

CONCLUSION

The PPV diblock copolymers comprising BEH PPV, BAMH PPV and BEHM PPV segments were synthesized following the PPV block polymerization synthetic strategy.^{7,8} The chemical modifications were made on the diblock copolymers of BEH-co-BAMH PPV and BEH-co-BEHM PPV and obtained BEH-co-QBAMH PPV and BEH-co-BEHSO PPV. These were confirmed by GPC, ¹HNMR, FT-IR, excitation/emission spectroscopy.

ACKNOWLEDGEMENTS

We would like to thank SPRING, U.S. Air Force and the U.S. Naval Airwarfare Center for their financial support.

REFERENCES

- Hoope, H.; Sariciftci, N. S.; *J. Mater. Chem.*, 2006, 16, 45-61
- Chang, E.C.; Chao, C.I.; Lee, R.H.; *J. App. Polym. Sci.*, 2006, 101, 1919-19243.
- Kraabel, B.; Hummelen J.C.; Vacar, D.; Sariciftci, N.S.; Heeger, A.J.; Wudl, F.; *J. Chem. Phys.*, 1996, 104 (11), 15
- Stalmach, B. *et al*; *J. Am. Chem. Soc.*, 2000, 122, 5464-5472
- Van de Wetering, K. *et al*; *Macromolecules*, 2006, 39, 4289-4297.
- Sun, S.S.; Bonner, C.E.; *Synthetic Metals*, 2005, 154, 65-68
- Neef, C. J.; Ferraris, J. P.; *Macromolecules* 2000, 33, 2311-2314
- Ferraris J. P.; Gutierrez, J.J.; *U.S. Patent* 7,135,241 Nov 1, 2006 22 pp

resulting polymer was completely soluble in both THF and chloroform ($M_w = 169,031$, $PDI = 2.84$).

The increase in polymerization yield at low temperature was also observed in the synthesis of BEHM-PPV (entries 5 and 6). However, unlike BDMOM-PPV, the polymerization yield was only 43 %. Moreover, the soluble fraction corresponded to only 31 % yield. This result suggests that the incorporation of the 3,7-dimethyl octyl chain was effective in improving the solubility of the sulfur-containing PPV. The fact that the yield is so much lower at room temperature suggests that side reactions may be taking place at room temperature. The polymerization mechanism is currently under study.

Figure 1 shows the $^1\text{H-NMR}$ spectrum of BDMOM-PPV and the polymer precursor. Note that the polymer lacks the signal for the bromomethyl protons (4.61 ppm). A new signal appears at 7.66 ppm, corresponding to the vinyl protons. Additionally, the signal for the aromatic protons is shifted down-field (7.56 ppm) compared to that of the aromatic protons in the monomer (7.34 ppm).

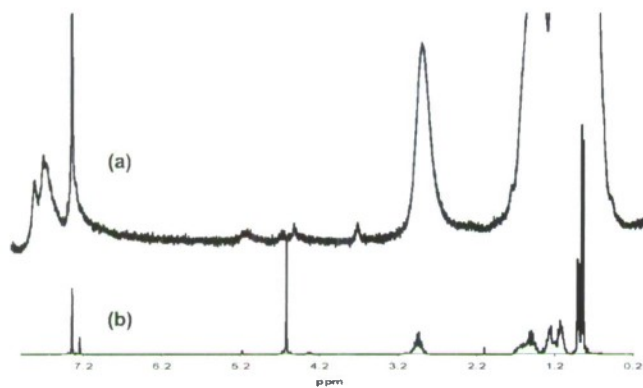


Figure 1. $^1\text{H-NMR}$ spectrum of BDMOM-PPV (a) and its precursor (b)

Figure 2 shows the absorption (solid line) and emission (dotted line) spectra of BDMOM-PPV. The spectra were obtained from 10^{-5}M solutions in THF.

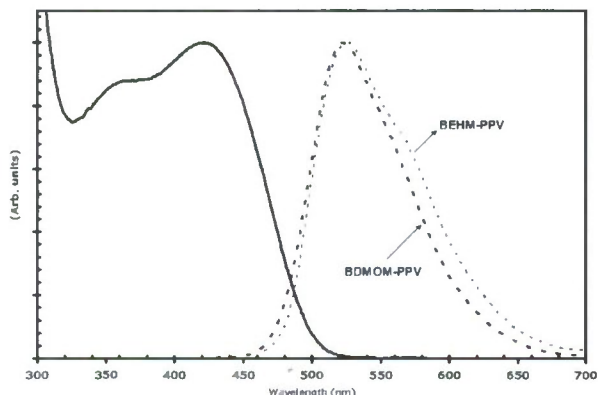


Figure 2. UV-Visible absorption (solid) and photoluminescence (dotted) spectra of BDMOM-PPV

BDMOM-PPV displays an absorption maximum at 425 nm with a shoulder at 360 nm. This corresponds to the absorption spectrum of BEHM-PPV reported previously. The emission spectrum of both BDMOM-PPV and BEHM-PPV display a maximum at 525 nm. However, the emission profile of BEHM-PPV (Figure 2) is broader, with a shoulder at around 670 nm. This has been attributed to interchain interactions between polymer strands.¹² The sharper emission of BDMOM-PPV may be attributed to the introduction of a bulkier side chain compared with BEHM-PPV. The bulky side chain impedes polymer aggregation.

CONCLUSIONS

A novel sulfur-containing PPV was successfully prepared in high yield at 0 °C. The resulting polymer was completely soluble in THF and chloroform and displayed a molecular weight of 169,031 with a polydispersity of 2.84. The incorporation of a bulkier side chain resulted in increased polymerization yield and solubility compared to other sulfur-containing PPVs. The emission spectrum of BDMOM-PPV was sharper compared with other sulfur-containing PPVs. This was also attributed to the introduction of the bulky side chain, which impeded polymer aggregation.

ACKNOWLEDGEMENTS

We would like to thank the Welch Foundation (grant number BG-0017) and the UTPA Faculty Research Council (grant number 135 CHEM 02) for their support of this work.

REFERENCES

- Kraft, A.; Grimsdale, A. C.; Holmes, A. B. *Angew. Chem., Int. Ed.* **1998**, *37*, 403-428.
- Zhang, F. L.; Johansson, M.; Andersson, M. R.; Hummelen, J. C.; Inganäs, O. *Synthetic Metals* **2003**, *137*, 1401-1402.
- Zhou, Q.; Zheng, L.; Sun, D.; Deng, X.; Yu, G.; Cao, Y. *Synthetic Metals* **2003**, *135-136*, 825-826.
- Munters, T.; Martens, T.; Goris, L.; Vrindts, V.; Manca, J.; Lutsen, L.; De Ceuninck, W.; Vanderzande, D.; De Schepper, L.; Gelan, J.; Sariciftci, N. S.; Brabec, C. J. *Thin Solid Films* **2002**, *403-404*, 247-251.
- Yoon, C.-B.; Kang, I.-N.; Shim, H.-K. *Journal of Polymer Science, Part A: Polymer Chemistry* **1997**, *35*, 2253-2258.
- Shim, H. K.; Yoon, C. B.; Ahn, T.; Hwang, D. H.; Zyung, T. *Synthetic Metals* **1999**, *101*, 134-135.
- Haliburton, J. H.; Sun, S.-S. *Polymer Preprints (American Chemical Society, Division of Polymer Chemistry)* **2003**, *44*, 890.
- Sun, S.; Fan, Z.; Wang, Y.; Haliburton, J.; Taft, C.; Maaref, S.; Seo, K.; Bonner, C. E. *Synthetic Metals* **2003**, *137*, 883-884.
- Sun, S.-S.; Fan, Z.; Wang, Y.; Taft, C.; Haliburton, J. H.; Maaref, S. *Proceedings of SPIE-The International Society for Optical Engineering* **2003**, *4801*, 114-124.
- Sun, S.-S. *Polymeric Materials Science and Engineering*, **2003**, *88*, 158.
- Gutierrez, J. J.; Luong, N.; Zepeda, D.; Ferraris, J. P. *Polymer reprints* **2004**, *45*, 172-173.
- Hou, J.; Fan, B.; Huo, L.; He, C.; Yang, C.; Li, Y.; *Journal of Polymer Science Part A: Polymer Chemistry* **2006**, *44*, 1279-1290.

Mesoporous Molecular Sieve Derived TiO₂ Nanofibers Doped with SnO₂

Chunrong Xiong and Kenneth J. Balkus, Jr.*

Department of Chemistry and the UTD Nanotech Institute, The University of Texas at Dallas, Richardson, Texas 75083-0688

Received: March 15, 2007; In Final Form: May 10, 2007

Mesoporous silica spheres were used as templates to prepare 5 to ~10 nm Sn doped TiO₂ (TDT) nanofibers using SnCl₄ and TiCl₄ as precursors. The as-made nanofibers were crystalline anatase but transformed into the rutile phase after annealing above 700 °C. The Sn dopant amount in the TDT nanofibers can be controlled by changing the molar ratio of SnCl₄ to TiCl₄. The dopant Sn atoms were incorporated into the anatase lattice at a level of ~15%. The photodegradation of various dyes was catalyzed by the TDT nanofibers and was shown to be more effective than P25 and the undoped TiO₂ nanofibers.

Introduction

Both efficient light-to-energy conversion and photooxidation of organics require avoiding the accumulation of electrons on metal oxide semiconductors that would increase the recombination rate of electron hole pairs. The anatase phase of TiO₂ is often considered to be the most suitable material for widespread environmental applications due to its high photoelectrochemical activity and its stability with respect to photo and chemical corrosion.¹ However, due to inefficient use of photogenerated electron hole pairs, further studies are needed to improve the activity of this semiconductor. Suppression of the recombination of photogenerated electrons and holes in a semiconductor particulate system is essential for improving the efficiency of the net charge transfer in photocatalysis and solar cells.² A variety of methods has been employed for this purpose, including modification of the TiO₂ surface with noble metals (Pd, Au, Ag, etc.)³ and coupling of two semiconductor particles with different Fermi levels.⁴ Among these coupled semiconductors, the TiO₂–SnO₂ system has been the focus of a number of studies because of the structural analogy between both oxides.⁵ They have the same crystal system with two molecular units per unit cell. The bandgaps of SnO₂ and TiO₂ are 3.8 and 3.2 eV, respectively. When the two semiconductor particles are coupled, the conduction band of SnO₂ acts as a sink for photogenerated electrons.^{5a,6} Since the photogenerated holes move in the opposite direction, they accumulate in the valence band of the TiO₂ particle, therefore leading to efficient spatial separation of photogenerated charges, suppressing recombination. In addition, the Sn dopant also enhances the photoinduced charge rate of TiO₂.⁷

Several methods have been developed to produce TiO₂–SnO₂ materials. TiO₂ capped SnO₂ particles were prepared by the addition of titanium isopropoxide to a colloidal suspension of SnO₂.⁸ A patterned TiO₂–SnO₂ bilayer catalyst has been prepared by creating strips of anatase TiO₂ on SnO₂ film coated soda-lime glass using the photolysis of an organically modified sol–gel film.⁹ Ultrafine SnO₂–TiO₂ coupled particles have been prepared by homogeneous solution precipitation.¹⁰ TiO₂–SnO₂ particulate films were deposited on glass slides using the plasma

enhanced chemical vapor deposition of SnCl₄ and TiCl₄.¹¹ Rutile Ti_xSn_{1-x}O₂ solid solutions were prepared using a citric acid complexing method.¹² In these studies, the morphologies of the mixed oxides were particles or particulate films. However, many applications would benefit from both high surface to volume and efficient transport of electrons and excitons in nanofibers or nanotubes. Recently, side-by-side bicomponent TiO₂/SnO₂ was fabricated by electrospinning;¹³ the average diameter of the fibers was 100 nm. Furthermore, Sn substitution for Ti in a TiO₂ lattice matrix can more effectively slow down the recombination rate. For example, it was found that the photocatalytic activity of Sn doped TiO₂ was increased up to 15 times in the oxidation of acetone.¹² Such results encourage the fabrication of anatase TiO₂ nanofibers doped with Sn (TDT).

To substitute Sn for Ti in TiO₂ nanofibers, the atomic level dispersion of the Sn precursor in the Ti species is important to avoid phase separation, which often occurs in sol–gel systems. Although a number of efforts has been made to prepare TiO₂ nanofibers or nanorods,¹⁴ TDT nanofibers have not been reported. Traditionally, porous materials have been used to make one-dimensional nanosized metals and metal oxides inside confined channels.¹⁵ However, the host matrix must be dissolved to recover the encapsulated nanoparticles, which can lead to chemical corrosion of the oxide nanofibers. We recently reported a novel method to produce crystalline TiO₂ nanofibers by templating with mesoporous silica.¹⁶ In the present work, we have extended this effort to produce TDT nanofibers from mesoporous silica spheres. Furthermore, Sn atoms were incorporated into the TiO₂ lattice, which is much different from the previous TiO₂–SnO₂ materials.^{5–11}

Experimental Procedures

Preparation of Mesoporous Silica Spheres. Dallas amorphous material-1 (DAM-1) spheres were synthesized according to a literature procedure.¹⁷ In a typical preparation, 1.8 g of vitamin E α -tocopheryl polyethylene glycol 1000 succinate (TPGS) was dissolved in a solution containing 36 mL of water, 27 mL of concentrated HCl, 25 mL of formamide, and 15 mL of ethanol. The solution was stirred for 4 h at room temperature. Then, 1.07 g of tetraethylorthosilicate (TEOS) was added to the homogeneous mixture with stirring at room temperature for 30 min and aged at room temperature for 4 days. The final molar

* Corresponding author. Tel: (972) 883-2659; fax: (972) 883-2925; e-mail: balkus@utdallas.edu.

composition of the gel was 617 H₂O/54.4 HCl/107.8 HCONH₂/24 vitamin E TPGS/52.9 ethanol/1.0 TEOS. The product DAM-1 spheres were isolated by vacuum filtration, washed with deionized water, then dried at 90 °C for 12 h, and calcined at 550 °C for 15 h. The BET surface area was found to be 808 m²/g with a pore size of 2.2 nm.

Preparation of TDT Nanofibers. Mesoporous silica spheres were placed in a 120 mesh stainless steel screen basket that was positioned in a 23 mL Teflon-lined autoclave 4 cm above 4 mL of SnCl₄ and TiCl₄. The filling of SnCl₄ and TiCl₄ into the DAM-1 mesopores was conducted by heating the autoclave at 135 °C for 24 h under autogenous pressure. After cooling to room temperature, the silica spheres were transferred to a 20 mL beaker with the opening sealed by Parafilm, under a controlled air flow of 70 mL/min, for ~3 h. After hydrolysis, the TDT nanofibers were dried at 90 °C followed by calcination at 500 °C. To remove the mesoporous silica spheres, 3% HF was used to treat the samples for 5 min, followed by suction filtration, washing with deionized water, and drying at ~90 °C for ~12 h.

Characterization. The crystallinity of the TDT nanofibers was determined by powder X-ray diffraction (XRD) (Scintag XDS 2000 X-ray diffractometer with Cu K α radiation). The fiber morphology was evaluated by scanning electron microscopy (LEO 1530 VP field emission SEM) from Au/Pd coated samples. The BET surface area of the template DAM-1 spheres was measured on a Quantachrome Autosorb 1 using N₂ adsorption–desorption, and the pore sizes were calculated using the branch of adsorption curves based on the Barrett–Joyner–Halenda (BJH) model. The microstructure was observed by transmission electron microscopy (TEM) using an FEI CM200 FEG transmission electron microscope at 200 kV.

Photodegradation Evaluation. The photocatalytic degradation of methylene green (MG, Aldrich, the dye content is ca. 65%) was used to evaluate the photocatalytic activity of the products. The initial MG concentration was 3.0×10^{-5} M with pH = 5.6. The TDT nanofibers were annealed at 500 °C for 10 h, and DAM-1 spheres were removed by 3% HF. For all experiments, 0.025 g of catalyst was added to 45 mL of MG aqueous solution. The mixture was sonicated for 10 min and then magnetically stirred in a dark environment at room temperature for 30 min to establish an adsorption–desorption equilibrium. The catalytic reactions were carried out in a 100 mL quartz flask at room temperature. The light source was a water-cooled 450 W Hanovia quartz mercury arc lamp with ~65% of the radiation energy falling in visible spectrum and ~35% in the UV spectrum. The concentrations of MG at different intervals were calculated from UV–vis absorption spectra at 657.5 nm, the band corresponding to MG.

Photodegradation of methylene blue (MB), indigo carmine, rhodamine B, and rose bengal were also investigated at room temperature using the same reactor and light source as stated previously. The initial concentrations were 4.28×10^{-5} , 1.715×10^{-4} , 5×10^{-5} , and 9.83×10^{-5} M, respectively, with initial pH values of 6.1, 5.7, 4.5, and 6.5, respectively. The catalyst was hollow TDT nanofiber shells with a Sn/Ti atomic ratio of 0.1 annealed at 500 °C. When MB, indigo carmine, and rose bengal were used as substrates, the reaction solution contained 25 mg of catalyst and 45 mL of dye solution and 20 mg of catalyst and 100 mL of dye solution for rhodamine B. The concentrations of MB, indigo carmine, rhodamine B, and rose bengal were calculated from the absorption peak at 661, 610.5, 554, and 549 nm, respectively.

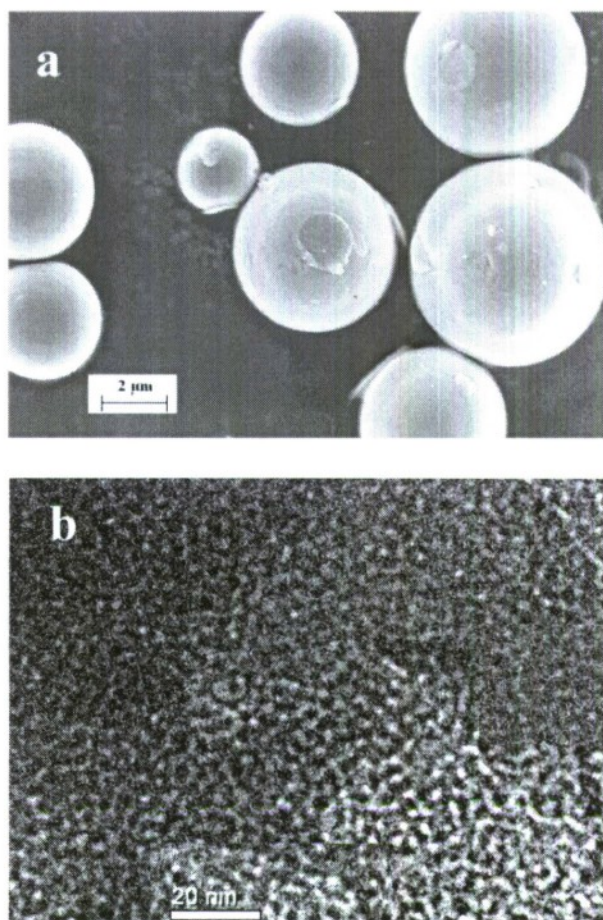
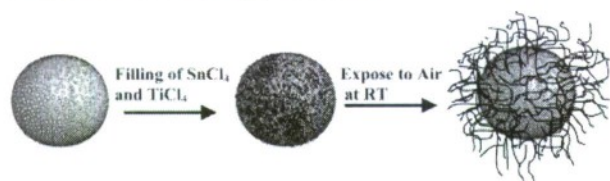


Figure 1. Mesoporous DAM-1 spheres characterized by (a) SEM and (b) TEM images.

Results and Discussion

Preparation of TDT Nanofiber. An SEM image of the mesoporous silica spheres is shown in Figure 1a. Mesoporous silica spheres were demonstrated to have a wormhole structure as shown in the TEM image in Figure 1b. The pore size and pore volume were determined by N₂ absorption. The pore size of the silica spheres was 2.2 nm with a wall thickness of 4.2 nm. The pore volume was ~0.36 cm³/g, and the surface area was 808 m²/g. The volatile precursors, SnCl₄ and TiCl₄, were placed at the bottom of a Teflon-lined autoclave along with the DAM-1 spheres. At 135 °C, the vapor pressures of SnCl₄ and TiCl₄ were 980 and 760 mmHg, respectively. SnCl₄ and TiCl₄ penetrated into the mesoporous templates and remained inside the pores under the autogenous pressure. The impregnated DAM-1 particles were taken out of the autoclave after 1 day of vapor phase filling. SnCl₄ and TiCl₄ then diffused out of the pores owing to the high volatility of the precursors at room temperature and standard pressure as described previously.¹⁶ Upon contact with moisture, hydrolysis occurred, and TDT nanofibers were generated on the outside surface of the mesoporous silica as illustrated in Scheme 1.

When the molar ratio of SnCl₄ to TiCl₄ was 1 in the Teflon container, and mesoporous DAM-1 spheres were used as templates, TDT nanofibers were grown from the mesoporous silica spheres as shown in Figure 2. Thus, it was not required that the mesoporous silica spheres be dissolved for access to the TDT nanofibers. In contrast to other methods where semiconductive fibers were grown inside confined pores,¹⁵ one-

SCHEME 1: Formation Process of Sn Doped TiO₂ Nanofibers from Mesoporous Silica


dimensional nanosized metal oxide fibers can be grown outside the molecular sieve channels. It can be seen in Figure 2b that the TDT nanofibers have a uniform diameter of ~ 30 nm owing to the uniform DAM-1 pore size. However, the fibers were coated with ~ 10 nm of Au/Pd to prevent charging; therefore, TEM was used to determine the diameter as shown in Figure 2c. The mesopores play an important role in directing the formation of a fibrous morphology for the complex oxides. Dispersion of gaseous SnCl₄ and TiCl₄ after diffusing out of the pores as well as the fusion of growing fibers from adjacent pores resulted in fiber diameters larger than the DAM-1 pore size (2.2 nm). The atomic ratio of Sn to Ti was determined by EDS to be 0.15. The fiber Sn/Ti ratio was much lower than the molar ratio of 1 in the precursor mixture. A possible explanation for this is that moisture sensitivity of SnCl₄ is much less than TiCl₄. Thus, some of the SnCl₄ precursor is lost during the hydrolysis step. Additionally, SnCl₄ has a higher vapor pressure (20 mmHg) than TiCl₄ (10 mmHg) at room temperature.

The TEM images in Figure 2c clearly show highly crystalline anatase. The (101) lattice planes show a *d*-spacing of 3.57 Å, compared with 3.52 Å for pure TiO₂. The lattice fringes of (101) planes on the nanofibers grow along the fiber growth direction, but some also grow perpendicular to the fiber growth axis. The average diameter of the TDT nanofibers is about 5–10 nm. Although TiO₂ fibers have been generated by electrospinning,

the fiber diameter is usually over 50 nm.^{18–21} To further study if Sn atoms were incorporated into TiO₂ lattice, an EDS measurement was made through focusing an electron beam into a ~ 3 nm diameter spot on the lattice matrix. EDS spectrum indicated a Sn/Ti ratio of 0.10. This further suggests that the hydrolysis of the vapor phase precursors results in atom level mixing during fiber formation.

The mesoporous silica spheres may be removed by etching with 3% HF for 5 min. After removal of most of the silica core, a hollow TDT nanofiber shell structure was generated as shown in Figure 2d. There is a thin shell of silica (confirmed by EDAX) under the TDT nanofibers that holds the hollow sphere together. It can also be observed that TDT nanofibers were shortened by 50% owing to etching by HF. Interestingly, the fiber diameter did not significantly change after HF etching (see Figure S1a). Heating the nanofibers in 1 M HCl at 100 °C for 10 h did not affect the Sn/Ti ratio. However, the Sn/Ti ratio was decreased from 0.15 to ~ 0.10 after HF treatment. The SEM image as well as the maps for Ti and Sn for the core shell TDT nanofibers with a Sn/Ti ratio of 0.1 are shown in Figure 3, which shows the uniform dispersion of Sn atoms after HF etching. The effect of HF etching on the Sn/Ti ratio also depends on the annealing temperatures of the TDT nanofibers. When the annealing temperatures before HF etching were 300, 500, 700, and 800 °C, the Sn/Ti ratios after HF etching were 0.06, 0.10, 0.11, and 0.11, respectively. In addition, there was still trace Si remaining in the samples, and the Si/Ti atomic ratio was $\sim 5\%$ determined by EDS. Without annealing, the as-made TDT nanofibers were completely dissolved by HF.

The X-ray diffraction (XRD) patterns in Figure 4 reveal a change in the crystalline phase of the TDT nanofibers (Sn/Ti = 0.15) with annealing temperature. The as-made nanofibers are composed of the anatase phase (40 °C), which was further confirmed by its TEM image (shown in Figure S2). Increasing

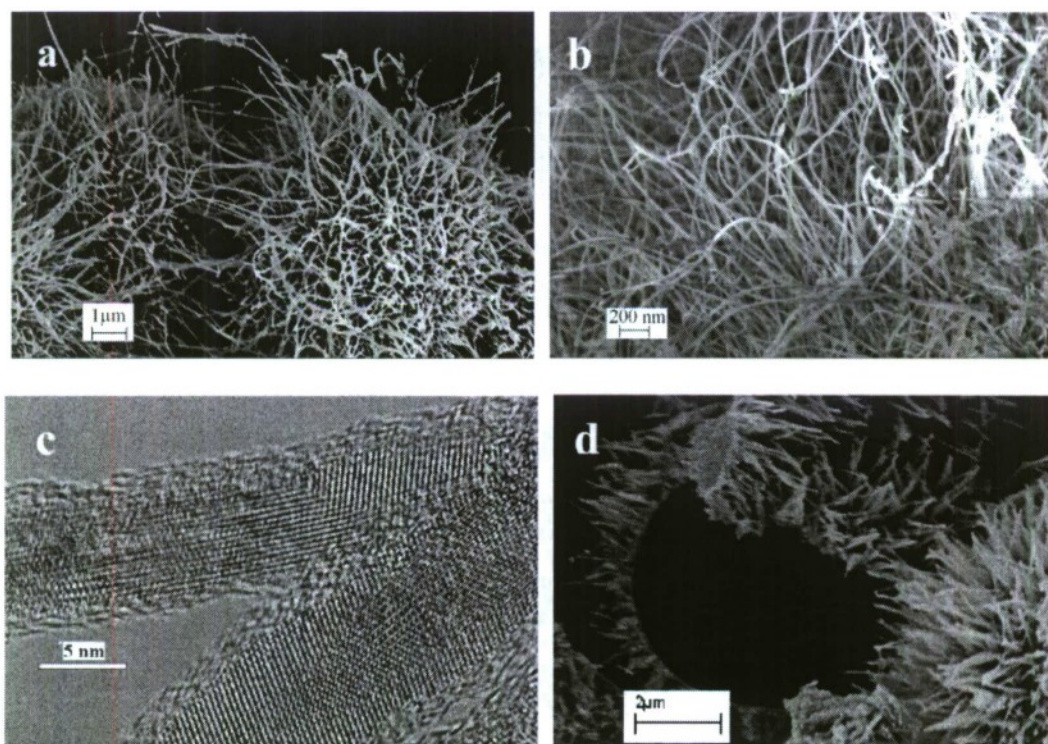


Figure 2. TDT nanofibers prepared with a molar ratio of SnCl₄ to TiCl₄ equal to 1 and annealed at 500 °C. (a) SEM, (b) high magnification SEM, (c) HRTEM images before HF etching, and (d) core-shell structure after removal of silica spheres by HF etching.

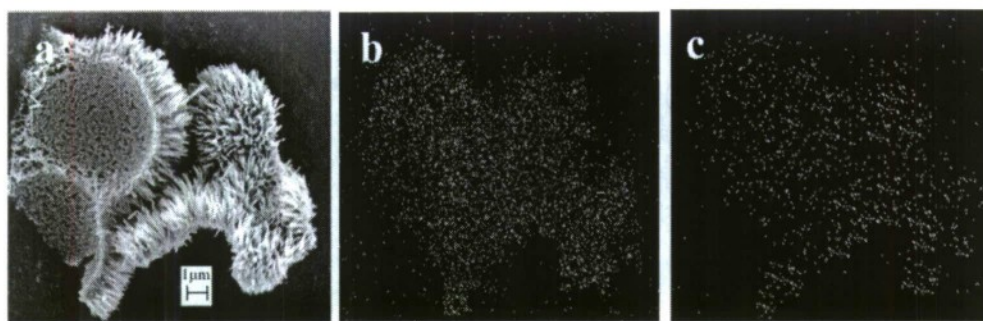


Figure 3. SEM image of (a) the hollow shell TDT nanofibers (Sn/Ti = 0.1) and corresponding elemental map for (b) Ti and (c) Sn.

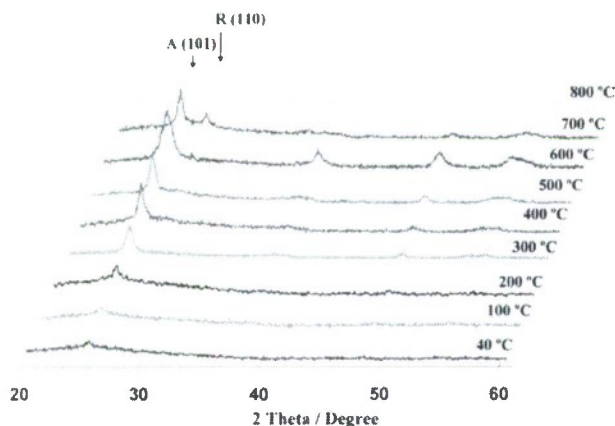


Figure 4. XRD patterns of Sn doped TiO_2 nanofibers (Sn/Ti = 0.15) prepared with a molar ratio of SnCl_4 to TiCl_4 of 1 and annealed at different temperatures.

the annealing temperature resulted in an increase in all the peaks attributed to the anatase phase and eventually formation of the rutile phase. For the TDT nanofibers (Sn/Ti = 0.15), the phase transformation from anatase to rutile occurred at about 700 °C, about 100° higher than that for pure TiO_2 (Figure S3) because of the introduction of Sn, which hinders the phase transformation from anatase to rutile.^{14a} When annealed at 700 °C, the TDT nanofibers consisted of 80% anatase and 20% rutile and 40% anatase and 60% rutile for 800 °C. The XRD peak ascribed to the 101 reflection of anatase shifted from a d -spacing of 3.52 to 3.57 Å. Similarly, it can be seen that the 110 reflection of rutile shifted from 3.25 to 3.32 Å. All of these shifts are related to the larger radius of Sn^{4+} as compared with Ti^{4+} , indicating that Sn atoms were incorporated into the TiO_2 lattice. The unit cell parameters for the Sn/Ti = 0.15 sample were enlarged with $a = 3.820$ Å and $c = 10.198$ Å as shown in Table 1.

The percent of SnO_2 in the TDT nanofibers was varied by simply changing the molar ratio of the precursors (summarized in Table 1). The atomic ratio of Sn to Ti in the nanofibers was decreased to 0.08 when the molar ratio of SnCl_4 to TiCl_4 in the autoclave was 0.5, and the unit cell parameters were $a = 3.826$ Å and $c = 10.04$ Å. Increasing the molar ratio of SnCl_4 to TiCl_4

to 2 resulted in an increase in the Sn/Ti atomic ratio in the nanofibers to 0.19, but the unit cell parameters did not further increase as compared to the sample with a molar ratio of SnCl_4 to TiCl_4 of 1, which implies that there is a limit for the incorporation of Sn atoms into the TiO_2 lattice. Substitution of Ti by Sn in an anatase lattice has been reported up to a limit of 10 atom %, ²² Beyond this value, SnO_2 appeared as a separated phase. No SnO_2 phase was observed in the XRD patterns (Figure S4) of TDT nanofibers prepared with different molar ratios of SnCl_4 to TiCl_4 .

SEM images of the TDT nanofibers prepared with different molar ratios of SnCl_4 to TiCl_4 are shown in Figure 5. The fiber length changed with the Sn/Ti molar ratio of the precursors. When the $\text{SnCl}_4/\text{TiCl}_4$ molar ratio was decreased to 0.3, the fiber length was ~ 3 μm as shown in Figure 5a. Figure 5b displays the hollow shell structure obtained after HF etching, and the fiber length was reduced to 2 μm . With an increase in the molar ratio of SnCl_4 to TiCl_4 , the TDT nanofiber length decreased as shown in Table 1. When the $\text{SnCl}_4/\text{TiCl}_4$ ratio was 0.5, the fiber length was ~ 2 μm as seen in Figure 5c,d and ~ 1 μm for a $\text{SnCl}_4/\text{TiCl}_4$ ratio of 2. The corresponding hollow TDT nanofiber shells after HF etching are also shown in Figure 5e,h, where the fiber length was 1 μm . Meanwhile, the Sn/Ti atomic ratios of the TDT nanofibers after HF treatment were decreased to 0.03, 0.05, and 0.13, respectively, as shown in Table 1. When the $\text{SnCl}_4/\text{TiCl}_4$ molar ratio in the precursor mixture was 3, only trace amounts of fibers formed (Figure S5). A higher molar ratio of SnCl_4 to TiCl_4 (≥ 3) may result in a greater loss of precursors during hydrolysis owing to the lower moisture sensitivity and higher vapor pressure of SnCl_4 versus TiCl_4 . This may also explain why the fiber length decreased with increasing the Sn/Ti molar ratio of the precursors, and pure SnO_2 nanofibers were not obtained by this approach. Highly crystalline anatase nanorods were revealed in the previous samples by the HRTEM images shown in Figure 6. Two kinds of growth directions of the 101 lattice planes can be observed along and perpendicular to the fiber growth axis. The fiber diameters did not change significantly with the $\text{SnCl}_4/\text{TiCl}_4$ molar ratio as expected because of the fixed DAM-1 pore size (2.2 nm) and the constant

TABLE 1: Effect of Molar Ratio of SnCl_4 to TiCl_4 on TDT Nanofibers^a

molar ratio of SnCl_4 to TiCl_4	atomic ratio of Sn to Ti ^b		fiber diameter determined by TEM (nm) ^d	fiber length determined by SEM (μm) ^d	unit cell (Å) ^c	
	before HF etch	after HF etch			a	c
0.3	0.05	0.03	5 to ~ 10	~ 3	3.812	10.021
0.5	0.08	0.05	5 to ~ 10	~ 2	3.816	10.039
1	0.15	0.10	5 to ~ 10	~ 2	3.820	10.198
2	0.19	0.13	5 to ~ 10	~ 1	3.820	10.198

^a TDT nanofibers were annealed at 500 °C for 10 h. ^b Sn/Ti molar ratio in the fibers was determined by EDS measurements using a LEO field emission SEM. ^c Pt was used a reference to calibrate the peak positions. ^d Without HF etching.

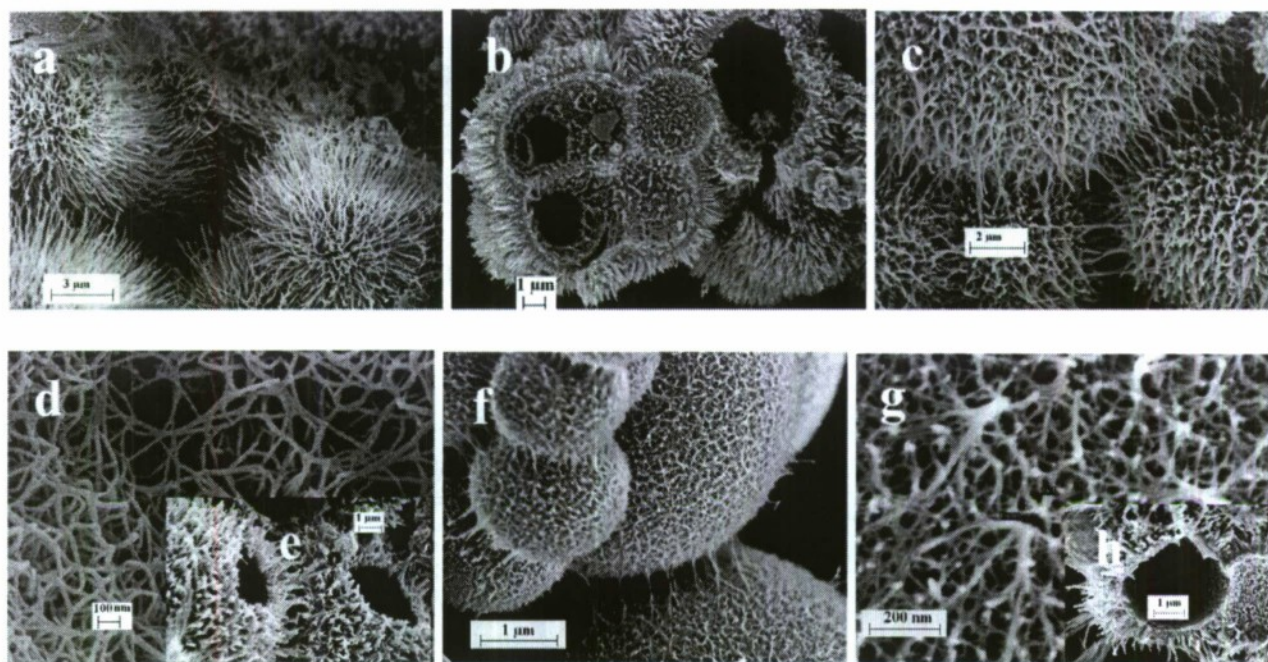


Figure 5. SEM of TDT nanofibers annealed at 500 °C. (a) Prepared with a molar ratio of SnCl₄ to TiCl₄ of 0.3 before and (b) after HF etching, respectively. (c) Prepared with a ratio of 0.5, (d) with different magnification before etching, (e) after etching. (f) Prepared with a ratio of 0.2, (g) with different magnification before etching, and (h) after etching.

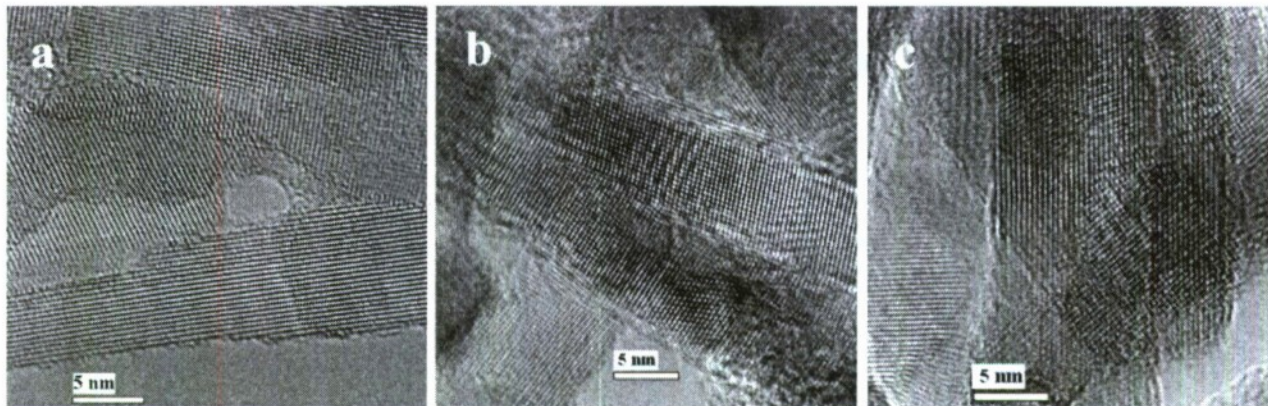


Figure 6. HRTEM images of TDT nanofibers annealed at 500 °C before etching and prepared with a molar ratio of SnCl₄ to TiCl₄ of (a) 0.3, (b) 0.5, and (c) 2.

hydrolysis conditions. Meanwhile, HF etching did not greatly change the fiber diameter according to the TEM images (Figure S1b,d).

Photodegradation of Dyes. Although mesoporous TiO₂ fibers have been produced by electrospinning,²³ the photocatalytic properties fell far below P25 owing to the larger diameter size (~600 nm) and the collapse of mesopores upon calcination. Side-by-side bicomponent TiO₂/SnO₂ fibers were fabricated by electrospinning with an average fiber diameter of 100 nm.¹³ The photodegradation rate of rhodamine B dye on the bicomponent fibers was twice that for the pure TiO₂ fibers with a diameter of 50 nm. Cao et al. prepared Sn doped TiO₂ nanoparticulate films by plasma-enhanced CVD.¹¹ The catalytic activity was nearly twice as effective as the analogue TiO₂ film in the photodegradation of phenol.²⁴ Similarly, Sn doped TiO₂ particles were reported to be over twice as active as P25 in the photodegradation of toluene,²⁵ which was further demonstrated in the photodecomposition of methylelohexane.²⁶ Sn doped TiO₂ thin films on glass also exhibited better catalytic activity in the photodegradation of methylene green than undoped TiO₂

films.²⁷ There is precedence for enhanced photocatalytic activity in Sn doped TiO₂ systems.

To investigate the effect of Sn substitution in the DAM-1 templated TiO₂ nanofibers on the photocatalytic properties, the room temperature photodegradation of MG, MB, indigo carmine, rhodamine B, and rose bengal was conducted. The molecular structures of these dyes are shown in Figure 7. The results for the photodegradation of MG catalyzed by all samples are shown in Figure 8. It can be seen that the TDT nanofibers displayed faster photocatalysis reaction rates as compared to pure TiO₂ nanofibers and Degussa P25, which indicated that the Sn substitution for Ti can effectively suppress the recombination of electron hole pairs and increase photodegradation efficiency. In the absence of a catalyst, the MG dye slowly photobleached, but there was only a few percent conversion after 3.5 h as shown in Figure 8. Out of the four different Sn doped TiO₂ nanofibers, the TDT nanofibers with a Sn/Ti atomic ratio of 0.10 exhibited the most efficient catalytic activity with complete conversion after 60 min. This can be compared to the commercial P25 catalyst (30 nm TiO₂ nanoparticles having a

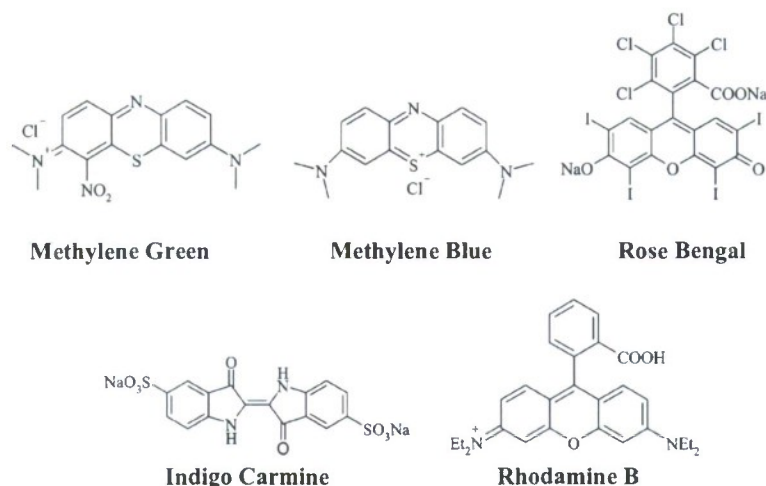


Figure 7. Molecular structures of methylene green (MG), methylene blue (MB), rose bengal, indigo carmine, and rhodamine B.

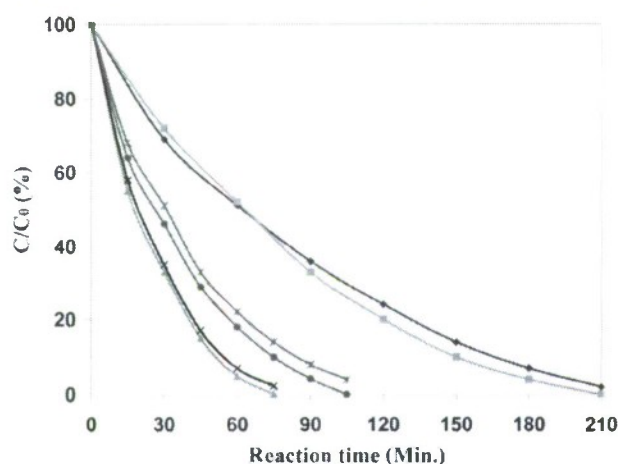


Figure 8. Plot of conversion vs time for the photodegradation of MG catalyzed by P25 and hollow TDT nanofiber shells and hollow TiO₂ nanofiber shells annealed at 500 °C. (Blue diamonds) P25, (pink squares) TiO₂ nanofiber, (tan stars) TDT nanofiber with Sn/Ti = 0.03, (blue circles) TDT nanofiber with Sn/Ti = 0.05, (red triangles) TDT nanofiber with Sn/Ti = 0.10, and (×) TDT nanofiber with Sn/Ti = 0.13.

surface area of ~ 50 m²/g and an anatase/rutile ratio of 3) and TiO₂ nanofibers where complete conversion required more than 210 min. Meanwhile, TDT nanofibers exhibited a faster reaction rate than Sn doped TiO₂ nanoparticles,²⁷ on which the time to photodegrade MG was over 100 min under UV light irradiation and over 300 min under visible light irradiation.

Since P25 is a mixture of anatase and rutile, the effect of the annealing temperature of the TDT nanofibers on photodegradation activities of MG was investigated. As the annealing temperature was increased, more of the rutile phase formed. Figure 9 shows the conversion of MG versus time for the TDT nanofibers prepared with a molar ratio of SnCl₄ to TiCl₄ of 1. Without annealing, the TDT nanofibers were completely dissolved by HF, so the lowest annealing temperature was 300 °C. The TDT nanofibers annealed at 500 °C exhibited the best photodegradation activity. When the annealing temperatures were 700 and 800 °C, it was found that the degradation rate of MG decreased due to the formation of the rutile phase, which is generally less catalytically active than the anatase phase.^{28–31} The TDT nanofibers annealed at 800 °C contain $\sim 60\%$ rutile as compared to P25 ($\sim 25\%$ rutile); however, the activity of the Sn doped catalyst is still better. Additionally, for TDT nanofibers

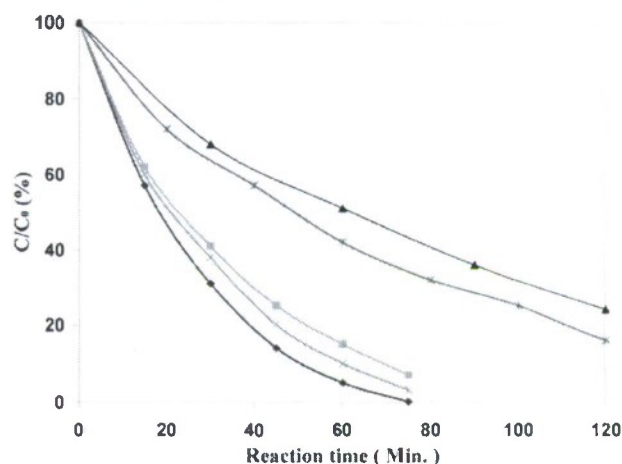


Figure 9. Plot of conversion vs time for the photodegradation of MG on hollow TDT nanofiber shells (Sn/Ti = 0.1) annealed at different temperatures. (▲) P25, (pink squares) TDT nanofibers annealed at 300 °C, (blue diamonds) TDT nanofibers annealed at 500 °C, (tan ×) TDT nanofibers annealed at 700 °C, and (brown stars) TDT nanofibers annealed at 800 °C.

annealed at 300 °C, the photodegradation activity was also decreased because TDT nanofibers after HF etching have a lower Sn/Ti atomic ratio of 0.06, as compared to 0.10 for the TDT nanofibers annealed at 500 °C.

In addition to MG, the dyes MB, indigo carmine, rose bengal, and rhodamine B were also investigated as substrates for photodegradation by TDT nanofibers. As compared to P25 and undoped TiO₂ nanofiber shells, the TDT nanofibers exhibited a better activity in the photodegradation of MB as shown in Figure 10. The time to completely bleach MB was 75 min on the TDT nanofibers, ~ 3 times faster than the pure TiO₂ nanofibers and P25 catalyst. Figure 10 also shows that the MB dye itself photobleaches to only a minor extent over the course of the experiment. In comparison, Ag doped TiO₂ nanoparticles took over 180 min to completely photobleach MB.³²

Another cationic dye, rhodamine B, was examined. The complete conversion time of the dye was 75 min for TDT nanofibers (Sn/Ti = 0.1) and 170 and 200 min for pure TiO₂ nanofibers and P25, respectively, as shown in Figure 11. The photocatalytic activity of TDT nanofibers was apparently faster than P25 and undoped TiO₂ nanofibers. Meanwhile, TiO₂ nanofibers exhibited a better catalytic activity than P25 after 45 min, so it took a shorter amount of time (170 min) to

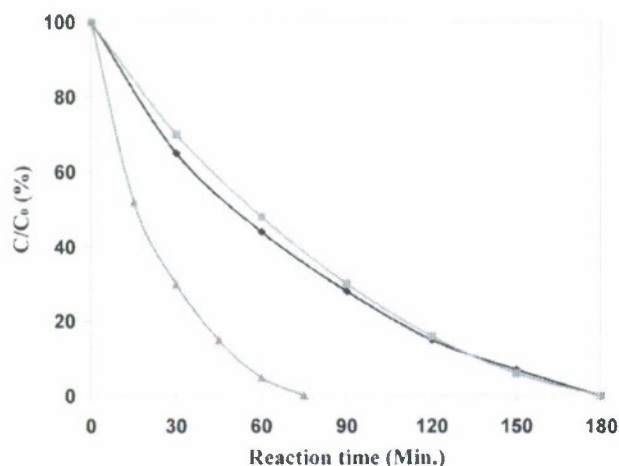


Figure 10. Plot of conversion vs time for the photodegradation of MB on (blue diamonds) P25, (pink squares) hollow TiO₂ nanofiber shells, and (red triangles) hollow TDT nanofiber shells (Sn/Ti = 0.1) annealed at 500 °C.

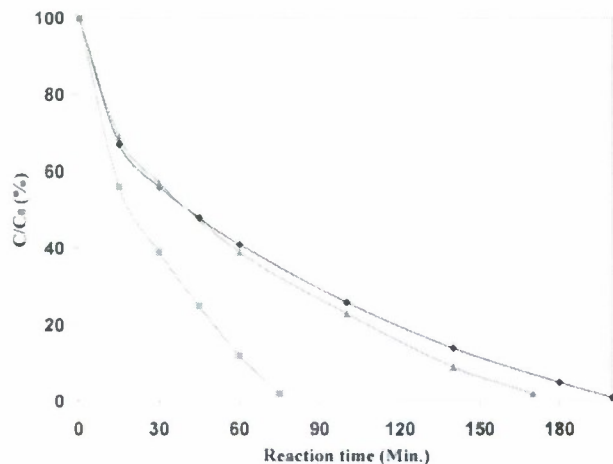


Figure 11. Plot of conversion vs time for the photodegradation of rhodamine B on (blue diamonds) P25, (red triangles) hollow TiO₂ nanofiber shells, and (pink squares) hollow TDT nanofiber shells (Sn/Ti = 0.1) annealed at 500 °C.

completely photodegrade the dye. The photocatalytic activity of the TDT nanofibers was also better than a Sn doped TiO₂ thin film,³³ which was reported to take over 160 min to finish the photodegradation of rhodamine B. For side-by-side TiO₂/SnO₂ fibers, the complete conversion time was reported to be 45 min with a UV lamp (254 nm) as the light source.¹³ However, the light source we used was a water-cooled Hanovia quartz mercury arc lamp with ~65% of the radiation energy falling in the visible spectrum and ~35% in the UV spectrum.

For the anionic dye indigo carmine, a higher concentration (1.72×10^{-4} M) was used in the photodegradation experiments as compared to MB (4.62×10^{-5} M) and MG (3.0×10^{-5} M). However, the complete photobleaching time was 40 min for the TDT nanofibers (Sn/Ti = 0.1) as shown in Figure 12 and 75 min for P25 and pure TiO₂ nanofibers, which was faster than a SBA-15 supported TiO₂ catalyst (>140 min).³⁴ Indigo carmine was bleached faster than MB and MG because it is considered to be a light sensitive dye,³⁰ where electrons from the dye can be excited by visible light and injected into the conduction band of the TiO₂, accelerating light harvesting and improving the photodegradation efficiency. Additionally, the general bleaching rate of anionic dyes is faster than cationic

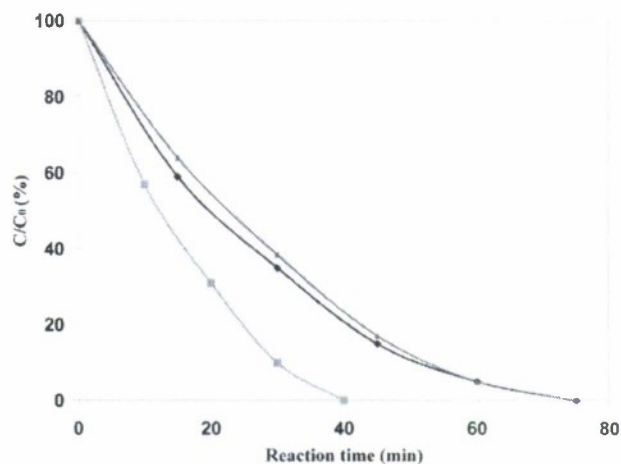


Figure 12. Plot of conversion vs time for the photodegradation of indigo carmine on (blue diamonds) P25, (brown triangles) hollow TiO₂ nanofiber shells, and (pink squares) hollow TDT nanofiber shells (Sn/Ti = 0.1) annealed at 500 °C.

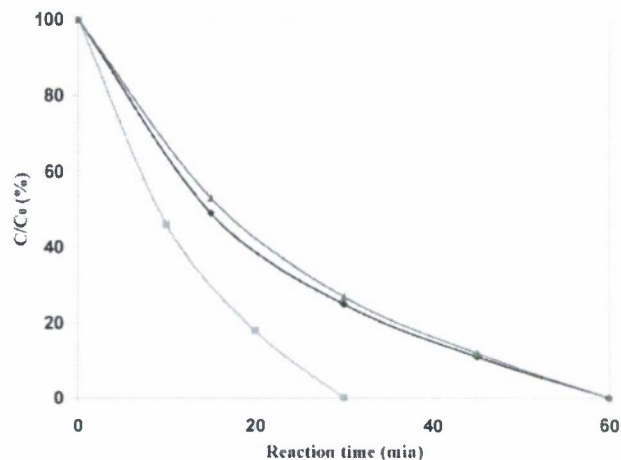


Figure 13. Plot of conversion vs time for the photodegradation of rose bengal on (blue diamonds) P25, (brown triangles) hollow TiO₂ nanofiber shells, and (pink squares) hollow TDT nanofiber shells (Sn/Ti = 0.1) annealed at 500 °C.

dyes.³⁰ This was further demonstrated by the photodegradation of another anionic dye, rose bengal, as shown in Figure 13. It took only 30 min to completely photodegrade rose bengal for TDT nanofibers (Sn/Ti = 0.1) and 60 min for P25 and TiO₂ nanofibers.

In the previous dye photodegradation experiments, the TDT nanofiber catalysts have a hollow shell structure obtained by HF etching. The catalyst activity for the TDT nanofibers with a Sn/Ti ratio of 0.15 before HF etching (i.e., with DAM-1 spheres) in the photodegradation of indigo carmine is shown in Figure 14. To study the differences in photodegradation efficiency, TDT nanofibers before etching were compared with P25 and the hollow shell TDT nanofibers. When the same weight of catalysts was used, it was found that TDT nanofibers before HF etching exhibited poor photoactivity. The activity was not comparable to 25 mg of hollow shell TDT nanofibers until 100 mg of TDT nanofibers with the DAM-1 core intact was used, which implies that the weight ratio of the TDT nanofibers to the mesoporous template (DAM-1 spheres) is small. To improve the weight ratio in an as-synthesized catalyst, a mesoporous template with a larger pore volume might store more of the oxide precursors to produce more TDT nanofibers per unit weight of mesoporous template. It should also be noted

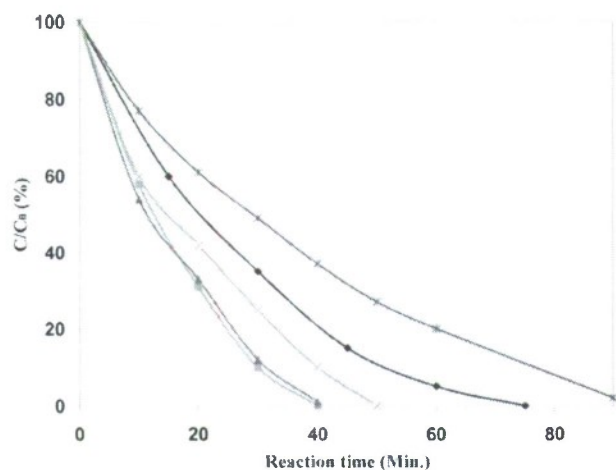


Figure 14. Plot of conversion vs time for the photodegradation of indigo carmine on P25 and TDT nanofibers annealed at 500 °C before and after removal of DAM-1 spheres. (Blue diamonds) 25 mg of P25, (pink squares) 25 mg of TDT nanofibers after removal of DAM-1 spheres, Sn/Ti = 0.1, (tan stars) 25 mg of TDT nanofibers before removal of DAM-1 spheres, Sn/Ti = 0.15, (orange ×) 75 mg of TDT nanofibers before removal of DAM-1 spheres, Sn/Ti = 0.15, and (brown triangles) 100 mg of TDT nanofibers before removal of DAM-1 spheres, Sn/Ti = 0.15.

that the hollow shell of TDT nanofibers can be broken up by mechanical grinding. This may also occur in a stirred reactor with time. There is no change in activity observed when the TDT nanofiber catalysts are cycled multiple times, which implies that there is no little or no change in accessible surface area between the fresh hollow sphere catalyst configuration and the used catalyst that likely contains dispersed individual TDT nanofibers after prolonged stirring.

Conclusion

In summary, TDT nanofibers have been successfully made by impregnation of SnCl₄ and TiCl₄ in mesoporous DAM-1 followed by controlled hydrolysis. TDT nanofibers with a diameter of 5 to ~10 nm have been generated from mesoporous silica spheres, and a hierarchical structure of a TDT nanofiber shell and a mesoporous template core formed. The as-made TDT nanofibers were in the anatase phase but transformed into rutile when the annealing temperature was 700 °C. The Sn atoms incorporated into the TiO₂ lattice matrix effectively suppressed the recombination rate of the electron hole pairs in the photodegradation reaction of dyes. The Sn content in the TDT nanofibers was adjustable by changing the molar ratio of SnCl₄ to TiCl₄, but with an upper limit of ~15%. In the photodegradation of dyes, TDT nanofibers exhibited better catalytic activity than P25 and pure TiO₂ nanofibers with an optimum Sn/Ti atomic ratio of 0.1. The TDT nanofibers should have a further application in the deep mineralization of recalcitrant organics. Additionally, the TDT nanofibers should have the same advantages in solar cells, where electron hole recombination is an issue.

Acknowledgment. We thank the Robert A. Welch Foundation and SPRING for financial support.

Supporting Information Available: HRTEM and TEM images and XRD patterns. This material is available free of charge via the Internet at <http://pubs.acs.org>.

References and Notes

- (1) (a) Lin, J.; Yu, J. C.; Lo, D.; Lam, S. K. *J. Catal.* **1999**, *183*, 368–372. (b) Hoffmann, M. R.; Martin, S. T.; Choi, W.; Bahnemann, D. W. *Chem. Rev.* **1995**, *95*, 69–96.
- (2) (a) Hiroshi, Y.; Shigeo, H. *J. Phys. Chem.* **1989**, *93*, 4833–4837. (b) Gerischer, H.; Heller, A. *J. Phys. Chem.* **1991**, *95*, 5261–5267. (c) Gopidas, K. R.; Bohorquez, M.; Kamat, P. V. *J. Phys. Chem.* **1994**, *98*, 3822–3831.
- (3) (a) Borgarello, E.; Kiwi, J.; Grätzel, M.; Pelizzetti, E.; Visca, M. *J. Am. Chem. Soc.* **1982**, *104*, 2996–3002. (b) Martin, S. T.; Morrison, C. L.; Hoffman, M. R. *J. Phys. Chem.* **1994**, *98*, 13695–13704. (c) Klosck, S.; Raftery, D. *J. Phys. Chem. B* **2001**, *105*, 2815–2819. (d) Asahi, R.; Morikawa, T.; Ohwaki, T.; Aoki, K.; Taga, Y. *Science* **2001**, *293*, 269–271. (e) Tahir, M. N.; Eberhardt, M.; Therese, H. A.; Kolh, U.; Theato, P.; Müller, W. E. G.; Schröder, H. C.; Tremel, W. *Angew. Chem., Int. Ed.* **2006**, *45*, 4803–4809.
- (4) (a) Stafford, U.; Gray, K. A.; Kamat, P. V. *Heterog. Chem. Rev.* **1996**, *3*, 77–104. (b) Kamat, P. V.; Vinodgopal, K. *Organic and Inorganic Photochemistry*; Marcel Dekker: New York, 1998.
- (5) (a) Pilkenton, S.; Raftery, D. *Solid State Nucl. Magn. Reson.* **2003**, *24*, 236–253. (b) Chappel, S.; Chen, S. G.; Zaban, A. *Langmuir* **2002**, *18*, 3336–3342. (c) Turrión, M.; Bisquert, J.; Salvador, P. *J. Phys. Chem. B* **2003**, *107*, 9397–9403. (d) Levy, B.; Liu, W.; Gilbert, S. E. *J. Phys. Chem. B* **1997**, *101*, 1810–1816. (e) Vassiliev, Y. S.; Yusipovich, A. I.; Rogynskaya, Y. E.; Chibirova, F. K.; Skundin, A. M.; Kulova, T. L. *J. Solid State Electrochem.* **2005**, *9*, 698–705.
- (6) Stafford, U.; Gray, K. A.; Kamat, P. V. *Heterog. Chem. Rev.* **1996**, *3*, 77–104.
- (7) Jing, L.; Fu, H.; Wang, B.; Wang, D.; Xin, B.; Li, S.; Sun, J. *Appl. Catal., B* **2006**, *62*, 282–291.
- (8) Bedja, I.; Kamat, P. V. *J. Phys. Chem.* **1995**, *99*, 9182–9188.
- (9) (a) Hattori, A.; Tokihisa, Y.; Tada, H.; Tohge, N.; Ito, S.; Hongo, K.; Shiratsuchi, R.; Nogami, G. *J. Sol-Gel Sci. Technol.* **2001**, *22*, 53–61. (b) Tada, H.; Hattori, A.; Tokihisa, Y.; Imai, K.; Tohge, N.; Ito, S. *J. Phys. Chem. B* **2000**, *104*, 4585–4587.
- (10) Shi, L.; Li, C.; Gu, H.; Fang, D. *Mater. Chem. Phys.* **2000**, *62*, 62–67.
- (11) Cao, Y.; Zhang, X.; Yang, W.; Du, H.; Bai, Y.; Li, T.; Yao, J. *Chem. Mater.* **2000**, *12*, 3445–3448.
- (12) Lin, J.; Yu, J. C.; Lo, D.; Lam, S. K. *J. Catal.* **1999**, *183*, 368–372.
- (13) Liu, Z. Y.; Sun, D. D.; Guo, P.; Leckie, J. O. *Nano Lett.* **2007**, in press.
- (14) (a) Sui, R. H.; Rizkalla, A. S.; Charpentier, P. A. *Langmuir* **2005**, *21*, 6150–6153. (b) Chae, W. S.; Lee, S. W.; Kim, Y. R. *Chem. Mater.* **2005**, *17*, 3072–3074. (c) Li, D.; Xia, Y. N. *Nano Lett.* **2004**, *4*, 933–938. (d) Ding, B.; Kim, C. K.; Kim, H. Y.; Sco, M. K.; Soo, J. P. *Fibers Polym.* **2004**, *5*, 105–109.
- (15) (a) Ormer, D.; Ivana, S.; Neil, C.; Geoffroy, A. O. *Adv. Funct. Mater.* **2003**, *13*, 30–36. (b) Atsushi, F.; Hidenobu, A. Y.; Yusuke, A.; Masaru, I. *Nano Lett.* **2002**, *2*, 793–795. (c) Shin, H. J.; Ryoo, R.; Liu, Z.; Terasaki, O. *J. Am. Chem. Soc.* **2001**, *123*, 1246–1247. (d) Coleman, N. R. B.; Morris, M. A.; Spalding, T. R.; Holmes, J. D. *J. Am. Chem. Soc.* **2001**, *123*, 187–188. (e) Gao, F.; Lu, Q.; Zhao, D. Y. *Adv. Mater.* **2003**, *15*, 739–742. (f) Han, Y. J.; Kim, J. M.; Stucky, G. D. *Chem. Mater.* **2000**, *12*, 2068–2069. (g) Sander, M. S.; Cote, M. J.; Gu, W.; Kile, B. M.; Tripp, C. P. *Adv. Mater.* **2004**, *16*, 2052–2057.
- (16) (a) Xiong, C. R.; Balkus, K. J., Jr. *Chem. Mater.* **2005**, *17*, 5136–5140. (b) Xiong, C. R.; Kim, M. J.; Balkus, K. J., Jr. *Small* **2006**, *2*, 52–55.
- (17) Coutinho, D.; Orozio-Tevan, R. A.; Reidy, R. F.; Balkus, K. J., Jr. *Microporous Mesoporous Mater.* **2002**, *54*, 229–248.
- (18) Kim, D., II; Rothschild, A.; Lee, B. H.; Kim, D. Y.; Jo, S. M.; Tuller, H. L. *Nano Lett.* **2006**, *6*, 2009–2013.
- (19) Li, D.; Xia, Y. *Nano Lett.* **2003**, *3*, 555–560.
- (20) Onozuka, K.; Ding, B.; Tsuge, Y.; Naka, T.; Yamazaki, M.; Sugi, S.; Ohno, S.; Yoshikawa, M.; Shiratori, S. *Nanotechnology* **2006**, *17*, 1026–1031.
- (21) Son, W. K.; Cho, D.; Park, W. H. *Nanotechnology* **2006**, *17*, 439–443.
- (22) Aldon, L.; Kubiak, P.; Picard, A.; Jumas, J. C.; Olivier-Fourcade, J. *Chem. Mater.* **2006**, *18*, 1401–1406.
- (23) Madhugiri, S.; Sun, B.; Smirniotis, P. G.; Ferraris, J. P.; Balkus, K. J., Jr. *Microporous Mesoporous Mater.* **2004**, *69*, 77–83.
- (24) Cao, Y.; Yang, W. S.; Zhang, W. F.; Liu, G. Z.; Yue, P. *New J. Chem.* **2004**, *28*, 218–222.
- (25) Fresno, F.; Tudela, D.; Maira, A. J.; Rivera, F.; Coronado, J. M.; Soria, J. *Appl. Organomet. Chem.* **2006**, *20*, 220–225.
- (26) Fresno, F.; Coronado, J. M.; Tudela, D.; Soria, J. *Appl. Catal., B* **2005**, *55*, 159–167.

(27) Arpaç, E.; Sayılkan, F.; Asiltürk, M.; Tatar, P.; Kiraz, N.; Sayılkan, H. *J. Hazard. Mater.* **2007**, *140*, 69–74.

(28) Watanabe, T.; Nakajima, A.; Wang, R.; Minabe, M.; Koizumi, S.; Fujishima, A.; Hashimoto, K. *Thin Solid Films* **1999**, *351*, 260–263.

(29) Kominami, H.; Murakami, S.; Kato, J. I.; Kera, Y.; Ohtani, B. *J. Phys. Chem. B* **2002**, *106*, 10501–10507.

(30) Epling, G. A.; Lin, C. *Chemosphere* **2002**, *46*, 561–570.

(31) Sumita, T.; Yamaki, T.; Yamamoto, S.; Miyashita, A. *Appl. Surf. Sci.* **2002**, *200*, 21–26.

(32) Senthilkumar, S.; Porkodi, K.; Gomathi, R.; Maheswari, G. A.; Manonmani, N. *Dyes Pigm.* **2006**, *69*, 22–30.

(33) Zheng, S. K.; Wang, T. M.; Hao, W. C.; Shen, R. *Vacuum* **2002**, *65*, 155–159.

(34) Ding, H. M.; Sun, H.; Shan, Y. K. *J. Photochem. Photobiol., A* **2005**, *169*, 101–107.



ELSEVIER

Proton conductivity of acid-doped *meta*-polyaniline

Zhiwei Yang, Decio H. Coutinho, Richard Sulfstede,
Kenneth J. Balkus Jr. *, John P. Ferraris *

Department of Chemistry, The Alan G. MacDiarmid Nanotech Institute, The University of Texas at
Dallas Richardson, 2601 N. Floyd Road, TX 75083-0688, USA

Received 7 October 2004; received in revised form 13 December 2007; accepted 26 December 2007

Available online 8 January 2008

Abstract

Linear *meta*-polyaniline (*m*-PAni) has been synthesized and proton-conducting polymer membranes have been prepared through solution casting of acid-doped *m*-PAni. The obtained membranes show good proton conductivities at temperatures above 100 °C, achieving $10^{-2.7}$ S/cm at 120 °C under extremely low-humidity conditions. The effect of doping acids, doping levels and humidity, on the conductivity is discussed.

© 2008 Elsevier B.V. All rights reserved.

Keywords: *meta*-Polyaniline; Acid doping; Proton exchange membrane; Proton conductivity

1. Introduction

Proton exchange membrane fuel cells (PEMFC) are considered as promising alternatives to traditional internal combustion engines for automobiles as well as portable power generation because of high-energy conversion efficiency, high-power density, fast startup and environmental friendliness [1]. The proton exchange membrane (PEM) is the central part in a PEMFC system and has a major influence on the system's operating conditions and overall performance. Perfluorosulfonic acid (PFSA) polymers, such as Dupont's Nafion® [2], show superior durability and performance over other available materials, and are therefore used as the "standard" PEM material in the current PEMFCs. Since PFSA polymer membranes need to be fully hydrated to perform well, the current PEMFCs typically operate at high-relative humidity, low temperatures (<80 °C) and ambient pressure. At the present time, the chief technical barrier besides cost limiting the wide spread applications of current PEMFCs is their inability to use abundant and economical reformed fuel. This is because the unavoidable trace amounts of CO (typically >10 ppm) in reformed fuels poison the anode catalyst at low-operating temperatures. This problem would

be alleviated if stable high-temperature (>130 °C) PEMs were available [3,4].

PFSA polymer membranes are not suitable for high-temperature PEMs because of significant loss in proton conductivity at elevated temperatures and low-humidity conditions due to dehydration of the membranes. Previous efforts in the development of high-temperature PEMs include modification of PFSA polymers with hygroscopic materials to enhance their water-uptake ability [5,6], and the synthesis of novel aromatic-based polymers, which directly incorporate sulfonic acid groups, to enhance the membranes' heat-resistance as well as water-uptake ability at high-temperature and low-humidity conditions [7–10]. However, since the conduction of protons in these membranes is achieved through the mobility of protons combined with water molecules in the form of $H^+ \cdot nH_2O$ clusters (vehicular mechanism), these materials still need some humidification to maintain acceptable proton conductivity. The ideal high-temperature PEMs would involve a material that can efficiently conduct protons under low to zero humidity conditions.

Recently, polybenzimidazole (PBI)/H₃PO₄ and ionic liquids based Brønsted base–acid systems such as organic amine/trifluoromethanesulfonimide (HTFSA) molten salts have been reported to be highly proton conducting under elevated temperature (100–200 °C) and water-free conditions [11,12]. Systems based on poly(ethylenimine) doped with sulfuric acid or phosphoric acid that are well-behaved solid proton con-

* Corresponding authors. Fax: +1 972 883 2925.

E-mail addresses: balkus@utdallas.edu (K.J. Balkus Jr.),
ferraris@utdallas.edu (J.P. Ferraris).

ductors under anhydrous conditions have appeared in the literature [13,14]. The proton conduction in equimolar acid-doped amine electrolytes is believed to follow the Grotthuss mechanism, where the transfer of protons is achieved through deprotonation–protonation processes without transport of small molecules [15]. Considering that the activation energy of the deprotonation–protonation processes could depend on the pK_a difference of doping acids and the conjugate acids of amine groups ($\equiv\text{NH}^+$), the matching of the pK_a values can be expected to increase the ease of proton hopping between these sites, thus leading to a higher proton conductivity. The activation energy of proton transport in electrolytes also depends in part upon the distance between the amine/acid sites, and a higher density of amine/acid groups in the PEM would reduce this distance, also leading to potential conductivity enhancements.

meta-Polyaniline (*m*-PAni) possesses a high density of amine functional groups in its backbone, which are capable of conducting protons after acid doping. The pK_a of Ar_2NH_2^+ is ~ 1 , which is close to H_3PO_4 ($pK_a \sim 2$) [16]. The *meta*-structure of *m*-PAni precludes the possible electrical conductivity present for *para*-polyaniline. Although the long-term chemical stability of *m*-PAni may not be as high as the currently used perfluorinated PFSA polymers, the high-ion exchange capacity of phosphoric acid-doped *m*-PAni (5.3 mequiv. vs. 0.9 mequiv. for Nafion[®]) and its potential to conduct protons at higher temperatures and lower relative humidity make this system an important one for detailed study. *m*-PAni prepared by another method has been shown to exhibit superior performance with respect to fuel crossover in a direct methanol fuel cell [17].

In this study, *m*-PAni was synthesized and doped with H_3PO_4 at \leq equimolar amounts based on nitrogen sites of *m*-PAni to form freestanding membranes through solution casting. The proton conductivities of the resultant membranes were measured by ac impedance. *m*-PAni membranes showed reasonable proton conductivity (2×10^{-3} S/cm) at elevated temperature ($\geq 120^\circ\text{C}$) and water-free conditions.

2. Experimental

2.1. Materials

1,3-Phenylenediamine (flakes, 99+%, Aldrich), 1,3-dibromobenzene (97%, Aldrich), sodium *tert*-butoxide (97%, Aldrich), *rac*-2,2'-bis(diphenylphosphino)-1,1'-binaphthyl (97%, Aldrich), tris(dibenzylideneacetone)dipalladium(0) (Aldrich), H_3PO_4 (85 wt.%, Fisher), phenylphosphonic acid (PPA) (98%, Aldrich), diphenylphosphate (99%, Aldrich) and Nafion[®]-117 membrane (Aldrich) were used as received.

2.2. Synthesis and characterization of linear *m*-PAni

m-PAni was prepared according to a modified literature procedure [18,19] as follows: In a N_2 filled glove box, 2.17 g (20 mmol) of 1,3-phenylenediamine, 5.77 g (60 mmol) of sodium *tert*-butoxide, 0.963 g (1.5 mmol) of *rac*-2,2'-bis(diphenylphosphino)-1,1'-binaphthyl and 0.458 g (0.5 mmol) of tris(dibenzylideneacetone)dipalladium(0) were weighed into

a 250 mL flask. The flask was sealed and brought outside the box. Freshly distilled toluene (120 mL) and 1,3-dibromobenzene (4.8 g, 20 mmol) were added into the flask without air contact at room temperature. The reaction mixture was heated to 100°C under a N_2 blanket for 1 day. After cooling to room temperature, the product was precipitated by methanol, reprecipitated from tetrahydrofuran (THF)/hexanes and soxhlet extracted overnight using CH_2Cl_2 . A tan polymer was isolated in 70% yield.

^1H and ^{13}C NMR spectra were obtained using an Eclipse 270 MHz spectrometer (JEOL). ^1H NMR ($\text{DMSO}-d_6$): δ 7.97 (s, 1H, NH), 7.01 (t, 1H, aryl), 6.81 (s, 1H, aryl) 6.54 (d, 2H, aryl). ^{13}C NMR: δ 144.88, 130.09, 109.20, 106.11. The molecular weight (Mw) and polydispersity index (PDI) of the product were 18,700 and 2.12, respectively, measured by gel permeation chromatography (GPC) using a Viscotek VE 2001 apparatus (column: Viscotek[™] GMHHRH 17360; eluant: THF at 1.0 mL/min).

2.3. Membrane preparation

m-PAni was dissolved in THF to form a 10 wt.% solution. A \leq equimolar amount (vs. nitrogen sites of *m*-PAni) of phosphoric acid was added and stirred for 1 h at room temperature. The solution was cast onto a PTFE sheet, air dried at room temperature, and then annealed at 50°C under vacuum (~ 0.1 mmHg) for 3–4 h to remove the solvent and form a freestanding, flexible membrane. The thickness of the membranes (~ 100 μm) was controlled through adjusting the solution amount during casting. The doping percentage of amine groups in *m*-PAni was determined as follows:

$$\text{Doping (\%)} = \frac{\text{weight of } \text{H}_3\text{PO}_4 \times 0.929}{\text{weight of } m\text{-PAni}}$$

The morphology of the prepared membranes was studied by scanning electron microscopy (SEM) using a Phillips 60XL LaB6 microscope (3.00 kV).

2.4. Proton conductivity

Symmetric electrodes were deposited on both sides of membrane using commercially available Pt black (fuel cell grade, E-TEK) to form membrane-electrode-assemblies (MEAs). The electrode surface area was 3.75 cm^2 and the Pt catalyst loading was $4\text{--}7\text{ mg/cm}^2$. The resulting MEAs were assembled in a 5 cm^2 single cell and then installed in a fuel cell testing station (Fuel Cell Technologies Inc.) for temperature and humidity control. The ac complex impedance measurements were carried out over the frequency range $10^5\text{--}1\text{ Hz}$ with an oscillating voltage of 10 mV, using a PC controlled frequency response analyzer (VoltaLab[®] PGZ301, Radiometer Analytical S.A.).

3. Results and discussion

3.1. *m*-PAni and acid-doped membranes

Linear *m*-PAni was chosen as a proton-conducting material because of the high density of amine groups in the polymer

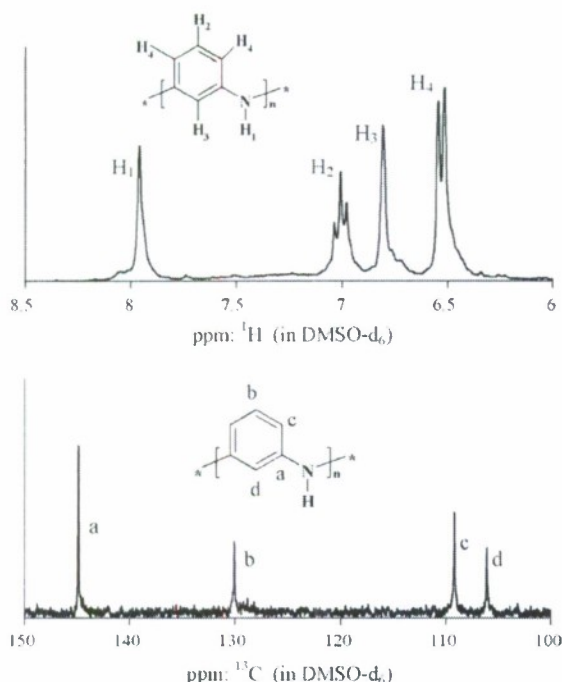


Fig. 1. ^1H and ^{13}C NMR spectra of *meta*-PAni.

backbone and the similar $\text{p}K_{\text{a}}$ values of their conjugate acids with H_3PO_4 . The *meta*-structure of *m*-PAni also precludes the high-electrical conductivity exhibited by *para*-PAni. *m*-PAni was prepared by palladium-catalyzed condensation reaction between equimolar amounts of 1,3-phenylenediamine and 1,3-dibromobenzene. Its linear, *meta* structure was confirmed by both ^1H and ^{13}C NMR, as evidenced by peaks at δ 7.01, 6.81 and 6.54 in a 1:1:2 ratio in the ^1H NMR spectrum and peaks at δ 144.88, 130.09, 109.20, 106.11 in ^{13}C NMR spectrum, which are consistent with the 1,3-substitution of benzene ring (Fig. 1). GPC with a THF eluant revealed that the product polymer had a PDI of 2.12 and Mw of 18,700, which is lower than that reported in the literature [19] (Mw=42,400 using DMF eluant). Others [18] have reported a GPC molecular weight of a *m*-PAni polymer as 8800 and 39,000 when using THF and NMP, respectively. This difference could be due to the dramatic effect of solvent on the hydrodynamic volume of the polymer in solution. Slight discrepancies in the stoichiometry of 1,3-phenylenediamine and 1,3-dibromobenzene during the condensation reaction could also lead to a lower Mw. The polymer was quite soluble in THF, and after mixing with an acid in THF and solution casting, freestanding membranes were formed. The resulting membranes appear to be continuous, homogenous and crack free, as shown by the SEM images (Fig. 2).

3.2. Proton conductivity of H_3PO_4 -doped *meta*-PAni

The typical impedance curves of an H_3PO_4 -doped *m*-PAni membrane at 70 and 100 °C under practically water-free conditions are shown as Nyquist plots in Fig. 3. The membrane resistance was determined from the point where the impedance curve intersects the real axis. In order to accurately measure

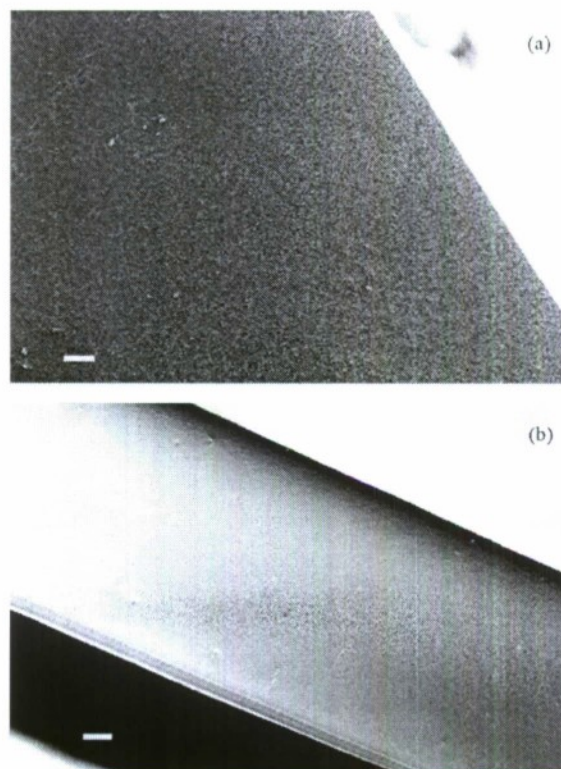


Fig. 2. SEM of H_3PO_4 -doped *m*-PAni: (a) air-side surface image (bar = 2 μm); (b) cross-sectional image (bar = 10 μm).

membrane resistances, nano-sized Pt black powder (fuel cell grade), working as electrodes, was hot pressed onto both sides of the membranes to generate sufficient electrical contact between the electrodes and the membranes. The high-surface area of Pt black electrodes also provides a large capacitance (C). Therefore, compared to the resistance of the membrane, the impedance of the electrode–membrane interface, which is equal to $1/\omega C$, is small enough to be negligible at the high-frequency range. Here, $\omega = 2\pi f$, f is the frequency, and C is the capacitance. The proton conductivity, σ , in S/cm , was calculated using the following equation:

$$\sigma = \frac{L}{R} \quad (1)$$

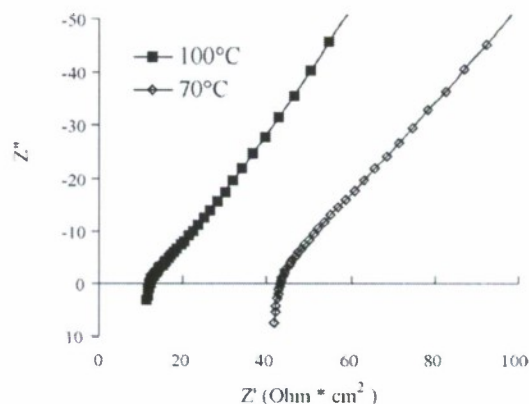


Fig. 3. Nyquist curves of H_3PO_4 -doped *meta*-PAni at various temperatures.

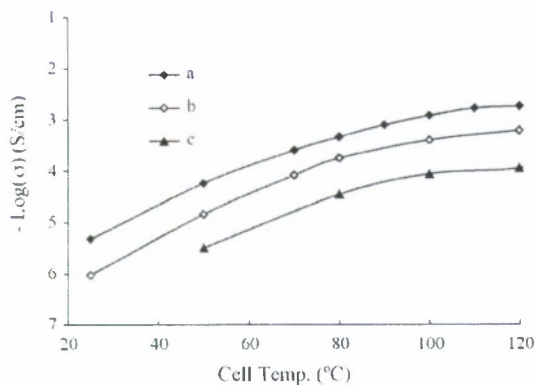


Fig. 4. A plot of proton conductivity vs. cell temperature for acid-doped linear *meta*-PANI under dry condition: (a) 100% doped with H_3PO_4 ; (b) 80% doped with H_3PO_4 ; (c) 100% doped with PPA.

where L is the membrane thickness (cm) and R is the measured membrane resistance ($\Omega \text{ cm}^2$).

Fig. 4 shows that the proton conductivities of 100% H_3PO_4 -doped *m*-PANI membranes steadily increase with an increase in temperature, reaching a maximum of $2 \times 10^{-3} \text{ S/cm}$ at 120°C under water-free conditions. Since the $\text{p}K_a$ of H_3PO_4 and Ar_2NH_2^+ are ~ 2 and ~ 1 , respectively [16], the nitrogen sites in the membranes were partially protonated. Therefore, various species may coexist in the membranes and could be involved in the proton transfer, including H_3PO_4 , $>\text{NH}_2^+$, H_2PO_4^- and $>\text{NH}$. In such a situation, the proton conduction in the membranes can be rationalized as follows: H_3PO_4 and $>\text{NH}_2$ act as proton donors and H_2PO_4^- and $>\text{NH}$ act as proton acceptors. Under essentially water-free conditions, the proton conduction in these membranes is achieved through the hopping of protons between donors and acceptors accompanied by the rotation and reorientation of donors and acceptors. The essential role of *m*-PANI in the proton-conducting process includes providing $>\text{NH}_2^+ / >\text{NH}$ as proton donor/acceptor as well as being a solid matrix [20].

Since there are free- H_3PO_4 molecules in the membranes, the possibility of a vehicular component, in which free- H_3PO_4 molecules act as vehicles to transfer protons through the membranes, could not be excluded. However, a study of the (PBI)/ H_3PO_4 system [21,22] proposed that even in a high-doping level (630%) PBI/ H_3PO_4 system, which contains a large amount of free- H_3PO_4 and a proton conductivity of $>10^{-2} \text{ S/cm}$, the free acids are likely confined in the polymer matrix with little long-distance migration. Therefore, protons mainly transfer between the proton donors (H_3PO_4 and $>\text{NH}_2^+$) and acceptors (H_2PO_4^- and $>\text{NH}$) (the Grotthuss mechanism). The similarity between *m*-PANI/ H_3PO_4 system and PBI/ H_3PO_4 system suggests that the proton conduction in H_3PO_4 -doped *m*-PANI could mainly follow the Grotthuss mechanism as well.

Since the transfer of protons is associated with the regional mobility of proton-conducting active groups [22,23], increasing the operating temperatures results in an increase in proton conductivity (Fig. 4). Increasing the acid/amine ratio from 0.8 to 1.0 also led to an increase in proton conductivity by approximately five times. Higher acid doping levels in the *m*-PANI/ H_3PO_4

system as well as the proton-conduction mechanism are under investigation.

The nature of the doping acids can also affect the proton conductivity of the membranes. In the Grotthuss mechanism, the hopping of protons is realized through deprotonation–protonation processes, which strongly depend on the structure, number and mobility of these of proton donor and acceptor sites in the membranes. PPA, a diprotic acid, is more sterically demanding, possesses one less deprotonation–protonation site and has a slightly higher first $\text{p}K_a$ than H_3PO_4 (triprotic acid). The combination of these features is consistent with the observation that PPA-doped *m*-PANI membranes exhibit proton conductivities 16 times lower than H_3PO_4 -doped membranes under the same temperature and humidity conditions (Fig. 4). Diphenylphosphate (DPP), a larger acid than H_3PO_4 or PPA, would have even lower mobility in the polymer matrix, has only one deprotonation–protonation site, and is a weaker acid than either H_3PO_4 or PPA. Thus, the proton conductivity of DPP-doped *m*-PANI membranes was too low to be measured under our experimental conditions.

In the case of a Nafion[®]-117 membrane, in which proton conduction typically follows the vehicular mechanism, dehydration of the membrane significantly reduces its proton conductivity. In contrast, H_3PO_4 -doped *m*-PANI membranes (100% doping level) exhibited ~ 1.2 orders of magnitude higher proton conductivity than Nafion[®]-117 at 120°C under low-humidity ($\sim 1.5\%$ relative humidity) conditions (Fig. 5). The relative humidity has a significant effect on the proton conductivities of H_3PO_4 -doped *m*-PANI membranes (Fig. 6). The humidity in a fuel cell operating atmosphere introduces water molecules into the membrane, which facilitates the proton transfer between proton donors (H_3PO_4 and $>\text{NH}_2^+$) and acceptors (H_2PO_4^- and $>\text{NH}$). It has been reported [21] that the rates of proton transfer between proton donors and acceptors are in the order of: H_3PO_4 to H_2O to $\text{H}_2\text{PO}_4^- > \text{H}_3\text{PO}_4$ to $\text{H}_2\text{PO}_4^- > \text{N}-\text{H}^+$ to H_2PO_4^- , and $\text{N}-\text{H}^+$ to H_2O to $\text{N}-\text{H} > \text{N}-\text{H}^+$ to $\text{N}-\text{H}$. In the presence of water, the protons likely transfer faster through the membrane via the Grotthuss mechanism, leading to higher proton conductivity. The water molecules in the membranes may also result in additional proton conduction through the vehicular mechanism, partially contributing to the overall proton conductivity. Compared with dry conditions, the membrane's proton conductivity was ~ 2 –

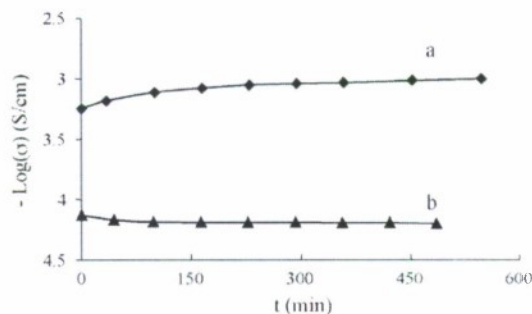


Fig. 5. A plot of proton conductivity vs. time for Nafion[®]-117 and H_3PO_4 -doped *m*-PANI membranes at 120°C and 1.5% RH: (a) 100% H_3PO_4 -doped *m*-PANI; (b) Nafion[®]-117.

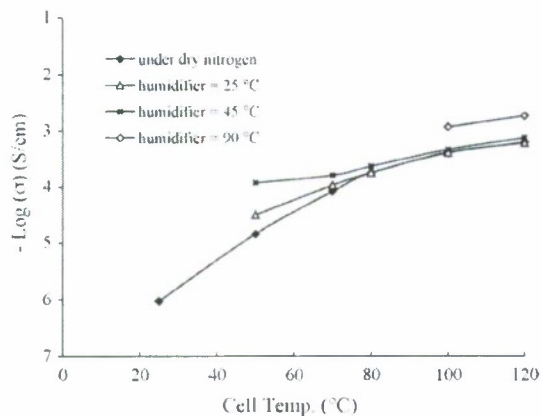


Fig. 6. A plot of proton conductivity vs. cell temperature for H_3PO_4 -doped *m*-PANI at different humidities.

times higher at 100 °C with the humidifier temperature of 90 °C. In this situation, it is not clear whether the Grotthuss mechanism or vehicular mechanism is the dominant proton-conducting mechanism in operation. A color change and flexibility loss of H_3PO_4 -doped *m*-PANI membranes were observed during the experiments at elevated temperatures (≥ 120 °C), especially in the presence of O_2 , indicating that the long-term stability of the membranes would be a problem in a PEM fuel cell. The degradation of the membranes is most likely due to the chemical/thermal decomposition of *m*-PANI polymer. The stability of *m*-PANI polymer could be greatly improved by perfluorinating and/or substituting the phenylene in the polymer backbone, which will be an attractive topic in the future study.

4. Conclusions

Linear *m*-PANI has been synthesized and proton-conducting polymer membranes using acid-doped *m*-PANI solution were prepared by solvent casting. The H_3PO_4 -doped *m*-PANI membranes show good proton conductivity ($10^{-2.7}$ S/cm) at high temperatures (120 °C) and essentially zero humidity conditions. Under water-free conditions, the proton conduction of membranes likely follows the Grotthuss mechanism and can be enhanced by increasing the density of proton donors/acceptors. An increase in relative humidity leads to an increase in the membranes' proton conductivities by enhancing the proton transfer rates through the Grotthuss mechanism and/or introducing possible proton conduction through a vehicular mechanism.

Acknowledgements

We would like to thank LANL, THECB-ATP, SPRING and R.A. Welch Foundation for the financial support of this work.

References

[1] S.J.C. Cleghorn, X. Ren, T.E. Springer, M.S. Wilson, C. Zawodzinski, T.A. Zawodzinski, S. Gottesfeld, PEM fuel cells for transportation and stationary power generation applications, *Int. J. Hydrogen Energy* 22 (1997) 1137.

[2] D.L. Reichert, Dupont and PEM fuel cells, *Prepr. Symp. -Am. Chem. Soc., Div. Fuel Chem.* 46 (2001) 443.

[3] R.K.A.M. Mallant, PEMFC systems: the need for high temperature polymers as a consequence of PEMFC water and heat management, *J. Power Sources* 118 (2003) 424.

[4] C. Yang, P. Costamagna, S. Srinivasan, J. Benziger, A.B. Bocarsly, Approaches and technical challenges to high temperature operation of proton exchange membrane fuel cells, *J. Power Sources* 103 (2001) 1.

[5] V. Ramani, H.R. Kunz, J.M. Fenton, Investigation of Nafion®/HPA composite membranes for high temperature/low relative humidity PEMFC operation, *J. Membr. Sci.* 232 (2004) 31.

[6] P. Costamagna, C. Yang, A.B. Bocarsly, S. Srinivasan, Nafion® 115/zirconium phosphate composite membranes for operation of PEMFCs above 100 °C, *Electrochim. Acta* 47 (2002) 1023.

[7] T. Soczka-Guth, J. Baurmeister, G. Frank, R. Knauf, International Patent WO 99/29763, 1999.

[8] R. Nolte, K. Ledjeff, M. Bauer, R. Mülhaupt, Partially sulfonated poly(arylene ether sulfone)—a versatile proton conducting membrane material for modern energy conversion technologies, *J. Membr. Sci.* 83 (1993) 211.

[9] J. Kerres, W. Cui, S. Reichle, New sulfonated engineering polymers via the metalation route. I. Sulfonated poly(ethersulfone) PSU Udel® via metalation-sulfonation-oxidation, *J. Polym. Sci. A: Polym. Chem.* 34 (1996) 2421.

[10] T. Kobayashi, M. Rikukawa, K. Sanui, N. Ogata, Proton-conducting polymers derived from poly(ether-etherketone) and poly(4-phenoxybenzoyl-1,4-phenylene), *Solid State Ionics* 106 (1998) 219.

[11] J.S. Wainright, J.T. Wang, D. Weng, R.F. Savinell, M. Litt, Acid-doped polybenzimidazoles: a new polymer electrolyte, *J. Electrochem. Soc.* 142 (1995) L121.

[12] Md.A.B.H. Susan, A. Noda, S. Mitsushima, M. Watanabe, Brønsted acid-base ionic liquids and their use as new materials for anhydrous proton conductors, *Chem. Commun.* 8 (2003) 938.

[13] R. Tanaka, H. Yamamoto, S. Kawamura, T. Iwase, Proton conducting behavior of poly(ethylenimine)- H_3PO_4 systems, *Electrochim. Acta* 40 (1995) 2421.

[14] M.F. Daniel, B. Desbat, F. Cruege, O. Trinquet, J.C. Lassegues, Solid state protonic conductors: poly(ethylenimine) sulfates and phosphates, *Solid State Ionics* 28–30 (1988) 637.

[15] K.-D. Kreuer, Proton conductivity: materials and applications, *Chem. Mater.* 8 (1996) 610.

[16] Calculated Using ACD/pK_a, Advanced Chemistry Development Inc., 110 Yonge Street, 14th floor, Toronto, Ontario, Canada M5C 1T4.

[17] H. Akita, M. Ichikawa, M. Iguchi, H. Hiroyuki, Proton Conducting Polymer, Method for Producing the Same, Solid Polymer Electrolyte and Electrode, US Patent No. 6,478,987 B1, November 12, 2002.

[18] N. Spetseris, R.E. Ward, T.Y. Meyer, Linear and hyperbranched *m*-polyaniline: synthesis of polymers for the study of magnetism in organic systems, *Macromolecules* 31 (1998) 3158.

[19] T. Kanbara, K. Izumi, Y. Nakadani, T. Narise, K. Hasegawa, Preparation of poly(imino1,3-phenylene) and its related polymer by palladium-catalyzed polycondensation, *Chem. Lett.* 11 (1997) 1185.

[20] R. Tanaka, H. Yamamoto, A. Shono, K. Kubo, M. Sakurai, Proton conducting behavior in non-crosslinked and crosslinked polyethylenimine with excess phosphoric acid, *Electrochim. Acta* 45 (2000) 1385.

[21] Y.-L. Ma, J.S. Wainright, M.H. Litt, R.F. Savinell, Conductivity of PBI membranes for high-temperature polymer electrolyte fuel cells, *J. Electrochem. Soc.* 151 (1) (2004) A8.

[22] R.H. He, Q.F. Li, G. Xiao, N.J. Bjerrum, Proton conductivity of phosphoric acid doped polybenzimidazole and its composites with inorganic proton conductors, *J. Membr. Sci.* 226 (2003) 169.

[23] M. Eikerling, A.A. Kornyshev, A.M. Kuznetsov, J. Ulstrup, S. Walbran, Mechanisms of proton conductance in polymer electrolyte membranes, *J. Phys. Chem. B* 105 (2001) 3646.



Proton-conducting membranes based on HTFSI-doped PEI/SiO₂ nanocomposites

Zhiwei Yang, Decio H. Coutinho, Duck-Joo Yang,
Kenneth J. Balkus Jr. *, John P. Ferraris *

Department of Chemistry and The Alan G. MacDiarmid NanoTech Institute, The University of Texas at Dallas, Richardson, TX 75083-0688, USA

Received 5 January 2005; received in revised form 28 December 2007; accepted 31 December 2007

Available online 9 January 2008

Abstract

Novel proton-conducting membranes comprising polymer/inorganic materials based on linear polyethyleneimine (LPEI)/SiO₂ nanocomposites synthesized through sol–gel processing have been prepared. 3-Glycidyloxypropyl-trimethoxysilane (GLYMO) has been used to cross-link the LPEI to afford improved heat resistance. The addition of trifluoromethanesulfonimide (HTFSI) during membrane processing doped the amine groups of LPEI to form immobilized Brønsted acid–base pairs, which provide the hybrid membrane's proton conductivity. The resulting membranes show a proton conductivity as high as 1×10^{-2} S/cm at 90 °C, 100% relative humidity and 5.6×10^{-3} S/cm at high temperatures (≥ 130 °C) under anhydrous conditions. The effects of temperature, humidity and mobility of active groups on the conductivity are discussed.
© 2008 Elsevier B.V. All rights reserved.

Keywords: Linear polyethyleneimine; Hybrid nanocomposites; Membrane; Proton conductivity

1. Introduction

The interest in high temperature (≥ 130 °C) proton exchange membrane fuel cells (PEMFCs) has grown dramatically since they can allow the direct use of inexpensive and abundant reformed fuels at these operating temperatures [1]. The proton exchange membrane (PEM), which conducts protons between the anode and cathode, plays a central part in PEMFCs [2]. Proton conduction in PEMs follows either the vehicular or Grotthuss mechanism. In the vehicular mechanism, protons transfer through the PEM together with small molecules such as H₂O. In the Grotthuss mechanism, protons hop via hydrogen bonds from one active site to neighboring ones without the transport of associated molecules [3,4]. PEMs incorporating sulfonic acid groups, such as perfluorosulfonic acid (PFSA) polymers and sulfonated aromatic-based polymers [5] conduct protons mainly through the mobility of H⁺–*n*H₂O clusters (the vehicular mechanism). As such, they may not be intrinsically suitable for

high temperature PEMFC applications, since dehydration of the membranes at elevated temperature (≥ 100 °C) and low humidity conditions ($\leq 25\%$ relative humidity) leads to a decrease in the membrane's proton conductivity and FC efficiency [6]. Thus, PEMs that can efficiently conduct protons under low to zero humidity conditions are essential for high temperature PEMFCs.

Recently, a new class of inorganic/organic composite membranes comprising SiO₂ nanocomposites and polymers have been prepared through the sol–gel process and investigated for PEM applications [7,8]. Although introduction of SiO₂ clusters into the polymer matrix significantly improved the mechanical and thermal properties, these membranes only exhibited proton conductivity $\sim 10^{-3}$ S/cm under nearly saturated humidity conditions.

Brønsted acid–base ionic liquids, prepared from equimolar amounts of small organic amines and HTFSI, are known to be highly proton conducting ($>10^{-2}$ S/cm) under anhydrous conditions in their melt phase (≥ 130 °C) [9–11]. In order to overcome migration and leakage in electrochemical devices, cations and/or anions of ionic liquids are often covalently bound to organic or polymeric chains to form solid-state electrolytes [12]. One highly studied example is polybenzimidazole (PBI), an aromatic-based polymer containing amine functional groups

* Corresponding authors. Fax: +1 972 883 2925.
E-mail addresses: balkus@utdallas.edu
(K.J. Balkus Jr.), ferraris@utdallas.edu (J.P. Ferraris).

on its polymer backbone which, when doped (300–650 mol% doping level) with H_3PO_4 , holds promise for high temperature PEMFC, because of its excellent thermal/chemical/mechanical stability and high proton conductivity ($\sim 6 \times 10^{-3}$ S/cm) at high temperature (150 °C) and low (5–30%) relative humidity conditions. It is believed that H_3PO_4 is confined in the polymer matrix through hydrogen bonds, and the proton conduction follows the Grotthuss mechanism [13,14]. A review of recent advances in PEM materials for high temperature fuel cells has appeared [15].

The hopping of protons strongly depends on the distance between active sites. Thus, increasing the density of amine/acid groups in membranes is expected to lead to higher proton conductivity. In the present investigation, linear polyethyleneimine which possesses the highest density of amine groups in polyamine polymers, was synthesized. Owing to its relatively low T_g (–23 °C) [16] and melting point (~ 60 °C) [17], LPEI was reacted with 3-glycidyloxypropyl-trimethoxysilane to form a LPEI/SiO₂ hybrid nanocomposite. The resulting hybrid material was then doped with HTFSI to form Brønsted acid–base pairs and cast into membranes that exhibited proton conductivity of 5.6×10^{-5} S/cm under elevated temperatures (130 °C) and essentially zero humidity conditions, increasing to 10^{-2} S/cm at 90 °C, 100% relative humidity.

2. Experimental

2.1. Materials

Poly(2-ethyl-2-oxazoline) (MW = 500k, Aldrich), lithium trifluoromethanesulfonimide (3M company), H_2SO_4 (96%, Mallinckrodt), 3-glycidyloxypropyl-trimethoxysilane (97%, Fluka), imidazole (99%, ACROS), and dipropylamine (99%, Aldrich) were used as received. Trifluoromethanesulfonimide, mp 55.5–56.5 °C, was prepared according to a literature method [18], NMR (DMSO-*d*₆), δ -¹H: 13.81 (s); ¹³C: 112.57 (s), 117.30 (s), 122.04 (s), 126.78 (s).

2.2. Synthesis of linear PEI

Linear polyethyleneimine was prepared by a slight modification of a literature method [17] as follows: 10 g of linear poly(2-ethyl-2-oxazoline) and 250 mL of 7 M HCl solution were heated at reflux for 5 days. The product was cooled to room temperature and precipitated using 250 mL of 7.4 M NaOH. The solid was collected by filtration and washed thoroughly with DI water until neutral, then re-precipitated from ethanol/water (5/6, v/v) and dried overnight at ~ 90 °C under vacuum (~ 0.1 mmHg). A >90% yield of LPEI was obtained. NMR (methanol-*d*₄), δ -¹H: 2.73 (s, 4H), 4.84 (s, 1H); ¹³C: 48.45 (s).

2.3. Preparation of organic amine/HTFSI salts

An equimolar amount of imidazole or dipropylamine (vs. HTFSI) was mixed with 2.81 g (10 mmol) of HTFSI in ~ 6 mL of absolute ethanol. The mixtures were stirred for ~ 1 h at room temperature, followed by removal of the solvent under vacuum (~ 0.1 mmHg) at 80 °C to give white granular crystals.

Melting point—imidazole/HTFSI salt: 74.0–75.0 °C; dipropylamine/HTFSI salt: 107.2–107.8 °C.

2.4. Membrane preparation

LPEI was dissolved in absolute ethanol to form a 10 wt% solution. GLYMO (18 mol% vs. LPEI repeat units) was added and stirred for 0.5 h at room temperature. An equimolar amount of HTFSI (vs. >NH groups, 50 wt% in ethanol) was added dropwise and stirred for another 0.5 h at room temperature. The resulting solution was cast on a level PTFE surface, air dried at room temperature for 1 day, and then heated at 80 °C overnight to give freestanding, flexible membranes. Membrane thickness (~ 150 μm) was easily controlled by varying the solution amount during casting. The doping percentage of amine groups in LPEI was determined using the following equation:

$$\text{doping (\%)} = \frac{\text{weight of HTFSI} \times 0.153}{\text{weight of LPEI}}$$

The membranes comprising organic amine/HTFSI salts were prepared by adding either the imidazole/HTFSI or dipropylamine/HTFSI salt into the above described solution followed by stirring for 15 min before casting.

2.5. Characterization

¹H and ¹³C NMR spectra were obtained using an Eclipse 270 MHz spectrometer (JEOL). IR samples were prepared as KBr pellets. FTIR spectra were recorded on a Nicolet Avatar 360 FTIR spectrophotometer with a resolution of 4 cm⁻¹, in the range of 4000–400 cm⁻¹. Scanning electron micrographs (SEMs) of the membranes were obtained on a Phillips 60XL LaB₆ microscope. The thermal stability of the membranes under O₂ atmosphere was investigated by thermogravimetric analysis (TGA) using a PerkinElmer Pyris 1 TGA. The samples were loaded into Pt pans and heated at the rate of 10 °C/min until no further weight loss was detected. The mechanical strength and strain of the membranes were characterized by tensile tests on an Instron 5848 MicroTester at room temperature, with 10 mm gauge length and 0.1 mm/min extension rate.

2.6. Proton conductivity measurements

For all proton conductivity measurements, the membranes were coated on both sides (~ 3.5 cm²) with Pt nanosize catalyst (fuel cell grade, E-TEK) by hot pressing at ~ 85 °C and ~ 300 psig, before placement in a 5 cm² single cell (Fuel Cell Technologies Inc.). The single cell's temperature and humidity were controlled using a fuel cell testing station (Fuel Cell Technologies Inc.). The through-membrane proton conductivities were measured by the ac impedance method using a PC controlled VoltaLab[®] PGZ301 (Radiometer Analytical S.A.) over the frequency range of 100 kHz to 0.1 Hz with a 10 mV amplitude ac signal. Membrane areal resistances, R (Ω cm²), were determined from the point where the Nyquist curve intersects the real axis and the proton conductivities (σ , Ω⁻¹ cm⁻¹) were obtained from L/R , where L is the membrane thickness (cm).

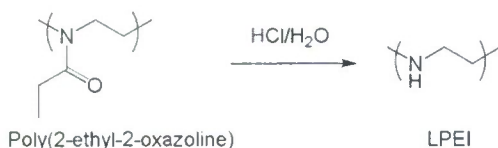


Fig. 1. Scheme of linear PEI preparation.

3. Results and discussion

3.1. Synthesis and structural characterization

Linear PEI was prepared by hydrolyzing poly(2-ethyl-2-oxazoline) (MW = 500k) in aqueous HCl solution (Fig. 1) [17]. FTIR spectra of the product confirmed successful conversion to LPEI as evidenced by the N–H stretching bands between 3200 and 3400 cm^{-1} and the characteristic N–H bending modes near 820 cm^{-1} [19]. The precursor polymer's strong C=O absorption peak at $\sim 1650 \text{ cm}^{-1}$ was replaced by a very weak absorption at $\sim 1660 \text{ cm}^{-1}$, which could be ascribed to several possibilities, including (1) C=O stretch of unhydrolyzed amido groups of poly(2-ethyl-2-oxazoline), and (2) a C=O stretch of carbamate formed between the LPEI amines and adsorbed CO_2 [20]. The ^1H and ^{13}C NMR spectra of the product only exhibited peaks at ^1H : δ 2.73 (s, 4H), 4.84 (s, 1H) and ^{13}C : δ 48.45 (s), respectively, which is consistent with the clean conversion of poly(2-ethyl-2-oxazoline) into LPEI. Since no other peaks appeared in the ^1H and ^{13}C NMR spectra of the polymer product, the unhydrolyzed

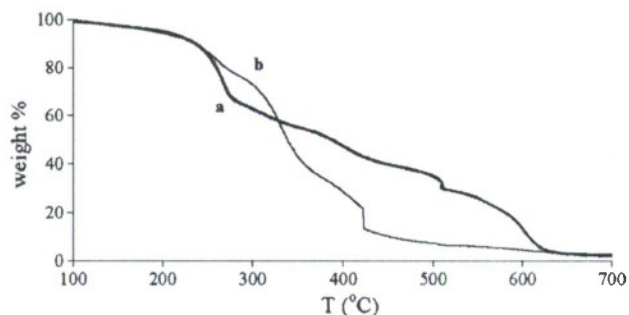
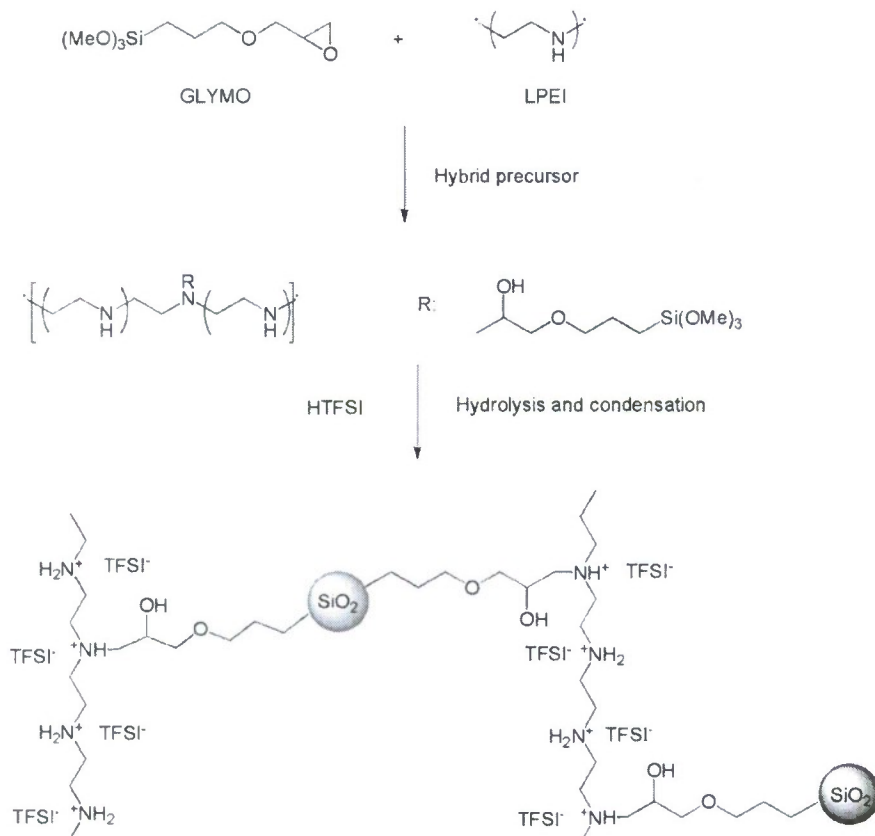


Fig. 2. TGA of the LPEI polymer (a) and HTFSI-doped LPEI/GLYMO (b).

amido groups and/or carbamate groups cannot be present in concentrations greater than a few mol% versus amines. The obtained LPEI had a low melting point (70–80 °C) and calculated molecular weight of $\sim 215\text{k}$. The actual molecular weight of the LPEI could not be determined by GPC due to its strong absorption to the column despite using a variety of packing materials and eluants. Nevertheless, the extremely clean ^1H and ^{13}C NMR spectra, the high yield (>90%) of the hydrolysis product, and its good film-forming properties all suggest a low degree of chain scission. Thermogravimetric analysis of the LPEI with a heating rate of 10 °C/min under an O_2 atmosphere, shows a small gradual weight loss ($\sim 7 \text{ wt}\%$) preceding the major weight loss ($\sim 80\%$) starting at $\sim 230 \text{ }^\circ\text{C}$ (Fig. 2). Comparison of the FTIR spectra of as-synthesized LPEI and a sample heated to 150 °C

Fig. 3. Scheme for the preparation of HTFSI-doped LPEI/SiO₂ hybrid membranes.

under an O₂ atmosphere, showed no distinguishable changes, but some growth in the peak appearing at 1660 cm⁻¹ occurred when the sample was heated to 220 °C in air.

In an attempt to increase the LPEI's heat resistance at elevated temperatures, the polymer was cross-linked using small amounts of GLYMO (18 mol% vs. amines of LPEI) [21]. Each GLYMO molecule has an epoxy end group and a trimethoxysilane end group. When mixed with LPEI in an alcohol solution, the epoxy groups can react with the secondary amines of PEI to form tertiary amines, and the trimethoxysilane groups hydrolyze and condense to form inorganic silica clusters as illustrated in Fig. 3. The FTIR spectrum of the LPEI/GLYMO composite membrane shows a broad peak in the 1000–1200 cm⁻¹ range indicative of the formation of SiO₂ clusters.

HTFSI, working as a protonator, was added to dope the amine groups in the LPEI/GLYMO composite during the sol-gel condensation to form >NH₂⁺/TFSI⁻ pairs. The large differences between the pK_a values of the conjugate acids of secondary (~11) and tertiary (10–11) alkyl amines versus that of HTFSI (~2), means that the amine groups in the LPEI/GLYMO composite are completely protonated by HTFSI to form the Brønsted acid–base pairs. The HTFSI-doped composites afforded free-standing, continuous and pinhole free membranes after solution casting, as shown by the SEM images in Fig. 4. These cross-linked membranes exhibited dimensional stability at the temperature and pressure (~85 °C and ~300 psig) conditions used during the Pt coating processes. The FTIR spectra of the resulting membranes exhibited characteristic peaks at 1350

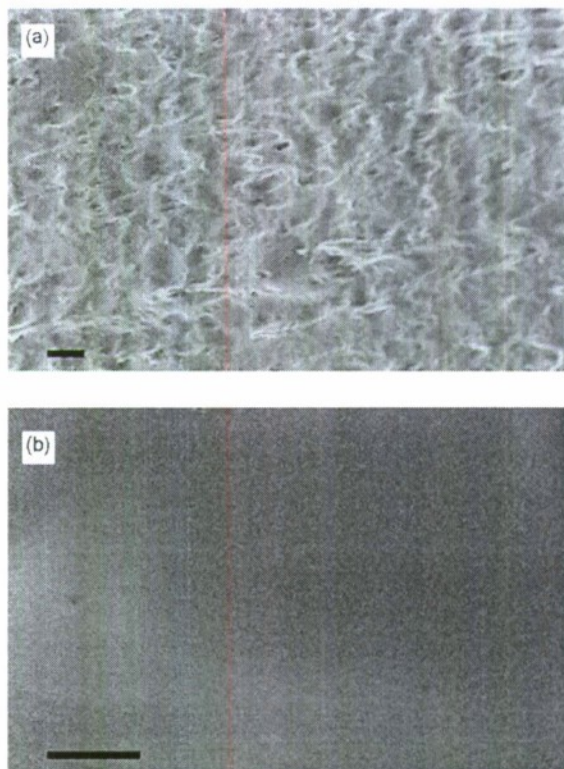


Fig. 4. SEM images of HTFSI-doped LPEI/SiO₂ membrane: (a) cross-sectional image and (b) air-side surface image. Bar = 2 μm.

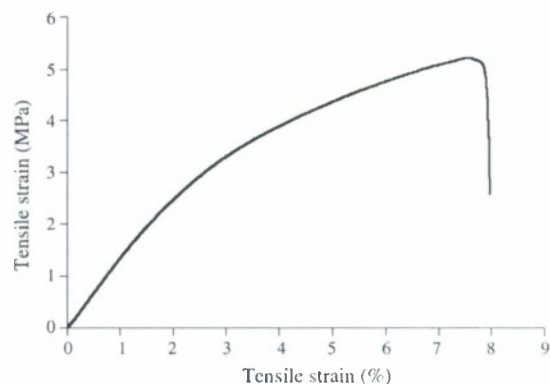


Fig. 5. The stress–strain behavior of HTFSI-doped LPEI/SiO₂ membranes under ambient condition.

and 1197 cm⁻¹, assigned to asymmetric and symmetric S(=O)₂ stretches, respectively, as well as peaks at 1331 and 1142 cm⁻¹ arising from the asymmetric and symmetric C–F stretching modes. Thermogravimetric analysis shows that the major weight loss behavior of HTFSI-doped LPEI/SiO₂ membranes occurs at a somewhat higher temperature than LPEI. Since HTFSI accounts for approximately 77 wt% of the composite and has a relatively low boiling point (90–91 °C), such weight loss behavior further supports the complete protonation of the LPEI polymer.

The strength and % extension of HTFSI-doped LPEI/SiO₂ membranes at the break point were 5.2 MPa and 7.7%, respectively (Fig. 5). Though less than the corresponding values for Nafion[®]-117 membranes (43 MPa, 225% at 23 °C and 50% RH), the LPEI composite membranes were sufficiently strong for PEM conductivity testing.

3.2. Proton conductivity

LPEI was chosen in this study because it has the highest amine density among the polyamine polymers. During the sol-gel processes, HTFSI was added to dope the amine groups to form Brønsted acid–base ionic couples. Under a dry N₂ atmosphere, the proton conductivity of HTFSI-doped LPEI/SiO₂ increased with increasing temperature and reached 5.6×10^{-5} S/cm at 130 °C (Fig. 6). Since this is an essentially water-free system and the proton-conducting active sites were part of the polymer's backbone, proton conduction via a Grotthuss mechanism is the most likely. Compared with the proton conductivity of non-immobilized 1:1 salts derived from organic amine/HTFSI combinations [11] the proton conductivity at 130 °C under anhydrous conditions of the immobilized HTFSI-doped LPEI/GLYMO membranes was over two orders of magnitude lower. The proton conduction in organic amine/HTFSI molten salts has been ascribed to a combination of proton hopping (Grotthuss) and vehicular mechanisms [22]. For the Grotthuss mechanism, the hopping of protons is always associated with the regional vibration, rotation and/or reorientation of proton-conducting active groups. The regional mobility in the HTFSI-doped LPEI/SiO₂ membranes, was expected to be lower since the amine groups are part of the polymer's back-

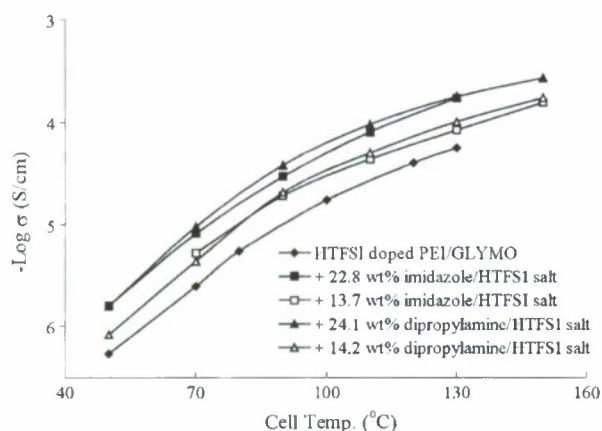


Fig. 6. A plot of proton conductivity vs. temperature for LPEI/GLYMO-based membranes under water-free conditions.

bone. This also precluded the free migration that is possible in the non-immobilized molten salt systems that provide an additional vehicular component to the overall proton conduction. In order to access this conduction mode, 1:1 molten salts comprising dipropylamine/HTFSI or imidazole/HTFSI were added to the HTFSI-doped LPEI/SiO₂ membranes during the sol-gel processing. A proton conductivity enhancement of ~0.5 order of magnitude was observed upon addition of 24.1 wt% of the dipropylamine/HTFSI or 22.8 wt% of the imidazole/HTFSI molten salts (Fig. 6). Thus the mobility of proton-conducting functional groups has a significant positive impact on the proton conductivity. Higher temperatures also increase the regional mobility of functional groups in the membranes, also leading to higher proton conductivity (Fig. 6).

The relative humidity also had a significant effect on the proton conductivity of HTFSI-doped LPEI/SiO₂ membranes (Fig. 7). The respective contributions of the two proton conduction mechanisms under hydrated conditions for these membranes is not clear, since water molecules can contribute to the overall proton conductivity in two ways. For the Grotthuss mechanism water can facilitate hopping of protons between the proton donors and acceptors. It has been reported [14] that the proton transfer rate of N–H⁺ to H₂O to N–H is higher than from N–H⁺ to N–H directly. The other possibility is that water enables additional proton conduction through a traditional vehicular mechanism. Compared with the water-free conditions, the membrane proton conductivity was up to 100 times higher at

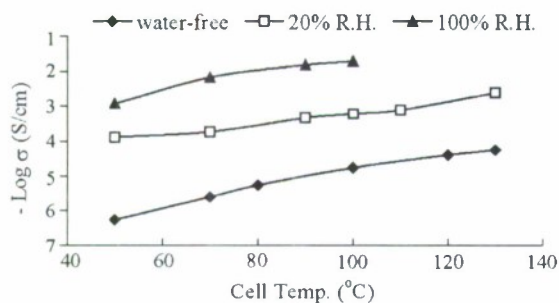


Fig. 7. Proton conductivity vs. temperature for 100% HTFSI-doped LPEI/GLYMO membranes under different RH conditions.

20% RH, and reached values of 0.01 S/cm at 90 °C, 100% relative humidity.

4. Conclusions

HTFSI-doped LPEI/GLYMO membranes containing a high density of immobilized amine/HTFSI groups exhibit good proton conductivities at high temperature and low to zero humidity conditions. Under water-free conditions, the proton conduction of these membranes follows the Grotthuss mechanism and strongly depends on the mobility of the amine/HTFSI groups. An increase in relative humidity led to an increase in the proton conductivities of the membranes by enhancing the proton-hopping rate through either the Grotthuss mechanism and/or by introducing additional proton conduction through the vehicular mechanism.

Acknowledgements

The work is supported by LANL, THECB-ATP, SPRING, Samsung Advanced Institute of Technology and R.A. Welch Foundation.

References

- [1] Q. Li, R. He, J.O. Jensen, N.J. Bjerrum, Approaches and recent development of polymer electrolyte membranes for fuel cells operating above 100 °C, *Chem. Mater.* 15 (2003) 4896.
- [2] L. Carrette, K.A. Friedrich, U. Stimming, Fuel cells—fundamentals and applications, *Fuel Cells* 1 (2001) 5.
- [3] T. Norby, Solid-state protonic conductors: principles, properties, progress and prospects, *Solid State Ionics* 125 (1999) 1.
- [4] K.-D. Kreuer, Proton conductivity: materials and applications, *Chem. Mater.* 8 (1996) 610.
- [5] M. Hogarth, X. Glipa, High temperature membranes for solid polymer fuel cells, ETSU F/02/00189/REP DTI/Pub URN 01/893.
- [6] G. Alberti, M. Casciola, L. Massinelli, B. Bauer, Polymeric proton conducting membranes for medium temperature fuel cells (110–160 °C), *J. Membr. Sci.* 185 (2001) 73.
- [7] I. Honma, S. Hirakawa, K. Yamada, J.M. Bae, Synthesis of organic/inorganic nanocomposites protonic conducting membrane through sol-gel processes, *Solid State Ionics* 118 (1999) 29.
- [8] H.Y. Chang, C.W. Lin, Proton conducting membranes based on PEG/SiO₂ nanocomposites for direct methanol fuel cells, *J. Membr. Sci.* 218 (2003) 295.
- [9] M. Yoshizawa, W. Xu, C.A. Angell, Ionic liquids by proton transfer: vapor pressure, conductivity, and the relevance of pK_a from aqueous solutions, *J. Am. Chem. Soc.* 125 (2003) 15411.
- [10] W. Xu, C.A. Angell, Solvent-free electrolytes with aqueous solution-like conductivities, *Science* 302 (2003) 422.
- [11] Md.A.B.H. Susan, A. Noda, S. Mitsushima, M. Watanabe, Brønsted acid–base ionic liquids and their use as new materials for anhydrous proton conductors, *Chem. Commun.* 8 (2003) 938.
- [12] S. Washiro, M. Yoshizawa, H. Nakajima, H. Ohno, Highly ion conductive flexible films composed of network polymers based on polymerizable ionic liquids, *Polymer* 45 (2004) 1577.
- [13] J.S. Wainright, J.T. Wang, D. Weng, R.F. Savinell, M. Litt, Acid-doped polybenzimidazoles: a new polymer electrolyte, *J. Electrochem. Soc.* 151 (1) (2004) A8–A16.
- [14] Y.L. Ma, J.S. Wainright, M.H. Litt, R.F. Savinell, Conductivity of PBI membranes for high-temperature polymer electrolyte fuel cells, *J. Electrochem. Soc.* 151 (2004) A8.

- [15] Q. Li, R. He, J.O. Jensen, N. Bjerrum, Approaches and recent development of polymer electrolyte membranes for fuel cells operating above 100 °C, *Chem. Mater.* 15 (2003) 4896–4915.
- [16] G.A. Giffin, R. Frech, F. Yopez Castillo, J. Eisenblatter, D.T. Glatzhofer, Polymer electrolytes derived from poly(*N*-methyleneimine) and poly(*N*-ethyleneimine), Abstracts, 60th Southwest Regional Meeting of the American Chemical Society SEPT04-178, 2004.
- [17] R. Tanaka, I. Ueoka, Y. Takaki, K. Kataoka, S. Saito, High molecular weight linear polyethyleneimine and poly(*N*-methylethylenimine), *Macromolecules* 16 (1983) 849.
- [18] D.D. Desmarreau, M. Witz, *N*-Fluorobis (trifluoromethanesulfonyl)imide. An improved synthesis, *J. Fluor. Chem.* 52 (1991) 7.
- [19] S.S. York, S.E. Biesch, R.A. Wheeler, R. Frech, Vibrational assignments for high molecular weight linear polyethyleneimine (LPEI) based on monomeric and tetrameric model compounds, *Macromolecules* 36 (2003) 7348–7351.
- [20] E.D. Bates, R.D. Mayton, I. Ntai, J.H. Davis Jr., CO₂ capture by a task-specific ionic liquid, *J. Am. Chem. Soc.* 124 (2002) 926.
- [21] M.L. Sforca, I.V.P. Yoshida, S.P. Nunes, Organic–inorganic membranes prepared from polyether diamine and epoxy silane, *J. Membr. Sci.* 159 (1999) 197.
- [22] A. Noda, M.D.A.B.H. Susan, K. Kudo, S. Mitsushima, K. Hayamizu, M. Watanabe, Bronsted acid–base ionic liquids as proton-conducting nonaqueous electrolytes, *J. Phys. Chem. B* 107 (2003) 4024.



Microwave synthesis of gallium zinc phosphate NTHU-4

Jose A. Losilla, Decio Coutinho, Kenneth J. Balkus Jr. *

Department of Chemistry, UTD NanoTech Institute, University of Texas at Dallas, Richardson, TX 75083-0688, United States

Received 2 May 2007; received in revised form 21 November 2007; accepted 23 November 2007

Available online 23 December 2007

Abstract

There is growing interest in white light emitting diodes for solid-state lighting and novel approaches for the synthesis of white light emitting materials is essential. The large pore gallium zinc phosphate NTHU-4 has been shown to emit light when photoexcited. NTHU-4 was successfully synthesized after only 4 h at 160 °C using a microwave oven, compared to 48 h at 160 °C by conventional heating. The effects of synthesis parameters on phase purity, crystal morphology and emission properties were explored.

© 2008 Published by Elsevier Inc.

Keywords: Microwave synthesis; NTHU-4; LED; Gallium zinc phosphate; White light

1. Introduction

The average person is exposed to an increasing amount of artificial color and light. The scientific interest in light can be traced as far back as 1671 with Isaac Newton's Theory of Light [1] showing white light decomposition into colors, or the slit interference experiments in 1804 by Thomas Young [2]. In 1931, the International Commission on Illumination (CIE) [3] established a system of colorimetry based on the experiments of Wright [4,5] and Guild [6]. Despite the evolution, from oil lamps to high resolution displays, the perception and development of artificial light sources is still a challenging subject.

At the present time, many technological devices such as cell phones, digital cameras, televisions, computer monitors, traffic signals, automotive applications, indoor and outdoor building lighting, etc., are based on displaying images or emitting light. The growing applications demand greater economic and energy conservation. At the same time, energy and economical considerations get more demanding. According to the US Department of Energy lighting represented 16% of the total primary energy consumption in buildings in 2004 [7]. Electrical energy con-

sumption is expected to increase 1.6% annually, going from 3729 billion kilowatt hours in 2004 to 5208 billion kilowatt hours in 2025 [7]. Finally, unlike space heating, water heating and refrigeration, the trend of energy consumption for lighting and other devices will increase per household despite increasing efficiency [7]. The need for efficient lighting requires great progress in the design of new materials.

Compared to incandescent bulbs and fluorescent lamps, new devices and associated materials are expected to provide higher brightness, reliability, lower power consumption and longer life. For instance, light emitting diodes (LEDs) report a luminous efficacy around 100 lumens per watt (lm/W) [8], compared to 16 lm/W for incandescent and 85 lm/W for fluorescent bulbs [9]. Comparable to Moore's law for semiconductors [10], Haitz's law states that the LED luminous output doubles every 18–24 months [11]. At this rate, the theoretical maximum for LEDs of ~200 lm/W will be achieved around year 2020 [9,12,13]. For 2001, the value of a white LED was \$0.20/lm; for 2012 the projected price is \$0.01/lm [13]. With the expected drop in production costs, increased luminous output and increased life-time of up to 100,000 h [9], LED technology appears as the favorite alternative for lighting.

The development of solid-state lighting depends in part on the human perception of color which is based on three

* Corresponding author. Tel.: +1 972 883 2659; fax: +1 972 883 2925.
E-mail address: balkus@utdallas.edu (K.J. Balkus Jr.).

photoreceptor cones that perceive red, green and blue. The cones are divided into three classes based on their wavelength sensitivity: the short (S) expressed by genes on chromosome 7, medium (M) and long (L) both expressed by chromosome X. The ratio and distribution of L and M cones varies between individuals but S cones are present in a smaller amount (under 5%) as described by Roorda [14]. Short cones perceive radiation up to 520 nm, allowing a good blue-yellow but a limited green-red discrimination on color blind individuals, which lack L or M cones [3,14–17].

The design of LED devices is related to the study of photoreceptor cones. The emission of white light can be achieved by three different methods. The first approach involves the combination of three monochromatic sources; one red, one green and one blue and is called the RGB approach. This approach presents the highest theoretical efficiency for the emission of white light, and presents the best color rendering properties [11,18]. As different light emitting sources contribute in different amounts, a big challenge is to balance and control each source's intensity. In the second approach, a GaN LED pump provides blue light that also excites a yellow phosphor layer. This relatively simple and common device provides white light of irregular spectral composition due to the absence of red light, with poor color rendering [19]. The third method uses a UV-LED to excite a RGB phosphor layer. Color is produced according to the phosphor mixture. Using this technique good color rendering is obtained. However, finding a near-UV high absorption phosphor and the degradation of materials by UV radiation are important challenges to overcome [11,18–20].

It is clear that a single source emission of white light that provides low cost, high efficiency and long life would represent a great advance in LED technology. One possible alternative may be found with NTHU-4, which was first reported by Liao et al. [21]. This gallozinc phosphate uses 4,4'-trimethylenedipyridine amine as a template, forming 14-membered ring channels along the c-axis as shown in Fig. 1. The building blocks are GaO_4 and ZnO_4 tetrahedra,

with PO_4 and HPO_4 units on the corners. This promising material, which was synthesized after heating for 7 days at 160 °C, emits white light when excited by UV radiation [21]. Reducing the synthesis time will considerably lower the production cost of NTHU-4. Microwave heating has been successfully used for several organic and inorganic products, dramatically reducing heating time [22–36]. In this paper, we describe the successful synthesis of NTHU-4 by microwave heating in less than 4 h.

2. Experimental section

2.1. Precursor preparation

In a typical synthesis 4.4 g of H_3PO_4 (EM Science, 85.0%) and 0.88 g of ZnCl_2 (Fisher Scientific, 98.0%) were combined with 33 mL of deionized water. 0.6 g of Ga_2O_3 (Aldrich, 99.99%) were added and stirred at room temperature for 20 min. In a separate vessel, 8.16 g of 4,4'-trimethylenedipyridine (TMDP) (Aldrich, 98%) were mixed with 28.4 mL of ethylene glycol (Fisher Scientific, 99+%) and 10 mL of deionized water. Then, 0.96 g of oxalic acid dihydrate (Aldrich, 99%) was added and the solution stirred for 20 min at room temperature. The TMDP solution was combined with the zincgallo phosphate solution and stirred from 30 min to 72 h at room temperature.

2.2. Microwave synthesis of NTHU-4

The thick white, NTHU-4 precursor solution was placed in a 95 mL CEM XP-1500 Plus Teflon reaction vessel and heated to 160–200 °C in a CEM MARSXpress™ microwave (CEM Corporation) at 2.45 GHz. The heating time was varied from 60 to 600 min. A 20 min ramp time was used to reach the desired temperature and the power used was 400 W at 100%. The reaction temperature was controlled via a reference vessel, using temperature and pressure sensors through a ramp to temperature method. In this method, power constantly adjusts to maintain the desired temperature ± 2 °C, preventing over heating. The

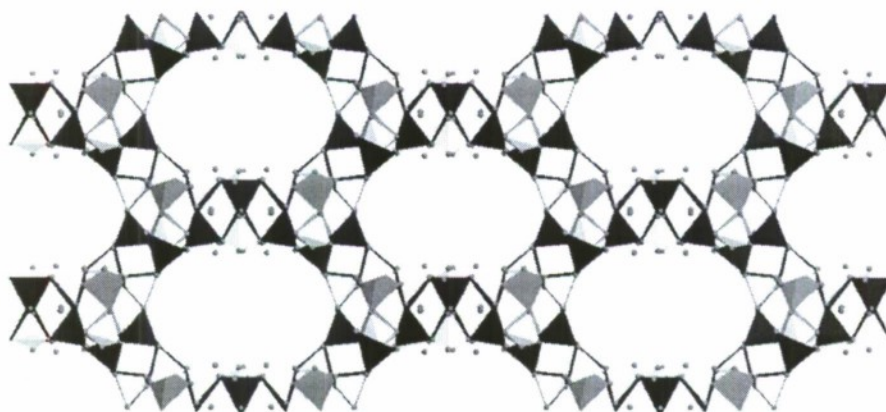


Fig. 1. NTHU-4 structure calculated using with Materials Studio, and the crystallographic data in Ref. [21]. (Black = Gallium, Gray = Zinc, White = Phosphor, Small Spheres = Oxygen.)

reaction vessel is secured on a rotating turntable, minimizing the effect of hot spots for a homogeneous heating. The resulting product was filtered, washed with deionized water and dried at 45 °C for 24 h.

2.3. Conventional heating synthesis

The NTHU-4 precursor solution was placed in a 23 mL Teflon-lined Parr autoclave and heated at 160 °C for a period of 1–7 days. The product was then filtered, washed with deionized water and dried at 45 °C for 24 h.

2.4. Analysis

Powder X-ray diffraction patterns were obtained using a Rigaku Ultima III X-ray diffractometer using Cu K α radiation. Samples for scanning electron microscopy were coated with Pd/Au and micrographs obtained on a Leo 1530 VP Field emission scanning electron microscope. Fluorescence spectra were recorded using a SPEX FLU-ROLOG 1680 0.22 Double Spectrometer. CIE numbers were obtained by using a Photo Research PR-650 Spectra-Scan[®] Colorimeter.

3. Results and discussion

Liao et al. [21], reported a mixture of TMDP, Ga₂O₃, ZnCl₂, oxalic acid and H₃PO₄ with the molar ratio of 12.8:1:2:2.4:12 in combination with a certain amount of water and ethylene glycol produced NTHU-4. Table 1 show a series of samples where the synthesis variables including molar ratios, temperature and time were explored for a conventional oven synthesis of NTHU-4. Non-luminescent and luminescent materials of different colors; orange, yellow, blue and white resulted from different conditions and molar ratios while trying to obtain the NTHU-4 material. Using conventional heating the synthesis of NTHU-4 was studied from 1 to 7 days at 160 °C. Impure NTHU-4 materials were formed after 24 h. However, pure NTHU-4 was obtained after 48 h. In contrast with the results reported by Liao [21], the product started disappearing with time, until no NTHU-4 material was left after 7 days of heating. The XRD patterns for the samples from 1 to 7 days are shown in Fig. 2. The XRD pattern for

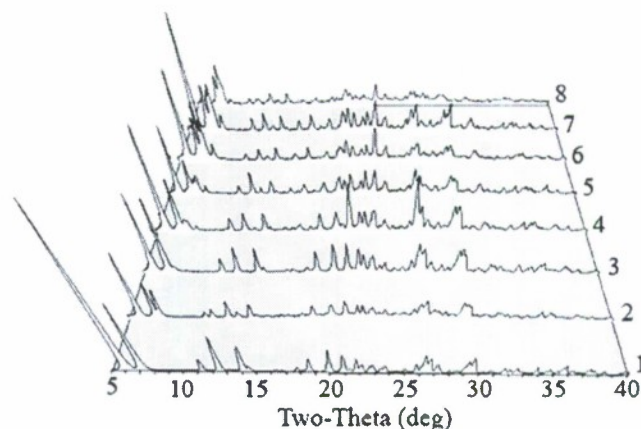


Fig. 2. Powder XRD patterns of NTHU-4. (1) Pattern calculated using Materials Studio and the data from Ref. [21], and NTHU-4 synthesized by conventional heating for (2) 1 day, (3) 2 days, (4) 3 days, (5) 4 days, (6) 5 days, (7) 6 days, (8) 7 days.

sample CH2, the 2 day product, best matches the simulated XRD pattern (Fig. 2, pattern 1). With increasing time, the NTHU-4 material starts converting into unknown materials. However, all of the samples prepared by conventional heating are photoluminescent as shown in Table 3.

According to Liao et al. [21], substitution of water in the synthesis precursor by ethylene glycol, produced a white light emitting material (NTHU-4w) instead of the original yellow light (NTHU-4y). White light emission could also be obtained from NTHU-4y, after reducing crystal defects, by heating at 280 °C for 4 h [21]. For our samples, luminescence was lost after heating at 280 °C for 4 h. Sample CH2 also showed a low intensity emission of yellow color light under UV excitation at 390 nm as shown in Fig. 3. The products in Table 1 were also analyzed by SEM to observe the change in morphology. After one day at 160 °C inter-crossing aggregates of plate like crystals are observed for NTHU-4 as shown for Sample CH1 in Fig. 4A. For the two day synthesis (Sample CH2), the NTHU-4 crystals were bigger with dimensions of $\sim 150 \times 160 \mu\text{m}$ as shown in Fig. 4B. After three days, the crystal morphology starts to change, from stacked plates to inter-crossing crystals as shown in Fig. 4C for sample CH3. From the XRD patterns in Fig. 2 it is clear that there is a mixture of NTHU-4 and some impurity phase. The SEM in Fig. 4D shows sample

Table 1

The synthesis conditions for NTHU-4 using conventional heating at 160 °C (OA = oxalic acid, EG = ethylene glycol)

Sample	TMDP	Ga ₂ O ₃	ZnCl ₂	OA	H ₃ PO ₄	H ₂ O	EG	Time (h)
CH1	12.7	1.0	2.0	2.4	12.2	1157.8	109.7	24
CH2	12.5	1.0	2.0	2.4	11.9	802.8	107.7	48
CH3	12.5	1.0	2.0	2.4	11.9	802.8	107.7	72
CH4	12.5	1.0	2.0	2.4	11.9	802.8	45.4	96
CH5	5.3	0.0	1.4	1.0	5.1	478.9	107.7	96
CH6	12.5	1.0	2.0	2.4	11.9	802.8	107.7	120
CH7	12.5	1.0	2.0	2.4	11.9	802.8	107.7	144
CH8	12.5	1.0	2.0	2.4	11.9	802.8	107.7	168
CH9	12.5	1.0	2.0	2.4	11.9	802.8	107.7	192

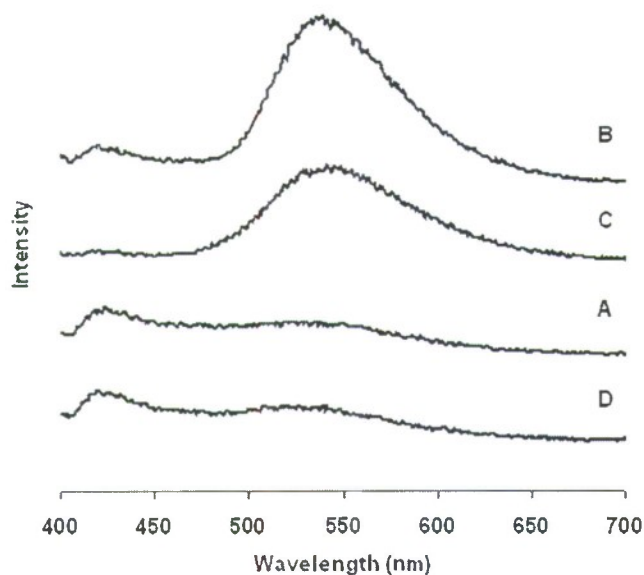


Fig. 3. Emission spectra under a 390 nm excitation for NTHU-4 samples produced by regular heating after (A) 1 day, (B) 2 day, (C) 5 day, (D) 7 day.

CH8 after 7 days of conventional heating. In this case both square laminates (right) as small aggregates of plate like crystals (right) are observed.

3.1. Microwave oven synthesis

Once the reaction profile by conventional heating was obtained, the microwave synthesis of NTHU-4 was studied

as shown in Table 2. First, the product obtained after stirring the precursor for 30 min at room temperature was studied. The synthesis was performed for 2, 3, 4, 5, 7, 8 and 10 h. After 2–10 h, samples MW1 to MW7, consisted of white-yellow intense light emitting NTHU-4 particles and a mixture of NTHU-4 fine yellow powder and other less emissive material. However, based on the particle size, the larger NTHU-4 crystals could be easily separated from the fine powder. The XRD patterns for the larger NTHU-4 particles were obtained as shown in Fig. 5. The formation of NTHU-4 by microwave heating starts to occur after 2 h at 160 °C, however, there is an impurity peak at $\sim 7.6^\circ$ similar to conventional heating. The SEM image for MW1, in Fig. 6, shows the stick-like morphology. The emission spectrum for sample MW1 with a white–yellow emission color, showed an emission maxima at 420 nm and 540 nm for 365 nm and 390 nm excitation as shown in Fig. 7. For sample MW2, the 3 h synthesis, the impurity peak at $\sim 7.6^\circ$ diminishes in Fig. 5, but a new impurity appears at $\sim 10.8^\circ$ which is attributed to zinc phosphate. This impurity is present in the as-synthesized material, before separation. After 4 h, the NTHU-4 crystals continue to grow into bigger ($\sim 60 \mu\text{m}$) laminates as shown in Fig. 8. This tendency continues for the 5 h, 7 h and 8 h syntheses. Finally for sample MW7, the 10 h synthesis, the SEM images in Fig. 9 show both small inter-crossed laminates ($< 20 \mu\text{m}$), along with big laminates ($\sim 120 \mu\text{m}$) of NTHU-4. The resulting solid produces a white-yellow emission. In general the plate-like crystals increase in size without greatly changing the basic morphology.

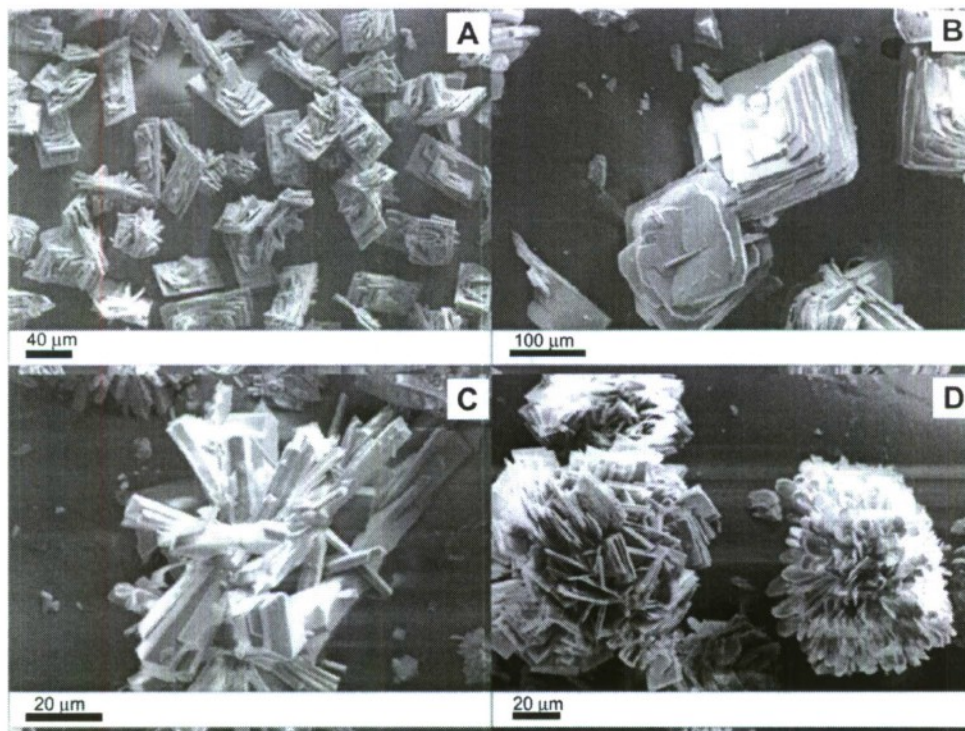


Fig. 4. SEM image for NTHU-4 by conventional heating after (A) 1 day (sample CH1), (B) 2 days (sample CH2), (C) 3 days (samples CH3) and (D) 7 days (sample CH8) at 160 °C.

Table 2

The synthesis conditions for NTHU-4 using microwave oven at 160 °C and 400 W (OA = oxalic acid, EG = ethylene glycol)

Sample	TMDP	Ga ₂ O ₃	ZnCl ₂	OA	H ₃ PO ₄	H ₂ O	EG	Time (h)	Mix time
MW1	12.8	1.0	2.0	2.3	11.9	812.2	107.2	2.0	0.5
MW2	12.6	1.0	2.0	2.4	12.0	808.5	106.3	3.0	0.5
MW3	12.6	1.0	2.0	2.3	11.8	806.7	106.1	4.0	0.5
MW4	12.6	1.0	2.0	2.3	12.0	807.5	106.2	5.0	0.5
MW5	10.3	1.0	1.4	1.6	8.1	547.8	72.0	7.0	0.5
MW6	10.8	1.0	1.7	2.0	10.2	691.5	90.9	8.0	0.5
MW7	10.8	1.0	1.7	2.0	10.2	691.5	90.9	10.0	0.5
MW8	12.9	1.0	2.0	2.4	12.0	845.0	160.0	2.0	24.0
MW9	12.9	1.0	2.1	2.4	12.1	845.0	159.0	5.0	48.0
MW10	12.9	1.0	2.1	2.4	12.1	845.0	159.0	2.0	56.0
MW11	12.9	1.0	2.1	2.4	12.1	845.0	159.0	1.0	64.0
MW12	12.9	1.0	2.1	2.4	12.1	845.0	159.0	3.0	72.0

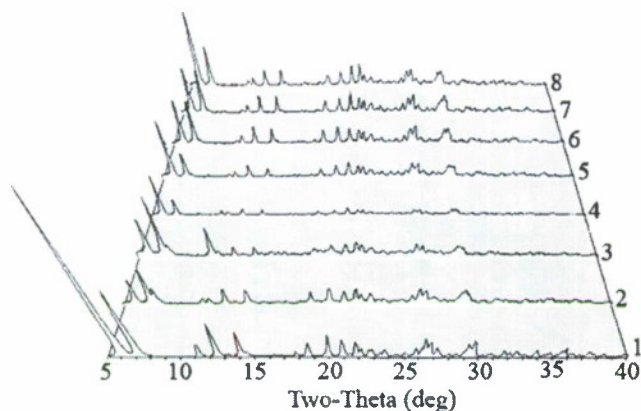


Fig. 5. Powder XRD patterns of (1) simulated NTHU-4, and the microwave products for (2) 1 h, (3) 2 h, (4) 3 h, (5) 4 h, (6) 5 h, (7) 7 h, and (8) 10 h.

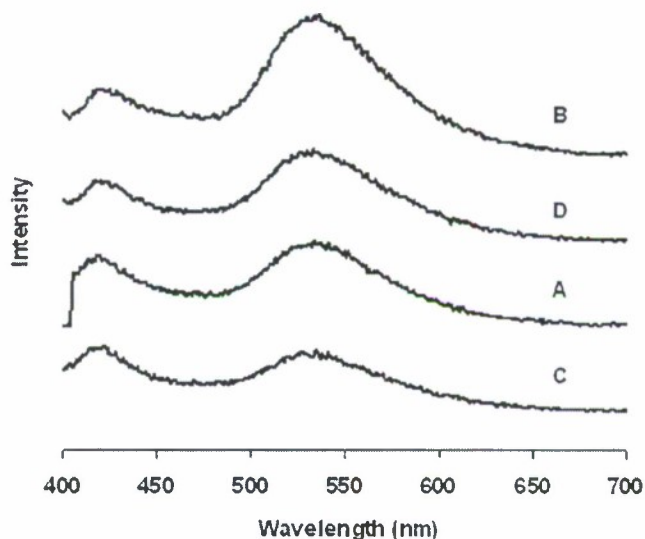


Fig. 7. Emission spectra for sample MW1 for 2 h (A) 365 nm excitation, (B) 390 nm excitation and 10 h (C) 365 nm excitation and (D) 390 nm excitation.

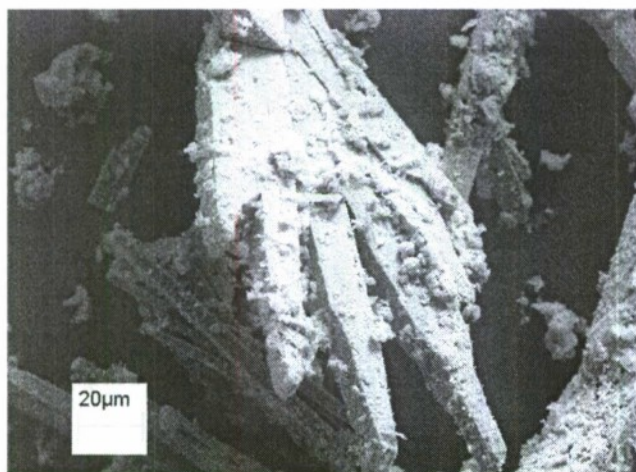


Fig. 6. SEM image for a NTHU-4 sample MW1, with crossing stick morphology after 2 h at 160 °C using microwave oven.

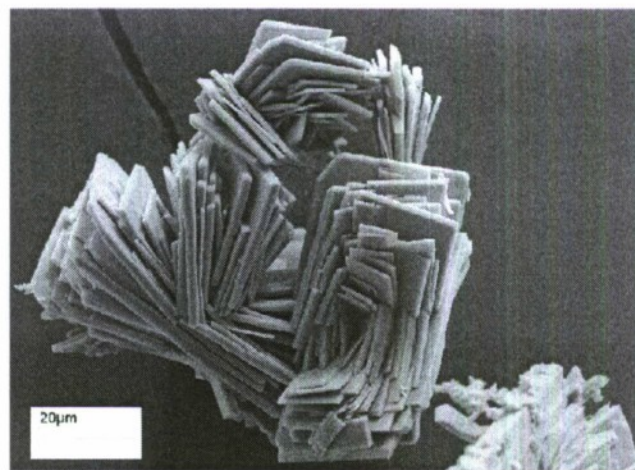


Fig. 8. SEM image for NTHU-4 sample MW3 after 4 h synthesis by microwave oven.

It should be noted that the NTHU-4 synthesis without zinc produced sword-like crystals that exhibited no photoluminescence and different a XRD pattern. If gallium is removed from the NTHU-4 recipe, white crystals and an

XRD pattern consistent with the impurity in sample MW2 at ~10.8° are obtained.

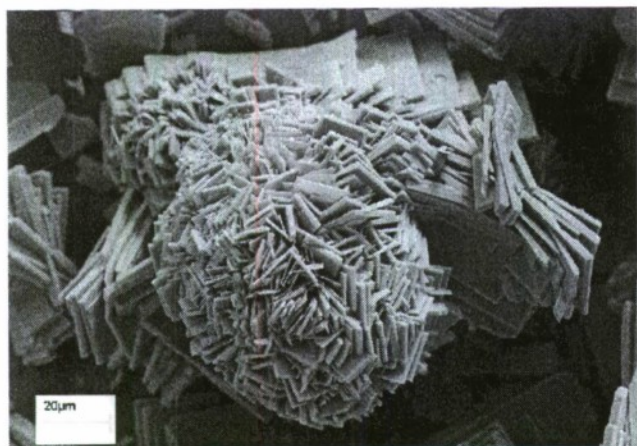


Fig. 9. SEM image for a NTHU-4 sample after 10 h at 160 °C, using the microwave oven.

3.2. Heating temperature

The effect of heating temperature was also studied in an effort to reduce synthesis time. The XRD patterns obtained for the NTHU-4 as-synthesized powders after microwave heating for 4 h at 155, 160, 165 and 175 °C are shown in Fig. 10. It can be observed that heating at a temperature of 155 °C, results in a powder that is the closest to the NTHU-4 pattern, with some impurities. This suggests that a longer heating time will be required at this temperature. The sample at 160 °C, contains impurity peaks as well as a low intensity peak at $\sim 7.2^\circ$. This shows that little NTHU-4 is present in the product. The samples at 165 °C and 170 °C show the appearance of an extra peak at $\sim 7.6^\circ$. This sample is comparable to the degradation product of NTHU-4 material after 3 days under conventional heating conditions. Therefore using the current molar ratios, it is not possible to reduce the synthesis time for NTHU-4 by heating at higher temperature using microwave heating.

3.3. Mixing time

The most homogeneous samples were obtained with a longer mixing time. The synthesis was performed for 1, 2,

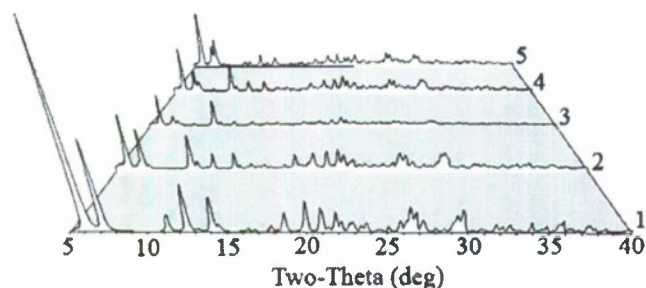


Fig. 10. (1) XRD pattern of simulated NTHU-4 pattern and microwave synthesis powder after 4 h at (2) 155 °C, (3) 160 °C, (4) 165 °C and (5) 170 °C.

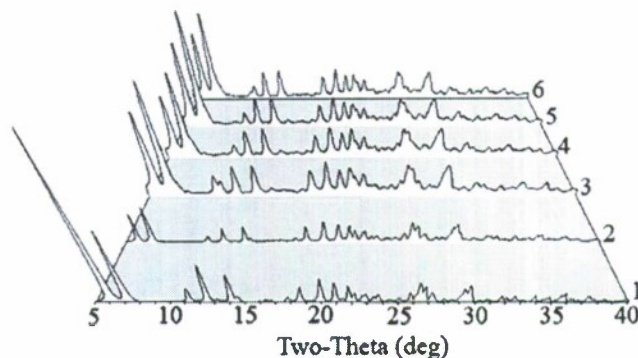


Fig. 11. (1) XRD pattern of simulated NTHU-4 pattern and NTHU-4 products by microwave heating at 160 °C with after mixing the precursor for (2) 24 h, (3) 48 h, (4) 56 h, (5) 64 h and (6) 72 h.

3 and 5 h with mixing times of 24, 48, 56, 64 and 72 h. XRD patterns shown in Fig. 11, match with the simulated pattern without the presence of additional peaks or impurities. As shown in Fig. 11, there are no apparent changes on the XRD patterns produced by increasing the heating time after mixing for 24 h. Once the mixing time was increased to more than 24 h, the samples appear to be pure NTHU-4 as evidenced by XRD. Continued mixing while heating produced low emitting materials and was not investigated further.

The emission spectra for samples heated for 1–5 h after mixing for 48, 56, 64 and 72 h are shown in Fig. 12. When the emission spectra are compared, it is evident that the samples show two main peaks: one at ~ 420 nm and the other at ~ 530 nm. This emission peaks are from 10 to 20 nm less than the reported values of 433 nm and 550 nm by Liao et al. [21]. Under 365 nm excitation, the intensity of the 420 nm peak is higher than the 530 nm in all cases. However, under 390 nm excitation, both peaks present very similar intensities for the 48 and 56 h syntheses. For longer periods of time, 64 h and 72 h, the intensity

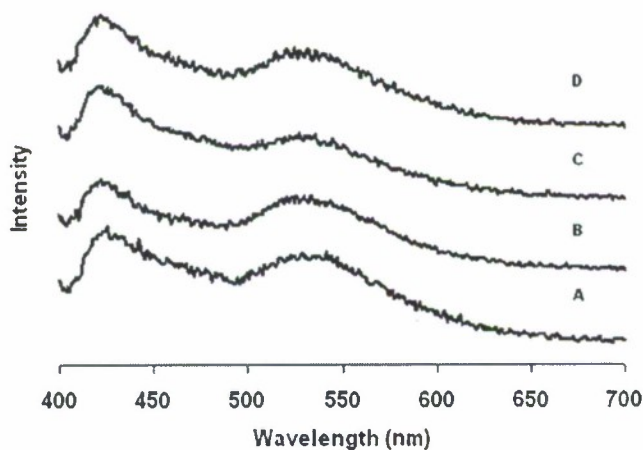


Fig. 12. Emission spectra for NTHU-4 samples synthesized by microwave heating with a mixing time of (A) 48 h, (B) 56 h, (C) 64 h, (D) 72 h, excitation at 390 nm.

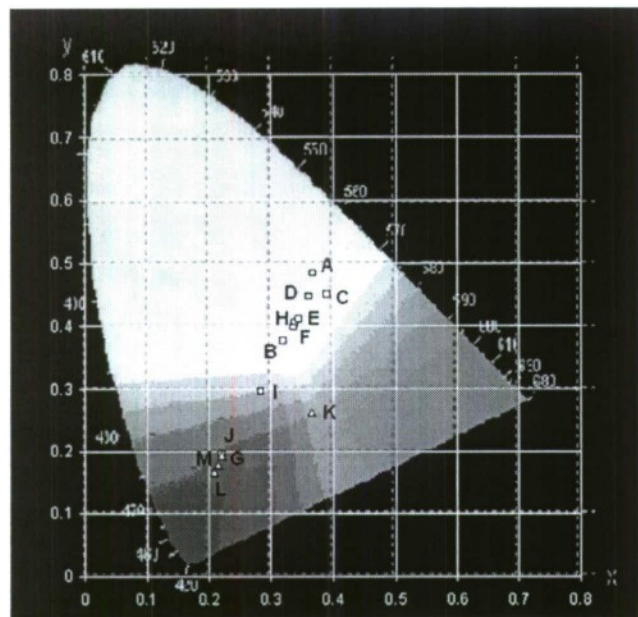


Fig. 13. CIE number diagram for NTHU-4 products excited at 365 nm.

of the 420 nm peak is higher than the 530 nm peak. Based on these results one could expect an emission closer to white light under 390 nm excitation than under 365 nm.

To have a better description of the emitted color of the samples, the CIE coordinates were obtained. In the original NTHU-4 paper by Liao et al. [21], CIE coordinates of (0.29, 0.34) were reported under 390 nm excitation. For a better visualization our coordinates were plotted in a CIE diagram; as shown in Fig. 13 for 365 nm excitation and in Fig. 14 for 390 nm excitation. From Figs. 13 and 14, it is clear that the samples made by conventional heating, emit a wide distribution of colors, between light green

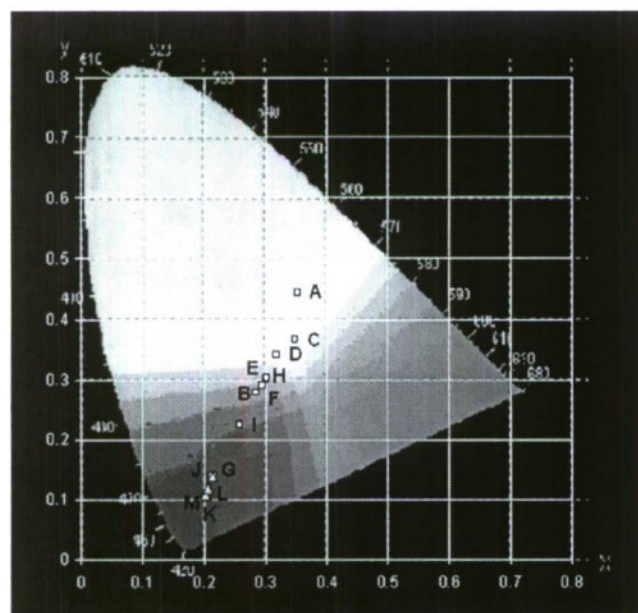


Fig. 14. CIE number diagram for NTHU-4 products excited at 390 nm.

Table 3
CIE number coordinates for different NTHU-4 samples

Sample	CIE (365 nm)	CIE (390 nm)	Diagram nomenclature
CH1	(0.334, 0.375)	(0.289, 0.272)	A
CH2	(0.319, 0.377)	(0.285, 0.278)	B
CH3	(0.390, 0.452)	(0.350, 0.367)	C
CH4	(0.361, 0.446)	(0.319, 0.343)	D
CH5	(0.367, 0.484)	(0.353, 0.443)	E
CH6	(0.339, 0.406)	(0.300, 0.301)	F
CH7	(0.336, 0.399)	(0.295, 0.291)	G
CH8	(0.220, 0.196)	(0.215, 0.139)	H
CH9	(0.283, 0.297)	(0.303, 0.303)	I
MW9	(0.365, 0.263)	(0.204, 0.110)	J
MW10	(0.220, 0.195)	(0.214, 0.139)	K
MW11	(0.209, 0.168)	(0.202, 0.107)	L
MW12	(0.241, 0.178)	(0.206, 0.119)	M

and light blue with no apparent correlation with heating time. On the other hand, the microwave samples are centered in the blue region of the diagram. The emission color of these samples seems to be independent of the excitation source (365 nm or 390 nm). Only microwave sample (MW10) showed an excitation dependent emission with a CIE number of (0.365, 0.263) under 365 nm excitation under the light pink region. Further details on the CIE numbers are presented on Table 3.

Compared to the results by Liao et al. [21], it was observed that in order to obtain a light emission close to white, it is necessary to decrease the water content while adding ethylene glycol. In the case of microwave heating, mixing time proved to be the critical factor in obtaining a product matching the XRD of NTHU-4. Liao et al. reported that NTHU-4 was brown in color while the microwave samples were generally white in color, especially after mixing for more than 24 h. This color difference could be caused by template decomposition.

In general, when comparing our galliumphosphate material with NTHU-4 there is important similarities and differences. Based on the XRD pattern of the microwave products, there is a good agreement with the NTHU-4 structure. In contrast, the products obtained by conventional heating for 7 days, did not show similar XRD patterns to NTHU-4. Second, both heating techniques produce photoluminescent materials, but no material produced the same CIE coordinates as reported for NTHU-4. Considering that light emission of many the metal oxide photoluminescent materials is based on defects, is possible that microwave heating does not produce same the amount and/or degree of framework defects obtained by conventional heating. So, while the microwave heating after 24 h of RT mixing produced NTHU-4 samples that were crystalline and pure, the conventional heating produce material with emission closer to white light.

4. Conclusions

The successful synthesis of NTHU-4 was achieved by microwave synthesis. While the NTHU-4 materials pre-

pared by microwave synthesis heating produced a whitish blue light when excited with ultraviolet radiation, the materials prepared by conventional heating were closer to the ideal white based on CIE numbers. We are currently working to better understand the key parameters that produce white light from these materials.

Acknowledgments

We thank the Dr. Bruce Gnade for use of the equipment to make the CIE measurements. We also thank the Robert A. Welch Foundation and SPRING, for the supporting of this project.

References

- [1] I. Newton, *Philosophical Transactions* 6 (1665–1678) (1671) 3075.
- [2] T. Young, *Philosophical Transactions of the Royal Society of London* 94 (1804) 1.
- [3] R.M. Boynton, *Journal of the Optical Society of America A* 13 (1996) 1609.
- [4] W.D. Wright, *Transactions of the Optical Society* 29 (1928) 225.
- [5] W.D. Wright, *Transactions of the Optical Society* 30 (1929) 141.
- [6] J. Guild, *Philosophical Transactions of the Royal Society of London: Series A* 230 (1932) 149.
- [7] *Annual Energy Outlook, 2006*, U.S.D.o. Energy, 2006. <[http://www.eia.doe.gov/oiaf/aco/pdf/0383\(2006\).pdf](http://www.eia.doe.gov/oiaf/aco/pdf/0383(2006).pdf)>.
- [8] A. Mills, *III-Vs Review* 17 (2004) 39.
- [9] J.Y. Tsao, *Circuits and Devices Magazine IEEE* 20 (2004) 28.
- [10] G.E. Moore, *Proceedings of the IEEE* 86 (1998) 82.
- [11] D.A. Steigerwald, J.C. Bhat, D. Collins, R.M. Fletcher, M.O. Holcomb, M.J. Ludowise, P.S. Martin, S.L. Rudaz, *IEEE Journal of Selected Topics in Quantum Electronics* 8 (2002) 310.
- [12] A. Mills, *III-Vs Review* 18 (2006) 30.
- [13] A. Bergh, G. Craford, A. Duggal, R. Haitz, *Physics Today* 54 (2001) 42.
- [14] A. Roorda, D.R. Williams, *Nature (London)* 397 (1999) 520.
- [15] D.M. Dacey, *Proceedings of the National Academy of Sciences of the United States of America* 93 (1996) 582.
- [16] V.C. Smith, J. Pokorny, *Vision Research* 15 (1975) 161.
- [17] Y. Uchida, T. Taguchi, *Optical Engineering (Bellingham, WA, United States)* 44 (2005) 124003/1.
- [18] S. Muthu, F.J.P. Schuurmans, M.D. Pashley, *IEEE Journal of Selected Topics in Quantum Electronics* 8 (2002) 333.
- [19] V. Sivakumar, U.V. Varadaraju, *Journal of the Electrochemical Society* 152 (2005) H168.
- [20] V. Sivakumar, U.V. Varadaraju, *Journal of the Electrochemical Society* 153 (2006) H54.
- [21] Y.C. Liao, C.H. Lin, S.L. Wang, *Journal of the American Chemical Society* 127 (2005) 9986.
- [22] T. Yamamoto, Y. Wada, H. Miyamoto, S. Yanagida, *Chemistry Letters* 33 (2004) 246.
- [23] D. Coutinho, J.A. Losilla, K.J. Balkus, *Microporous and Mesoporous Materials* 90 (2006) 229.
- [24] M.H. Masaharu Tsuji, Yuki Nishizawa, Masatoshi Kubokawa, Takeshi Tsuji, 2005, pp. 440.
- [25] S. Tierney, M. Heeney, I. McCulloch, *Synthetic Metals* 148 (2005) 195.
- [26] M. Larhed, C. Moberg, A. Hallberg, *Accounts of Chemical Research* 35 (2002) 717.
- [27] S. Tierney, M. Heeney, L. McCulloch, *Synthetic Metals* 148 (2005) 195.
- [28] M. Tsuji, M. Hashimoto, Y. Nishizawa, M. Kubokawa, T. Tsuji, *Chemistry – A European Journal* 11 (2005) 440.
- [29] F. Bensebaa, N. Patrito, Y. Le Page, P. L'Ecuyer, D. Wang, *Journal of Materials Chemistry* 14 (2004) 3378.
- [30] E.H. Hong, K.H. Lee, S.H. Oh, C.G. Park, *Advanced Functional Materials* 13 (2003) 961.
- [31] K.J. Rao, B. Vaidhyanathan, M. Ganguli, P.A. Ramakrishnan, *Chemistry of Materials* 11 (1999) 882.
- [32] O.G. Somani, A.L. Choudhari, B.S. Rao, S.P. Mirajkar, *Materials Chemistry and Physics* 82 (2003) 538.
- [33] D.S. Kim, J.S. Chang, J.S. Hwang, S.E. Park, J.M. Kim, *Microporous and Mesoporous Materials* 68 (2004) 77.
- [34] C.G. Wu, T. Bein, *Chemical Communications* (1996) 925.
- [35] P.M. Slangen, J.C. Jansen, H. van Bekkum, *Microporous Materials* 9 (1997) 259.
- [36] C.O. Kappe, *Angewandte Chemie – International Edition* 43 (2004) 6250.

Fabrication of Silver Vanadium Oxide and V_2O_5 Nanowires for Electrochromics

Chunrong Xiong,[†] Ali E. Aliev,^{‡,⊥} Bruce Gnade,^{†,§} and Kenneth J. Balkus, Jr.^{†,⊥,*}

[†]Department of Chemistry, [‡]Department of Physics, [§]Department of Electrical Engineering, and [⊥]Alan G. MacDiarmid NanoTech Institute, University of Texas at Dallas, Richardson, Texas 75083-0688

The ease with which V_2O_5 can be reduced and its ions intercalated into layered structures makes it a promising material for applications such as lithium batteries,^{1–3} catalysts,^{4–6} electrochromic devices (ECDs),^{7–9} and supercapacitors.^{10–12} Recently, silver-doped V_2O_5 (silver vanadium oxide, SVO) was shown to significantly improve the intercalation rate, specific capacity, and cycling performance in lithium ion batteries.¹³ It has also been used in implantable cardioverter defibrillators due to its long-term stability.^{14,15} In earlier reports, SVO films were made by pulse laser deposition (PLD),^{16–18} sputtering,¹⁹ evaporation, and vapor deposition.^{20,21} Bulk SVO was also synthesized by heat, melting a silver salt with vanadium oxide.^{22,23} Recently, $Ag_2V_4O_{11}$ nanowires and nanobelts were prepared by a hydrothermal approach.^{24,25}

V_2O_5 nanorods and nanowires have attracted attention due to their novel applications as sensors,²⁶ field-effect transistors,^{27–29} electric actuators,³⁰ and nanolithography templates.³¹ V_2O_5 nanowire sheets as actuators display a high Young's modulus, high actuator-generated stress, and high actuator stroke at low applied voltage.³² Vanadium oxide nanowires have been prepared by several methods. Nesper *et al.*³³ synthesized tubular vanadium oxide by a sol-gel reaction of vanadium alkoxides with a primary amine. Niederberger *et al.*³⁴ synthesized mixed-valence vanadium oxide nanorods *via* a nonaqueous low-temperature procedure. V_2O_5 nanorods and nanowires have also been synthesized in reverse micelles.³⁵ Cao *et al.*³⁶ reported the growth of V_2O_5 nanorod arrays using electrophoretic deposition combined with templating. For these syntheses, the length of the nanowires was usually less than 10 μm . Longer nanowires are ex-

ABSTRACT Silver vanadium oxide (SVO) and V_2O_5 nanowires have been hydrothermally synthesized. The as-made nanowires are over 30 μm long and 10–20 nm in diameter. The nanowires have a layered structure with a *d*-spacing of 1.07 nm. The nanowires can be fabricated into free-standing and flexible sheets by suction filtration. The electrical conductivity of the SVO nanowires is 0.5 S/cm, compared to 0.08 S/cm for the V_2O_5 nanowires. The Li ion diffusion coefficient in the SVO nanowires was 7 times higher than that in the V_2O_5 nanowires. An electrochromic device was fabricated from the SVO nanowires that displayed a color-switching time of 0.2 s from the bleached state (green) to the colored state (red-brown) and 60% transmittance contrast.

KEYWORDS: silver vanadium oxide · V_2O_5 · nanowires · electrochromic device

pected to facilitate formation of free-standing sheets or films. Hydrated V_2O_5 nanowires, 10 μm long, were synthesized by the polycondensation of vanadic acid in water at room temperature.^{32,37} This process requires several weeks due to the slow ion exchange between Na^+ and H^+ ions in a resin from sodium metavanadate solutions at room temperature. In this paper, we introduce a facile method to make high-aspect-ratio SVO and V_2O_5 nanowires with layered structure in one day, where the as-made nanowires are over 30 μm long and ~10–20 nm wide.

V_2O_5 films display a color change when lithium ions are injected into or extracted from the layer spaces by applying a small voltage. V_2O_5 films have been used as a working electrode in ECDs. Traditionally, V_2O_5 films have been made by sputtering,³⁸ chemical vapor deposition (CVD),³⁹ vacuum evaporation,⁴⁰ and sol-gel processes.⁴¹ To improve the intercalation and extraction kinetics of lithium ions in V_2O_5 , a short diffusion distance, bigger interlayer space, and good electrical conductivity are desired.⁴² Recently, $\text{TiO}_2/\text{V}_2\text{O}_5$,⁴³ $\text{Nb}_2\text{O}_5/\text{V}_2\text{O}_5$,⁴⁴ and polyaniline/ V_2O_5 ⁴⁵ composite films have been proposed to shorten the

*Address correspondence to balkus@utdallas.edu.

Received for review September 27, 2007 and accepted December 19, 2007.

Published online January 10, 2008
10.1021/nn700261c CCC: \$37.00

© XXXX American Chemical Society

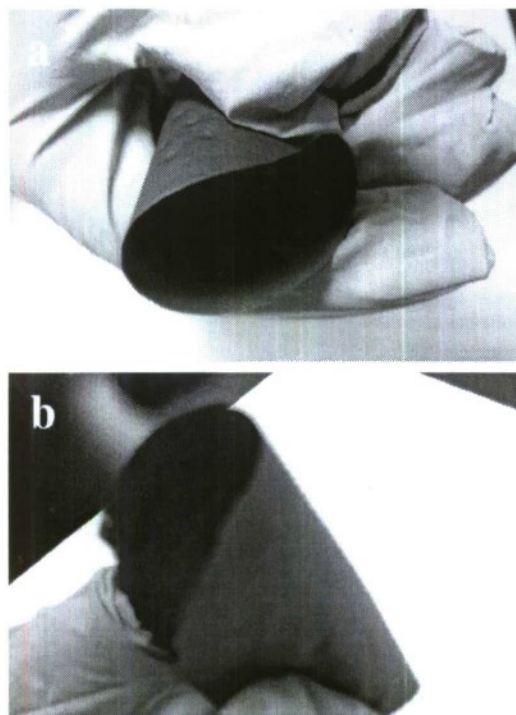


Figure 1. Digital photographs of free-standing sheets fabricated by suction filtration of (a) SVO nanowires and (b) V_2O_5 nanowires.

switching time. Meanwhile, V_2O_5 nanorod and nanowire films have been investigated.^{42,46} In this report, an ECD was constructed by dip-coating SVO nanowires onto ITO-coated glass. The resulting device displayed a much shorter color-switching time and a bigger transmittance contrast compared to the V_2O_5 nanowires.

RESULTS AND DISCUSSION

A digital photograph of a free-standing SVO nanowire sheet peeled off a filter paper is shown in Figure

1a. As can be seen in the image, the sheet was brown, and it was flexible and could be folded without breaking. The SVO nanowire paper has potential applications in supercapacitors and actuators. A V_2O_5 nanowire sheet was also fabricated by the same strategy. The free-standing sheet composed of V_2O_5 nanowires was green-brown, as shown in Figure 1b. The green-brown color suggests partial reduction of the V^{5+} in the nanowires. Both sheets were $\sim 50 \mu\text{m}$ thick. The top-view scanning electron microscopy (SEM) images of the SVO film dip-coated onto ITO glass show that the SVO film comprises entangled nanowires with an aspect ratio of over 1500, $30 \mu\text{m}$ long and $10\text{--}20 \text{ nm}$ wide, as can be seen in Figure 2a,b. The SVO film on the ITO glass was $\sim 500 \text{ nm}$ thick, as shown in the SEM image of the film cross section in Figure 2c. A V_2O_5 nanowire film with the same thickness was also made by the same method and is shown in Figure 2d. It can be seen from the top-view SEM images in Figure 2e,f that the V_2O_5 nanowires have the same aspect ratio as the SVO nanowires.

The X-ray diffraction (XRD) pattern in Figure 3a reveals that the as-made SVO nanowires matched the $\text{Ag}_{0.35}\text{V}_2\text{O}_5$ phase (PDF No. 00-028-1027) with characteristic peaks at $2\theta = 12.24, 18.78, 23.25, 25.52, 29.25, 34.48, 46.08,$ and 50.65° . These peaks can be assigned to (002), (200), (−104), (011), (104), (113), (−504), and (020) lattice planes, respectively. Two weak peaks at $2\theta = 38.1$ and 44.3° , characteristic of Ag metal, can also be found in the XRD pattern of the SVO nanowires. The size of the Ag particles was 3.6 nm , as calculated from the Scherrer equation. The peak at $2\theta = 8.2^\circ$ can be assigned to the (001) reflection, corresponding to a d -spacing of 1.07 nm . The XRD pattern of the V_2O_5 nanowires in Figure 2b shows the 00 l reflections consistent with the layered structure of hydrated V_2O_5 .^{11,47}

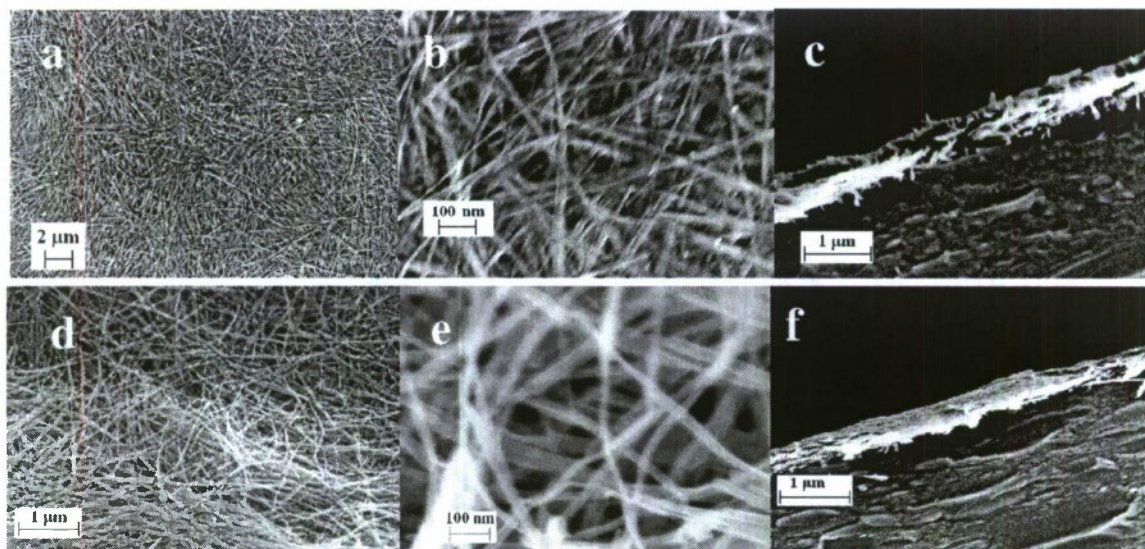


Figure 2. (a,b) Top-view SEM images of a SVO nanowire thin film on ITO glass. (c) SEM image of a cross section of the SVO nanowire thin film on glass. (d,e) Top-view SEM images of a V_2O_5 nanowire thin film on ITO glass. (f) SEM image of a cross section of the V_2O_5 nanowire thin film on glass.

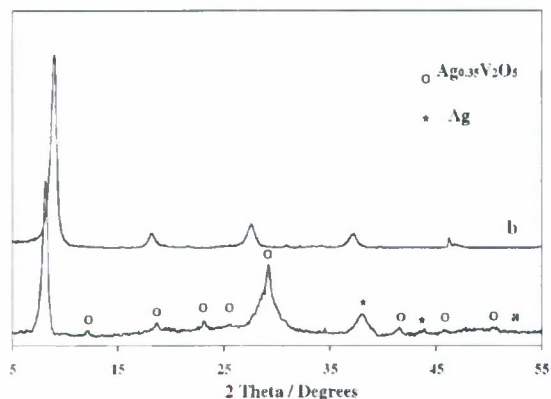


Figure 3. XRD patterns of (a) SVO nanowires and (b) V_2O_5 nanowires.

The peaks at $2\theta = 9.1, 18.3, 27.7, 37.2,$ and 46.0° are assigned to (001), (002), (003), (004), and (005) lattice planes, respectively. The d -spacing of the V_2O_5 nanowires was 1.01 nm, which is smaller than that for the SVO nanowires in which Ag metal is positioned between or among the V_2O_5 chains spanning the layer space.³⁷ In the XRD pattern of the V_2O_5 nanowires, four weak peaks at $2\theta = 31.0, 32.5, 39.8,$ and 47.2° are also observed. They can be assigned to (200), (131), (022), and (241) lattice planes of NH_4VO_3 (PDF No. 01-076-0191), respectively, which indicates that there were trace amounts of unreacted NH_4VO_3 in the V_2O_5 sample but not in the SVO sample.

To determine the content of coordinated water in the SVO and V_2O_5 nanowires, thermogravimetric analy-

ses (TGA) were carried out. The derivative thermogravimetric curve of SVO nanowires shown in Figure 4a reveals three peaks due to removal of physisorbed and chemisorbed water molecules, as previously reported.⁴⁸ The low-temperature weight loss peak at 130°C may be attributed to the loss of free water. The second weight loss, located at $\sim 235^\circ\text{C}$, is due to the loss of physically adsorbed water. For these two low-temperature peaks, the weight losses were 3.8% and 2.7%, respectively, as can be seen in Figure 4b. The maximum peak temperature for weight loss was centered at 350°C , and the weight loss was 11.2%, which was ascribed to the loss of coordinated water. Thus, the molar ratio of the coordinated water to $Ag_{0.35}V_2O_5$ in the hydrated nanowires may be ~ 1.14 . The derivative thermogravimetric curve shown in Figure 4c also displays three weight loss peaks for the V_2O_5 nanowires at 130, 257, and 400°C , which correspond to 2.0%, 4.5%, and 12.3% weight loss, respectively. The maximum weight loss peak occurred at 400°C , 50 degrees higher than that of the SVO nanowires. This is probably because the coordinated water hydrogen-bonds with the oxygens located in the V_2O_5 framework, and embedding of silver in the V_2O_5 framework hinders this interaction. For the V_2O_5 nanowires, the molar ratio of the coordinated water to V_2O_5 was determined to be ~ 1.25 , according to the weight loss curve in Figure 4d.

The transmission electron microscopy (TEM) image of the SVO nanowires displays many silver nanoparticles on the nanowire surface, as can be seen in Figure

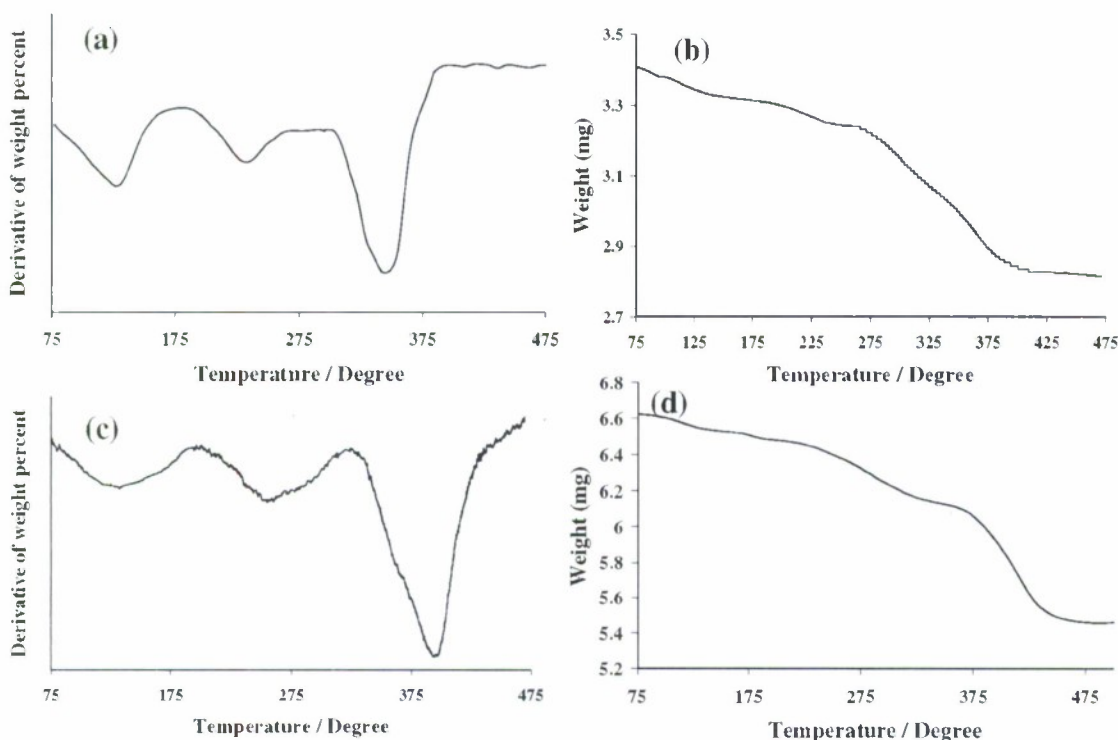


Figure 4. (a) TGA curve and (b) weight loss curve with respect to temperature ($^\circ\text{C}$) for the as-made SVO nanowires. (c) TGA curve and (d) weight loss curve with respect to temperature ($^\circ\text{C}$) for the as-made V_2O_5 nanowires. Test conditions: N_2 flow rate, 20 mL min^{-1} ; heating rate, 4 K min^{-1} .

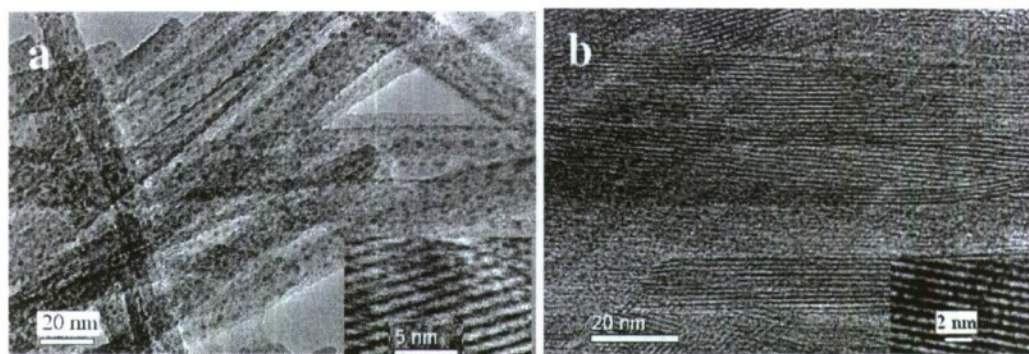


Figure 5. HRTEM images of (a) SVO nanowires and (b) V_2O_5 nanowires. Insets: images with high magnification.

5a. The inset image in Figure 5a shows a layered structure with a lattice spacing of 1.04 nm, a little smaller than that determined from the XRD pattern, probably because of dehydration upon exposure to the high-voltage electron beam under the high-vacuum environment. The nanowires grow along the [010] direction. The crystalline layered structure can also be observed in the V_2O_5 nanowires, as shown in Figure 5b, and the interlayer spacing is 0.97 nm, as determined from the high-resolution (HR) TEM image shown in the inset. The lattice fringes of (001) planes on the nanofibers grow along the fiber growth direction, as previously reported.^{9,35}

The FT-IR spectra of the SVO and V_2O_5 nanowires are shown in Figure 6. In both cases, the spectra exhibited characteristic IR bands attributed to V_2O_5 . The band centered at 976 cm^{-1} is assigned to the $V=O$ stretching vibration, and the bands at 850 and 542 cm^{-1} correspond to the $V-O-V$ bending vibration and edge-sharing $V-O$ stretching vibration, respectively.⁴⁹ In the IR spectrum of the SVO nanowires, the relative intensity of the band at 850 cm^{-1} with respect to the band at 542 cm^{-1} or the band at 976 cm^{-1} decreased compared to that of V_2O_5 nanowires. Such a decrease of the band relative intensity could be due to introduction of Ag^+ into the nanowire framework, which interrupts the $V-O-V$ linkages and produces more

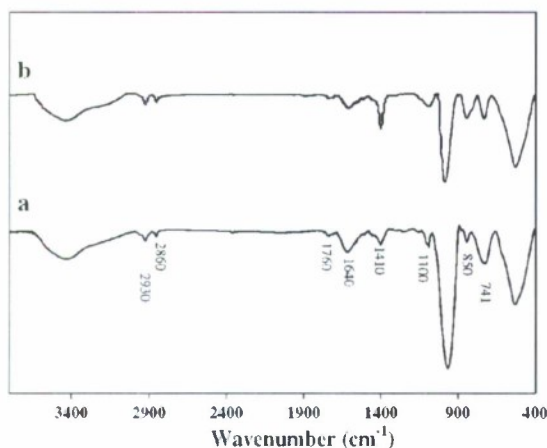


Figure 6. FT-IR spectra of (a) SVO nanowires and (b) V_2O_5 nanowires.

edge-sharing $V-O$ bonds and terminal $V=O$ bonds.⁵⁰ The band at 741 cm^{-1} could be assigned to a $V-OH_2$ stretching mode due to coordinated water.⁵¹ Two IR bands at 3470 and 1640 cm^{-1} are attributed to stretching and bending vibrations of water molecules.⁵² The bands at 1100 cm^{-1} in the spectra are related to $-OR$ groups of the organic P123, which indicated that trace organics could be present inside the interlayer space of the nanowires, although the nanowires were sufficiently washed with water and acetone. Additionally, the bending vibration of $-CH_2$ is also observed at 1410 cm^{-1} , and the bands at 2930 and 2860 cm^{-1} correspond to the asymmetrical and symmetrical stretching bands of $-CH_2$, respectively. Although there was trace organic existing in the nanowires, it was not observed as an obvious weight loss peak in thermogravimetric analyses, because most weight loss was caused by complexed water, which could hide the contribution of organics. Intercalation of P123 could play a structure-directing role in the preparation of high-aspect-ratio nanowires, as reported by others.^{53,54} Moreover, P123 also may act as a reductant to reduce Ag^+ to Ag , along with partial reduction of V^{5+} to V^{4+} during the hydrothermal condensation. X-ray photoelectron spectroscopy (XPS) showed the main binding energy of the $V2p_{3/2}$ electrons located at 517.5 eV, as can be seen in Figure 7a, suggesting a $5+$ oxidation state for most of the vanadium ions. In addition, a small peak at 516.2 eV indicates partial reduction of the V^{5+} ions to V^{4+} during the hydrothermal condensation. The molar ratio of V^{4+} to V^{5+} was 0.11 for the SVO nanowires and 0.14 for the V_2O_5 nanowires. In the XPS spectra of both SVO and V_2O_5 nanowires (as shown in the Supporting Information), the peak at 289 eV suggests formation of some carbonate groups due to oxidation, which is further supported by the band at 1760 cm^{-1} , assigned to $C=O$ groups, shown in Figure 6. The XPS spectrum in Figure 7b shows that the silver species in the SVO sample include Ag^+ and metallic Ag , and the atomic ratio of Ag^+ to Ag is 0.13. It was reported that the Ag-doped $Ag_{0.35}V_2O_5$ phase contains both Ag^0 and Ag^+ ,^{16,18,50} but the atomic ratio of Ag^+ to Ag^0 in the SVO was not reported. The XRD pattern reveals that metallic Ag nanoparticles and $Ag_{0.35}V_2O_5$ coexist in the

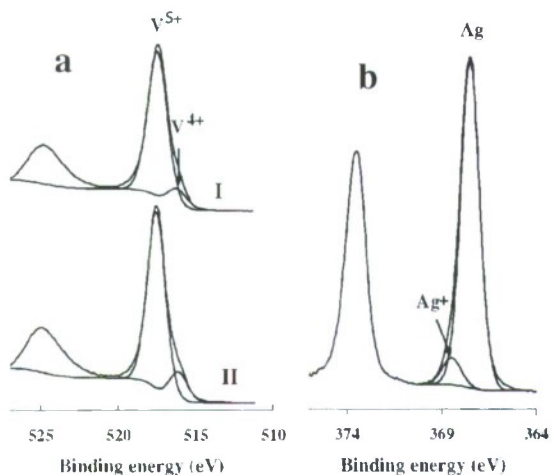


Figure 7. XPS spectra of (a) V2p for (I) the SVO and (II) V_2O_5 nanowires and (b) Ag3d for the SVO nanowires.

sample. To evaluate the atomic ratio of Ag^+ to metallic Ag in the $Ag_{0.35}V_2O_5$ phase, it is necessary to determine the molar ratio of Ag in the metallic Ag nanoparticles covering the SVO nanowires versus intercalated or framework Ag in the SVO ($Ag_{0.35}V_2O_5$) nanowires. The atomic ratio of total silver to vanadium in the sample was determined by energy-dispersive spectrometry (EDS) to be 0.244, so the molar ratio of Ag in the metallic Ag nanoparticle phase to that in the SVO ($Ag_{0.35}V_2O_5$) nanowires was 0.39 by calculation. This assumes the SVO phase has a ratio of $Ag_{0.35}V_2O_5$, which is reasonable because if the Ag ratio changes by a small amount, such as $Ag_{0.33}V_2O_5$, then the XRD pattern changes.¹⁹ The atomic ratio of Ag^+ to metallic Ag in the SVO nanowires can be calculated to be 0.23, and the chemical composition of SVO ($Ag_{0.35}V_2O_5$) could be $Ag_{0.08}^+Ag_{0.27}^0V_{1.78}^{5+}V_{0.22}^{4+}O_x$.

Nanowires having a layered structure are very interesting due to their short diffusion distance, which allows reversible intercalation of a variety of ions. Electrochromic devices were made from the as-made nanowires. The bleaching (oxidized) and coloration (reduced) states of the SVO-based ECD are red-brown and green, respectively, as shown in Figure 8a,b. Although the V_2O_5 nanowire sheet looks green-brown in Figure 1b, the nanowire-based ECD also displayed a red-brown color after one cycle of color-switching, because the vanadium was completely oxidized to V^{5+} under the applied voltage. The "SVO" and " V_2O_5 " labels behind the ECDs can be clearly seen through the nanowire films. Figure 9 shows the optical transmittance spectra of both states for SVO and V_2O_5 nanowire-based ECDs. Each state was scanned five times with an interval of 25 min. For the SVO nanowire-based ECD, the bleached state is very stable, and all spectra almost overlap, as can be seen in Figure 9a. However, in the colored state, the transmittance of the ECD increased with time, indicating that the reduced state was not very stable because Ag nanoparticles could promote catalytic

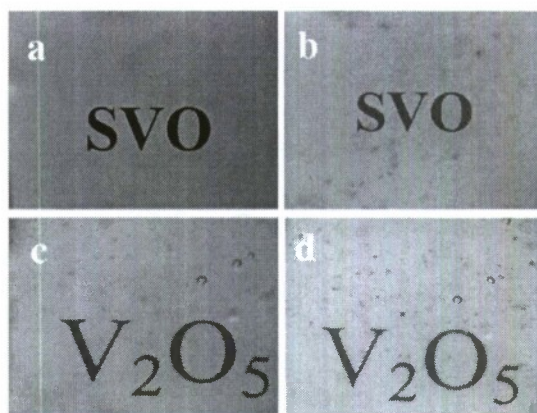


Figure 8. Digital photographs of (a) bleached and (b) colored states for a SVO nanowire-based ECD and (c) bleached and (d) colored states for a V_2O_5 nanowire-based ECD.

oxidation.^{55,56} The maximum transmittance change, ΔT , was 60% at 1020 nm. The UV-vis transmittance spectra of the V_2O_5 nanowire-based ECD displayed good stability in both states, as can be seen in Figure 9b. The maximum ΔT was 33.7% at 1005 nm.

The color-switching time of the ECD was measured by a Si photosensor. The EDC with SVO nanowires deposited on ITO glass as an anode and ITO glass as counter electrode was very stable in the applied voltage window from -2.5 to $+3.8$ V. The applied voltage vs time plot shown in Figure 10 displays the coloration-bleaching processes: $U = -1.5$ V for bleaching (green color) and $U = 2.5$ V for coloration (red-brown color). The color-switching time, defined as half the total transmittance change, was about 0.2 s from green to red-

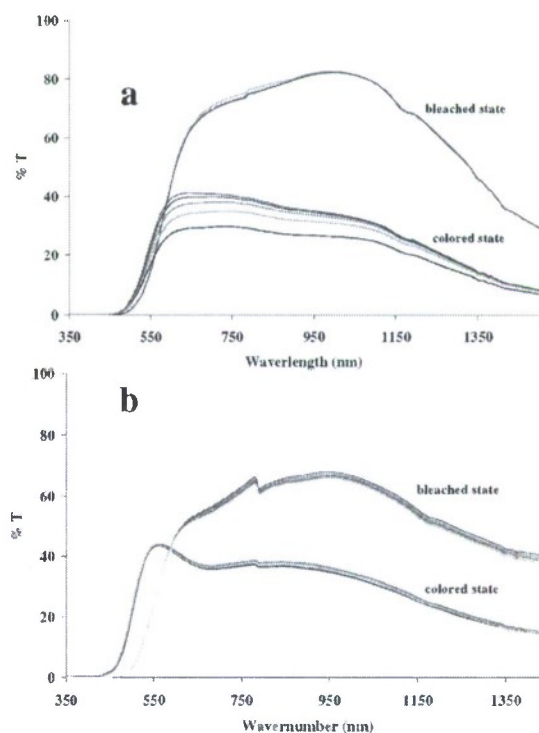


Figure 9. Optical transmittance spectra of (a) a SVO nanowire ECD and (b) a V_2O_5 nanowire ECD.

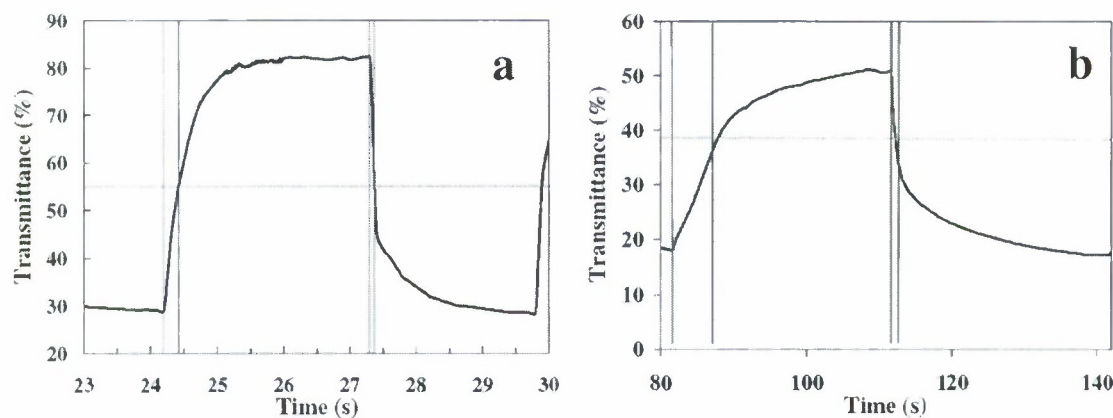


Figure 10. Transmittance vs time during coloration and bleaching cycles of (a) a SVO nanowire-based ECD and (b) a V_2O_5 nanowire-based ECD.

brown and 0.1 s for the reverse process at 633 nm, as shown in Figure 10a. For V_2O_5 nanowires, the color-switching time was 6 s from green to brown and 1 s for the reverse process, as shown in Figure 10b, apparently much slower than that for SVO nanowires. Cheng *et al.*⁴⁶ reported the color-switching time of a V_2O_5 nanowire ECD to be 6 s from the colored state to the bleached state and 5 s from the bleached state to the colored state. Takahashi *et al.*⁹ reported that a 30% transmittance change at 700 nm took 50 s for a V_2O_5 nanorod ECD when 3.0 V was applied, and 300 s was required for a sol-gel V_2O_5 ECD. For electrochromic applications, immediate color-switching is important. The rates of coloring and bleaching depend on the lithium

ion diffusion rate and the diffusion distance in the interlayer space of the nanowires. In our case, both the SVO and V_2O_5 nanowires are 10–20 nm wide, which provides a short diffusion distance. In the reported V_2O_5 nanowire or nanorod ECDs, the diameter sizes were ~ 100 nm.^{9,46} Moreover, the SVO nanowire sheets are more electroconductive (0.5 S/cm) than the V_2O_5 nanowire sheets (0.08 S/cm), and the SVO nanowires have a bigger interlayer spacing (1.04 nm) than the V_2O_5 nanowires (0.97 nm), which may contribute to a higher Li diffusion coefficient in the SVO nanowires than in the V_2O_5 nanowires.

To evaluate the Li ion diffusion coefficient in the SVO and V_2O_5 nanowires, cyclic voltammetry (CV) was

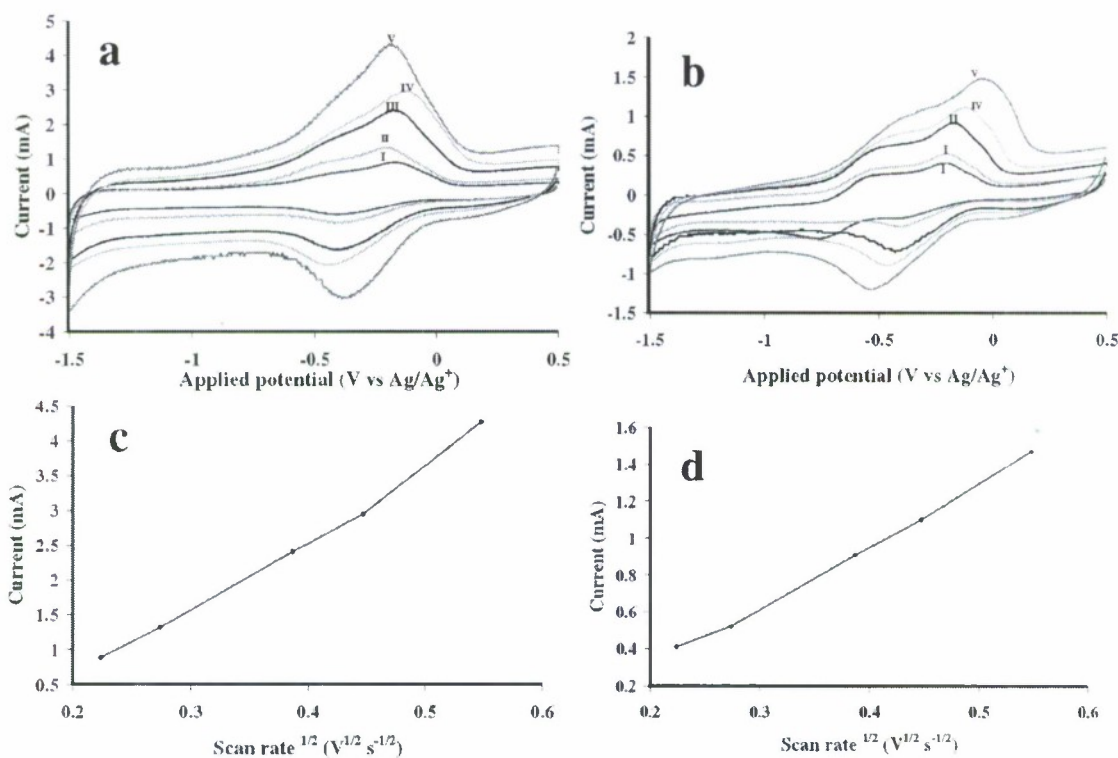


Figure 11. Cyclic voltammograms of (a) SVO nanowires and (b) V_2O_5 nanowires. The scan rates of traces I, II, III, IV, and V are 50, 75, 150, 200, and 300 mV s^{-1} , respectively. Plots of peak current (i_p) as a function of the square root of the scan rates ($v^{1/2}$) for (c) the SVO nanowires and (d) the V_2O_5 nanowires.

carried out with different potential scanning rates on the ~ 500 nm thick SVO and V_2O_5 nanowire thin films coated on ITO glass. Two oxidation peaks can be seen at -0.15 and -0.45 V in Figure 8a. As reported in the literature,^{57,58} V^{4+} ions were partially oxidized first, leaving a mixture of V^{4+} and V^{5+} . The remaining V^{4+} ions were further oxidized to V^{5+} at -0.15 V. This was associated with a different crystalline phase of $Li_xV_2O_5$.⁵⁷ The reverse reactions take place, as indicated by the two corresponding reduction peaks at -0.2 and -0.45 V. The Li ion diffusion coefficient can be calculated from a linear relationship between i_p and $v^{1/2}$ according to the following equation,⁵⁹

$$i_p = (2.69 \times 10^5) n^{3/2} a D_{Li}^{1/2} C_{Li}^* v^{1/2}$$

where i_p is the peak current (A), a is the electrode area (cm^2), D_{Li} is the apparent diffusion coefficient of the Li^+ ion in the electrode ($cm^2 s^{-1}$), C_{Li}^* is the bulk concentration of the Li^+ ion in the electrode ($mol cm^{-3}$), and v is the potential scan rate ($V s^{-1}$).

By using CV, the kinetic response was examined to determine the dependence of peak currents on scan rates. Cyclic voltammograms of the SVO nanowire film were obtained at various sweep rates, as shown in Figure 11a. Figure 11c shows a good linear relationship between i_p and $v^{1/2}$ at scan rates lower than 300 $mV s^{-1}$. The diffusion coefficient of the Li^+ ion in the SVO thin film was estimated to be 5.3×10^{-10} $cm^2 s^{-1}$. For the V_2O_5 nanowire thin film, the diffusion coefficient of the Li ions was 7.5×10^{-11} $cm^2 s^{-1}$ according to the linear relationship shown in Figure 11d. The SVO nano-

wires have a Li diffusion coefficient 7 times higher than that of the V_2O_5 nanowires. Lantelme *et al.*⁶⁰ reported that the lithium diffusion coefficient was $10^{-12} - 10^{-13}$ $cm^2 s^{-1}$ in a V_2O_5 thin film deposited by atomic layer CVD. McGraw *et al.*⁶¹ reported that the maximum diffusion coefficient was 1.7×10^{-12} $cm^2 s^{-1}$ in an amorphous V_2O_5 film prepared by PLD. Julien *et al.*⁶² gave a value of $\sim 10^{-12}$ $cm^2 s^{-1}$ for flash-evaporated V_2O_5 films. Seman *et al.*⁶³ reported a diffusion coefficient of $\sim 1 \times 10^{-11} - 2 \times 10^{-12}$ $cm^2 s^{-1}$ for a V_2O_5 thin film deposited by plasma-enhanced CVD. Therefore, the Li ion diffusion coefficient for the SVO nanowires may be the fastest reported for a V_2O_5 system.

CONCLUSIONS

Layered silver vanadium oxide nanowires with a high aspect ratio have been hydrothermally synthesized. The 10–20 nm wide nanowires have a short Li ion diffusion distance. The SVO nanowires have a better electrical conductivity (0.5 S/cm) than V_2O_5 nanowires (0.08 S/cm) prepared using the same method. Introduction of Ag atoms in the V_2O_5 framework further enlarged the interlayer spacing as well as coordinated water. These contributed to a Li ion diffusion coefficient for SVO nanowires that was 7 times higher than that of V_2O_5 nanowires. A faster Li ion diffusion coefficient could make the SVO nanowires a promising material in applications that include Li ion batteries, supercapacitors, and electrochromic devices. The SVO nanowire-based ECD displayed color-switching over 20 times faster than that of the V_2O_5 nanowire-based ECD in our experiments and the literature reports.

METHODS

Preparation of SVO and V_2O_5 Nanowires. SVO nanowires were prepared by the hydrothermal polycondensation of ammonium metavanadate (Aldrich) and reduction of $AgNO_3$ in an autoclave. In a typical synthesis, 0.3 g of ammonium metavanadate and 0.50 g of P123 ($EO_{20}PO_{70}EO_{20}$) were dissolved in 30 mL of deionized (DI) water containing 2 mL of 1 M HNO_3 . This mixture was stirred at room temperature for 7 h, and then 1.1 g of $AgNO_3$ was added. After stirring for 1 h, the mixture was transferred to a 50 mL Teflon-lined autoclave and heated to 120 °C for 24 h. The resulting precipitate was dispersed in 50 mL of DI water with vigorous stirring. The product was suction-filtered and rinsed with DI water and acetone. The nanowires were dried at 80 °C for 12 h. The SVO can be peeled off the filter paper as a sheet. For comparison purposes, V_2O_5 nanowires were prepared with the same procedure: 0.3 g of ammonium metavanadate and 0.50 g of P123 were dissolved in 30 mL of DI water containing 1.5 mL of 2 M HCl instead of HNO_3 . This mixture was stirred at room temperature for 7 h and then transferred to an autoclave and heated to 120 °C for 24 h. The resulting precipitate was treated by the same process as that used to make the SVO nanowire sheet.

Electrochromic Device. First, 0.25 g of nanowires was dispersed into 20 mL of DI water with vigorous stirring at room temperature, and the solution was concentrated to 5 mL by solvent evaporation at room temperature. The suspension was dip-coated onto ITO glass and dried at 80 °C for 10 min. The ECDs were fabricated by mounting a 1 mm thick adhesive tape on the four sides of the nanowire thin film on ITO glass, and then an-

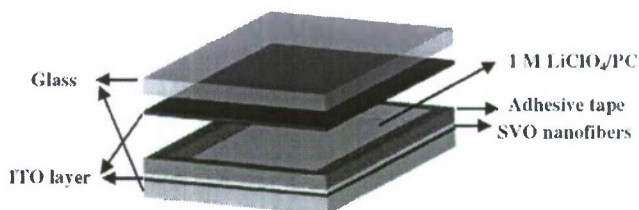


Figure 12. Setup of the electrochromic device (ECD).

other ITO glass was placed on top of the tape, leaving a 1 mm thick space, as shown in Figure 12. Finally, 1 M lithium perchlorate in propylene carbonate (PC) electrolyte was injected into the mounted cell until all air was replaced.

Characterization. XRD patterns were collected using a Scintag XDS 2000 X-ray diffractometer with $Cu K\alpha$ radiation. FT-IR spectra were recorded from KBr pellets between 400 and 4000 cm^{-1} using a Nicolet Avatar 360 FT-IR spectrometer. Scanning electron micrographs were recorded using a LEO 1530 VP field emission scanning electron microscope. The atomic ratio of Ag to V was determined using ED5 analysis with Genesis microanalysis software combining energy-dispersive analysis of X-rays (EDAX) algorithms for standardless quantification. The microstructure of the nanowires was observed by TEM using an FEI CM200 FEG transmission electron microscope at 200 kV. XPS analyses were conducted on a PHI5701 L5ci instrument with monochromated Al $K\alpha$ 1486.6 eV as the X-ray source. The takeoff angle was 65°.

and the analysis area was 2.0×0.8 mm. The calculation of the atomic ratio of Ag^+ to Ag was based on the area ratio of the binding energy peaks. Cyclic voltammograms were measured using an EG&G Princeton Applied Research potentiostat/galvanostat (model 273A). The nanowire-coated ITO glass served as working electrode, Pt was used as the counter electrode, and Ag/AgCl was used as the reference electrode. The electrolyte was 1 M LiClO_4/PC . The optical transmittance spectra of nanowire ECDs were recorded from 350 to 1500 nm using a Perkin-Elmer Lambda 900 UV-vis-NIR spectrophotometer with the ITO-coated glass/electrolyte/ITO-coated glass as a reference. The color-switching of the ECDs as a function of time was measured by using a Si photosensor with a sun imitator lamp as a light source. The EDC with SVO nanowire deposited on ITO-coated glass was used as an anode, and ITO-coated glass was the counter electrode. The electrical conductivity of the nanofiber sheets was measured using a four-point technique, in which four equally spaced probes were placed in contact with the sheet, and then a known current was passed through the outside probes and the voltage was sensed at the two inside probes using a Keithly 2000 multimeter.

Acknowledgment. We gratefully acknowledge financial support from the Robert A. Welch Foundation and SPRING.

Supporting Information Available: XPS spectra of C1s for the SVO and V_2O_5 nanowires. This information is available free of charge via the Internet at <http://pubs.acs.org>.

REFERENCES AND NOTES

- Poizot, P.; Grugeon, S.; Dupont, L.; Tarascon, J. M. Nano-Sized Transition-Metal Oxides as Negative-Electrode Materials for Lithium-Ion Batteries. *Nature* **2000**, *407*, 496–499.
- Julien, C.; Haro-Poniatowski, E.; Camacho-López, M. A.; Escobar-Alarcón, L.; Jiménez-Jarquín, J. Growth of V_2O_5 Thin Films by Pulsed Laser Deposition and Their Applications in Lithium Microbatteries. *Mater. Sci. Eng.*, **8** **1999**, *65*, 170–176.
- Takahashi, K.; Limmer, S. J.; Wang, Y.; Cao, G. Synthesis and Electrochemical Properties of Single-Crystal V_2O_5 Nanorod Arrays by Template-Based Electrodeposition. *J. Phys. Chem. B* **2004**, *108*, 9795–9800.
- Ponzi, M.; Duschatzky, C.; Carrascull, A.; Ponzi, E. Obtaining Benzaldehyde via Promoted V_2O_5 Catalysts. *Appl. Catal., A* **1998**, *169*, 373–379.
- Sun, Q.; Jehng, J. M.; Hu, H.; Herman, R. G.; Wachs, I. E.; Klier, K. In Situ Raman Spectroscopy During the Partial Oxidation of Methane to Formaldehyde over Supported Vanadium Oxide Catalysts. *J. Catal.* **1997**, *165*, 91–101.
- Banares, M. A. Supported Metal Oxide and Other Catalysts for Ethane Conversion: A Review. *Catal. Today* **1999**, *51*, 379–384.
- Talledo, A.; Granqvist, C. G. Electrochromic Vanadium Pentoxide Based Films: Structural, Electrochemical and Optical Properties. *J. Appl. Phys.* **1995**, *77*, 4655–4666.
- Liu, P.; Lee, S. H.; Tracy, C. E.; Tuener, J. A.; Pitts, J. R.; Deb, S. K. Electrochromic and Chemochromic Performance of Mesoporous Thin-Film Vanadium Oxide. *Solid State Ionics* **2003**, *165*, 223–228.
- Takahashi, K.; Wang, Y.; Cao, G. Z. Growth and Electrochromic Properties of Single-Crystal V_2O_5 Nanorod Arrays. *Appl. Phys. Lett.* **2005**, *86*, 053102.
- Kudo, T.; Ikeda, Y.; Watanabe, T.; Hibino, M.; Miyayama, M.; Abe, H.; Kajita, K. Amorphous $\text{V}_2\text{O}_5/\text{Carbon}$ Composites as Electrochemical Supercapacitor Electrodes. *Solid State Ionics* **2002**, *152*, B33–B41.
- Lee, H. Y.; Goodenough, J. B. Ideal Supercapacitor Behavior of Amorphous $\text{V}_2\text{O}_5 \cdot n\text{H}_2\text{O}$ in Potassium Chloride (KCl) Aqueous Solution. *J. Solid State Chem.* **1999**, *148*, B1–B4.
- Kim, I. H.; Kim, J. H.; Cho, B. W.; Lee, Y. H.; Kim, K. B. Synthesis and Electrochemical Characterization of Vanadium Oxide on Carbon Nanotube Film Substrate for Pseudocapacitor Applications. *J. Electrochem. Soc.* **2006**, *153*, 989–996.
- Coustier, F.; Hill, J.; Owens, B. B.; Passerini, S.; Smyrl, W. H. Doped Vanadium Oxides as Host Materials for Lithium Intercalation. *J. Electrochem. Soc.* **1999**, *146*, 1355–1360.
- Crespi, A.; Schmidt, C.; Norton, J.; Chen, K.; Skarstad, P. Modeling and Characterization of the Resistance of Lithium/SVO Batteries for Implantable Cardioverter Defibrillators. *J. Electrochem. Soc.* **2001**, *148*, A30–A37.
- Leising, R. A.; Takeuchi, E. S. Solid-State Synthesis and Characterization of Silver Vanadium Oxide for Use as a Cathode Material for Lithium Batteries. *Chem. Mater.* **1994**, *6*, 489–495.
- Chu, Y. Q.; Qin, Q. Z. Fabrication and Characterization of Silver- V_2O_5 Composite Thin Films as Lithium-Ion Insertion Materials. *Chem. Mater.* **2002**, *14*, 3152–3157.
- Zhang, J.; McGraw, J. M.; Turner, J.; Ginley, P. Charging Capacity and Cycling Stability of VO_x Films Prepared by Pulsed Laser Deposition. *J. Electrochem. Soc.* **1997**, *144*, 1630–1634.
- Lee, J. M.; Hwang, H. S.; Cho, W.-I.; Cho, B. W.; Kim, K. Y. Effect of Silver Co-Sputtering on Amorphous V_2O_5 Thin Films for Microbatteries. *J. Power Sources* **2004**, *136*, 122–131.
- Gulbinski, W.; Suszko, T.; Sienicki, W.; Warcholinski, B. Tribological Properties of Silver and Copper Doped Transition Metal Oxide Coatings. *Wear* **2003**, *254*, 129–135.
- Khan, G. A.; Hogarth, C. A. A. Conduction through MIM Sandwich Samples of Evaporated Thin Films of V_2O_5 and $\text{V}_2\text{O}_5/\text{B}_2\text{O}_3$. *J. Mater. Sci.* **1991**, *26*, 1087–1092.
- Julien, C.; Guesdon, J. P.; Gorenstein, A.; Khelifa, A.; Ivanov, I. The Influence of the Substrate Material on the Growth of V_2O_5 Flash-Evaporated Films. *Appl. Surf. Sci.* **1995**, *90*, 389–391.
- Wenda, E. Phase Diagram of $\text{V}_2\text{O}_5\text{-MoO}_3\text{-Ag}_2\text{O}$ —I. Phase Diagram of $\text{V}_2\text{O}_5\text{-Ag}_2\text{O}$ System. *J. Therm. Anal.* **1985**, *30*, 879–887.
- Takeuchi, K. J.; Leising, R. A.; Palazzo, M. J.; Marschilok, A. C.; Takeuchi, E. S. Advanced Lithium Batteries for Implantable Medical Devices: Mechanistic Study of SVO Cathode Synthesis. *J. Power Sources* **2003**, *119*, 73–978.
- Zhang, S.; Li, W.; Li, C.; Chen, J. Synthesis, Characterization, and Electrochemical Properties of $\text{Ag}_2\text{V}_4\text{O}_{11}$ and AgVO_3 1-D Nano/Microstructures. *J. Phys. Chem. B* **2006**, *110*, 24855–24863.
- Shen, G.; Chen, D. Self-Coiling of $\text{Ag}_2\text{V}_4\text{O}_{11}$ Nanobelts into Perfect Nanorings and Microloops. *J. Am. Chem. Soc.* **2006**, *128*, 11762–11763.
- Livage, J. Vanadium Pentoxide Gels. *Chem. Mater.* **1991**, *3*, 578–593.
- Muster, J.; Kim, G. T.; Krstic, V. Electrical Transport through Individual Vanadium Pentoxide Nanowires. *Adv. Mater.* **2000**, *12*, 420–424.
- Kim, G. T.; Muster, J.; Park, J. G.; Krstic, V.; Park, Y. W. Field-Effect Transistor Made of Individual V_2O_5 Nanofibers. *Appl. Phys. Lett.* **2000**, *76*, 1875–1877.
- Lamarque-Forget, S.; Pelletier, O.; Dozov, I.; Davidson, P.; Martinot-Lagarde, P.; Livage, J. Electrooptic Effects in the Nematic and Isotropic Phases of Aqueous V_2O_5 Suspensions. *Adv. Mater.* **2000**, *12*, 1267–1270.
- Kim, Y. K.; Park, S. J.; Koo, J. P.; Kim, G. T.; Hong, S.; Ha, J. S. Control of Adsorption and Alignment of V_2O_5 Nanowires via Chemically Functionalized Patterns. *Nonotechnology* **2007**, *18*, 015304.
- Ancona, M. G.; Kooi, S. E.; Kruppa, W. A.; Snow, W.; Foos, E. E.; Whitman, L. J.; Park, D.; Shirey, L. Patterning of Narrow Au Nanocluster Lines using V_2O_5 Nanowire Masks and Ion-Beam Milling. *Nano Lett.* **2003**, *3*, 135–138.
- Gu, G.; Schmid, M.; Chiu, P. W.; Minett, A.; Fraysse, J.; Kim, G. T.; Roth, S.; Kozlov, M.; Muñoz, E.; Baughman, R. H. V_2O_5 Nanofibre Sheet Actuators. *Nat. Mater.* **2003**, *2*, 316–319.
- Patzke, G. R.; Krumeich, F.; Nesper, R. Oxidic Nanotubes and Nanorods—Anisotropic Modules for a Future

- Nanotechnology. *Angew. Chem., Int. Ed.* **2002**, *41*, 2446–2461.
- 34 Niederberger, M.; Bard, M. H.; Stucky, G. D. Benzyl Alcohol and Transition Metal Chlorides as a Versatile Reaction System for the Nonaqueous and Low-Temperature Synthesis of Crystalline Nano-Objects with Controlled Dimensionality. *J. Am. Chem. Soc.* **2002**, *124*, 13642–13643.
- 35 Pinna, N.; Willinger, M.; Weiss, K.; Urban, J.; Schlögl, R. Local Structure of Nanoscopic Materials: V_2O_5 Nanorods and Nanowires. *Nano Lett.* **2003**, *3*, 1131–1134.
- 36 Cao, A. M.; Hu, J. S.; Liang, H. P.; Wan, L. J. Self-Assembled Vanadium Pentoxide (V_2O_5) Hollow Microspheres from Nanorods and their Application in Lithium-Ion Batteries. *Angew. Chem., Int. Ed.* **2005**, *44*, 4391–4395.
- 37 Livage, J. Synthesis of Polyoxovanadates via “Chimie Douce”. *Coord. Chem. Rev.* **1998**, *178*, 999–1018.
- 38 Cazzanelli, E.; Mariotto, G.; Passerini, S.; Smyrl, W. H.; Gorenstein, A. Raman and XPS Characterization of Vanadium Oxide Thin Films Deposited by Reactive RF Sputtering. *Sol. Energy Mater. Sol. Cells* **1999**, *56*, 249–258.
- 39 Krishna, M. G.; Debaugé, Y.; Bhattacharya, A. K. X-ray Photoelectron Spectroscopy and Spectral Transmittance Study of Stoichiometry in Sputtered Vanadium Oxide Films. *Thin Solid Films* **1998**, *312*, 116–122.
- 40 Rajendra Kumar, R. T.; Karunakaran, B.; Venkatachalam, S.; Mangalaraj, D.; Narayandass, S. K.; Kesavamoorthy, R. Influence of Deposition Temperature on the Growth of Vacuum Evaporated V_2O_5 Thin Films. *Mater. Lett.* **2003**, *57*, 3820–3825.
- 41 Ozer, N. Electrochemical Properties of Sol-Gel Deposited Vanadium Pentoxide Films. *Thin Solid Films* **1997**, *305*, 80–87.
- 42 Takahashi, K.; Wang, Y.; Lee, K.; Cao, G. Fabrication and Li^+ -Intercalation Properties of V_2O_5 - TiO_2 Composite Nanorod Arrays. *Appl. Phys. A: Mater. Sci. Process.* **2006**, *82*, 27–31.
- 43 Ivanova, T.; Harizanova, A. Electrochromic Investigation of Sol-Gel-Derived Thin Films of TiO_2 - V_2O_5 . *Mater. Res. Bull.* **2005**, *40*, 411–419.
- 44 Chen, W.; Kaneko, Y.; Kinomura, N. Preparation and Electrochromic Properties of V-Nb Mixed-Oxide Films by Evaporation. *J. Appl. Electrochem.* **2003**, *32*, 515–518.
- 45 Huguenin, F.; Ferreira, M.; Zucolotto, V.; Francisco, C. N.; Roberto, M. T.; Osvaldo, N. O., Jr. Molecular-Level Manipulation of V_2O_5 /Polyaniline Layer-by-Layer Films to Control Electrochromogenic and Electrochemical Properties. *Chem. Mater.* **2004**, *16*, 2293–2299.
- 46 Cheng, K. C.; Chen, F. R.; Kai, J. J. V_2O_5 Nanowires as a Functional Material for Electrochromic Device. *Sol. Energy Mater. Sol. Cells* **2006**, *90*, 1156–1165.
- 47 Li, G. C.; Pang, S. P.; Jiang, L.; Guo, Z. Y.; Zhang, Z. K. Environmentally Friendly Chemical Route to Vanadium Oxide Single-Crystalline Nanobelts as a Cathode Material for Lithium-Ion Batteries. *J. Phys. Chem. B* **2006**, *110*, 9383–9386.
- 48 Liu, J.; Wang, X.; Peng, Q.; Li, Y. Vanadium Pentoxide Nanobelts: Highly Selective and Stable Ethanol Sensor Materials. *Adv. Mater.* **2005**, *17*, 764–767.
- 49 Liu, X.; Huang, C.; Qiu, J.; Wang, Y. The Effect of Thermal Annealing and Laser Irradiation on the Microstructure of Vanadium Oxide Nanotubes. *Appl. Surf. Sci.* **2006**, *253*, 2747–2751.
- 50 Huang, F.; Fu, Z. W.; Chu, Y. Q.; Liu, W. Y.; Qin, Q. Z. Characterization of Composite 0.5Ag: V_2O_5 Thin-Film Electrodes for Lithium-Ion Rocking Chair and All-Solid-State Batteries. *Electrochem. Solid State Lett.* **2004**, *7*, A180–A184.
- 51 Sanchez, C.; Livage, J.; Lucazeau, G. Infrared and Raman Study of Amorphous V_2O_5 . *J. Raman Spectrosc.* **1982**, *12*, 68–72.
- 52 Vanova, T.; Harizanova, A. Electrochromic Investigation of Sol-Gel-Derived Thin Films of TiO_2 - V_2O_5 . *Mater. Res. Bull.* **2005**, *40*, 411–419.
- 53 Niederberger, M.; Muhr, H. J.; Krumeich, F.; Bieri, F.; Günther, D.; Nesper, R. Low-Cost Synthesis of Vanadium Oxide Nanotubes via Two Novel Non-alkoxide Routes. *Chem. Mater.* **2000**, *12*, 1995–2000.
- 54 Nordlinder, S.; Nyholm, L.; Gustafsson, T.; Edström, K. Lithium Insertion into Vanadium Oxide Nanotubes: Electrochemical and Structural Aspects. *Chem. Mater.* **2006**, *18*, 495–503.
- 55 Chaki, N. K.; Tsunoyama, H.; Negishi, Y.; Sakurai, H.; Tsukuda, T. Effect of Ag-Doping on the Catalytic Activity of Polymer-Stabilized Au Clusters in Aerobic Oxidation of Alcohol. *J. Phys. Chem. C* **2007**, *111*, 4885–4888.
- 56 Konova, P.; Arve, K.; Klingstedt, F.; Nikolov, P.; Naydenov, A.; Kumar, N.; Murzin, D. Yu. A Combination of Ag/Alumina and Ag Modified ZSM-5 to Remove NO_x and CO During Lean Conditions. *Appl. Catal. B: Environ.* **2007**, *70*, 138–145.
- 57 Cogan, S. F.; Nguyen, N. M.; Perrotti, S. J.; Rauh, D. R. Optical Properties of Electrochromic Vanadium Pentoxide. *J. Appl. Phys.* **1989**, *66*, 1333–1337.
- 58 Benmoussa, M.; Outzourhit, A.; Bennouna, A.; Ameziane, E. L. Electrochromism in Sputtered V_2O_5 Thin Films: Structural and Optical Studies. *Thin Solid Films* **2002**, *405*, 11–16.
- 59 Young, H. R.; Kiyoshi, K. Li^+ -Ion Diffusion in $LiCoO_2$ Thin Film Prepared by the Poly(vinylpyrrolidone) Sol-Gel Method. *J. Electrochem. Soc.* **2004**, *151*, A1406–A1411.
- 60 Lantelme, F.; Mantoux, A.; Groult, H.; Lincot, D. Electrochemical Study of Phase Transition Processes in Lithium Insertion in V_2O_5 Electrodes. *J. Electrochem. Soc.* **2003**, *150*, A1202–1208.
- 61 McGraw, J.; Bahn, C.; Parilla, P.; Perkins, J.; Readey, D.; Ginley, D. Li Ion Diffusion Measurements in V_2O_5 and $Li(Co_{1-x}Al_x)_2O_2$ Thin-Film Battery Cathodes. *Electrochim. Acta* **1999**, *45*, 187–196.
- 62 Julien, C.; Gorenstein, A.; Khelifa, A.; Guesdon, J. P.; Ivanov, I. Fabrication of V_2O_5 Thin Films and their Electrochemical Properties in Lithium Microbatteries. *Mater. Res. Soc. Symp. Proc.* **1995**, *369*, 639–647.
- 63 Seman, M.; Marino, J.; Yang, W.; Wolden, C. A. An Investigation of the Role of Plasma Conditions on the Deposition Rate of Electrochromic Vanadium Oxide Thin Films. *J. Non-Cryst. Solids* **2005**, *351*, 1987–1994.



Thermal properties of carbon inverse opal photonic crystals

Ali E. Aliev*, Sergey B. Lee, Ray H. Baughman, Anvar A. Zakhidov

NanoTech Institute, University of Texas at Dallas, Richardson, TX, USA

Available online 11 September 2006

Abstract

The thermal conductivity of thin-wall glassy carbon and graphitic carbon inverse opals, fabricated by templating of silica opal has been measured in the temperature range 10–400 K using transient pulse method. The heat flow through 100 Å-thick layers of graphite sheets tiled on spherical surfaces of empty overlapping spheres arrayed in face-centered-cubic lattices has been analyzed in term of anisotropy factor. Taking into account high anisotropy factor in graphite, $\gamma = 342$, we found that the thermal conductivity of inverse opal prepared by chemical vapor deposition infiltration is limited by heat flow across the graphitic layers in bottleneck, $\kappa_{\perp} = 3.95$ W/m K. The electronic contribution to the thermal conductivity, $\kappa_{e(300\text{K})} = 3.7 \times 10^{-3}$ W/m K is negligible comparing to the measured value, $\kappa_{(300\text{K})} = 0.33$ W/m K. The obtained phonon mean free path, $l = 90$ nm is comparable with the graphite segments between hexagonal array of interconnections.

© 2006 Elsevier B.V. All rights reserved.

Keywords: Photonic crystals; Opals; Inverse opals; Thermal conductivity

1. Introduction

In the last decade a new material called photonic crystal (PC) has attracted much attention from both basic and applied science viewpoint. Photons' behavior in PCs is very much like electrons' in semiconductors [1,2]: the photonic band structure may show forbidden gaps in which photons cannot exist, therefore many of the devices and concepts based on the band gap phenomena may be extended to PC. This novel concept was developed for various new applications of PC, such as threshold-less lasers and optical transistors [3]. It should be specially mentioned here, that Kaplyanskii [4–7] and his group were pioneering in optical studies of opals, and they were certainly first who studied opals as example of naturally existing PCs. The obstacles to obtain this kind of PCs with a complete gap in the desired spectral region represent a big challenge. PCs can be defined as mesoporous material with a periodic distribution of submicrometric pores. Mainly, there are two parameters that determine the existence of a photonic gap. First, the refractive index contrast, defined as the ratio between the

refractive indices of the material and the surrounding substance; secondly, the filling fraction, defined as the percentage volume occupied by the voids. Also, the topology of the structure will be decisive to explain the band structure.

Among the various preparation methods of three-dimensional periodic structures, a self-assembly method utilizing sedimentation of monodispersed nanoscale spheres is the simplest. Silica opal is a type of naturally occurring PC that consist of well-ordered three-dimensional arrays of SiO₂ spheres, which have diameters in the wavelength range of visible light [8]. As a consequence of periodicity they show opalescence colors that come from Bragg diffraction of the periodic distribution of particles. Bragg diffraction constitutes the fingerprint of photonic band gap (PBG) properties. However, theory predicts that inverse opals would show much better PBG properties than direct opals. Inverse opals that can be regarded as the negative replica of opals, have a well-ordered array of nanometric spherical cavities surrounded by a high refractive index material, in which both the cavities and the high refractive material is connected throughout the structure. To achieve complete PBG many laboratories trying to fabricate the high-quality inverse opals with high contrast and filling factor [9–14].

*Corresponding author. Tel.: +1 9728836543.

E-mail address: Ali.Aliev@utdallas.edu (A.E. Aliev).

At the same time the unusual mesoscopic structure of the synthetic opal attracted a large effort to improve the efficiency of thermoelectric materials [15,16]. A good thermoelectric material has low thermal conductivity κ , high electrical conductivity σ , and a high Seebeck coefficient, in order to maximize the thermoelectric figure of merit $Z = \sigma S^2 / \kappa$. Z has units of inverse absolute temperature and is generally quoted as ZT . For more than 40 years, the search for better thermoelectrics has not provided a material with ZT significantly larger than one. ZT of about four would make thermoelectric coolers able to compete with gas-compression technology. Assuming that the Seebeck coefficient in opal where silicon spheres replaced by thermoelectric materials will not be affected by the opal structure, if the thermal conductivity is reduced much more than the electrical conductivity, the opals could be useful thermoelectric materials. Unfortunately, many experimental works [11,16,17] and theoretical calculation [18] shows that the overall reduction for electrons and phonons in synthetic face-centered-cubic (f.c.c.) opal structure will be the same.

On the other hand, such porous and highly ordered materials like inverse opal open up new opportunities for further development of multifunctional nanodevices. Particularly, at the low filling factor usually achieved by infiltration of pores by sol-gel route or chemical vapor deposition (CVD), inverse opal has two independent nets of pores divided by very thin shell: one resulted by removing SiO_2 spheres, other net of pores is octahedral and tetrahedral pores reduced by thin wall covered on SiO_2 spheres but still has interconnected windows. Both net could be tuned independently: first net by changing the SiO_2 sphere size, second net by filling factor. Moreover, at some condition they could be filled by functional materials divided by shell material.

In this paper, we study the behavior of the heat flow through the thin-wall carbon inverse opal produced by two different methods.

2. Experimental part

The porous silica opal used as template, infiltration and carbon inverse opal synthesis processes described in details by Zakhidov et al. [10,11,19]. Briefly, the carbon inverse opal was fabricated by infiltrating silica opal with a phenolic resin, thermally curing this resin at low temperature, dissolving the SiO_2 from the infiltrated opal with aqueous HF, and pyrolyzing the resulting phenolic inverse opal at progressively increased temperatures up to 1000 °C. The graphitic carbon inverse opal was fabricated by CVD method using 1:3 molar ratio of propylene and N_2 as the feed gas followed by silica removal with aqueous HF.

Thermal and electrical conductivity measurements were performed using quantum design physical properties measurement system (PPMS). For the measurement of both types of carbon inverse opals two samples ($2.5 \times 1.8 \times 12 \text{ mm}^3$ and $6.0 \times 2.0 \times 17 \text{ mm}^3$) with the potential

electrode (thermometer leads) distances (6 and 10 mm) have been prepared. The gold-covered copper leads were glued to the sample by silver-filled epoxy resin H20E (EPO-TEK) using four-probe design: heater-thermometer T_1 -thermometer T_2 -sink. To eliminate the thermal radiation tail in the thermal conductivity data, usually appearing at high temperatures, the thermal conductivity measurements above 200 K were confirmed by comparative method involving the series connection of Ni-standard and studied samples. The electrical resistivity for some of samples was measured by a conventional four-probe method using Agilent HP4284A milliohmmeter. Heat capacity measurements were performed using Perkin Elmer Pyris Diamond DSC. The surface and fracture image of inverse opal were examined by a LEO 1530 VP scanning electron microscope (SEM).

3. Results and discussion

3.1. Structure

Fig. 1 shows typical SEM images of cleft edges of (001) and (111) planes of f.c.c. structure of the thin-walled inverse opal lattice with initial sphere diameters of 250 nm. For both glassy carbon inverse opal fabricated by a phenolic route and graphitic carbon inverse opal fabricated by CVD route a highly periodic structure throughout the whole volume have been obtained. The void structure consists of an f.c.c. arrangement of spherical carbon shells interconnected with 12 neighboring spherical shells via windows, which result from the sintering process.

3.2. Thermal conductivity

The temperature behaviors of thermal conductivity of both inverse carbon opals are almost similar (Fig. 2). The linear increase at low temperature shown in inset to Fig. 1 changes the slope at 20 K and further to the slight exponential growth above 75 K. About 20% difference in absolute value of thermal conductivities obtained for whole measured range was attributed to the difference in crystalline structure of shells. The X-ray diffraction spectrum shows the higher crystallinity for CVD-infiltrated samples. Moreover, the SEM and TEM electron micrographs shown in [10] indicate that the thin-wall shells consist of graphite sheets that are preferentially oriented parallel to the void surface created by removal of the SiO_2 spheres.

3.2.1. Effective thermal conductivity

There are a lot of approaches to calculate the thermal conductivity of porous materials and composites by known thermal conductivity of parent material. Within a continuum description the effective thermal conductivity of a composite with spherical voids ($d = 3$) or infinite cylindrical voids ($d = 2$) and thermal conductivity of host

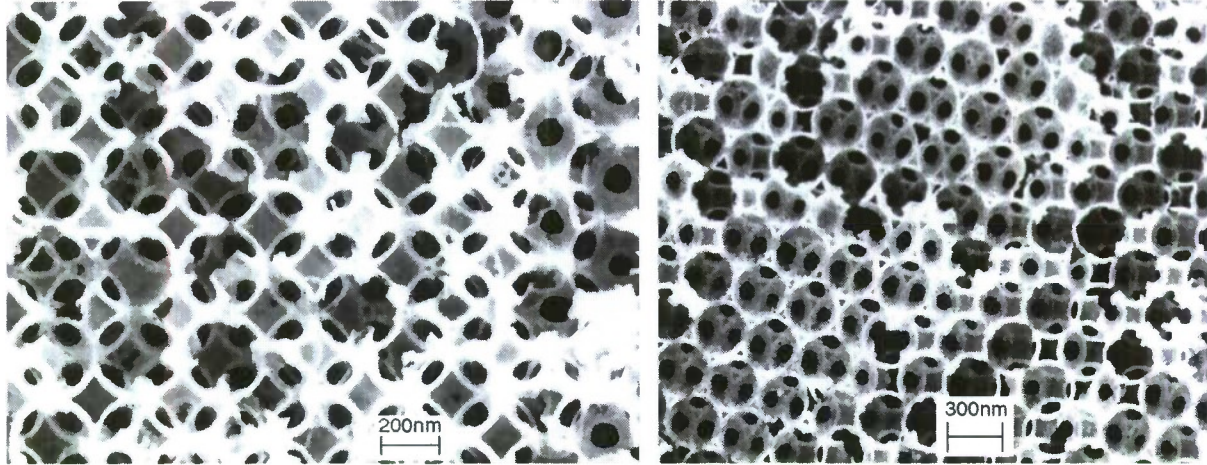


Fig. 1. SEM images of (100) and (111) planes of the surface-templated carbon inverse opal. The ragged appearance of a cleaved edge of carbon-infiltrated inverse opal is due to the occurrence of fracture through hollow spheres (rather than between spheres in direct silica opal). The large windows interconnecting the spherical cavities are due to the sintering of the opal template.

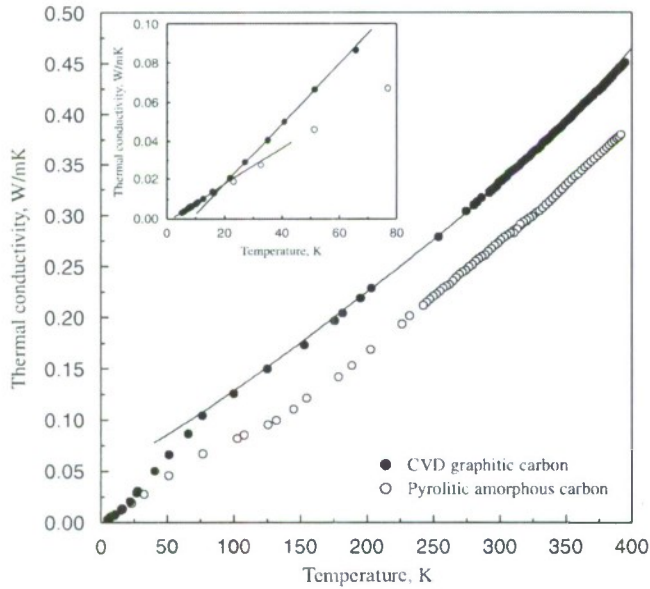


Fig. 2. Temperature dependence of thermal conductivity of graphitic carbon (CVD) and glassy carbon (pyrolytic amorphous carbon) inverse opals. Inset shows the expanded view of low-temperature region.

material κ_0 can be given by equation [20]

$$\kappa_{\text{eff}} = \frac{(1-p)\kappa_0}{1+p/(d-1)}, \quad (1)$$

where p is the fractional volume of the voids often called ‘porosity’. Another equation taking into account the thermal conductivity of the material in pores, κ_{pores} [21] were used in Refs. [22,23] for the f.c.c. opal

$$\frac{\kappa_{\text{eff}}}{\kappa_0} = (1-p)\sqrt{1-p} + p^{1/4}v, \quad (2)$$

where $v = \kappa_{\text{pores}}/\kappa_0$. The continuum approach to study the effective thermal conductivity of periodic composites was

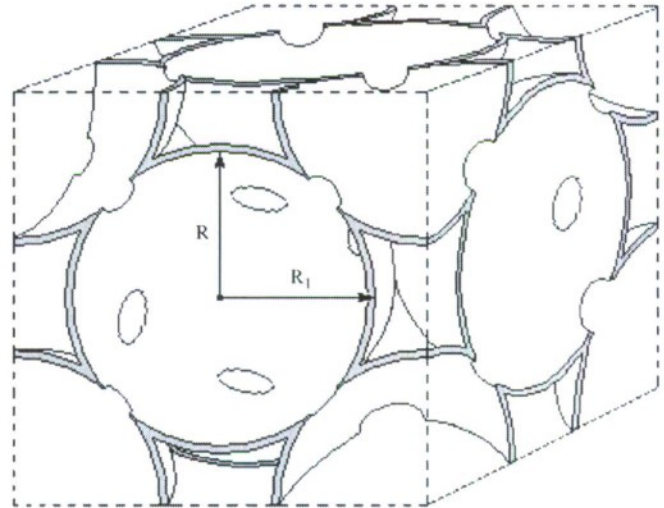


Fig. 3. Schematic representation of the surface-templated inverse opal.

examined by Albrecht et al. [24] for a number of two-dimensional and three-dimensional lattices.

3.2.2. Porosity

To calculate the effective thermal conductivity first of all we have to estimate the porosity of structure. The schematic representation of the f.c.c. structure of inverse opal is given below in Fig. 3. The volume of the f.c.c. structural unit is $V_{\text{cub}} = (2\sqrt{2}R)^3 = 16\sqrt{2}R^3$, where R is SiO_2 sphere radius. The unit comprises four spheres with volume $V_{\text{sphere}} = 4(4/3)\pi R^3 = (16/3)\pi R^3$. For opal structure we can find the filling factor F value as, $F = V_{\text{sphere}}/V_{\text{cub}} = \pi/3\sqrt{2} = 0.74$. For surface-templated inverse opal the cubic volume filled only with thin shells which thickness, $h = R_1 - R$, depends on filling conditions (Fig. 3).

For example, for sample presented in Fig. 1 ($D = 250$ nm) the averaged layer thickness is 10 nm. Then the volume of an

empty sphere is, $(4/3)\pi R_1^3 - (4/3)\pi R^3 = 0.26(4/3)\pi R^3$, where R_1 is longer than R by factor 1.08, i.e., $R_1 = 1.08R$. Filling factor for surface-templated inverse opal is $F = 0.74 \times 0.26 = 0.192$, and porosity is $P = 1 - F = 0.808$. In this calculation we neglected by the structure shrinkage at the first sintering providing the intersphere interconnection through which the SiO_2 spheres were removed after infiltration, and we neglected by volume of these circular interfaces (12 holes per each sphere). Subtraction of the volume of 24 holes with average diameter 76 nm results in reduction of the filling factor to 0.191. $P = 0.809$, respectively.

Now we can calculate the thermal conductivity of material of the shell (for graphitic carbon). For the room temperature ($T = 300 \text{ K}$), $\kappa_{\text{eff}} = 0.33 \text{ W/m K}$ (see Fig. 2). Considering that sphere voids and interstitials are air filled, for Eq. (2) we can write

$$\kappa_o = \frac{\kappa_{\text{effect}}}{(1 - P)^{3/2}} = 3.95 \text{ W/m K.}$$

By Albrecht approach for $\kappa_{\text{pores}}/\kappa_o = 0$ (air filling) giving $\kappa_{\text{eff}}/\kappa_o = 0.09$ for thermal conductivity of shell material we found very close result, $\kappa_o = 3.67 \text{ W/m K}$.

The density of measured samples is 0.22 g/cm^3 . Taking into account the porosity of studied inverse opal structure, $P = 19.1\%$ we have calculated the density of host material, $\rho = 1.15 \text{ g/cm}^3$ that is twice less than density of crystalline graphite, $\rho_c = 2.267 \text{ g/cm}^3$. Perhaps this difference is due to the porosity of the graphite layer and extended diameter of interconnected windows appeared at volume change during the pyrolysis.

The schematic representation of graphitic shell structure in Fig. 4 shows that for material with high anisotropy of conductivity, both electric and thermal, the conducting path would be strongly dependent of the anisotropy factor: $\gamma = \kappa_{\parallel}/\kappa_{\perp}$. For pyrolytic graphite at room temperature $\gamma = 342$ [25]. Heat flow from one sphere to another occurs only perpendicular to graphitic layers with thermal conductivity 5.7 W/m K . As far as heat transferred to the surface layers of another sphere the high thermal conductivity along the graphitic layers, 1950 W/m K shorts

the heat flow by sphere surface preventing the further penetration of heat to dipper layers. In such structures the thermal conductivity would be independent of the thickness of shell walls.

3.3. Electrical conductivity

Since graphite has a high electronic conductivity it allows us to estimate the electronic contribution to the thermal conductivity using Wiedemann–Franz law: $\kappa/\sigma = LT$, where $L = 2.45 \times 10^{-8} \text{ W}\Omega/\text{K}^2$ is a Lorenz number.

The temperature dependence of specific resistivity of studied inverse opal measured by two electrodes and four-probe methods is shown in Fig. 5A. The slope of the curve is in a good agreement with the data for crystalline graphite for this temperature region [26] and for carbon inverse opal with high filling factor studied in Refs. [11,27] for various heat treatment temperatures. However, the absolute value of resistivity for our inverse opals heat treated at 1000°C is much higher than those obtained in Refs. [11,27]. The anisotropy factor for electrical conductivity in highly crystalline graphite usually is much higher than for the thermal conductivity, $\gamma_e = 0.5(\Omega\text{cm})/0.5 \times 10^{-3}(\Omega\text{cm}) = 10^3$ [23]. The obtained resistivity of graphitic inverse opal normalized to porosity is in good agreement with the resistivity of crystalline graphite across the graphene layers. This result shows excellent evidence that the transport properties of graphitic inverse opal are determined by the tiled structure of contacted area of the shells.

The electronic contribution to the total thermal conductivity, $\lambda_{e(300\text{K})} = 3.7 \times 10^{-3} \text{ W/m K}$ is two order smaller than measured value, $\lambda_{(300\text{K})} = 0.33 \text{ W/m K}$. However, at low temperature, $T < 50 \text{ K}$ the electronic contribution to the thermal conductivity could dominate. The EM shielded and thermally insulated sample shows linear current–voltage dependence measured in the large applied voltage scale (see left-top inset to Fig. 5B).

The temperature dependence of the thermopower S measured along (111) direction shows steady almost linear

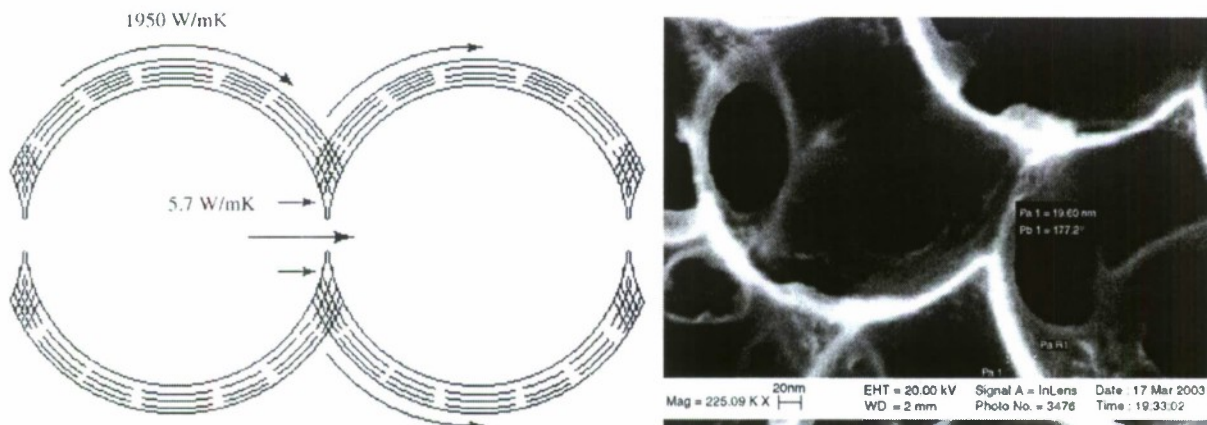


Fig. 4. Schematic representation of heat flow through graphitic shell structure and real structure of interconnecting windows.

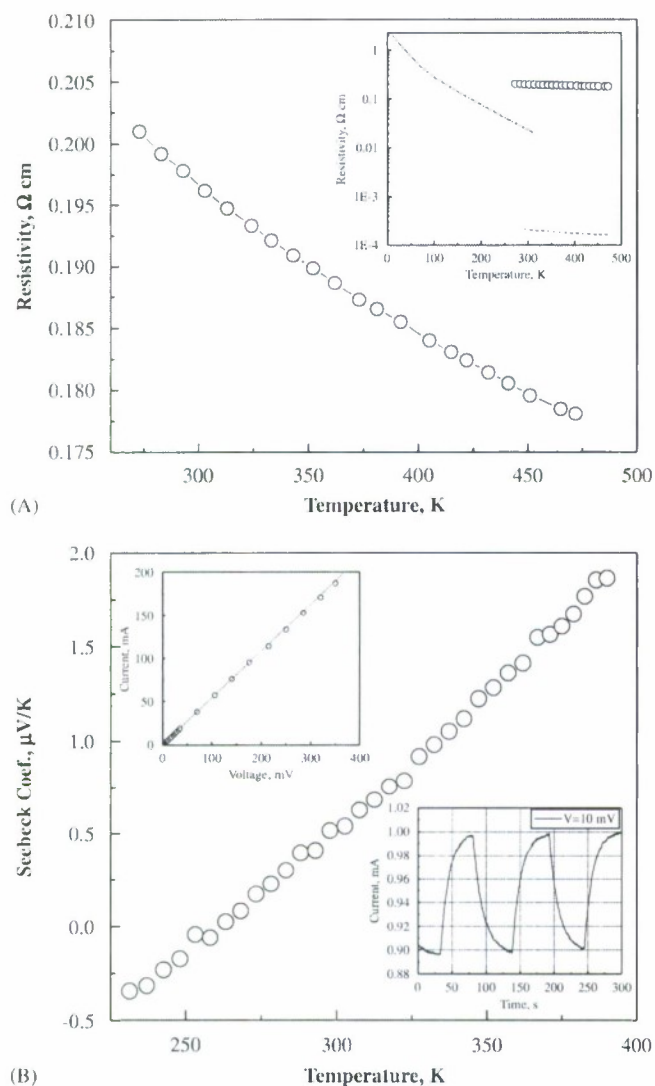


Fig. 5. (A). Temperature dependence of resistivity of the carbon inverse opal (carbon opal replica). The inset shows the comparative behavior of resistivity for studied inverse opal (open circles), phenol replica with high filling factor, heat treated at 830 °C (dash-dot line) [27], and POCO graphite (dot line) [26]. (B). Temperature dependence of thermopower of carbon inverse opal. Left-top inset shows linear I - V dependence at low applied voltages. Right-bottom inset shows the current response of bolometric device to the modulated incident light from halogen-tungsten lamp, $P = 9.8 \text{ mW/cm}^2$.

increase of a Seebeck coefficient. Positive sign of S above 250 K indicates on the hole (p-type) mechanism of conduction. Low thermopower combined with high resistivity at room temperature give low thermoelectric figure of merit, $Z = 4.1 \times 10^{-10} \text{ K}^{-1}$.

The extremely developed surface area of carbon inverse opal with blackbody thermal emissivity ($\epsilon = 1$) is very sensitive to the external radiation. Taken into account the high thermal coefficient of resistivity ($\alpha = 1.78 \times 10^{-3} \text{ K}^{-1}$) and low density the thin slab of carbon inverse opal demonstrates very high responsivity ($S = dV/dW = 150 \text{ V/W}$) to the modulated radiation. The current response of

0.5 mm-thick slab to the modulated light from 15 W halogen-tungsten lamp is shown in right-bottom inset to the Fig. 5B.

3.4. Heat capacity and sound velocity

Temperature dependence of the specific heat capacity of graphitic inverse opal is shown in Fig. 6. Within the measured temperature range the heat capacity exhibits the smooth rise closely resembling the two-dimensional-three dimensional behavior of the bulk planar graphite (solid line) [26]. For comparison the specific heat capacity values of POCO graphite was divided to the density ratio $\rho_{\text{POCO}}/\rho_{\text{invers opal}} = 1.82 \text{ g/cm}^3/0.22 \text{ g/cm}^3$. Both curves behaviors correspond to the temperature region far below of Debye temperature, $T < \theta_D$. Surprisingly the heat capacity of carbon inverted opal shows about 30% higher value per mass unit than the density normalized POCO graphite.

To gain a better understanding of the thermal transport properties in carbon inverted opal we have measured the sound velocity along the opal grown direction, $[111]$. The macroscopic f.c.c. structure of carbon inverted opal has isotropic elastic properties and can be characterized by velocity of longitudinal and transverse acoustical waves. The velocity of longitudinal (V_L) and transverse (V_T) waves was measured by resonance and pulse-echo methods along the $[111]$ direction (opal-growth direction). Two quartz transducers ($f_0 = 5 \text{ MHz}$, $D = 3 \text{ mm}$) were attached to the edges of rectangular cross-section bar ($2.5 \times 1.8 \times 12 \text{ mm}^3$, Sample #1 used for thermal conductivity measurements) by silver-epoxy glue (H20E). Special measures were taken to prevent the glue penetration into the bulk of the sample. Taken into account high porosity of specimen the measurements were conducted under high vacuum

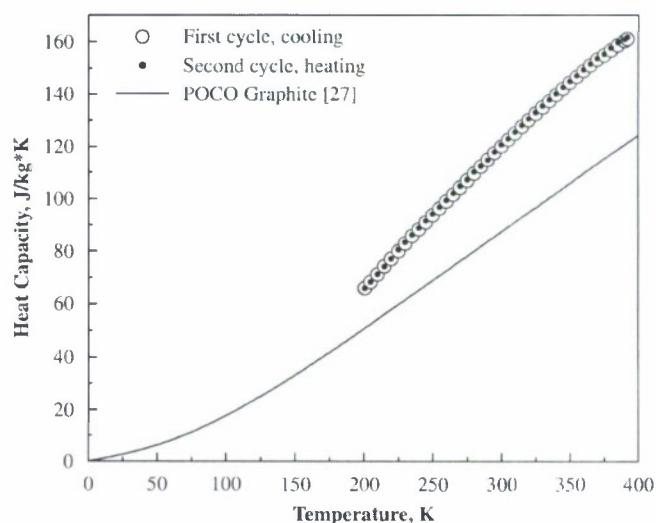


Fig. 6. Temperature dependence of specific heat capacity, C_p of graphitic inverse opal prepared by CVD method. Open circles show the first cooling cycle, small solid circles show second heating cycle. Solid line represent the C_p vs. T for pyrolytic POCO graphite normalized to the density of studied inverse opal, $(1.82 \text{ g/cm}^3/0.22 \text{ g/cm}^3)$.

($P = 10^{-4}$ mbar). Using both methods it was found that at room temperature $V_l = 1170 \pm 20$ m/s and $V_t = 360 \pm 40$ m/s. The V_l is twice lower than for direct silica opal (2100 m/s, [28]) and more than four times lower of V_l for graphite (4900 m/s, [29]) measured along graphene layers. The extremely low V_t confirms the high V_l/V_t ratio for layered structures [29,30].

Using the gas-kinetic formula for the thermal conductivity, we can write

$$\lambda = \frac{1}{3} C_p \rho V_D \bar{l}, \quad (3)$$

where C_p is the heat capacity at constant pressure, ρ is the density, \bar{l} is an average mean free path for the phonons, and the Debye speed V_D is related to the measured V_l and V_t , the longitudinal and transverse speed of sound, by

$$\frac{3}{V_D^3} = \frac{1}{V_l^3} + \frac{2}{V_t^3}. \quad (4)$$

Using measured room temperature values of $\lambda = 0.33$ W/m K, $C_p = 120.5$ J/kg K, $\rho = 0.22 \times 10^3$ kg/m³ and the averaged sound velocity $V_D = 410$ m/s we estimated the phonon mean free path, $\bar{l} = 90$ nm. This value is well comparable with the length of the hexagonal segment of graphitic shells shown in Fig. 4. Worth to note that the thermal conductivity of single-crystal C₆₀ at room temperatures ($\lambda = 0.4$ W/m K) is very close to the obtained value for carbon inverse opal and is explained by the low phonon density and weak molecular bonding between spheres [30]. The same is valid for carbon inverse opal considering that the heat propagation takes place along the thin layer of graphene sheets and the highly resistive interfaces with weak van der Waals bonding.

4. Conclusions

We measured the thermal conductivity of carbon inverse opal with different crystallinity of synthesized carbon shells. Obtained thermal conductivity in both samples is extremely low, 0.33 W/m K. The conducting path is strongly dependent on the anisotropy factor: $\gamma = \kappa_{11}/\kappa_{\perp}$. For highly crystalline pyrolytic graphite ($\gamma = 342$) the heat flow from one spherical shell to another occurs only perpendicular to graphitic layers with thermal conductivity 5.7 W/m K. These interconnecting interfaces determine the whole thermal conductance of system. The heat transferred to the surface layers of another sphere is rapidly shorted by high thermal conductivity along the graphitic layers (1950 W/m K) thus, preventing the further penetration of heat to dipper layers. In such structures the thermal conductivity would be independent of the thickness of shell walls. Using the measured room temperature values of $\lambda = 0.33$ W/m K, $C_p = 120.5$ J/kg K, $\rho = 0.22 \times 10^3$ kg/m³ and the averaged sound velocity $V_D = 410$ m/s we estimated the phonon mean free path, $\bar{l} = 90$ nm. This value is well comparable with the length of the hexagonal segments on graphitic shells of carbon inverse opal.

The electronic contribution to the thermal conductivity, $\kappa_{e(300\text{K})} = 3.7 \times 10^{-3}$ W/m K is negligible comparing to the measured value, $\kappa_{(300\text{K})} = 0.33$ W/m K.

The low thermal conductivity combined with high electronic resistivity and low thermopower give low thermoelectric figure of merit, $Z = 4.1 \times 10^{-10}$ K⁻¹. On the other hand, the extremely developed surface area of carbon inverse opal with blackbody thermal emissivity ($\varepsilon = 1$) is very sensitive to the external radiation. Taken into account the high thermal coefficient of resistivity ($\alpha = 1.78 \times 10^{-3}$ K⁻¹) and low density of the material the thin slab of carbon inverse opal demonstrate very high responsivity ($S = dV/dW = 150$ V/W) to the modulated radiation.

Acknowledgments

The support of 2005 SPRING (Strategic Partnership for Research in Nanotechnology Program, Texas) SEED GRANT Program via SPRING/AFOSR program is highly appreciated.

References

- [1] E. Yablonovitch, Phys. Rev. Lett. 58 (1987) 2059.
- [2] S. John, Phys. Rev. Lett. 58 (1987) 2486.
- [3] S. John, T. Quang, Phys. Rev. Lett. 78 (1997) 1888.
- [4] V. N. Astratov, V. N. Bogomolov, A. A. Kaplyanskii, A. V. Prokofiev, L. A. Samoilovich, S. M. Samoilovich, Yu. A. Vlasov, Nuovo Cimento della Societa Italiana di Fisica, D: Condensed Matter, Atomic, Molecular and Chemical Physics, Fluids, Plasmas, Biophysics 17D (11–12) 1995.
- [5] V. N. Astratov, V. N. Bogomolov, A. A. Kaplyanskii, A. V. Prokofiev, L. A. Samoilovich, S. M. Samoilovich, Yu. A. Vlasov, in: A. D'Andrea, L. G. Quagliano, S. F. Scler, (Eds.), Proceedings of the International meeting on Highlights of Light Spectroscopy on Semiconductors, Italy, September 11–12, 1995.
- [6] V.N. Astratov, Yu.A. Vlasov, O.Z. Karimov, A.A. Kaplyanskii, Yu.G. Musikhin, N.A. Bert, V.N. Bogomolov, A.V. Prokofiev, Phys. Lett. A 222 (1996) 349.
- [7] Yu. A. Vlasov, V.N. Astratov, O.Z. Karimov, A.A. Kaplyanskii, V.N. Bogomolov, A.V. Prokofiev, Phys. Rev. B 55 (1997) R13357.
- [8] J.V. Sanders, Nature 204 (1964) 1151.
- [9] C. Lopez, et al., Superlattices Microstruct. 22 (1997) 399.
- [10] A.A. Zakhidov, R.H. Baughman, Z. Iqbal, C. Cui, I. Khayrullin, S.O. Dantas, J. Marti, V.G. Ralchenko, Science 282 (1998) 897.
- [11] K. Yoshino, H. Kajii, Y. Kawagishi, M. Ozaki, A.A. Zakhidov, R.H. Baughman, Jpn. J. Appl. Phys. 38 (1999) 4926.
- [12] Y.A. Vlasov, N. Yao, D.J. Norris, Adv. Mater. 11 (1999) 165.
- [13] A. Stein, R.C. Schrodin, Curr. Opin. Solid State Mater. Sci. 5 (2001) 553.
- [14] T.M. Tritt, Science 283 (1999) 804.
- [15] F.J. DiSalvo, Science 285 (1999) 703.
- [16] R.H. Baughman, A.A. Zakhidov, I. Khayrullin, Z. Iqbal, P. Eklund, G.D. Mahan, in: K. Kaumoto (Ed.), Opals and Replicas. Proceedings of the XVII International Conference on Thermoelectrics, Nagoya, Japan, IEEE, New York, 1998.
- [17] V.N. Bogomolov, L.S. Parfen'eva, A.V. Prokofiev, I.A. Smirnov, S.M. Samoilovich, A. Jezyowski, J. Mucha, H. Miseric, Fiz. Tverd. Tela, (St.Petersburg) 37 (1995) 3411 (Phys. Solid State 37 (1995) 1874).
- [18] J.O. Sofo, G.D. Mahan, Phys. Rev. B 62 (2000) 2780.
- [19] A.A. Zakhidov, I. Khayrullin, R.H. Baughman, Z. Iqbal, K. Yoshino, Y. Kawagishi, S. Tatsuahara, Nanostruct. Mater. 12 (1999) 1089.

- [20] J.C. Maxwell, *A Treatise on Electricity and Magnetism*, New York, 1954, p. 435.
- [21] E.Y. Litovsky, *Inorg. Mater.* 16 (1980) 559.
- [22] V.N. Bogomolov, D.A. Kurdyukov, L.S. Parfen'eva, A.V. Prokofiev, S.M. Samoilovich, I.A. Smirnov, *Phys. Solid State* 39 (1997) 341.
- [23] A.E. Aliev, N.Kh. Akhmedjanova, *Uzbek Fiz. J.* 1 (1999) 373.
- [24] J.D. Albrecht, P.A. Knipp, T.L. Reinecke, *Phys. Rev. B* 63 (2001) 134303.
- [25] B.R. Lide (Ed.), *CRC Handbook of Chemistry and Physics*, 82nd ed., 2001–2002, pp. 12–221.
- [26] R.E. Taylor, H. Groot, *High Temp.–High Press.* 12 (1980) 147.
- [27] K. Yoshino, H. Kajii, Y. Kawagishi, M. Ozaki, A.A. Zakhidov, R.H. Baughman, *Jpn. J. Appl. Phys.* 38 (1999) 4926.
- [28] V.N. Bogomolov, I.A. Smirnov, N.V. Sharenkova, G. Bruls, *Phys. Solid State* 43 (2001) 194.
- [29] E.P. Papadakis, H. Bernstein, *J. Acoust. Soc. Am.* 35 (1963) 521.
- [30] R.C. Yu, N. Tea, M.B. Salamon, *Phys. Rev. Lett.* 68 (1992) 2050.

High- T_c superconductivity in nanostructured $\text{Na}_x\text{WO}_{3-y}$: sol-gel route

Ali E Aliev

Alan G MacDiarmid NanoTech Institute, University of Texas at Dallas, Richardson, TX 75083, USA

E-mail: Ali.Aliev@utdallas.edu

Received 12 July 2008, in final form 3 September 2008

Published 1 October 2008

Online at stacks.iop.org/SUST/21/115022

Abstract

Tungsten trioxide, WO_{3-y} , infiltrated into various nanoporous matrix structures such as carbon inverse opal, carbon nanotube paper or platinum sponge, and then intercalated with alkaline ions (Li^+ , Na^+) exhibits a pronounced diamagnetic onset in ZFC magnetization in a wide range of temperatures, 125–132 K. Resistivity measurements show nonzero jump and intensive fluctuations of electrical resistance below observed transition points. The observed magnetic and electrical anomalies in nanostructured tungsten bronzes ($\text{Li}_x\text{WO}_{3-y}$ and $\text{Na}_x\text{WO}_{3-y}$) suggest the possibility of localized non-percolated superconductivity.

1. Introduction

Due to the intercalation of Na^+ ions into the cavities in the WO_3 structure, leading to donation of their electrons to the conduction band of the WO_3 matrix, the tungsten trioxide transforms into tungsten bronze and changes its color and electrical conductivity. This coloration reaction is now being used in electro-chromic displays, for sunglasses, rear view mirrors in cars and smart windows in large buildings [1, 2].

WO_3 and related materials can be found in a large variety of crystal structures. The tungsten oxides consist of WO_6 octahedrons arranged in various corner-sharing or edge-sharing configurations. The simplest form is the defect perovskite or ReO_3 structure shown in figures 1(a) and (b). Actually, the perovskite structure is formed when the intercalated ion occupies the symmetry position within the center of the cube. Pure, bulky WO_3 does not generally exist in a cubic structure, but instead a monoclinic phase appears to be most stable at room temperature [3]. In thin films, however, it is most likely that the octahedrons are ordered hexagonally in crystallites with sizes depending on the fabrication route and deposition temperature [4]. Stoichiometric WO_3 is a wide bandgap n-type semiconductor (2.8 eV) which can be considered as a good insulator. Intercalation of monovalent or divalent cations in the interstices leads to intricate structural changes. The resulting materials form the so-called tungsten bronzes and exhibit a continuous color change and often a large increase in electrical conductivity, which becomes

metallic in nature [5]. The layered ABO_3 perovskite structure of tungsten bronze with a large diversity of structural changes during intercalation, leading to dramatic changes in electronic structure, is very attractive for high-temperature superconductivity (high- T_c SC) [6, 7].

The first observation of bulk SC in Na_xWO_3 for $x = 0.28$ – 0.35 at $T_c = 0.57$ K was described by Raub *et al* in 1964 [8]. Sheet SC along the twin walls of the orthorhombic-tetragonal twin boundaries of reduced WO_3 was found at $T_c = 3$ K [9, 10]. The single crystals of WO_3 that were deoxygenated using a gas transport reaction with Na vapor consist of a non-superconducting matrix of tetragonal WO_{3-y} and superconducting twin boundaries. The temperature dependence of the upper critical field shows BCS-type behavior below the SC transition temperature.

The possible nucleation of 2D SC with a critical temperature of 91 K was demonstrated in WO_3 single crystals doped on the surface with sodium [11–13]. The reported surface composition was $\text{Na}_{0.05}\text{WO}_3$ and, according to electro-spin-resonance measurements, exhibits gap opening in the SC state in good agreement with the weak-coupling DCS theory [13]. This discovery did not attract much attention perhaps of localized non-percolated SC or because of possible contamination of the Na_xWO_3 samples by YBCO as the origin of the SC signature with a $T_c = 91$ K. Moreover, the high- T_c SC in such materials is surprising, because the density of states at the Fermi level $N(E_F)$ is very small for the actual doping concentrations. High- T_c needs a large electron-phonon

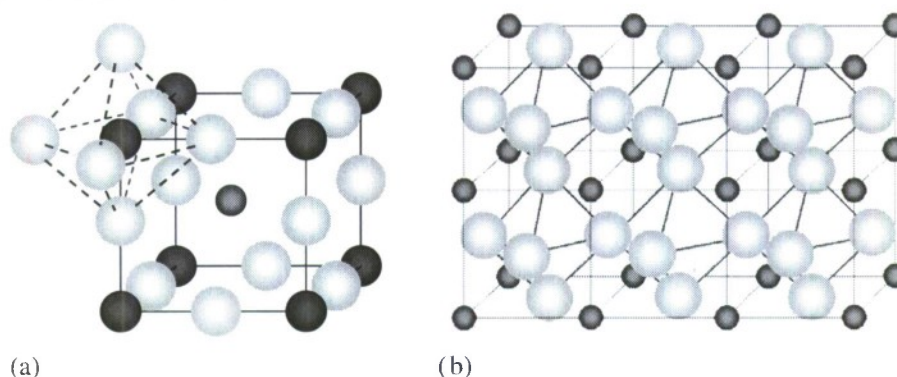


Figure 1. (a) Perovskite crystal structure for $(\text{Li, Na, K})\text{WO}_3$ with tungsten atoms as dark (blue) solid circles, oxygen atoms as empty (gray) circles, and Li, Na or K atoms as small (red) solid circles. (b) The ReO_3 structure, used as an approximation for monoclinic WO_3 , corresponds to omission of the alkali ion site. Octahedron layers, built up by oxygen atoms, surrounding the tungsten atom, separated by alkali-metal layers are shown in the right-hand side image.

coupling λ , which is proportional to $N(E_F)I^2/M\omega^2$, where I is the matrix element for the coupling, M is an atomic mass and ω is a representative phonon frequency [14].

In this work I used a sol-gel technique for preparation of tungsten bronzes inside porous nanostructured host matrices. The sol-gel route allows us to vary the structural parameters and concentrations of composition over a wide range: thus one can tune the electronic properties from a semiconductor to a metal by doping. To increase the volume fraction of the superconducting phase first I infiltrated WO_3 into nanoporous material with a high surface area and then electrochemically intercalated the resultant structure with alkali ions (Li^+ , Na^+ , K^+). To make the intercalation process controllable over a wide current and potential range I gave preference to highly conductive and chemically stable matrix materials such as carbon and platinum. As porous host matrices carbon inverse opal, platinum sponge and CVD-grown multi-walled carbon nanotube paper have been tested. The most pronounced and reproducible onset in magnetization and resistance measurements were found for $\text{Na}_x\text{WO}_{3-y}$ in the carbon inverse opal host matrix at $T_c = 125$ K.

2. Experimental details

2.1. Sample preparation

2.1.1. Peroxotungstic acid preparation. The infiltration and deposition of pure tungsten oxide films onto the highly developed surface area of the chosen matrices was performed by dipping the porous matrix into peroxotungstic acid, whose preparation procedure is almost the same as that described elsewhere [15, 16]. In our experiments, peroxotungstic acid (PTA)— $\text{WO}_{3-y}\cdot n\text{H}_2\text{O}$ was synthesized by dissolving the tungsten powder in an ice-cooled beaker containing a (2:1) mixture of hydrogen peroxide (31 vol%) and glacial acetic acid. All the chemicals were supplied by Aldrich and were used as received. This solution was very stable under excess of H_2O_2 . After filtration, the excess H_2O_2 was decomposed by dipping the platinum net into the solution. Decomposition of

H_2O_2 leads to the rapid formation of yellow colloidal particles which precipitate spontaneously after a few days. Precipitation of PTA can be stopped by adding oxalic acid [15] and reversed by intensive ultrasound treatment. For further use the solution was partially evaporated to substitute the excessive water with methanol (ethanol).

Deposition of $\text{WO}_{3-y}\cdot n\text{H}_2\text{O}$ on the host porous matrices was carried out by simply dipping the bar-shaped specimens into the prepared solution, followed by vacuum-assisted infiltration to increase the solution penetration rate into the inner parts of the nanoporous structure. To get a higher filling factor the samples were dipped into the solution at least 4–5 times, followed by drying at room temperature for 10 min and sintering at 130°C for 30 min after each infiltration. The sintering at 130°C makes the deposited film insoluble in water and peroxotungstic solution.

2.1.2. Host matrices: carbon inverse opal. The synthetic silica opals were used as templates for fabrication of carbon inverse opals [17]. Briefly, the highly periodic three-dimensional synthetic opal structures obtained by sedimentation of the monodispersed aqueous colloid of SiO_2 spheres were infiltrated with phenolic resin SPI-PON 812 (typical hard formulation: SPI-PON 812—47%; DDSA (softener)—17%; NMA (hardener)—34%; DMP-30—2%, SPI Supplies) and thermally cured at low temperature, 70°C and then pyrolyzed at progressively increased temperatures up to 1000°C in the argon gas furnace. An embedded opal sample was then placed in a 1% diluted aqueous HF solution for 12 h for soft etching of the SiO_2 spheres [18]. The carbon is not affected by the silica etching. The necks connecting the silica spheres (resulting from the sintering process) act as channels through which the etchant flows. The remaining three-dimensional periodic structure is a carbon inverse opal (also referred to as a 3D carbon opal replica). The obtained room temperature electrical resistivity ($2 \times 10^{-3} \Omega \text{ m}$) of carbon inverse opal has a negative slope and, after normalization to the porosity, is in good agreement with the resistivity of graphite across the graphene layers [19]. The double-layer

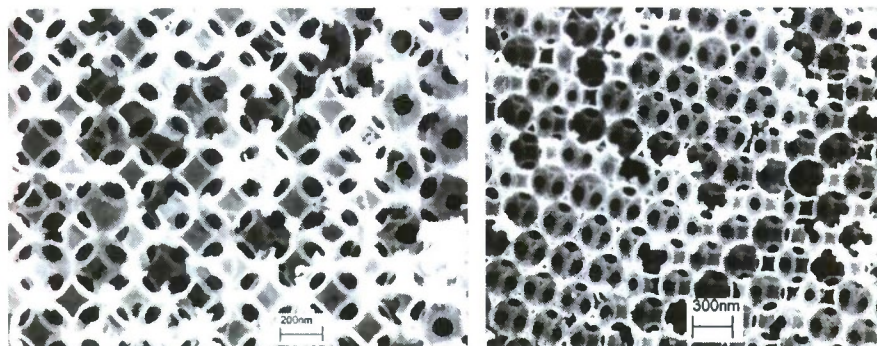


Figure 2. SEM images of (100) and (111) planes of the surface-templated carbon inverse opal. The ragged appearance of a cleaved edge of carbon-infiltrated inverse opal is due to the occurrence of fracture through hollow spheres (rather than between spheres in direct silica opal). The large windows interconnecting the spherical cavities are due to sintering of the initial opal template.

capacity of the carbon inverse opal is extremely high, 10–15 F g^{-1} . Figure 2 shows typical SEM images of the (001) and (111) planes of the face-centered cubic (fcc) structure of the carbon inverse opal with initial SiO_2 spherical diameters of 280 ± 6 nm.

Carbon nanotube paper. Carbon nanotube (CNT) paper is a perfect host matrix for electrochemical intercalation of transient metal oxides because of its high electronic conductivity, high electrochemically accessible surface area and useful mechanical properties. However, due to the catalytic growth most commercially available CNTs are significantly poisoned by ferromagnetic metallic particles. The resultant CNT paper contains 20–30 wt% of ferromagnetic inclusions that substantially suppresses the nucleation of a superconducting phase. Multi-walled carbon nanotube (MWCNT) paper fabricated by the vacuum filtration method from a CVD-grown MWCNT forest is less poisoned by metallic inclusions (<1 wt%), has huge surface area with a typical double-layer capacitance of 15–20 F g^{-1} , and can be used as a possible candidate for porous conductive matrix material.

Platinum sponge. Platinum sponge fabricated by pressing Pt nanopowder (5–6 nm) is a non-carbon alternative for conductive nanoporous matrices. Bulk platinum is a paramagnetic material with magnetic susceptibility of 26×10^{-5} . Platinum nanoparticles compaction-molded into a shaped article (pellet) has an extremely high surface area and a double-layer capacity typically of 20–30 F g^{-1} . The void volume (density measurements) was 82–87%, a little higher than for single-walled CNT papers (~77%). However, the WO_3 infiltration followed by annealing at 150 °C totally destroyed the pellets. To reinforce the structure of the platinum sponge the pellet specimen was annealed at 500 °C for 5 h: while the capacitance was about 100 times lower the obtained structure was very stable to infiltration and annealing processes (see inset to figure 5(d)).

2.1.3. Electrochemical intercalation. Alkaline metal ions intercalation was conducted using an EG&G potentiostat-galvanostat 273A employing a three-electrode experimental set-up. Small pieces of carbon inverse opal bar (typically

$2 \times 2 \times 10 \text{ mm}^3$) or any other of the mentioned host materials were connected to the working electrode by silver paste, H20E (Epoxy Technology). $20 \times 8 \times 2 \text{ mm}^3$ graphite plate (Alfa Aesar, 99.999%) and a saturated calomel electrode were used as the counter and reference electrodes, respectively. To avoid the current shunt through open terminals and silver paste they were covered with insulating silicon paste. Three aqueous electrolytes (2M (Li, Na, K)Cl) and a non-aqueous electrolyte of 1 M LiClO_4 in propylene/ethylene carbonate were used for intercalation experiments. The window for scanning potentials is limited according to the electrochemistry property of the electrolytes used and they are roughly -0.7 to $+0.2$ V for aqueous, and -2.0 to $+0.8$ V for non-aqueous electrolytes, respectively.

WO_3 deposited into a porous matrix was electrochemically charged by alkali ions at constant current (chronopotentiometry mode) with current density in the range of 1–10 mA cm^2 for 4–10 h and then dried at room temperature for 30 min. Then samples were sintered for 1 h at 300 °C in argon atmosphere and finally sealed in Parafilm-PM996.

2.2. Characterization technique

The magnetic properties of $\text{Na}_x\text{WO}_{3-y}$ infiltrated into nanoporous matrices were studied using a Quantum Design (QD) magnetic properties measurement system (MPMS) based on a superconducting quantum interference device magnetometer (SQUID) with a 7 T superconducting solenoid. The field-cooled (FC) and zero-field-cooled (ZFC) magnetization measurements were performed in the temperature range of 1.8–300 K with precise stabilization of each targeted temperature (0.01 K) for 60 s followed by four scans (4 cm) and data acquisition. For the DC magnetic measurements cylindrical shaped bars ($h = 10$ mm, $D = 2$ mm) sealed into moisture-resistant thermoplastic Parafilm were encapsulated into gelatin capsules (SPI supplied) and attached to the end of a diamagnetic rod using plastic straw (SPI, Part #AGC2). The measured signal was corrected with respect to the temperature-independent signal of the gelatin capsule with plastic straw. The precision of the measured magnetization value was tested using QD's standard Pd sample and the temperature accuracy was confirmed on Pb (99.9999%) specimens [20].

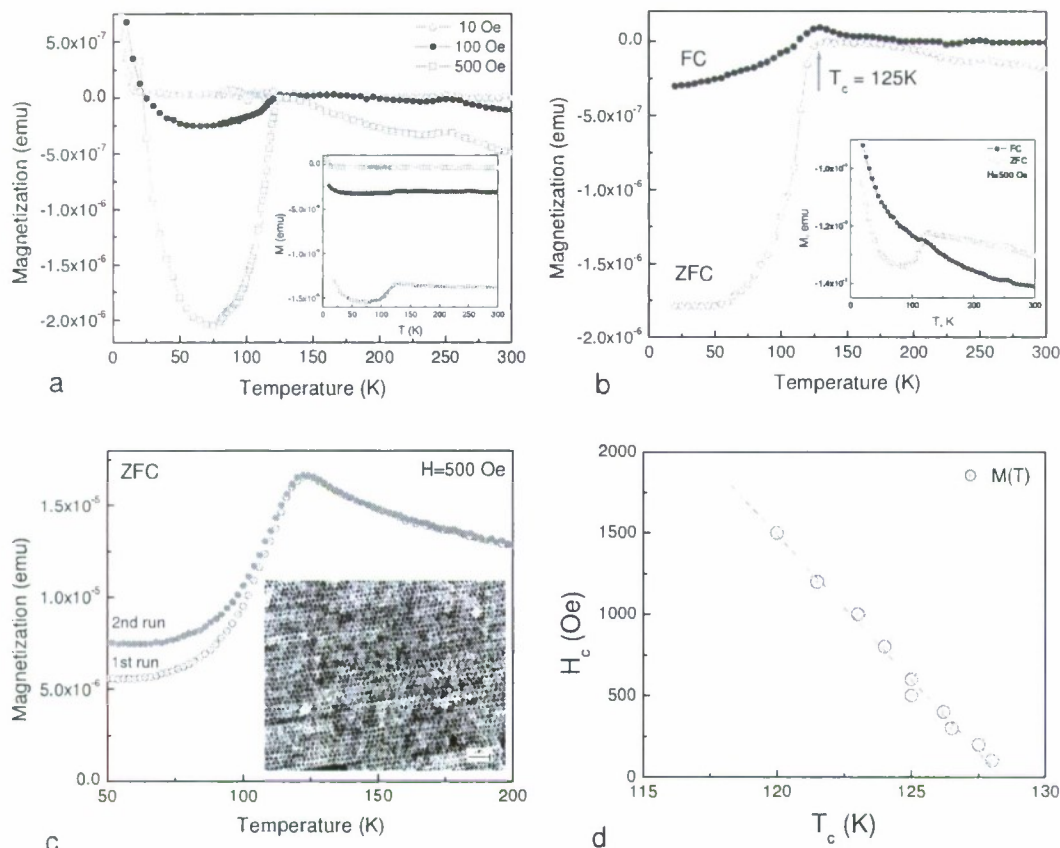


Figure 3. (a) The temperature dependence of ZFC magnetization for $\text{Na}_4\text{WO}_{3-y}$ infiltrated into carbon inverted opal at three different applied fields, 10, 100 and 500 Oe. For comparison all three curves were bound to $M = 0$ at $T = 130$ K by subtraction of the contribution from the host matrix. Inset shows the real distribution of measured magnetization. (b) FC and ZFC measurements of magnetization at $H = 500$ Oe shown with subtracted paramagnetic contribution. Inset shows the measured data. Curie paramagnetic contribution was subtracted using the following fitting parameters: $M = M_0 + C/T$, $M_0 = 1.35 \times 10^{-6}$ emu, $C = 12.64 \times 10^{-6}$ emu \times K. (c) ZFC $M(T)$ for $\text{Na}_4\text{WO}_{3-y}$ in the carbon inverse opal without additional heat treatment after intercalation (drying in air). First and second run measurements for an applied magnetic field of 500 Oe are shown by open circles (blue), and solid circles (red), respectively. Inset shows the SEM image of $\text{Na}_4\text{WO}_{3-y}$ islands (bright areas) in carbon inverse matrix. (d) Temperature dependence of critical field for $\text{Na}_4\text{WO}_{3-y}$ in carbon inverse opal.

The magnetoresistive properties of $\text{Na}_4\text{WO}_{3-y}$ were studied using the QD physical properties measurement system (PPMS) equipped with a 9 T superconducting solenoid. The rectangular shaped samples with attached gold electrodes connected by epoxy silver paste H20E were mounted on the PPMS sample puck assembly. Four-probe resistivity measurements were carried out using an AC user bridge board (PPMS Resistivity option) at a frequency of 1000 Hz with a current maintained at $1 \mu\text{A}$.

The scanning electron microscope (SEM) micrographs were taken with a LEO 1530 VP equipped with an energy-dispersive spectrometer (EDS). The elemental analysis of the $\text{Na}_4\text{WO}_{3-y}$ embedded into the inverse opal revealed some residue of anions (Cl^-) from electrolyte salt, indicating a lack of washing after charging of the sample.

On all the steps of sample preparation and characterization special measures were taken to avoid contamination of the samples with ferromagnetic or copper materials. Besides the magnetization tests for hysteresis loops, the precursor materials and synthesized compounds were vigorously tested for residual

ferromagnetic or copper contamination using EDS and x-ray photoemission spectroscopy (XPS) elemental analysis.

3. Results and discussion

3.1. Magnetization

The temperature dependence of the ZFC magnetization for $\text{Na}_4\text{WO}_{3-y}$ in a carbon inverse opal matrix is shown in figure 3(a) for three applied magnetic fields of 10, 100 and 500 Oe. The $M(T)$ behavior is very similar to that obtained by Reich *et al* [11] for a single crystal of WO_3 with surface-doped Na^+ . However, the pronounced onset which is increased for higher magnetic fields was observed at ~ 125 K. The sharp onset in appearance resembles an incomplete diamagnetic shielding. At lower temperatures the $M(T)$ curve turns into the increase of magnetization due to the Curie-type paramagnetic background of a low temperature $\epsilon\text{-WO}_{3-y}$ structural phase [21]. The paramagnetic background is stronger for higher magnetic fields (see low temperature

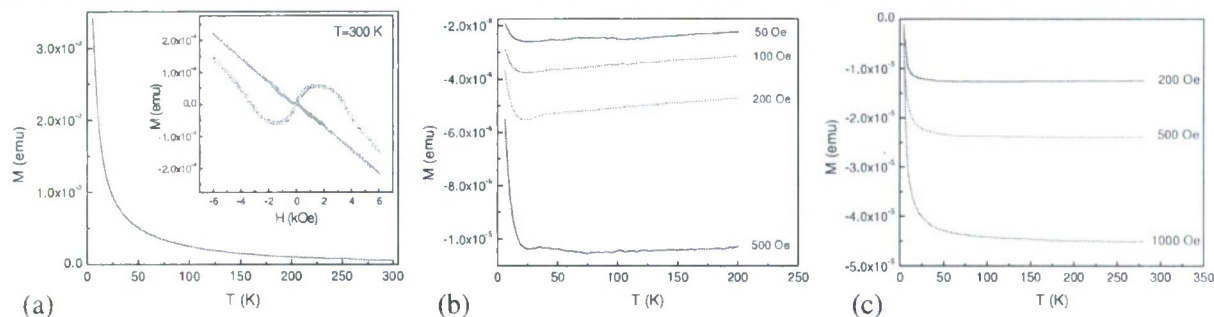


Figure 4. (a) Temperature dependence of magnetization of as-prepared bulk WO_3 measured in an external magnetic field of 1000 Oe. Inset shows the field dependence of magnetization at $T = 300$ K for as-prepared sample (open blue circles) and sintered in air for 4 h at 500°C (solid red circles). (b) Temperature dependence of magnetization of carbon inverse opal bar ($2 \times 2 \times 10 \text{ mm}^3$). (c) Magnetization behavior of WO_{3-y} infiltrated into pores of carbon inverse opal (without alkali ions).

shoulder). The paramagnetic contribution from tungsten trioxide is further enhanced at $T < 25$ K by a contribution from the carbon inverse opal. Despite the diamagnetic nature of the bulk carbon (graphite) with magnetic susceptibility of $\chi = -1.6 \times 10^{-5}$ the nanostructured carbon inverse opal with thickness of shells about 10 nm (with the negative curvature in voids, see figure 2), exhibit strong paramagnetic behavior at $T < 25$ K.

For comparison the ZFC and FC measurements at $H = 500$ Oe with subtracted paramagnetic contribution are shown in figure 3(b). The FC magnetization measurement shows a less pronounced onset at the same temperature ($T_c = 125 \pm 1$ K) buried in the Curie–Weiss slope of paramagnetic magnetization. Such a behavior is typical for type II superconductivity when the flux expulsion from the sample body (Meissner effect) works differently for ZFC and FC measurements. Unlike YBCO systems the coincidence of ZFC and FC onsets was also observed in $\text{Na}_x\text{CoO}_2 \cdot y\text{H}_2\text{O}$ [22, 23] with very similar layered structures. In contrast to the cuprate SCs, or recently discovered oxypnictides, $(\text{Ln}, \text{Sm})\text{FeAsO}_{1-x}\text{F}_x$ [24, 25], the parent compound WO_3 is nonmagnetic, indicating that, when WO_3 is doped with Na, antiferromagnetism could not be responsible for either the magnetization hysteresis or the high T_c . It is obvious that the Meissner effect in our samples is incomplete because of low filling factor and presence of the matrix. We believe that the obtained behavior of magnetization belongs to the superconducting phase of $\text{Na}_x\text{WO}_{3-y}$. It is unlikely that some magnetic phase transition or structural changes can give similar behavior.

The position of the magnetization curve highly depends on the amount of residual and physically absorbed water in $\text{Na}_x\text{WO}_{3-y} + n\text{H}_2\text{O}$. The positive magnetization background in the compound with high water concentration (see figure 3(c)) is switched to negative magnetization after sintering at 150°C in vacuum or argon. During the temperature scanning by the ZFC route the normal state shoulder does not change and is very stable from day to day. However, for the superconductive state we observed the shift of magnetization curve to the lower flux repulsion for the second ZFC cycle conducted on the next day.

As was mentioned above the magnetization onset observed in all experiments is low and the Meissner effect in our samples is incomplete because of low filling factor and the presence of a matrix. Inset to figure 3(c) shows the typical SEM image of sol–gel infiltrated $\text{Na}_x\text{WO}_{3-y}$ in the host matrix. The host matrix occupies about 19.1% of total volume (see figure 2). Randomly distributed $\text{Na}_x\text{WO}_{3-y}$ islands does not form interconnected network. The white color of $\text{Na}_x\text{WO}_{3-y}$ islands under an electron beam suggests high metallic conductivity of bronze. Actually more than 50% of pores can be filled with functional material to leave interconnected channels for the electrolyte for further intercalation. However, so far it is a major challenge to get a bulk interconnected structure with an infiltration factor greater than 25% [26].

From the temperature and field scanning measurements it was possible to find the temperature dependence of the critical field and plot the superconducting/normal phase diagram (figure 3(d)). The upper critical field H_{c2} was determined from the shift of the magnetization onset (T_c) at increased applied fields. At magnetic fields above 2500 Oe the magnetization step is totally quenched. The cross section of the critical field approximation line with abscissa axis gives the highest temperature of the superconducting phase transition of 128 ± 0.5 K.

Figure 4 shows contributions in magnetization of both the constituent, WO_{3-y} , and the carbon inverse opal. The magnetic properties of sol–gel–derived WO_{3-y} is quite unusual and will be described in detail elsewhere. The sample sintered at $T > 150^\circ\text{C}$ in air shows a diamagnetic background with magnetic susceptibility of -2.7×10^{-5} . However, as-prepared bulk (nanoporous) samples (dried in air) show paramagnetic properties ($dM/dF > 0$) with positive slope of the magnetization curve at low magnetic fields ($H < 1000$ Oe), which further turns to the negative magnetization ($dM/dF < 0$) at high fields (see inset to figure 4(a)). Here we have to mention that all the samples studied in this work (if it is not specified) were sintered after intercalation in argon atmosphere or in vacuum at least, at $T = 150^\circ\text{C}$ and had a diamagnetic response. At moderate temperatures the diamagnetism is dominant in a carbon inverse opal filled

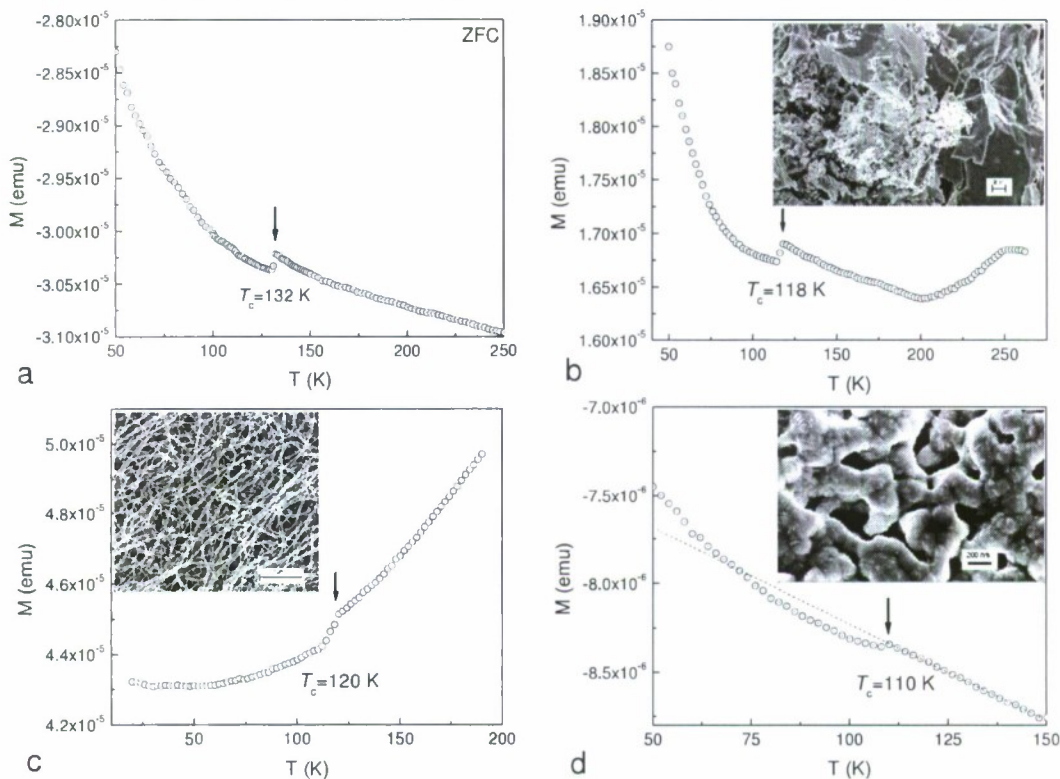


Figure 5. Temperature dependence of ZFC magnetization: (a) $\text{Li}_x\text{WO}_{3-y}$ in carbon inverse opal, ($H = 500$ Oe); (b) pressed pellet of $\text{Na}_x\text{WO}_{3-y}$ with embedded MWCNT network, ($H = 200$ Oe). Inset shows an SEM image of cleaved surface of $\text{Na}_x\text{WO}_{3-y}$ pellet. (c) $\text{Na}_x\text{WO}_{3-y}$ inserted into MWCNT bucky-paper (see inset), ($H = 500$ Oe); (d) $\text{Na}_x\text{WO}_{3-y}$ inserted into platinum sponge (see inset), ($H = 500$ Oe).

with WO_{3-y} . This results in the shift of the magnetization curve at increased magnetic fields down to negative values in accordance with the superimposed susceptibilities of carbon and WO_{3-y} .

Thus the temperature dependences of magnetization measured separately in bulk WO_{3-y} , pure carbon inverse opal matrix, carbon inverse opal infiltrated with WO_{3-y} and the last one just dipped in electrolyte without charging, do not show any diamagnetic onset in the studied range of temperatures, $2 \text{ K} < T < 250 \text{ K}$. However, we observed an intensive fluctuation in magnetization below $T \sim 110\text{--}130 \text{ K}$ for as-prepared bulk WO_{3-y} having high concentration of residual and physically absorbed water. Perhaps absorbed water or chemically bounded protons play an important role in the formation of the superconducting phase.

Intercalation of Li^+ ions with lower atomic mass can shift the phonon spectra of tungsten bronze to higher frequencies and change the phase transition temperature. Indeed the $\text{Li}_x\text{WO}_{3-y}$ compound prepared under the same conditions exhibit SC onset at $T_c = 132 \text{ K}$, (figure 5(a)). The observed magnetization jump is much lower than for $\text{Na}_x\text{WO}_{3-y}$. Is it the change in the phonon spectra rather than the structural changes that enhance the phonon–electron coupling? It is not clear so far and needs additional investigation. $\text{K}_x\text{WO}_{3-y}$ in the carbon inverse opal matrix does not show any onset in $M(T)$. Migration mobility of K^+ ions in a WO_3 structure is

much lower than Li^+ or Na^+ and can limit the concentration of intercalated ions. On the other hand, the large ionic radius of K^+ ions can severely deform the layered perovskite structure.

Numerous experiments with electrochemical intercalation reveal a wide range of concentrations within which the phenomenon exists, $x = 0.2\text{--}0.5$. However, the inserted amount of charge does not substantially change the T_c for a given ion. But the change of host matrix does. To separate the obtained behavior in magnetization from effects known in intercalated graphite below we test samples without a matrix or with a non-carbon matrix.

For comparison purposes, let us first test the bulk $\text{Na}_x\text{WO}_{3-y}$ compound. The WO_3 powder precipitated from sol–gel solution can be pressed into a pellet shape for further intercalation. However, the extremely low electronic conductivity of tungsten oxide does not allow electrochemical insertion of some noticeable amount of alkali ions. To increase the initial electronic conductivity of WO_3 I mixed the sol–gel powder with $\sim 0.1\text{--}0.2\%$ MWCNT grown by the CVD method. Due to the extremely high aspect ratio of carbon nanotubes (> 1000) the percolation threshold in well-dispersed mixtures is very low [27]. The round shaped pellet pressed

¹ Even a low concentration of alkaline ions ($x < 0.01$) drastically (3–5 orders) changes the electronic conductivity of WO_3 and after some level of conductivity the sample can be intercalated without any supporting substrates.

at room temperature under 0.5 GPa (5 T cm^{-2}) was charged with Na^+ ions at 5 mA current for 10^4 s. After intercalation in aqueous 1 M NaCl solution the sample was dried in air for 30 min and then sintered at 150°C for 4 h in argon atmosphere. The ZFC measurement shows sharp onset of magnetization at 118 K at an applied field of 200 Oe (figure 5(b)). A small hysteresis loop obtained for the field dependence of magnetization at $-2000 \text{ Oe} < H < +2000 \text{ Oe}$ perhaps indicating the presence of residual ferromagnetic inclusions in MWCNT. Apparently, a very small jump of magnetization at $T_c = 118 \text{ K}$ is a consequence of low intercalation rate. The SEM image (inset to figure 5(b)) shows that the ceramic structure of the pellet contains micron-sized dense grains covered with an MWCNT network. Weak interconnection of large size dense grains is a main obstacle for effective intercalation. EDS analysis shows that WO_{3-y} is weakly reduced with $3-y$, typically in the order of 2.95.

Another promising candidate for conducting high surface area host material is an MWCNT bucky-paper. High surface area, flexibility and chemical stability of carbon make MWCNT paper a perfect substrate material for sol-gel infiltration and further intercalation. The magnetization curve shown in figure 5(c) is floated towards the positive magnetic moment due to ferromagnetic inclusions in the host matrix. The onset shifted to $T_c = 120 \text{ K}$.

Platinum sponge fabricated by pressing Pt nanopowder is another alternative to carbon-based matrices. Bulk platinum metal is a paramagnetic material with magnetic susceptibility of 26×10^{-5} . However, infiltrated $\text{Na}_x\text{WO}_{3-y}$ shifted the magnetization curve towards negative values. The hardly noticeable onset in figure 5(d) at $T_c = 110 \text{ K}$ is buried in a steep increase of magnetization at low temperatures.

3.2. Resistivity measurements

The resistivity measurement in ceramic type $\text{Na}_x\text{WO}_{3-y}$ (without conductive matrix) reveals a sharp jump of resistance at $T_c = 125 \text{ K}$ (figure 6). The strong semiconductor response in the whole temperature range suggests that only a small part of WO_{3-y} was intercalated and turned into metallic $\text{Na}_x\text{WO}_{3-y}$. Similar to [11] the resistance does not go down to zero but just decreased twice and continues to increase at lower temperatures. Apparently the localized SC, due to the low intercalation level of ceramic type $\text{Na}_x\text{WO}_{3-y}$, does not create an interconnected network through the whole structure.

The failure to observe complete (zero) resistance onset for $\text{Na}_x\text{WO}_{3-y}$ in carbon inverse opal we explain first of all by the lack of through conductivity of any materials (even gold and platinum) infiltrated by sol-gel or CVD method. Another drawback of carbon type matrices is a high metallic conductivity of substrate that shunts the conductivity of the studied material. To avoid these obstacles we reduced the pyrolysis temperature of phenolic-resin-infiltrated opal to 600°C (see figure 2(c)). Despite this measure which substantially increased the sample resistance from several $\text{m}\Omega$ to $\sim 10 \Omega$, it does not help so far because of the low infiltration factor.

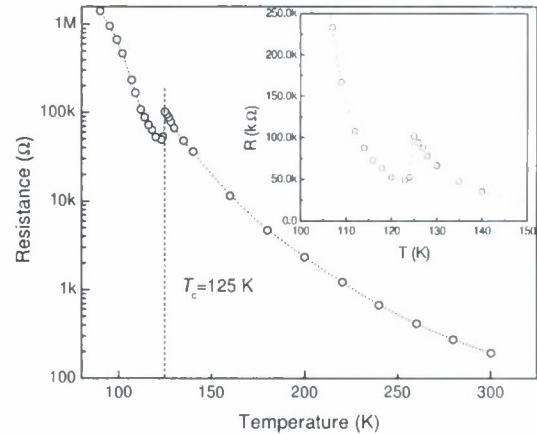


Figure 6. Temperature dependence of the four-probe measured resistance in ceramic-based $\text{Na}_{0.3}\text{WO}_{2.95}$. The applied AC ($f = 1 \text{ kHz}$) current was $1 \mu\text{A}$. Inset shows the resistance behaviour near T_c .

4. Discussion

The observed onset in ZFC and FC magnetization together with the temperature behavior of resistance points towards the possible existence of a superconducting phase in the studied samples. First of all I want to stress here that the structure of bulk single crystals of WO_3 with metallic sodium islands (surface composition of $\text{Na}_{0.05}\text{WO}_3$) described in [11] is different from our bulk intercalated $\text{Na}_x\text{WO}_{3-y}$. EDS analysis of cleft edges of $\text{Na}_x\text{WO}_{3-y}$ in carbon inverse opal (figure 3(c)) and ceramic type $\text{Na}_x\text{WO}_{3-y}$ (figure 5(b)) shows a deep volume intercalation of WO_{3-y} with sodium ions. The observed concentration of intercalated sodium ions is decreased from the edges to center of the specimen: $x > 0.5$ close to the sample surface and $x < 0.2$ in the central part. The average concentration is around $x = 0.3 \pm 0.05$. At the same time, the obtained structures are mostly amorphous and only the samples sintered at $T > 300^\circ\text{C}$ in argon atmosphere had polycrystalline structure. The samples sintered in argon environment had a deficiency of oxygen, with $3-y$ typically of the order of 2.7–2.8. These samples intercalated with low current ($I = 0.1 \text{ mA}$ for 2000 s, estimated $x < 0.1$) sometimes revealed an additional step in magnetization at $T_c = 91 \pm 1 \text{ K}$.

The smooth behavior of magnetization for WO_3 , inverted carbon opal matrix and WO_3 infiltrated in a nanoporous matrix (some samples of WO_3 infiltrated in the nanoporous matrix were just dipped in 1 M NaCl electrolyte without intercalation and dried following the same procedures as for intercalated samples) shown in figure 4 strongly confirms that the obtained anomalies are intrinsic properties of intercalated WO_3 .

Extensive studies of structural changes in tungsten trioxide [21] and tungsten bronzes ($(\text{H}, \text{Li}, \text{Na}, \text{K}, \text{Rb}, \text{Cs})_x\text{WO}_3$) [28] did not find any additional phases at low temperatures, $9 \times 10^{-5} \text{ K} < T < 250 \text{ K}$, except $\epsilon\text{-WO}_3$. The temperature dependences of the lattice parameters are smooth except the cell parameter in the a direction which saturates below $T = 125 \text{ K}$ and exhibits some fluctuations [21], perhaps displaying the lattice instability due to the soft phonon mode. Our

magnetic measurements on sol-gel derived WO_3 and magnetic studies of bulk single-crystal $\epsilon\text{-WO}_{3-y}$ [21] suggest that no superconductivity exists in pristine WO_{3-y} in the low temperature phase. However, all studied samples exhibit a small step or bump at the transition point between the δ -phase and the ϵ -phase at ~ 250 K.

Obtained tungsten bronzes have dark blue color with metallic conductivity. The optical absorption of W^{5+} in WO_3 shows the signature of small polaron formation at low temperatures. At low sodium doping levels, the sodium tungsten bronzes are nonmetallic with localized W^{5+} and W^{6+} ions and show polaronic states. The polaron state in WO_3 is caused by a strong interaction between the optical longitudinal phonons and electrons. Slightly reduced samples with doped Na^+ demonstrate bipolarons which are split into pairs of polarons [9]. Probably the strong intercalation of WO_3 with alkaline ions brings the compound to the compositionally induced nonmetal-to-metal transition with bipolaron current carriers [29]. The direct evidence of polaron formation from temperature dependence of photoemission spectra [30] and formation of bipolarons in weakly reduced WO_{3-y} with $3-y$ typically of the order of 2.95 suggest the bipolaron mechanism of a Bose-Einstein condensation of trapped electron pairs in doped WO_{3-y} .

On the other hand, the amorphous structure of sol-gel prepared WO_3 indicates a dominant role of soft phonon modes for enhancement of phonon-electron coupling λ , which is contradictory with short-range interactions, such as polarons, or bipolarons. Moreover, the requirement of large λ is favorable to lattice instabilities which should not be stabilized by this mechanism [31].

In summary, I observed pronounced anomalies in temperature dependencies of magnetization and resistance in wet (sol-gel) fabricated $\text{Na}_x\text{WO}_{3-y}$ at 125 K and $\text{Li}_x\text{WO}_{3-y}$ at 132 K. The behavior of ZFC and FC magnetization measurements and jump of resistance in all studied nanostructured tungsten bronzes ($\text{Li}_x\text{WO}_{3-y}$ and $\text{Na}_x\text{WO}_{3-y}$) suggest the possibility of localized non-percolated superconductivity. The mechanism of anomalies and optimal structures leading to the percolated superconductivity, as well as behavior of other related parameters, are under study.

Acknowledgments

The author is grateful to R H Baughman and A A Zakhidov for continuous support and interest in the work. I also wish to express my gratitude to Joseph V Mantese for valuable suggestions and useful discussions. The financial support of the SPRING Program (Strategic Partnership for Research in Nanotechnology Program, Texas) via the AFOSR program is highly appreciated.

References

- [1] Grangvist C G 1995 *Handbook of Inorganic Electrochromic Materials* (Amsterdam: Elsevier)
- [2] Monk P M S, Mortimer R J and Rosscinsky D R 1995 *Electrochromism: Fundamentals and Applications* (Weinheim: VCH)

- [3] Sahle W and Nygren M 1983 Electrical conductivity and high resolution electron microscopy studies of WO_{3-x} crystals with $0 < x < 0.28$ *J. Solid State Chem.* **48** 154
- [4] Nanba T and Yasui I 1989 X-ray diffraction study of microstructure of amorphous tungsten trioxide films prepared by electron beam vacuum evaporation *J. Solid State Chem.* **83** 304
- [5] Gardner W R and Danielson G C 1954 Electrical resistivity and hall coefficient of sodium tungsten bronze *Phys. Rev.* **93** 46
- [6] Ginsburg V L 1989 On two-dimensional superconductor *Phys. Scr. T* **27** 76
- [7] Bogomolov V N 2007 Superconductivity as Bose-Einstein condensation in high- and low-temperature superconductors (diluted metals) *Tech. Phys. Lett.* **33** 14
- [8] Raub Ch J, Sweedler A R, Jensen M A, Broadston S and Matthias B T 1964 Superconductivity of sodium tungsten bronzes *Phys. Rev. Lett.* **13** 746
- [9] Aird A and Salje E K H 1998 Sheet superconductivity in twin walls: experimental evidence of WO_{3-x} *J. Phys.: Condens. Matter* **10** L377
- [10] Aird A, Domeneghetti M C, Mazzi F, Tazzoli V and Salje E K H 1998 Sheet superconductivity in WO_{3-x} : crystal structure of the tetragonal matrix *J. Phys.: Condens. Matter* **10** L569
- [11] Reich S and Tsabba Y 1999 Possible nucleation of a 2D superconducting phase on WO_3 single crystals surface doped with Na^+ *Eur. Phys. J. B* **9** 1
- [12] Reich S *et al* 2000 Localized high- T_c superconductivity on the surface of Na-doped WO_3 *J. Supercond. Incorporating Novel Magn.* **13** 855
- [13] Shengelaya A, Reich S, Tsabba Y and Muller K A 1999 Electron spin resonance and magnetic susceptibility suggest superconductivity in Na doped WO_3 samples *Eur. Phys. J. B* **12** 13
- [14] Bardeen J, Cooper L N and Schrieffer J R 1957 Theory of superconductivity *Phys. Rev.* **106** 1175
- [15] Aliev A E and Park C 2000 Development of WO_3 thin films using nanosecale silicon particles *Japan. J. Appl. Phys.* **39** 3572
- [16] Aliev A E and Shin H W 2002 Nanostructured materials for electrochromic devices *Solid State Ion.* **154/155** 425
- [17] Zakhidov A A *et al* 1998 Carbon structures with three-dimensional periodicity at optical wavelengths *Science* **282** 897
- [18] Aliev A E, Zakhidov A A, Baughman R H and Yablonoitch E 2006 Chalcogenide inverted opal photonic crystal as infrared pigments *Int. J. Nanosci.* **5** 157
- [19] Aliev A E, Lee S B, Baughman R H and Zakhidov A A 2007 Thermal properties of carbon inverse opal photonic crystals *J. Lumin.* **125** 11
- [20] Aliev A E, Lee S B, Zakhidov A A and Baughman R H 2007 Superconductivity in Pb inverse opal *Physica C* **453** 15
- [21] Salje E K H *et al* 1997 Crystal structure and paramagnetic behavior of $\epsilon\text{-WO}_{3-x}$ *J. Phys.: Condens. Matter* **9** 6563
- [22] Takada K *et al* 2003 Superconductivity in two-dimensional CoO_2 layers *Nature* **422** 53
- [23] Jin R, Sales B C, Khalifah P and Mandrus D 2003 Observation of bulk superconductivity in $\text{Na}_x\text{CoO}_2 \cdot y\text{H}_2\text{O}$ and $\text{Na}_x\text{CoO}_2 \cdot y\text{D}_2\text{O}$ powder and single crystals *Phys. Rev. Lett.* **91** 217001
- [24] Kamihara Y *et al* 2008 Iron-based layered superconductor $\text{LaO}_{1-x}\text{F}_x\text{FeAs}$ ($x = 0.05-0.12$) with $T_c = 26$ K *J. Am. Chem. Soc.* **130** 3296
- [25] Chen X, Wu H T, Wu G, Liu R H, Chen H and Fang D F 2008 Superconductivity at 43 K in $\text{SmFeAsO}_{1-x}\text{F}_x$ *Nature* **453** 761
- [26] Aliev A E, Akhmedzhanova N Kh, Krivorotov V F, Kholmanov I N and Fridman A A 2003 Thermal conductivity of opal filled with a LiIO_3 *Solid State Phys.* **45** 61

- [27] Benoit J-M *et al* 2001 Transport properties of PMMA-carbon nanotubes composites *Synth. Met.* **121** 1215
- [28] Ingham B, Hendy S C, Chong S V and Tallon J L 2005 Density-functional studies of tungsten trioxide, tungsten bronzes, and related systems *Phys. Rev. B* **72** 075109
- [29] Edwards P P 2000 Polarons, bipolarons, and possible high- T_c superconductivity in metal-ammonia solutions *J. Supercond. Incorporating Novel Magn.* **13** 933
- [30] Raj S *et al* 2006 Angle-resolved photoemission spectroscopy of the insulating Na_xWO_3 : Anderson localization, polaron formation, and remnant Fermi surface *Phys. Rev. Lett.* **96** 147603
- [31] Jarlborg T 2000 Tuning of the electronic screening and electron-phonon coupling in doped SrTiO_3 and WO_3 *Phys. Rev. B* **61** 9887



Superconductivity in Pb inverse opal

Ali E. Aliev ^{*}, Sergey B. Lee, Anvar A. Zakhidov, Ray H. Baughman

NanoTech Institute, University of Texas at Dallas, Richardson, TX 75083-0688, United States

Received 27 December 2005; received in revised form 14 October 2006; accepted 8 December 2006

Available online 22 December 2006

Abstract

Type-II superconducting behavior was observed in highly periodic three-dimensional lead inverse opal prepared by infiltration of melted Pb in blue ($D = 160$ nm), green ($D = 220$ nm) and red ($D = 300$ nm) opals and followed by the extraction of the SiO_2 spheres by chemical etching. The onset of a broad phase transition ($\Delta T = 0.3$ K) was shifted from $T_c = 7.196$ K for bulk Pb to $T_c = 7.325$ K. The upper critical field H_{c2} (3150 Oe) measured from high-field hysteresis loops exceeds the critical field for bulk lead (803 Oe) fourfold. Two well resolved peaks observed in the hysteresis loops were ascribed to flux penetration into the cylindrical void space that can be found in inverse opal structure and into the periodic structure of Pb nanoparticles. The red inverse opal shows pronounced oscillations of magnetic moment in the mixed state at low temperatures, $T < 5.5$ K. The shape of these oscillations and their temperature dependence indicate on phase transitions in the fluxoid state of Pb core. The weak matching effect in the field dependence of magneto-resistivity measurement at low magnetic fields and $T > 0.9T_c$ has been observed for all of the samples studied. The magnetic field periodicity of resistivity modulation is in good agreement with the lattice parameter of the inverse opal structure. We attribute the failure to observe pronounced modulation in magneto-resistive measurement to difficulties in the precision orientation of the sample along the magnetic field.

© 2006 Elsevier B.V. All rights reserved.

Keywords: Superconducting network; Mesoscopics; Vortex; Magnetization; Fluxoid state

1. Introduction

Recent progress in the fabrication of mesoscopic structures such as quantum dots, nanowires, nanoparticles and 3D nanostructures has stimulated many of experimental and theoretical studies directed at tailoring the quantum properties of functional materials. In this paper, we present the superconducting properties of highly periodic 3D nanostructures of pure metallic lead. By modifying the sample topology of this well known superconducting material we pursued two objectives: to create a type-II superconductor with extra large surface-to-volume ratio and tailored pinning potentials, and to study the commensurability effects of 3D array of void channels with the vortex lattice. The ordered array of defects composed of either simple point

or extended pinning centers on planar surface and their effect on the vortex lattice are vigorously studied [1–4]. However, the studies of 3D mesoscopic structures remain a challenge because of fabrication difficulties and lack of theoretical approaches [5,6]. Additionally, 3D nanostructure requires very high precision of sample orientation to study the interactions of the vortex lattice with 3D sublattices. Even for macroscopic samples this problem arose in Little and Parks experiments [7] and was mentioned by De Gennes [8].

On the other hand 3D nanostructures can be considered as assemblies of small metallic particles with weak electrical connections. The superconductivity of small metallic particles (SMP) with dimensions less than the superconducting coherence length has been the object of many theoretical [9–13] and experimental works [14–18]. There are a lot of controversial predictions and experimental observations of the superconducting transition temperature T_c of SMP as a function of the radius R . For weak- and

^{*} Corresponding author. Tel.: +1 972 883 6543; fax: +1 972 883 6529.
E-mail address: ali.aliev@utdallas.edu (A.E. Aliev).

intermediate-coupling SMP superconductors like Al [14,15] and In [15,16] it was found that $T_c(R)$ is a smooth increasing function of R^{-1} down to the smallest values of R investigated. On the other hand, no clear evidence of $T_c(R)$ was found for Sn, In, and Pb [17,18]. Moreover, for thin lead films [19,20], for sponge-like structure of Pb particle films [21], or for lead particles embedded in porous glass [22], T_c is lowered, corresponding to the mean particle diameter or film thickness. Actually, at very small particle size ($d_{pb} < 5$ nm) according to Anderson [23] for grains so small that the electron level spacing is larger than the bulk gap Δ , superconductivity should not exist, since such a grain would not have even one condensed level.

Most previous measurements of superconductivity in ensembles of small particles were done for electrically isolated particles [14] or in disordered networks of weakly connected particles [22,24]. The electrical isolation of these particles from one another was carried out to eliminate excess diamagnetism caused by supercurrents flowing between the particles.

Recently we have developed a templating technology for the fabrication of fcc metallic photonic crystals and inverse photonic lattices with variable lattice parameters, particle size, and particle interaction [25–27]. The highly periodic 3D metallic structure provides a new opportunity to investigate the peculiarities of the superconducting transition in various lattice directions and more precisely examine the validity of theoretical predictions for size, temperature and field dependence of the measured susceptibility near and away from T_c . The extended surface of inverse opals should effect flux trapping and irreversible magnetization properties.

Generally the term “small particles” depends on which physical properties are under scrutiny. For superconductivity of small metallic particles the critical size is $R^3 = \lambda_L^2(0) \cdot \xi_0$, where $\lambda_L(0)$ is the London penetration depth, and ξ_0 is the coherence length in BCS theory. For bulk lead, $\xi_0 = 83$ nm and $\lambda_L(0) = 37$ nm, thus $R = 63$ nm. The close-packed face-centered-cubic (fcc) lattice of lead inverse opal

involves octahedral and tetrahedral shaped particles which can be represented as spheres ($r_o = 0.414 \cdot r$, $r_t = 0.225 \cdot r$) connected through cylindrical channels ($r_{ch} = 0.155 \cdot r$), where r is a radius of the silica voids. Among the chosen samples all characteristic sizes are close to or below the critical size R (see Table I).

We report here two phenomena related to confinement of lead into the pore structure of fcc opal. The first phenomenon leads to particle size dependent superconductivity and the second to modulation of the magnetization moment by phase transitions in the vortex state. The very precise orientation of the [111] direction of the fcc lattice along the applied magnetic field leads to the commensurability effect at temperatures close to T_c .

2. Experimental part

The porous silica opals used as templates, infiltration and metallic inverse opal fabrication processes are as described in details by Zakhidov et al. [25–27]. Briefly, the highly periodic three-dimensional synthetic opal structures obtained by sedimentation of the monodispersed aqueous colloid of SiO_2 spheres was infiltrated with melted Pb (99.999%, Aldrich) by a typical preparation process: a rectangular piece of opal ($5 \times 5 \times 5$ mm³) was surrounded with metallic powder that tightly filled a 9 mm diameter stainless steel cylinder. Using a piston-cylinder pressure cell, this cylinder was held at 400 °C under a pressure of 5 kbar for 30 min. During this time, the melt entirely filled the void space available through the interconnections. The pressure was lowered during solidification and then was completely released. An embedded opal sample was then carefully cut from the surrounding pure metal using a jeweler’s saw and placed in a 1% diluted aqueous HF solution for 12 h for soft etching of the SiO_2 spheres [28]. The metallic lead is not affected by the silica etching. The necks connecting the silica spheres (resulting from the sintering process) act as channels through which the etchant flows. The remaining three-dimensional periodic structure is a lead inverse opal (also referred to as 3D lead opal replica). Fig. 1 shows the SEM image of the cleaved edge of (111) plane of the lead inverse opal with void sphere diameter 300 nm. Almost 100% filling was achieved.

The magnetic properties of Pb inverse opals were studied using a Quantum Design magnetic properties measurement system (MPMS) based on superconducting quantum interference device magnetometer (SQUID) with a 7 T superconducting solenoid. The field-cooled (FC) and zero-field-cooled (ZFC) magnetization measurements were performed in the temperature range of 1.8 K–50 K with precise stabilization of each targeted temperature (0.01 K) for 60 s followed by 4 scans (4 cm) and data averaging. For the DC magnetic measurements three identical samples of the inverse opal with different void sphere diameters were prepared: blue ($D = 160$ nm), green ($D = 220$ nm) and red ($D = 300$ nm). The size and the shape of the sample were determined by crystalline domains usually oriented

Table I
Sample parameters

Parameter	Red inverse opal	Green inverse opal	Blue inverse opal	Bulk lead, Pb
Octahedral radius, nm	62.1	45.54	33.14	
Tetrahedral radius, nm	33.7	24.75	18.0	
Radius of channel, nm	23.2	17.05	12.4	
Weight, mg	24.8	24.8	24.8	211.88
Volume, mm ³	8.5	8.5	8.5	18.75
Density, g/cm ³	2.92	2.92	2.92	11.3

The radius of the lead infiltrated octahedral pores represented by big spheres in right inset to Fig. 1 is $r_o = R(\sqrt{2} - 1)$, the radius of tetrahedral pores is $r_t = R(\sqrt{3}/2 - 1)$, and the radius of the interconnected channels is $r_{ch} = R(2/\sqrt{3} - 1)$. R is the radius of void spheres remaining after chemical extraction of silica spheres of direct opal.

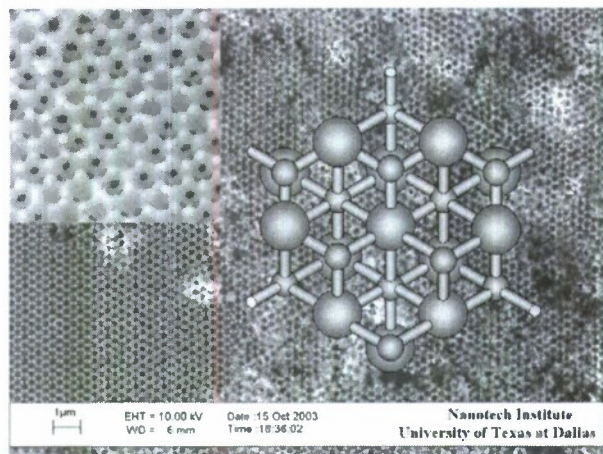


Fig. 1. SEM image of the (111) plane of the cleaved edge of a lead inverse opal. Highly crystalline structure is observable throughout the whole region. The top left corner inset shows a detail where the three channels in each void sphere connect with the spheres in the underlying layer. The void sphere diameter is 300 nm, which correspond to a red opal. The right inset shows a schematic representation of a lead inverse opal: octahedral and tetrahedral pores of fcc opal infiltrated with Pb can be represented as spheres ($r_o = 0.414 \cdot r$, $r_t = 0.225 \cdot r$) connected through cylindrical channels ($r_{ch} = 0.155 \cdot r$).

along the opal growth direction. To reduce the demagnetization effect the single crystal samples of $a \times b \times c = 2 \times 2.45 \times 2.45 \text{ mm}^3$ cut out from the infiltrated opal were ground and polished to an ellipsoid shape before etching. The average volumes of the samples measured by hydrostatic weighting were 8.5 mm^3 . The measured density of the lead inverse opal, $\rho = 2.92 \text{ g/cm}^3$ is close to the theoretical value, $\rho = 2.94 \text{ g/cm}^3$, calculated using the total volume of voids for fcc structure, $V = 26\%$, and density of bulk lead, $\rho_o = 11.3 \text{ g/cm}^3$ [29]. Details of studied samples are presented in Table 1.

The applied external field H was parallel to the [111] direction of the fcc structure of the inverse opal (perpendicular to the surface of SEM image, Fig. 1). To compare the superconducting behavior of the inverse lead opal to that of bulk lead, we first calibrated our system using a Quantum Design provided Palladium reference sample (Pd-837, $P = 0.2382 \text{ g}$, cylinder with a base radius of 1.5 mm and a height of 3 mm) and then by using a bulk lead sample (1.5 mm in diameter and 5 mm long lead cylinder (99.999%, Aldrich)).

The magnetoresistive properties of Pb infiltrated opals were studied using Quantum Design physical properties measurement system (PPMS) equipped with a 9 T superconducting solenoid. For four-probe magneto-resistance measurements samples with a rectangular shape ($0.5 \times 2 \times 5 \text{ mm}^3$) and polished surface were mounted on the Torque Magnetometer platform board assembly. The copper contact springs of the platform board assembly give very reliable electrical contact to the nanostructured lead in all the studied temperature range compared to silver colloid (Dotite D-550, Fujikura Kasei Co., Ltd.), silver paste (Plus, SPI Supplies), epoxy silver paste (H20E, Epoxy

Technology), or conductive carbon paint (Colloidal graphite, Structure Probe, Inc.). Four-probe resistivity measurements were carried out using an AC user bridge board (PPMS Resistivity option) at a frequency of 1000 Hz and a current range of $10 \mu\text{A}$ –5 mA. For precision sample orientation in a magnetic field with resolution 0.0045° we used PPMS horizontal rotator.

The scanning electron microscope (SEM) micrographs were taken with a LEO 1530 VP equipped with energy dispersive spectrometer (EDS) for X-ray microanalysis. The elemental analysis of the red inverse opal revealed some residue of silicon (6 at.%) and oxygen (8 at.%), indicating on the lack of access of the etchant to some central parts of sample.

3. Results and discussion

3.1. Magnetization

The temperature dependence of the ZFC magnetization obtained for the red inverse opal and the bulk lead samples in the magnetic field of 5 Oe are shown in Fig. 2. All three inverse opals (red, green, blue) have very similar temperature behavior with negligible alterations in the onset temperature and significant broadening of T_c . Taking into account the ellipsoid shape of the sample, the obtained value of magnetization was divided by the demagnetization factor of 0.6. For the particle sizes used in our experiments ($D = 160, 220, 300 \text{ nm}$) the shift of the superconducting transition temperature compared to each other is negligibly small and below measurement accuracy. It is important to note that even for the large variation of particle sizes used in [14] for Al powder, T_c was found to vary smoothly but not very rapidly with particle size – being 1.156 K for

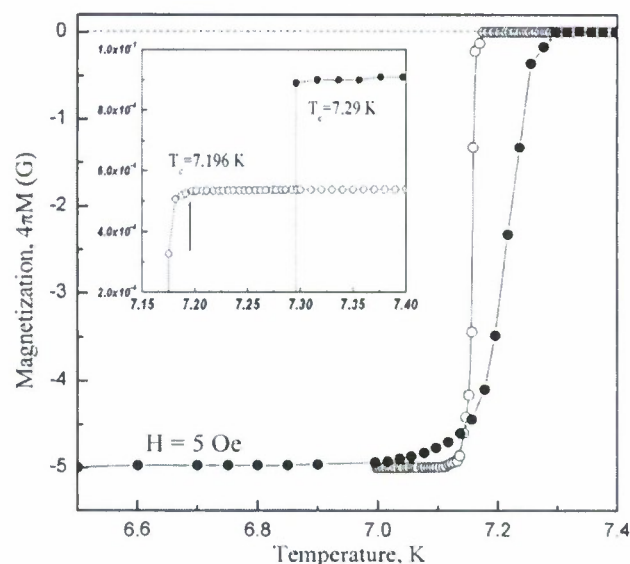


Fig. 2. The temperature dependences of ZFC magnetization for red Pb inverse opal (solid circles) and bulk Pb (open circles) at 5 Oe. The inset shows the ZFC magnetization near T_c .

$R_{c1} = 400$ nm and 1.228 K for $R_{c1} = 25.5$ nm. However, the shift of T_c for Pb inverse opal against bulk Pb is appreciable, $\Delta T = 0.1$ K. There is a sharp onset of diamagnetism near 7.29 K with complete diamagnetic shielding at lower temperatures, ($-4\pi M = H$). The field-cooled (FC) magnetization measurement shows a less pronounced onset (0.1 G) at the same temperature. The paramagnetic background above T_c is little raised for inverse opal, perhaps due to paramagnetic impurities (non-stoichiometric oxides) on the extended surface.

Fig. 3 shows the temperature dependence of ZFC magnetization for various applied fields. For the field above 1000 Oe diamagnetic shielding is incomplete up to the lowest measured temperatures. Increasing the applied magnetic field above 200 Oe gives a substantial shift in the transition temperature. The sharp diamagnetic shielding is changed to a smooth declining curve. The saturation point of the magnetization curve above the superconducting onset rises at higher applied fields.

To obtain the upper and lower critical fields, H_{c2} and H_{c1} , between which the flux expulsion and Meissner effect is incomplete, we measured the hysteresis loops for wide temperature and magnetic field ranges. Fig. 4 shows the series of field scanning measurements of the magnetic moment in the red Pb inverse opal at various fixed temperatures. The complete high field hysteresis loop at 5.0 K is shown in the inset. The fish-tale hysteresis loop which is typical for hard type-II superconductors has a different shape from those obtained in [24] for opals infiltrated with Ga. The irreversibility of magnetization versus applied field is the characteristic of the flux trapping in type-II superconductors. The irreversibility disappears at low applied fields, ($H < 200$ Oe). Fig. 5 shows the development of the hysteresis loops at 3 K. At fields below 200 Oe one can see the linear dependence typical for diamagnetic materials. The further increase of the field broadens the line and gives rise

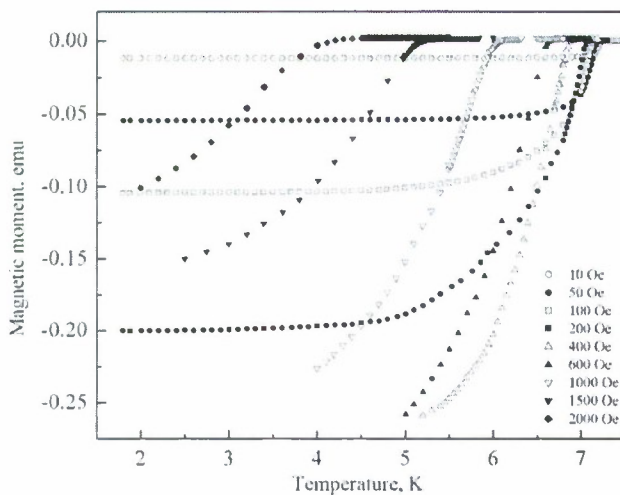


Fig. 3. Temperature dependence of ZFC magnetization for red Pb inverse opal at various applied fields. The stronger the applied field the higher the pedestal above the superconducting onset.

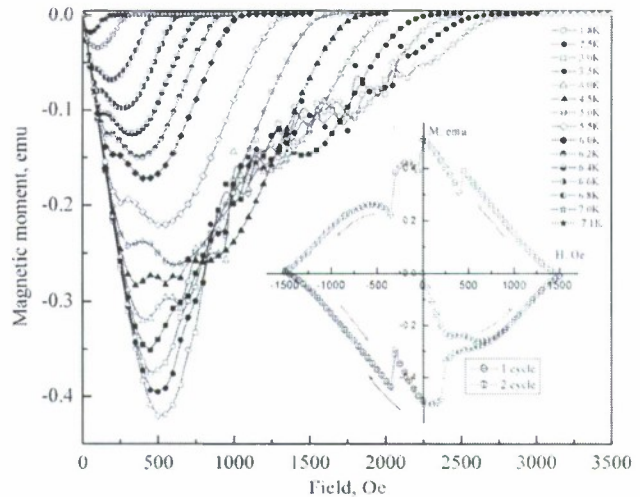


Fig. 4. Magnetization vs. external field for different temperatures. Two well-distinguished peaks have different behavior. Below 5 K the second maximum is dampened by the oscillation of the magnetic moment which disappears again at higher fields, $H > 0.8H_{c2}$. The inset shows the whole hysteresis loop for temperature 5 K. The symmetrical jump in the magnetization in the hysteresis loops is completely reproducible. The back scanning of the magnetic field (2nd cycle) shows the complete reproduction of the first cycle jump.

to loops. However, the hysteresis loops have negative magnetic susceptibility up to the field H_{max} at a given temperature, when there appeared a maximum in the $M(H)$ plot. The region from maximum to the total suppression of the superconductivity is characterized by flux trapping (dotted line in Fig. 5). Note that for the low filling factor, the magnetic behavior was almost reversible.

Two well resolved maxima are seen in the $M(H)$ dependencies in Fig. 4. The nature of this splitting is perhaps based on the peculiarities of the opal structure. Here we

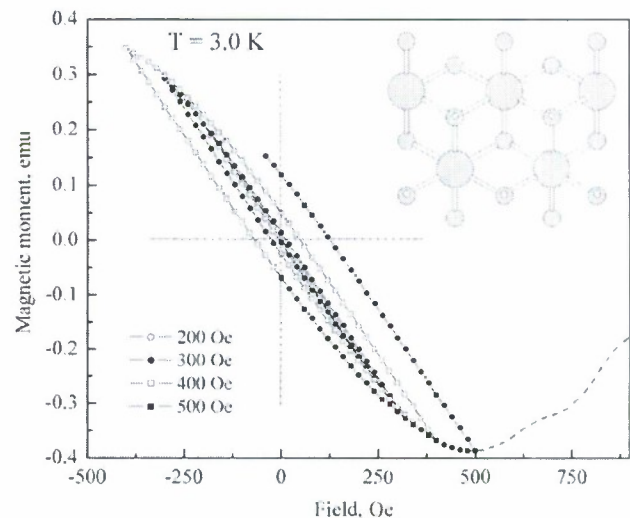


Fig. 5. Low-field hysteresis loop at the temperature 3 K. The loop closes at the lower critical field H_{c1} . Inset shows the fcc structure of opal pores infiltrated with Pb. Large spheres are octahedral pores ($r_{oct} = 62.1$ nm), and small spheres are tetrahedral pores ($r_{tetr} = 33.7$ nm).

propose that the flux penetration into the sample first occurs in the empty voids left by SiO₂ spheres. Thus, we believe that the first maximum, $H_{\text{Max}1}$ (left in Fig. 4) belongs to the flux penetration into the empty space of the sample. However, the Pb particles in the octahedral and tetrahedral pores interconnected through the channels are still superconductive. Further increase of the applied magnetic field leads to a gradual increase of the magnetization up to the next maximum at $H_{\text{Max}2}$. At $H_{\text{Max}2}$ the magnetic flux reaches the core of the Pb spheres. The smaller the particle size of the studied samples, the higher the position of the second maximum in the magnetic field in Fig. 4. The decrease in the particle size of the small insulated lead particles studied in [30] has linearly shifted the $M(H)$ maximum to higher fields, $(h/H_c = 1 + 7.62 \cdot 10^{-6} \cdot R^{-1})$ and increased the width of the magnetization peak. It is important to note that the magnetization in the metallic inverse opals has a very high anisotropy [31]. The particle density and the level of interconnections in the opal-like structures strongly depend on direction.

From the temperature and field scanning measurements it was possible to find the temperature dependence of the critical fields and plot the superconducting/normal phase diagram (Fig. 6). The upper critical field H_{c2} was determined from the shift of the onset T_c of superconductivity with increasing applied field (Fig. 3) and from high-field hysteresis loops, as the field at which a tangent to the rising branch of magnetization intersect the axis of the abscissa (Fig. 4). The lower critical field, H_{c1} , was found as the field at which the slope of the magnetization curve versus applied field started to decrease. Another characteristic

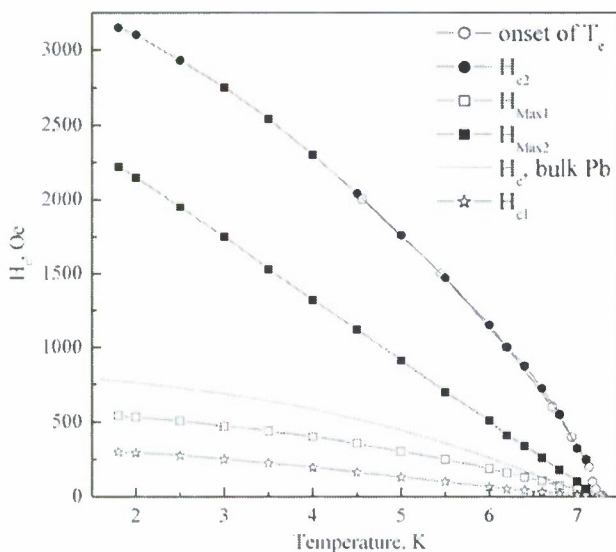


Fig. 6. Temperature dependence of various characteristic fields for lead inverse opal. The open circles are $T_c(H)$, the temperature of the onset of superconductivity. The solid circles correspond to the upper critical field H_{c2} at which a tangent to the rising branch of magnetization intersect the $H = 0$ line. $H_{\text{Max}1}$ and $H_{\text{Max}2}$ correspond to the two maximum on $M(H)$. H_{c1} is the lower critical field. The solid line is the $H_c(T)$ for the bulk Pb sample [32].

curve is the H_{FP} ; that is, when the flux penetration has reached the center of the sample. It was found from Fig. 4 as the field, when the magnetization reached a maximum. Due to the splitting of the maximum two curves have been plotted, Max 1 and Max 2, respectively. For comparison, the critical field curve (solid line) for bulk Pb [32] is presented as well. The region between H_{c1} and H_{c2} corresponds to the mixed state when vortex lines penetrate into the sample. Both curves show nonlinear behavior rather than linear as predicted by Ginzburg–Landau (GL) theory [33,34]. The GL theory provides exact results only near the transition. However, for temperatures below $0.9T_c$ strong pinning centers have a different temperature dependence which could be better described by the empirical relation $H_{c2}(T) = H_{c2}(0) [1 - (T/T_c)^2]$ [8]. Surprisingly the temperature dependence of Max 2 has a linear dependence while Max 1 behavior is close to $H_{c1}(T)$.

The two critical fields are related

$$H_{c2}(T) = \sqrt{2K(T)} \cdot H_{c1}(T), \quad (1)$$

where $K = \lambda/\xi = 2\sqrt{2}(e/\hbar c)H_c(T)\lambda^2(T) = \Phi_0/2\pi\xi(T)^2 = K_0/(1 + T^2/T_c^2)$ is the Ginzburg–Landau parameter, and $\Phi_0 = ch/2e = 20.75 \text{ Oe}/\mu\text{m}^2$ is a quantum of magnetic flux.

To determine the superconducting coherence length $\xi(0)$, we extrapolated the $T_c(H)$ curve to 0 K and using Eq. (1) we found $K = 2.73$ and thus, $\xi(0) = 38 \text{ nm}$. This value of the coherence length is significantly smaller than the BCS coherence length for Pb, $\xi_0 = 83 \text{ nm}$ [32], indicating that our structure is in the dirty limit. Using the dirty limit ($l < \xi_0$) expression $\xi(0) = 0.865(\xi_0 l)^{1/2}$ we determined the electron mean free path to be $l = 15.2 \text{ nm}$. The penetration depth $\lambda(0) = 57 \text{ nm}$ was derived from the dirty limit expression $\lambda(0) = 0.66\lambda_L(\xi_0/l)^{1/2}$, using $\lambda_L = 37 \text{ nm}$ as the London penetration depth. Now taking into account the dirty limit parameters the GL parameter, $K = \lambda(0)/l = 3.77$ we can conclude that the nanostructured lead inverse opal is a type-II superconductor. The obtained characteristic size of Cooper pairs (coherence length ξ) is comparable to the octahedral and tetrahedral Pb spheres in the studied inverse opals (see Table 1). This means that spatial confinement essentially changes the superconducting state and we can refer studied structures to mesoscopic superconductors.

Due to the extremely high surface area of inverted opal, the magnetization curve in Fig. 4 shows a pronounced long tail above H_{c2} extended up to the total depression of superconductivity at $H_{c3} = 1.695 \cdot H_{c2}$ [35]. However at temperatures below $0.9T_c$ this ratio is changed to $H_{c3} \approx 1.3 \cdot H_{c2}$. The highest critical field H_{c3} was found as the field at which the magnetization curve approaches zero.

For bulk superconductors the distinction between type-I ($K < 1/\sqrt{2}$) and type-II ($K > 1/\sqrt{2}$) superconductivity is completely determined by GL parameter $K = \lambda/\xi$. For mesoscopic superconductors type-I superconductors behave like type-II or even show some mixed behavior depending on the size of the system and therefore K is no longer the only determining parameter characterizing the vortex state of the system.

The intensive study of oscillations of the magnetic moment observed at temperatures below 5 K and high magnetic field ($H_{\max} < H < 0.8H_{c2}$) reveals some periodicity in the structure of the magnetization steps, which resemble in appearance the phase transitions in the fluxoid state recently observed in submicron individual superconducting disks and cylinders [36,37] and intensively discussed in theory [2,3]. Here we report some phase transition features in fluxoid states of the 3D mesoscopic superconductor. Fig. 7 shows a series of well-resolved phase transitions between fluxoid states in the red Pb inverse opal obtained at $T = 2$ K. Unlike the magnetization steps observed in thin superconducting films with regular pinning arrays [1], the observed steps are not equidistantly located on the H scale. When the magnetic field is swept in 10 Oe steps, the magnetization evolves along one of the fluxoid curves until it reaches its end and jumps to the next curve belonging to another fluxoid state. Then, the process repeats itself, exactly like in mesoscopic superconducting disk [37]. At the highest magnetic fields, the superconducting phase is totally repelled from the Pb spheres into the necks interconnecting the octahedral and tetrahedral Pb spheres. Each transition is completely reproducible – the back scanning of magnetic field in inset to Fig. 4 (5 K) shows the complete reproduction of the first cycle jump. On the other hand the complete hysteresis loop in the inset also shows clear evidence of vortex trapping, which is not the case for the mesoscopic disks [36]. The inverse opal structure for this consideration could be depicted as a periodic array of lead cylinders aligned along the magnetic field. Theoretical modeling of mesoscopic cylinder was carried out in [3]. With increasing magnetic field there is a continuous penetration of the magnetic field at the edge of the lead spheres, which leads to a smaller than linear increase of M vs. H . The number of transitions depends on the temperature and the lattice parameters of the inverse opal. Green and

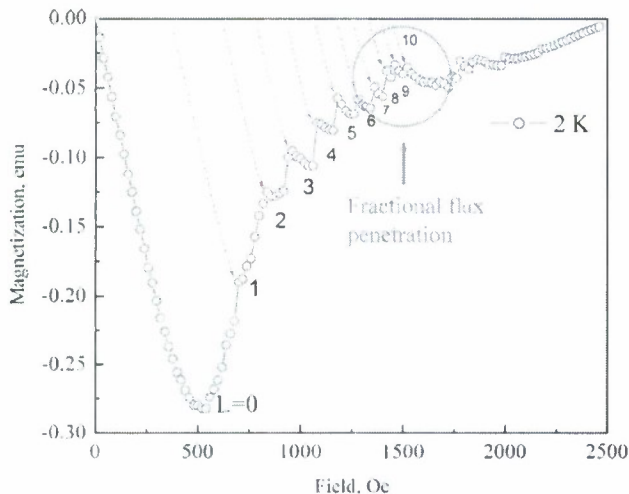


Fig. 7. Field dependence of magnetization in red Pb inverse opal at $T = 2$ K. Dashed curves show the imaginary multi-vortex states and arrows show the transition point in the giant vortex states as steps on magnetization curve.

blue inverse opals did not show well distinguished phase transitions. Green inverse opal exhibits some small instabilities in the mixed state but they are very irregular. Blue Pb inverse opal has smooth curvature in the mixed state.

Fig. 8 shows an extended view of the appearance of new fluxoid phases when the temperature is gradually decreased. For low magnetic fields ($H < 200$ Oe) we have a linear $M-H$ relation which is typical for an ideal diamagnet. With increasing magnetic field there is a continuous penetration of the magnetic field at the edge of the sample, which leads to a smaller than linear increase of M vs. H . This effect is enhanced by the demagnetization effect, which leads to an enhanced magnetic field at the edge of the sample. At temperatures above 5 K the energetically more favorable is the ground state ($L = 0$) with continuous penetration the vortices into the sample and liner decrease of M above $H_{\text{Max}2}$. We believe that the magnetic flux first penetrates into the empty channels running through whole structure. The flux penetration into empty spaces is complete at the first maximum. The rise in M continues with the further increase of magnetic field but with lower slope as shown by dashed line in Fig. 8, $T = 5$ K. At lower temperature (4.5 K) the increase of the magnetic field increases the energy of superconductor up to the point where it is energetically more favorable to transit to the $L = 1$ state [2], which correspond to one flux unit through the sphere (see inset in Fig. 8). In other words, at low temperatures the vortex diameter becomes comparable with the Pb sphere diameter:

$$r_{\text{vortex}} = \xi(T) = \xi(0)/(|1 - T/T_{c0}|)^{1/2} \quad (2)$$

where the $\xi(0)$ is the coherence length at zero temperature and T_{c0} is the critical temperature at zero magnetic field. The further decrease of the temperature decreases the vortex diameter and allows to enter the next flux unit into the Pb sphere at 4 K. By counting the number of jumps in the $M(H)$ curve it is possible to count the vorticity of the sample and therefore the number of vortices inside the spheres. At very low temperatures and high magnetic fields even fractional flux can penetrate into the spheres (see Fig. 7).

3.2. Magnetoresistance

It is obvious that periodically ordered magnetic particles at the proper temperature and magnetic field should exhibit commensurability effect. SQUID used in DC mode for magnetization measurement did not allow us to align the bulk 3D nanostructure with enough precision to achieve matching effect. Moreover for magnetization measurements we aspired to increase the length of the sample along the magnetic field to get lower demagnetization. Here we investigate the effect of the bulk magnetic periodic structure of a lead infiltrated opal on a periodic pinning by magneto-resistivity measurements. PPMS equipped with a 9 T superconducting solenoid and horizontal rotator with resolution 0.0045° can be utilized for any shape of samples

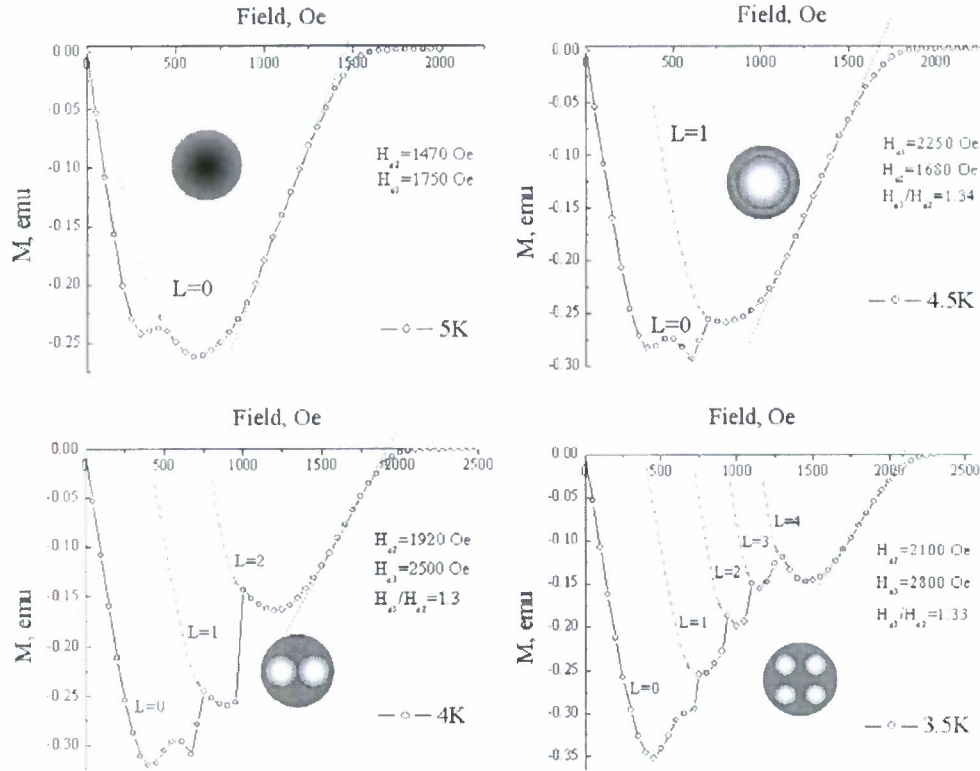


Fig. 8. The consequent appearance of new fluxoid phases in Pb inverse opal when the temperature is gradually decreased. Dashed lines indicate the multi-vortex fluxoid states and arrows indicate the transition point to the thermodynamically stable giant vortex state.

with precision orientation to the magnetic field. In terms of superconducting properties the infiltrated opal is equivalent to the inverse opal. For further experimentation we needed to attach electrodes, so the lead infiltrated opal was chosen as a mechanically stronger material than the lead inverse opal. Moreover the extraction of SiO₂ spheres can lead to partial oxidization of the inner surface of the lead inverse opal. Oxidization first would affect the interconnected channels (see inset in Fig. 5), which create the current flow path.

Fig. 9 shows the temperature dependence of the resistance of a lead inverse opal at zero magnetic field. Current was applied along the [111] direction. The sharp superconducting transition at the temperature of 7.325 K was found for the lowest applied current, 10 μA, using a resistance criterion of 50% of normal state resistance.

T_c is shifted to lower temperatures at higher applied currents. DC and AC applied currents give the same resistance. Fig. 10 shows the shift of the transition temperature versus applied current. The theoretical upper limit for the critical current is determined by depairing critical current I_c^{GL}(T) at which the superconducting Cooper pairs are destroyed [35].

$$I_c^{GL}(T) = \frac{4}{3\sqrt{6}} \frac{H_c(T)}{\lambda(T)} \quad (3)$$

In terms of this quantity, the critical current obtained from magnetic and transport measurements are much different.

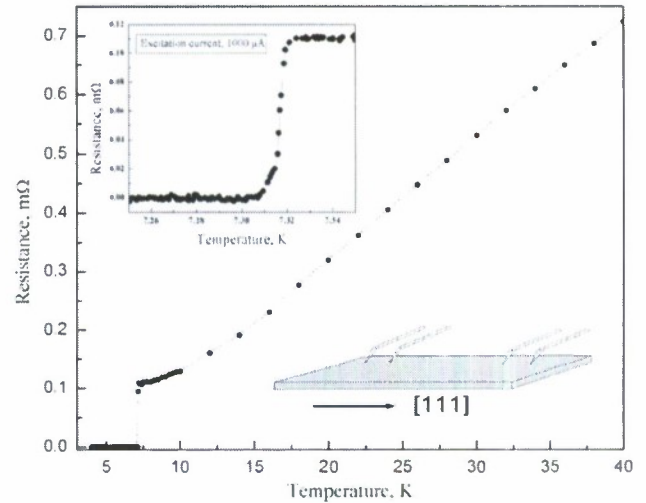


Fig. 9. Resistive transition of the red Pb infiltrated opal measured at H=0 Oe and I=1 mA (f=1 kHz) in the [111] direction. The top-left inset shows a precision measurement of the superconducting transition with temperature steps of 1 mK. The bottom-right inset shows the measurement arrangement of the sample showing 4 copper contact springs on the polished surface. The four probes are aligned along the [111] direction.

Eq. (3) gives I_c(0) = 7.7 × 10⁹ A/m² whereas the highest excitation current in transport measurements does not exceed I_c(0) = 2 × 10⁴ A/m². The reason for different values of the critical currents in the magnetic and transport measurements could be the difference in critical fields for Pb

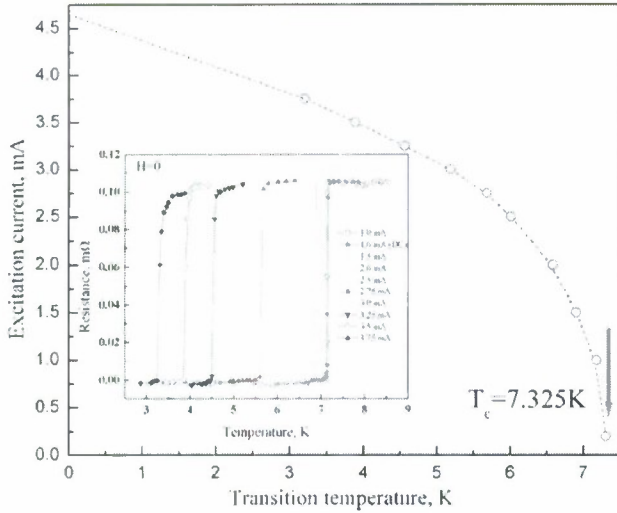


Fig. 10. Temperature shift of resistive transition determined from the onset of resistive transitions versus excitation currents measured at $f = 1$ kHz in $[111]$ direction. Inset shows the experimental procedure: the AC resistance was measured at fixed excitation current by scanning the temperature down and up at $H = 0$. DC (solid circles for 1 mA) and AC (open circles for 1 mA) measurements show the same results.

spheres and channels. The different size of these structural elements gives rise to different critical fields: $H(T) = \sqrt{32} \cdot H_c \cdot (\lambda(T)/r)$ (for r see Table 1). However this estimation gives only one order of magnitude difference in the critical current. Low excitation currents in Fig. 10 are apparently caused by the small cross section of point contacts between the copper springs and nanostructure.

At proper orientation of the sample (magnetic field strictly perpendicular to the (111) plane) the Pb infiltrated opal could be considered as a regular array of cylindrical holes (SiO_2 spheres) located around the octahedral and tetrahedral pores infiltrated with Pb. The infiltrated opal has

exhibited Little-Parks oscillations only after many attempts to precisely orient the (111) plane perpendicular to the magnetic field using the PPMS horizontal rotator option with resolution of 0.0045° . Fig. 11 shows the oscillation of the resistance as a function of the field for a thin plate of a green Pb infiltrated opal single crystal. Thicker samples did not exhibit resistance modulation because of a failure of complete crystallinity and alignment difficulties. Commensurability results in the resistance minimum at $H_1 = 380$ Oe and $H_2 = 760$ Oe. These minima correspond to the first and second flux quant in the cylindrical hole with a diameter of 250 nm. The equidistant magnetic field intervals ΔH_n coincide with the lattice parameter of the inverse opal, $\Delta H_n = n \cdot \Phi_0 / A$, where, Φ_0 was introduced above as the quantum of magnetic flux, $A = \pi \cdot r^2$ is the surface area of the pinning centers, r is the radius of the circulating current, and n is an integer. Taking into account the current pathway in the (111) plane of the fcc structure (see inset in Fig. 5) we can write, $\Delta H_1 = (2/\sqrt{3})\Phi_0 / D^2 = 380$ Oe. At a closer view between the minima, two additional anomalies were found related to the stable vortex configuration in the periodic pinning potential. These types of rational matching anomalies in [1] were explained by the stabilization of a flux lattice with a larger unit cell than the lattice unit of pinning centers. The red Pb infiltrated opal exhibits the same but less pronounced anomalies with magnetic field intervals $\Delta H_1 = 265$ Oe. Usually red opals have much better crystalline quality. However for magnetoresistance measurements we could not adjust the red Pb infiltrated opal sample properly to demonstrate the same rational matching anomalies as for green opal sample. Only weak anomalies matched to 300 nm periodicity have been obtained.

In conclusion, we studied the superconductivity of lead inverse opals. The superconducting onset temperature

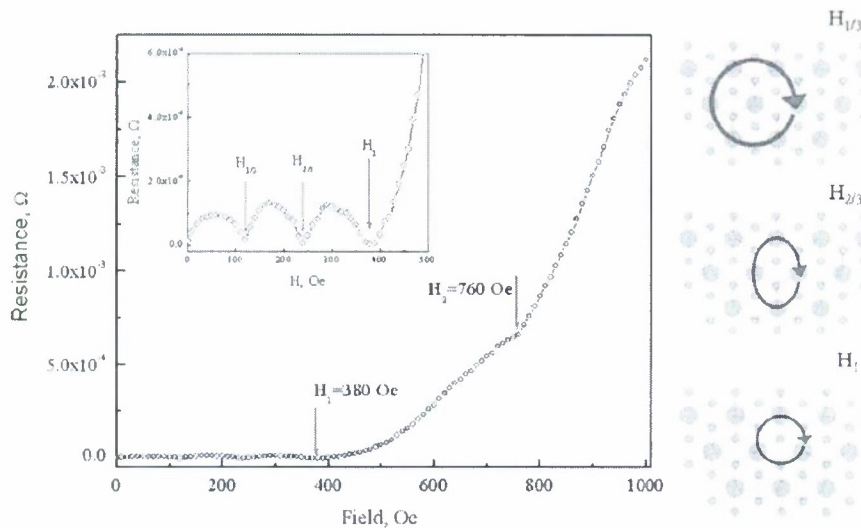


Fig. 11. Field dependence of the resistance at $T = 7.10$ K and $I = 0.5$ mA, for a green Pb infiltrated opal. The magnetic field was applied along the $[111]$ direction and the current was applied along the $[001]$ direction. The sample thickness is $124 \mu\text{m}$. The inset shows the magnification of the low-resistance part of resistance modulation and the sketch of possible vortex structure.

shifted from $T_c = 7.196$ K for bulk Pb to $T_c = 7.325$ K and the phase transition region broadened up to $\Delta T = 0.3$ K. The upper critical field H_{c2} (3150 Oe) measured from high-field hysteresis loops exceeds the critical field for bulk lead (803 Oe) fourfold. Two well distinguished peaks in the hysteresis loops are an exhibition of flux penetration into the empty holes made by silica spheres and then, at higher magnetic field, into the periodic structure of the Pb nanoparticles.

In the mixed state at relatively low temperatures, $T < 5.5$ K the Pb inverse opal reveals a series of magnetization anomalies resembling the magnetization response of phase transitions in the fluxoid states. This was achievable only for red opal with a particle size comparable to or bigger than the coherence length, $r \geq \xi$. The number of fluxoid transitions increases at lower temperatures (ξ is decreased). The transition between fluxoid states is reversible without measurable hysteresis. The present study suggests the fluxoid phase transition as a possible mechanism of our observation in array of Pb nanoparticles and do not exclude other explanations.

SQUID used in DC mode for magnetization measurement did not allow us to align the bulk 3D nanostructure with good precision to achieve the matching effect. Moreover for magnetization measurements we aspired to increase the length of the sample along the magnetic field to get lower demagnetization.

On the other hand PPMS equipped with a 9 T superconducting solenoid and horizontal rotator with resolution 0.0045° used for magnetoresistance measurements can be utilized for any shape samples with precise orientation to the magnetic field. By very precise alignment of the [111] direction of Pb infiltrated opal along the external magnetic field and using high crystallinity sample the magneto-resistive study at temperatures close to T_c reveals a commensurability effect in the periodic structure of lead infiltrated in SiO_2 opal.

Acknowledgements

The authors would like to thank Professor I.A. Lukyanchuk, Professor E.V. Charnaya and Dr. Y. Obukhov for helpful and informative discussions whilst preparing this manuscript. This work was supported by Texas Scientific Research Program "Strategic Partnership for Research in Nanotechnology" of the Air Force Office.

References

- [1] V.V. Moshchalkov, V. Bruyndocx, L. Van Look, M.J. Van Bael, Quantization and confinement phenomena in nanostructured superconductors, in: Handbook of Nanostructured Materials and Nanotechnology, Academic Press, 2000.
- [2] F.M. Peeters, B.J. Baelus, Vortex structure in mesoscopic superconductors, in: J.F. Annett, S. Kruchinin (Eds.), New trends in superconductivity, NATO Science Series, vol. 67, Kluwer Academic Publisher, 2002.
- [3] W.V. Pogosov, A.L. Rakhmanov, E.A. Shapoval, Physica C 356 (2001) 225.
- [4] A. Hoffmann, P. Prieto, I.K. Schuller, Phys. Rev. B 61 (2000) 6958.
- [5] A. Lungu, M. Bleiweiss, J. Amirzadeh, S. Saygi, A. Dimofte, M. Yin, Z. Iqbal, T. Datta, Physica C 349 (2001) 1.
- [6] A.A. Zhukov, E.T. Filby, M.A. Ghanem, P.N. Barlett, P.A.J. de Groot, Physica C 404 (2004) 455.
- [7] (a) W.A. Little, R.D. Parks, Phys. Rev. Lett. 9 (9) (1962); (b) W.A. Little, R.D. Parks, Phys. Rev. 133 (1964) A97.
- [8] P.G. de Gennes, Superconductivity of Metals and Alloys, New York, 1966.
- [9] V.L. Ginzburg, Fiz. Tverd. Tela 2 (1959) 2031.
- [10] P.W. Anderson, Phys. Rev. Lett. 3 (1959) 325.
- [11] A.A. Abrikosov, L.P. Gor'kov, Zh. Eksp. Teor. Fiz. 39 (1961) 480.
- [12] J.P. Hurault, K. Maki, M.R. Beal-Monod, Phys. Rev. B 3 (1971) 762.
- [13] B. Muhlshlegel, D.J. Scalapino, R. Denton, Phys. Rev. B 6 (1972) 1767.
- [14] R.A. Buhrman, W.P. Halperin, Phys. Rev. Lett. 30 (1973) 692.
- [15] S. Matsuto, H. Sugiura, S. Noguchi, J. Low Temp. Phys. 15 (1974) 481.
- [16] C.R. Leavens, E.W. Fenton, Phys. Rev. B 24 (1981) 5086, and references therein.
- [17] Y.G. Morozov, V.I. Petinov, Solid State Commun. 40 (1981) 991.
- [18] H. Akoh, A. Tasaki, J. Phys. Soc. Jpn. 42 (1997) 791.
- [19] M. Strongin, R.S. Thompson, O.F. Kammerer, J.E. Crow, Phys. Rev. B 1 (1970) 1078.
- [20] R.C. Dynes, J.P. Garno, J.M. Rowell, Phys. Rev. Lett. 40 (1978) 479.
- [21] W. Krahl, F. Baumann, Surf. Sci. 106 (1981) 373.
- [22] V. Novotny, P.P.M. Meincke, Phys. Rev. B 8 (1973) 4186.
- [23] P.W. Anderson, J. Phys. Chem. Solids 11 (1959) 26.
- [24] E.V. Charnaya, C. Tien, K.J. Lin, C.S. Wur, Yu.A. Kumzerov, Geometries. Phys. Rev. B 58 (1998) 467.
- [25] A.A. Zakhidov, R.H. Baughman, Z. Iqbal, C. Cui, I. Khayrullin, S.O. Dantas, J. Marti, V.G. Ralchenko, Science 282 (1998) 897.
- [26] K. Yoshino, H. Kajii, Y. Kawagishi, M. Ozaki, A.A. Zakhidov, R.H. Baughman, Jpn. J. Appl. Phys. 38 (1999) 4926.
- [27] A.E. Aliev, A.A. Zakhidov, R.H. Baughman, E. Yablonovith, Int. J. Nanosci. 5 (2006) 157.
- [28] F. Meseguer, A. Blanco, H. Miguez, F. Garcia-Santamaria, M. Ibisate, C. Lopez, A: Physicochem. Eng. Aspects 202 (2002) 281.
- [29] D.R. Lide (Editor-in-Chief), CRC Handbook of Chemistry and Physics, 82nd ed., CRC Press LLC, 2001.
- [30] S. Reich, G. Leitus, R. Popovitz-Biro, M. Schechter, Phys. Rev. Lett. 91 (2003) 147001.
- [31] L. Xu, L.D. Tung, L. Spinu, A.A. Zakhidov, R.H. Baughman, J.B. Wiley, Adv. Mater. 15 (2003) 1562.
- [32] C. Kittel, Introduction to Solid State Physics, Sixth ed., J. Wiley & Sons Inc., New York, 1986.
- [33] V.L. Ginzburg, L.D. Landau, Zh. Eksp. Teor. Fiz. 20 (1950) 1064.
- [34] J.R. Birchak, J. Phys. Chem. Solids 28 (1967) 917.
- [35] M. Tinkham, Introduction to Superconductivity, McGraw-Hill, New York, 1975.
- [36] A.K. Geim, I.V. Grigorieva, S.V. Dubonos, J.G.S. Lok, J.C. Maan, A.E. Filippov, F.M. Peeters, Nature 390 (1997) 259.
- [37] A.K. Geim, S.V. Dubonos, J.J. Palacios, I.V. Grigorieva, M. Henini, J.J. Schermer, Phys. Rev. Lett. 85 (7) (2000) 1528.



**Strong, Transparent, Multifunctional, Carbon
Nanotube Sheets**

Mei Zhang, *et al.*
Science **309**, 1215 (2005);
DOI: 10.1126/science.1115311

***The following resources related to this article are available online at
www.sciencemag.org (this information is current as of October 30, 2008):***

Updated information and services, including high-resolution figures, can be found in the online version of this article at:
<http://www.sciencemag.org/cgi/content/full/309/5738/1215>

Supporting Online Material can be found at:
<http://www.sciencemag.org/cgi/content/full/309/5738/1215/DC1>

This article **cites 30 articles**, 7 of which can be accessed for free:
<http://www.sciencemag.org/cgi/content/full/309/5738/1215#otherarticles>

This article has been **cited by 144 article(s)** on the ISI Web of Science.

This article has been **cited by 3 articles** hosted by HighWire Press; see:
<http://www.sciencemag.org/cgi/content/full/309/5738/1215#otherarticles>

This article appears in the following **subject collections**:
Materials Science
http://www.sciencemag.org/cgi/collection/mat_sci

Information about obtaining **reprints** of this article or about obtaining **permission to reproduce this article** in whole or in part can be found at:
<http://www.sciencemag.org/about/permissions.dtl>

would have to dissociate from the DNA binding domain. Second, a processive 360° rotation, or multiples thereof, has been observed when using an artificial substrate that has two sites mismatching in the central region of site I (27) and is not easily explained by the domain swap model.

The synaptosome. How this synaptic tetramer bound to site I can be accommodated in a model of the complete synaptosome is unclear. The relationship between the synaptic tetramer seen here and the rest of the complex must differ from the model proposed earlier (14) for a synaptosome structure. That model was constructed making the assumption, on the basis of extensive genetic data (12, 13), that dimers bound to sites I, II, and III of the same *res* site DNA are making the 2, 3' interactions. There are, however, no biochemical or structural data to support the proposed interaction between the three resolvase dimers bound to each of the two *res* sites. Our attempts to model the synaptic complex at site I (via the R and R' subunits) onto the structure of a site II and III complex presumed in earlier models (10, 14) show that, although the dimensions roughly match, an interaction of the 2, 3' type cannot be made.

We presume that resolvase dimers bound to sites II and III of two *res* sites contained in negatively supercoiled DNA are able to synapse and present two dimers bound to site I DNAs in such a manner that they promote the

formation of the synaptic complex structure seen here. Perhaps two resolvase dimers are bound to the two site I DNAs in a presynaptic conformation initially and then form a synaptic tetramer at site I, facilitated by an increase in the local concentration and orientation of site I dimers by the rest of the synaptosome. However, the transition to the tetramer structure by the site I-bound resolvase subunits is likely accompanied by release of their 2,3' interactions with the rest of the complex. It will doubtless be necessary to determine the structure of the whole synaptosome in order to understand how resolvase dimers bound to sites II and III promote synapsis at site I.

References and Notes

1. N. Craig, R. Craigie, M. Gellert, A. Lambowitz, Eds., *Mobile DNA II* [American Society for Microbiology (ASM), Washington, DC, 2002].
2. N. D. F. Grindley, in (1), p. 272.
3. R. R. Reed, N. D. F. Grindley, *Cell* 25, 721 (1981).
4. G. F. Hatfull, N. D. F. Grindley, *Proc. Natl. Acad. Sci. U.S.A.* 83, 5429 (1986).
5. S. A. Wasserman, J. M. Dungan, N. R. Cozzarelli, *Science* 229, 171 (1985).
6. W. M. Stark, D. J. Sherratt, M. R. Boocock, *Cell* 58, 779 (1989).
7. W. M. Stark, M. R. Boocock, *J. Mol. Biol.* 239, 25 (1994).
8. M. R. Sanderson et al., *Cell* 63, 1323 (1990).
9. P. A. Rice, T. A. Steitz, *Structure* 2, 371 (1994).
10. P. A. Rice, T. A. Steitz, *EMBO J.* 13, 1514 (1994).
11. W. Yang, T. A. Steitz, *Cell* 82, 193 (1995).
12. R. E. Hughes, G. F. Hatfull, P. Rice, T. A. Steitz, N. D. F. Grindley, *Cell* 63, 1331 (1990).

13. L. L. Murley, N. D. F. Grindley, *Cell* 95, 553 (1998).
14. G. J. Sarkis et al., *Mol. Cell* 8, 623 (2001).
15. F. Guo, D. N. Gopaul, G. D. van Duyn, *Nature* 389, 40 (1997).
16. A. E. Leschziner, N. D. F. Grindley, *Mol. Cell* 12, 775 (2003).
17. M. Nollmann, J. He, O. Byron, W. M. Stark, *Mol. Cell* 16, 127 (2004).
18. P. H. Arnold, D. G. Blake, N. D. F. Grindley, M. R. Boocock, W. M. Stark, *EMBO J.* 18, 1407 (1999).
19. Protein Data Bank codes are 1ZR2 and 1ZR4.
20. Materials and methods are available as supporting materials on Science Online.
21. Single-letter abbreviations for the amino acid residues are as follows: A, Ala; C, Cys; D, Asp; E, Glu; G, Gly; K, Lys; L, Leu; Q, Gln; R, Arg; S, Ser; V, Val; and Y, Tyr.
22. W. G. Krebs, M. Gerstein, *Nucleic Acids Res.* 28, 1665 (2000).
23. Y. Chen, P. A. Rice, *Annu. Rev. Biophys. Biomol. Struct.* 32, 135 (2003).
24. A. T. Brünger et al., *Acta Crystallogr. D* 54, 905 (1998).
25. G. Dhar, E. R. Sanders, R. C. Johnson, *Cell* 119, 33 (2004).
26. C. Chothia, J. Janin, *Nature* 256, 705 (1975).
27. M. J. Mdlwraith, M. R. Boocock, W. M. Stark, *J. Mol. Biol.* 266, 108 (1997).
28. This research was supported by NIH grants GM28470 to N.D.F.G. and GM57510 to T.A.S. The structures and the structure factors have been deposited in the Protein Data Bank under codes 1ZR2 and 1ZR4.

Supporting Online Material

www.sciencemag.org/cgi/content/full/1112064/DC1

SOM Text

Figs. S1 to S4

References and Notes

Movies S1 to S4

9 March 2005; accepted 15 June 2005

Published online 30 June 2005;

10.1126/science.1112064

Include this information when citing this paper.

REPORTS

Strong, Transparent, Multifunctional, Carbon Nanotube Sheets

Mei Zhang,¹ Shaoli Fang,¹ Anvar A. Zakhidov,¹ Sergey B. Lee,¹ Ali E. Aliev,¹ Christopher D. Williams,¹ Ken R. Atkinson,² Ray H. Baughman^{1*}

Individual carbon nanotubes are like minute bits of string, and many trillions of these invisible strings must be assembled to make useful macroscopic articles. We demonstrated such assembly at rates above 7 meters per minute by cooperatively rotating carbon nanotubes in vertically oriented nanotube arrays (forests) and made 5-centimeter-wide, meter-long transparent sheets. These self-supporting nanotube sheets are initially formed as a highly anisotropic electronically conducting aerogel that can be densified into strong sheets that are as thin as 50 nanometers. The measured gravimetric strength of orthogonally oriented sheet arrays exceeds that of sheets of high-strength steel. These nanotube sheets have been used in laboratory demonstrations for the microwave bonding of plastics and for making transparent, highly elastomeric electrodes; planar sources of polarized broad-band radiation; conducting appliqué; and flexible organic light-emitting diodes.

Carbon nanotube sheets are usually made using techniques from the ancient art of paper-making, typically by a week-long filtration of

nanotubes dispersed in water and then peeling the dried nanotubes as a layer from the filter (1, 2). Variations of the filtration route produce

ultrathin nanotube sheets that are highly transparent and highly conducting (3, 4). Although filtration-produced sheets are normally isotropic within the sheet plane, sheets having partial nanotube alignment result from the application of high magnetic fields during filtration (5) and from mechanical rubbing of nanotubes that are vertically trapped in filter pores (6). In other important advances, nanotube sheets have been fabricated from a nanotube aerogel (7), by Langmuir-Blodgett deposition (8), by casting from oleum (9), and by spin coating (10).

We produced highly oriented, free-standing nanotube sheets by a solid-state process that appears to be scalable for continuous high-rate production. This development builds on previous advances in the dry-state spinning of nanotube yarns from forests (11) and the introduction of twist to increase sheet strength a thousandfold (12).

¹NanoTech Institute, University of Texas at Dallas, Richardson, TX 75083-0688, USA. ²Commonwealth Scientific and Industrial Research Organization Textile & Fibre Technology, Post Office Box 21, Belmont, Victoria 3216, Australia.

*To whom correspondence should be addressed. E-mail: ray.baughman@utdallas.edu

REPORTS

These transparent nanotube sheets were drawn from a sidewall of multiwalled nanotube (MWNT) forests that were synthesized by catalytic chemical vapor deposition, using acetylene gas as the carbon source (12). The MWNTs were ~ 10 nm in diameter, and the range of investigated forest heights was 70 to 300 μm . Draw was initiated using an adhesive strip, like that on a 3M Post-it Note, to contact MWNTs teased from the forest sidewall. Meter-long sheets, up to 5 cm wide, were then made at 1 m/min by hand drawing (Fig. 1A and movie S1). Despite a measured areal density of only ~ 2.7 $\mu\text{g}/\text{cm}^2$, these 500- cm^2 sheets were self-supporting during draw. A 1-cm length of 245- μm -high forest converts to about a 3-m-long freestanding MWNT sheet. The sheet production rate was increased to 5 m/min by using an automated linear translation stage to accomplish draw (Fig. 1B) and was increased to up to 10 m/min by winding the sheet on a rotating centimeter-diameter plastic cylinder. The sheet fabrication process is quite robust, and no fundamental limitations on sheet width and length are apparent. The obtained 5-cm sheet width equaled the forest width when the draw rate was about

5 m/min or lower. At constant draw rates above ~ 7 m/min, the sheets progressively narrowed, and MWNT fibrils began to break at the intersection between the sheet sides and the forest.

This draw process does not work for all MWNT forests, and the maximum allowable draw rate depends on the structure of the forest. Intermittent bundling within the forest seems to be important, in which individual nanotubes migrate from one bundle of a few nanotubes to another. Bundled nanotubes are simultaneously pulled from different elevations in the forest sidewall, so that they join with bundled nanotubes that have reached the top and bottom of the forest, thereby minimizing breaks in the resulting fibrils (Fig. 1, B and C). Disordered regions exist at the top and bottom of the forests, where a fraction of the nanotubes form loops, which might help maintain continuity. For forests having similar topology, the highest forests were easiest to draw into sheets, probably because increasing the nanotube length increases interfibril mechanical coupling within the sheets.

Nanotube orientation is evident in the micrograph of Fig. 1B and in ultraviolet

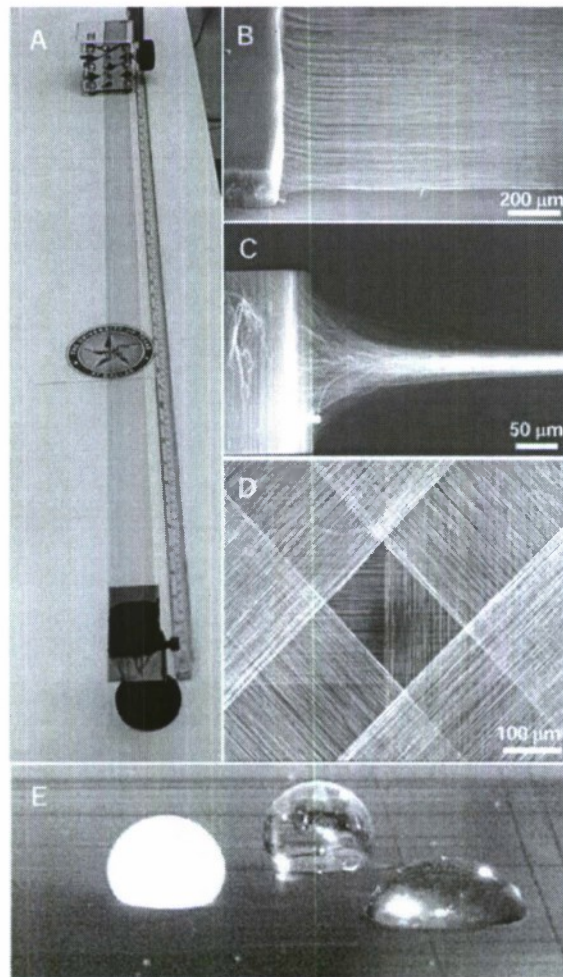
(UV)-visible absorption and Raman scattering measurements for as-drawn single MWNT sheets and sheet stacks. Depending on the sample, the ratio of Raman intensity (632.8-nm excitation) of the G band for polarization parallel and perpendicular to the draw direction is between 5.5 and 7.0 for the VV configuration (parallel polarization for incident light and Raman signal), which corresponds to polarization degrees of 0.69 and 0.75, respectively, for the investigated four-sheet stacks (fig. S1). Ignoring the effect of light scattering, the ratio of absorption coefficients for parallel and perpendicular polarizations for the as-drawn single sheet was 4.1 at 633 nm and monotonically increased to 6.0 at 2.2 μm .

The thickness of the as-produced MWNT sheet increased with increasing forest height and was ~ 18 μm in scanning electron microscopy (SEM) images of a sheet drawn from a 245- μm -high forest. From this thickness and the measured areal sheet density of ~ 2.7 $\mu\text{g}/\text{cm}^2$, the volumetric density was 0.0015 g/cm^3 . Hence, the as-produced sheets are an electronically conducting, highly anisotropic aerogel. These sheets, which can easily be stacked (Fig. 1D), can support millimeter-sized liquid droplets that are 50,000 times more massive than the supporting sheet region in contact with the droplet (Fig. 1E).

We can easily densify these highly anisotropic aerogel sheets into highly oriented sheets having a thickness of 50 nm (13) and a density of ~ 0.5 g/cm^3 . We obtain this 360-fold density increase simply by causing the as-produced sheet to adhere to a planar substrate (such as glass, many plastics, silicon, gold, copper, aluminum, or steel) by contact, vertically immersing the substrate with the attached MWNT sheet in a liquid (such as ethanol) along the nanotube alignment direction, and then retracting the substrate from the liquid. Surface tension effects during ethanol evaporation shrink the aerogel sheet thickness to ~ 50 nm. SEM micrographs taken normal to the sheet plane suggest a decrease in nanotube orientation as a result of densification. This observation is deceptive: The collapse of ~ 20 - μm sheets to ~ 50 -nm sheets without changes in lateral sheet dimensions means that out-of-plane deviations in nanotube orientation become in-plane deviations that are noticeable in the SEM micrographs. The aerogel sheets can be effectively glued to a substrate by contacting selected regions with ethanol and allowing evaporation to densify the aerogel sheet. Adhesion increases because the collapse of aerogel thickness increases the contact area between the nanotubes and the substrate.

The sheet resistance in the draw direction changes by $<10\%$ upon sheet densification by a factor of ~ 360 , which increases sheet transparency (Fig. 2, A and B). Although the

Fig. 1. MWNT forest conversion into sheets and assemblies of those sheets. (A) Photograph of a self-supporting 3.4-cm-wide, meter-long MWNT sheet that has been hand drawn from a nanotube forest at an average rate of 1 m/min. Its transparency is illustrated by the visibility of the NanoTech Institute logo that is behind the MWNT sheet. (B) SEM image, at a 35° angle with respect to the forest plane, capturing a MWNT forest being drawn into a sheet. (C) SEM micrograph showing the cooperative 90° rotation of MWNTs in a forest to form a sheet. (D) SEM micrograph of a two-dimensionally re-reinforced structure fabricated by overlaying four nanotube sheets with a 45° shift in orientation between successive sheets. The dark circle is the shadow of the in-lens detector. (E) Photograph showing two orthogonal as-drawn nanotube sheets supporting droplets of water (~ 2.5 mm in diameter), orange juice, and grape juice, where the mass of the droplet is up to 50,000 times that of the contacting nanotube sheets. The aerogel sheet regions under the aqueous droplets are densified during water evaporation.



anisotropy ratio for sheet resistance decreases from 50 to 70 for the undensified sheets to 10 to 20 for the densified sheets, this anisotropy ratio for the densified sheets is nearly temperature-invariant. In fact, the temperature dependence of sheet resistivity is nearly the same for the forest-drawn densified nanotube sheets and for sheets made by the filtration route using the same forest-grown MWNTs, and is much smaller than for single-walled nanotube (SWNT) sheets fabricated by filtration (14) (Fig. 2A). In addition, the low-frequency (f) noise power density in the draw direction for a densified forest-drawn sheet is 10^4 and is 10 times lower than for ordinary filtration-produced sheets of SWNTs and MWNTs, respectively (Fig. 2C). The literature reports high $1/f$ noise for individual SWNTs and SWNT mats (15) and low noise having either a $1/f$ (16) or a $1/f^2$ dependence (17) for individual MWNTs. In contrast with the latter single-MWNT results, the noise power density for our densified MWNT sheets has a $1/f$ frequency dependence.

A possible explanation for these electronic properties is found in SEM micrographs (fig. S2), which indicate that up to ~ 50 -nm-wide fibrils (containing many bundled MWNTs) laterally fork and then eventually recombine with the forked legs of other fibrils to form a laterally extended network. High resistance of interfibril contacts formed during densification, as compared with those within the original fibril network, might explain why sheet resistance changes little as a result of over 300-fold sheet densification. Because low-frequency noise inversely depends on the number of atoms at resistive contacts (15), the low $1/f$ noise of the solid-state fabricated MWNT sheets could result from the long path length where MWNTs overlap within the fibril network. Whatever the explanation for these properties, the low electrical noise and low temperature coefficient of resistivity for the forest-drawn sheets could be important for electronic applications such as chemical sensors.

The densified nanotube sheets showed high transparency in combination with usable electrical conductivity, a combination needed for such applications as displays, video recorders, solar cells, and solid-state lighting (3). The sheet resistivity was ~ 700 ohms per square in the draw direction before and after densification for the forest-drawn sheets, and 10 to 20 times higher in the orthogonal in-plane direction for the densified sheet. The transmittance for the densified MWNT sheet was $>85\%$ for perpendicular polarization, $>65\%$ for parallel polarization between 400 nm and 2 μm , and $>85\%$ for unpolarized radiation between 1.5 and 10 μm (Fig. 2B). These MWNT sheets will adhere to transparencies made of poly(ethylene terephthalate) and to silicone rubber sheets, thereby providing transparent bilayer composites that can be

bent in any direction without causing a substantial decrease in electrical conductivity (movie S2). This ability to bend without degradation of electronic conductivity is important for flexible electronic circuits and is not found in conventional transparent conductors such as indium tin oxide (ITO).

After an initial conditioning strain cycle, in which conductivity decreased $\sim 6\%$ with increasing strain, the nanotube/elastomer sheet was repeatedly deformable over 100% strain (fig. S3) without causing a substantial change in conductance (18). Ordinary conductors cannot undergo nearly such large strains without losing electrical contact with the actuating material. Although conducting greases are used to maintain electrical contact to electrostrictive actuator materials that generate 100% or higher strains (19), these greases are not suitable for use as electrodes for stacks of electrostrictive sheets that can generate large forces and high strains without requiring several-thousand-volt applied potentials.

Although no alternative solid-state conductors combine elastic deformability to 100% strain and essentially constant electronic conductivity, transparent doped SWNT sheets having ~ 20 times higher electrical conductivity are known (3). The transparency of those SWNT sheets (either doped or undoped)

strongly depends on wavelength in the visible and near-infrared. Thus, the monotonic increase in transmittance with increasing wavelength (Fig. 2B) of our MWNT sheets provides an advantage for broadband applications. Also, the electrical conductivity of those SWNT sheets decreases 10 times upon dedoping. Extension of the present solid-state sheet fabrication technology to doped MWNTs and doped SWNTs is desirable in order to increase electrical conductivity for transparent conductor applications, and even the latter appears feasible because of the recent development of 2.5-mm-high nanotube forests comprising SWNTs (20).

The forest-drawn MWNT sheets can be conveniently assembled into biaxially reinforced sheet arrays (Fig. 1D) and as conducting layers on nonplanar surfaces, such as by helically wrapping a sheet strip on a millimeter- or larger-diameter cylinder (fig. S4). Chiral structures, which will likely be optically active for long infrared and microwave wavelengths, can be made by stacking parallel sheets so that the orientation direction varies helically along the stack thickness and then densifying the stacked array so that the individual sheet thickness is ~ 50 nm.

Especially considering the absence of polymer binder, the mechanical properties of the

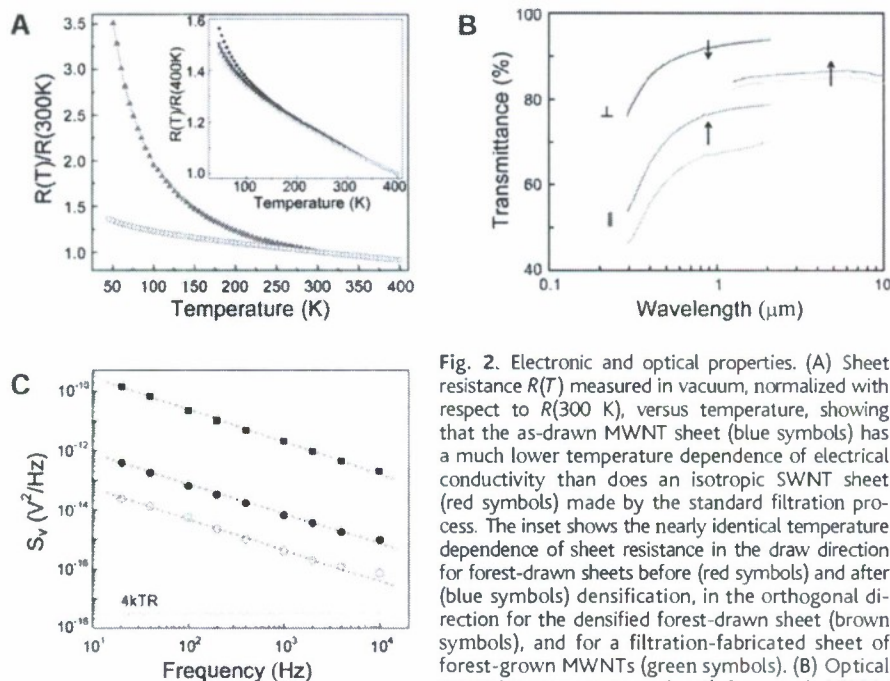


Fig. 2. Electronic and optical properties. (A) Sheet resistance $R(T)$ measured in vacuum, normalized with respect to $R(300\text{ K})$, versus temperature, showing that the as-drawn MWNT sheet (blue symbols) has a much lower temperature dependence of electrical conductivity than does an isotropic SWNT sheet (red symbols) made by the standard filtration process. The inset shows the nearly identical temperature dependence of sheet resistance in the draw direction for forest-drawn sheets before (red symbols) and after (blue symbols) densification, in the orthogonal direction for the densified forest-drawn sheet (brown symbols), and for a filtration-fabricated sheet of forest-grown MWNTs (green symbols). (B) Optical transmittance versus wavelength for a single MWNT sheet, before and after densification, for light polarized perpendicular to (\perp) and parallel to (\parallel) the draw direction and for unpolarized light (the two curves on the right), where the arrow points from the data for the undensified sample to those for the densified sample. (C) Noise power density (S_v , measured in air for 10-mA biasing) versus frequency (f) for a densified forest-drawn MWNT sheet (open circles), compared with that for ordinary filtration-produced MWNT sheets (solid circles) and SWNT sheets (solid rectangles) having the same 40-ohm resistance. The dashed lines are data fits for a $1/f^\alpha$ dependence, where α is 0.98 ± 0.04 , 0.97 ± 0.02 , and 1.20 ± 0.02 for the lower, middle, and upper data sets, respectively. The lower-limit noise power at temperature T (the product of $4kT$ and the sample resistance R , where k is Boltzmann's constant) is indicated by the horizontal dotted line.

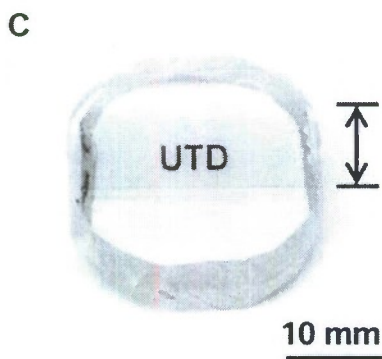
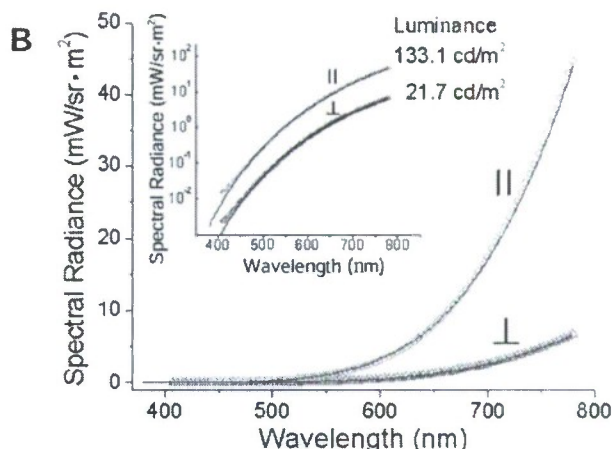
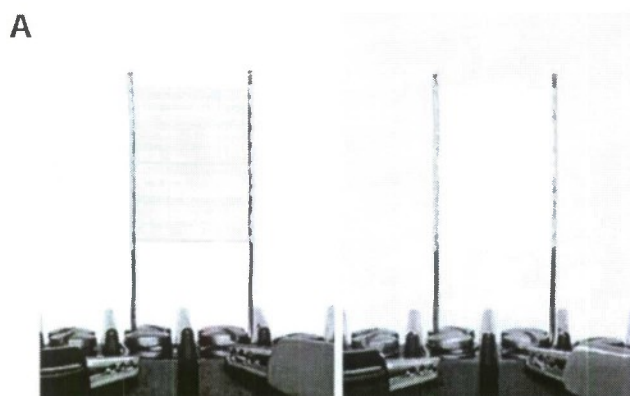


Fig. 3. Application as a broadband source of polarized incandescent light and for the microwave welding of plastics. (A) Photograph showing a free-standing undensified MWNT sheet (16 mm by 22 mm) used as a planar incandescent light source that emits polarized radiation. The background color of the unheated sheet (left) and the incandescent sheet (right) differs because of reflected incandescent light from a white paper sheet that is behind the light source. (B) Spectral radiance in directions parallel to (||) and perpendicular to (⊥) the draw direction of an as-drawn undensified MWNT sheet after an added inelastic stretch in the initial draw direction of 2.5%. The luminance polarized parallel to the sheet draw direction for the indicated spectral range is 6.1 times higher than for the perpendicularly polarized luminance, which corresponds to a polarization factor of 0.72. The inset shows these data on a semilogarithmic scale. Underlying solid lines (largely obscured by coincidence with the data points) are data fits assuming black-body radiation with $T = 1410$ K. (C) Photograph of two 5-mm-thick Plexiglas plates that have been welded together by microwave-induced heating of an as-drawn MWNT sheet strip that was sandwiched between these plates. The nanotube sheet strip at the welded interface (see arrow for vertical extension) remains oriented, highly conducting, and transparent, as indicated by the visibility of “UTD” printed on an underlying paper sheet.

acrogel-like and densified MWNT sheets are unexpectedly high, which is probably a consequence of the interconnected fibril network (fig. S2). The density-normalized mechanical strength is much more accurately determined than mechanical strength, because the sheet thickness is less reliably measured than the ratio of maximum force to mass-per-length in the stretch direction. Stacks of undensified sheets have an observed tensile strength of between 120 and 144 MPa/(g/cm³) (fig. S5, A and B). A densified stack containing 18 identically oriented sheets had a strength of 465 MPa/(g/cm³), which decreased to 175 MPa/(g/cm³) when neighboring sheets in the stack were orthogonally oriented to make a densified biaxial structure. These density-normalized strengths are already comparable to or greater than the ~160 MPa/(g/cm³) strength of the Mylar and Kapton films used for ultralight air vehicles and proposed for use in solar sails for space applications (21) and those for ultra-high-strength steel [~125 MPa/(g/cm³)] and aluminum alloy [~250 MPa/(g/cm³)] sheets.

Sheets generally have much lower limiting strengths than do fibers of the same material. However, at a value of 465 MPa/(g/cm³), the tensile strength of the densified MWNT sheet is comparable to or exceeds reported values for nanotube fibers and yarns that do not include a binding agent: 575 MPa/(g/cm³) for forest-spun twisted MWNT yarns (12), 500

MPa/(g/cm³) for aerogel-spun yarns (7), 105 MPa/(g/cm³) for SWNT yarns spun from superacids (22), and 65 MPa/(g/cm³) for SWNT yarns spun using an acidic coagulation bath (23). Order-of-magnitude or greater increases in mechanical strength have been observed when internanotube coupling is enhanced by polymer incorporation into nanotube sheets and yarns (23–26), and similar strength increases might be achievable by infiltration of suitable polymers into the present MWNT sheets.

Initial results suggest additional promising applications. One is as a stable planar source of polarized UV, visible, and infrared incandescent light (Fig. 3, A and B) for use in sensors, infrared beacons, infrared imaging, and reference signals for device calibration. The degree of polarization of emitted radiation for 2.5% stretched as-drawn sheets increases from 0.71 at 500 nm to 0.74 at 780 nm (Fig. 3B), which is substantially higher than the degree of polarization (0.33 for 500 to 900 nm) previously reported for a 600- μ m-long MWNT bundle with an emitting length of ~80 μ m (27). The wavelength dependence of light intensity for both polarizations fits the functional form expected for black-body radiation, and the degree of polarization does not significantly depend on sheet temperature for the observed temperature range between 1000 and 1600 K. Cost and efficiency benefits result from decreasing or eliminating the

need for a polarizer, and the MWNT sheet provides spatially uniform emission over a broad spectral range that is otherwise hard to achieve. The low heat capacity of these very-low-mass incandescent emitters means that they can turn on and off within the observed 0.1 ms or less in vacuum and provide current modulated light output on a shorter time scale.

By simply contacting the as-drawn MWNT sheets to ordinary adhesive tape, we have made optically transparent adhesive appliqué that could be used for electrical heating and for providing microwave absorption (14). Because of MWNT sheet porosity, the peel strength is largely maintained when an undensified MWNT sheet is laminated between an adhesive tape and a contacted plastic or metal surface (14) (fig. S6). We have used the known microwave absorption capability of MWNTs (28, 29) to demonstrate another possible application: polymer welding through heating of a transparent MWNT sheet that is sandwiched between plastic parts (14). Figure 3C shows two 5-mm-thick Plexiglas (polymethyl methacrylate) plates that were welded together using microwave heating of a sandwiched undensified MWNT sheet to provide a strong, uniform, and transparent interface in which nanotube orientation and sheet electrical conductivity are little changed. The combination of high transparency and ultrahigh thermal stability provides advantages

for microwave-based welding not found in the conducting polymers (30). This microwave heating process could be used to make polymer composites from stacks of polymer sheets that are separated by nanotube sheets, car windows that are electrically heated, or antennas in car windows that have high transparency.

The work function of these transparent MWNT sheets (~ 5.2 eV) is slightly higher than that of the ITO typically used as the transparent hole-injecting electrode in organic light-emitting diodes (OLEDs), and these sheets have the additional benefits of being porous and flexible. MWNT sheets made with previous techniques have not been successfully used for optically transmissive, hole-injecting layers in OLEDs: The sheet thickness and surface roughness dwarf the typical 100-nm layer thickness of emissive layers needed for OLEDs (31), thereby causing interelectrode shorts; and in thicker devices, the unbalanced hole and electron currents prevent light emission. However, black sheets of solution-spun MWNTs have been used as nontransmissive hole-collecting electrodes in solar cells (10), and transparent p-type SWNT sheets have been used as hole-injection electrodes in inorganic LEDs based on gallium nitride (32).

We have taken advantage of the nanometer-scale thickness, transparency, flexibility, porosity, and high work function of our densified MWNT sheets to demonstrate polymer-based OLEDs on both flexible plastic and rigid glass substrates (14). Hole injection occurs over the high-surface-area interior of the nanoporous nanotube electrode, as opposed to at a planar interface in the previous inorganic LEDs (32). The onset voltage for emission is quite low (2.4 V, about the same as for the highest-performance ITO in similar devices), and rather bright electroluminescence was obtained (up to 500 cd/m²) (fig. S7). The emitted light is slightly polarized, but in an orthogonal direction from that for the above incandescent light source, because the MWNT sheet acts as a polarizer. If a polymeric light-emitting layer were aligned using known methods (33) to provide emission in the same polarization direction, absorption due to the MWNT hole injector could be minimized, which is not possible for conventional ITO hole-injecting electrodes.

Although solution- or melt-based processing becomes increasingly difficult as nanofiber length increases, the opposite is true for the present solid-state sheet fabrication process: 300- μ m-long nanotubes are easier to convert into sheets than are 70- μ m-long nanotubes. Also, ultrasonication used for nanotube dispersion in solution-based processing decreases nanotube length, and this degradative step is absent from the present sheet fabrica-

tion process. These are important advantages of the present technology, because long, high-perfection nanotubes are needed for maximizing electrical and thermal conductivities and mechanical properties.

References and Notes

1. A. G. Rinzier et al., *Appl. Phys. A* **67**, 29 (1998).
2. M. Endo et al., *Nature* **433**, 476 (2005).
3. Z. Wu et al., *Science* **305**, 1273 (2004).
4. L. Hu, D. S. Hecht, G. Grüner, *Nano Lett.* **4**, 2513 (2004).
5. J. E. Fischer et al., *J. Appl. Phys.* **93**, 2157 (2003).
6. W. A. De Heer et al., *Science* **268**, 845 (1995).
7. Y. Li, I. A. Kinloch, A. H. Windle, *Science* **304**, 276 (2004).
8. Y. Kim et al., *Jpn. J. Appl. Phys.* **42**, 7629 (2003).
9. T. V. Sree Kumar et al., *Chem. Mater.* **15**, 175 (2003).
10. H. Ago, K. Petritsch, M. S. P. Shaffer, A. H. Windle, R. H. Friend, *Adv. Mater.* **11**, 1281 (1999).
11. K. Jiang, Q. Li, S. Fan, *Nature* **419**, 801 (2002).
12. M. Zhang, K. R. Atkinson, R. H. Baughman, *Science* **306**, 1358 (2004).
13. The per-sheet thickness measured by stylus profilometer varied from ~ 50 to ~ 150 nm, depending on forest height and draw and densification conditions. Atomic force microscopy provides a sheet thickness of down to 30 to 50 nm, which is close to the maximum width of fibrils in the sheet, which can be far from cylindrical.
14. See supporting data on Science Online.
15. P. G. Collins, M. S. Fuhrer, A. Zettl, *Appl. Phys. Lett.* **76**, 894 (2000).
16. H. Ouacha et al., *Appl. Phys. Lett.* **80**, 1055 (2002).
17. L. Roschier, R. Tarkkainen, M. Ahlskog, M. Paalanen, P. Hakonen, *Appl. Phys. Lett.* **78**, 3295 (2001).
18. A 1-mm-thick sheet of silicone rubber (ECOFLEX 0040 from Smooth-On) was stretched to 105% strain, and then a single as-drawn MWNT sheet was laid over it to provide self-generated adhesive contact before strain relaxation. The initial sheet resistance of the obtained unloaded silicone rubber/MWNT sheet composite was 755 ohms per square. However, after an initial increase in resistance by $\sim 6\%$, the resistance changed less than 3% during the subsequent four strain cycles to 100% strain.
19. R. Pelrine, R. Kornbluh, Q. Pei, J. Joseph, *Science* **287**, 836 (2000).
20. K. Hata et al., *Science* **306**, 1362 (2004).
21. D. E. Edwards et al., *High Perf. Polymers* **16**, 277 (2004).
22. L. M. Ericson et al., *Science* **305**, 1447 (2004).
23. M. E. Kozlov et al., *Adv. Mater.* **17**, 614 (2005).
24. J. N. Coleman et al., *Appl. Phys. Lett.* **82**, 1682 (2003).
25. B. Vigolo, P. Poulin, M. Lucas, P. Launois, P. Bernier, *Appl. Phys. Lett.* **81**, 1210 (2002).
26. A. B. Dalton et al., *Nature* **423**, 703 (2003).
27. P. Li et al., *Appl. Phys. Lett.* **82**, 1763 (2003).
28. P. C. P. Watts, W.-K. Hsu, A. Barnes, B. Chambers, *Adv. Mater.* **15**, 600 (2003).
29. J. Wu, L. Kong, *Appl. Phys. Lett.* **84**, 4956 (2004).
30. A. J. Epstein, A. G. MacDiarmid, *Synth. Metals* **69**, 179 (1995).
31. D. B. Romero, M. Carrard, W. De Heer, L. Zuppiroli, *Adv. Mater.* **8**, 899 (1996).
32. K. Lee, Z. Wu, Z. Chen, F. Ren, S. J. Pearton, A. G. Rinzier, *Nano Lett.* **4**, 911 (2004).
33. K. S. Whitehead, M. Grell, D. D. C. Bradley, M. Jandke, P. Strohriegel, *Appl. Phys. Lett.* **76**, 2946 (2000).
34. Supported by Defense Advanced Research Projects Agency/U.S. Army Research Office grant W911NF-04-1-0174, the Texas Advanced Technology Program grant 009741-0130-2003, the Air Force STTR program on topic AF04-TO20, Air Force grant F49620-03-1-0164, Robert A. Welch Foundation grant AT-0029, and the Strategic Partnership for Research in Nanotechnology consortium in Texas. The authors thank J. P. Ferraris and M. Zhou for the synthesis of the emissive polymer used for the OLEDs, A. Kuznetsov for assistance with OLED preparation, and V. H. Ebron for assistance with the microwave welding.

Supporting Online Material

www.sciencemag.org/cgi/content/full/309/5738/1215/DC1

Materials and Methods

Figs. 51 to 57

References

Movies 51 and 52

25 May 2005; accepted 13 July 2005

10.1126/science.1115311

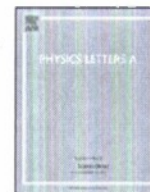
Understanding the Infrared Spectrum of Bare CH₅⁺

Oskar Asvany,^{1*} Padma Kumar P.,^{2*} Britta Redlich,³
Ilka Hegemann,² Stephan Schlemmer,^{1,4} Dominik Marx^{2†}

Protonated methane, CH₅⁺, continues to elude definitive structural assignment, as large-amplitude vibrations and hydrogen scrambling challenge both theory and experiment. Here, the infrared spectrum of bare CH₅⁺ is presented, as detected by reaction with carbon dioxide gas after resonant excitation by the free electron laser at the FELIX facility in the Netherlands. Comparison of the experimental spectrum at ~ 110 kelvin to finite-temperature infrared spectra, calculated by ab initio molecular dynamics, supports fluxionality of bare CH₅⁺ under experimental conditions and provides a dynamical mechanism for exchange of hydrogens between CH₃ tripod positions and the three-center bonded H₂ moiety, which eventually leads to full hydrogen scrambling. The possibility of artificially freezing out scrambling and internal rotation in the simulations allowed assignment of the infrared spectrum despite this pronounced fluxionality.

Protonated methane, CH₅⁺, is of great interest in vibrational spectroscopy (1–4) as the prototype of hypercoordinated carbon and three-center two-electron bonding (5, 6). The equilibrium structure—that is, the global minimum of its potential energy surface (PES)—can be viewed as a CH₃ tripod with a H₂

moiety attached to the carbon in an eclipsed C_s configuration, e-C_s, via a three-center bond (7). However, rapid hydrogen scrambling has called into question the notion of assigning it such a traditional molecular structure (8–11), despite the stability of CH₅⁺ once it is formed (12). This fluxionality has been traced back



The origin of polarized blackbody radiation from resistively heated multiwalled carbon nanotubes

Ali E. Aliev*, Alexander A. Kuznetsov

NanoTech Institute, University of Texas at Dallas, Richardson, TX 75083-0688, USA

ARTICLE INFO

Article history:

Received 5 April 2008

Accepted 21 April 2008

Available online 20 May 2008

Communicated by V.M. Agranovich

PACS:

73.63.Fg

78.67.Ch

81.07.De

Keywords:

Carbon nanotubes

Light polarization

Blackbody radiation

ABSTRACT

We observed very pronounced polarization of light emitted by highly aligned free-standing multiwall carbon nanotube (MWNT) sheet in axial direction which is turned to the perpendicular polarization when a number of layers are increased. The radiation spectrum of resistively heated MWNT sheet closely follows to the Plank's blackbody radiation distribution. The obtained polarization features can be described by a classical dielectric cylindrical shell model, taking into consideration the contribution of delocalized π -electrons (π surface plasmons). In absorption (emission) the optical transverse polarizability, which is much smaller than longitudinal one, is substantially suppressed by depolarization effect due to screening by induced charges. This phenomenon suggests very simple and precise method to estimate the alignment of nanotubes in bundles or large assemblies.

© 2008 Elsevier B.V. All rights reserved.

1. Introduction

Recently we observed polarized incandescent light emission from highly oriented transparent multiwall carbon nanotubes (MWNTs) sheet withdrawn from chemical vapor deposition (CVD) grown forest [1]. Emitted light is polarized along the nanotubes alignment direction. However the multilayered stack of sheets shows perpendicular polarization. Despite fundamental interest and significant potential of light polarization for various optical applications, there have been few experimental studies on the polarized emission from thin metallic wires and aligned 1D systems [2,3]. The attempt to explain the origin of the light polarization from resistively heated MWNT bundles was done in [4] using concept of accelerated and decelerated movement of confined electrons in the axial direction of the MWNTs. However, proposed in [4] mechanism should give very different emission spectra than the observed blackbody radiation. Taking into account the electron acceleration between collisions with lattice atoms (with extended mean free path of conducting electrons in MWNT for $T > 1000$ K, $\ell \sim 10$ nm) one can find that emission of accelerated electrons peaks at $\lambda_{\max} \sim 40$ m [5]. Moreover, the intensity of this type radiation according to Larmor formula, $P = (2e^2 a^2 / 3c^3) \sim 10^{-10}$ W, is negligibly small.

Since the ratio between emissivity and absorptivity is a constant for a body in thermal equilibrium (Kirchhoff's law of thermal radiation) the optical absorption studies in related materials may shed light on the mechanisms of polarized light emission [6,7]. The direct experimental confirmation that sub-band features are absent from the cross-polarized channel was presented in [6] for anisotropic absorption spectra in magnetically aligned SWNTs. The anisotropic optical absorption properties of well aligned SWNT forest grown on an optically polished quartz substrate in [7] are explained by polarization dependencies of absorption peaks at 4.5 and 5.25 eV. Moreover, because of the fact that these peaks were observed at almost the same positions regardless of SWNT diameter and preparation method, they made conclusion that obtained peaks reflecting optical properties of graphite.

Using multilayered structures of stacked MWNT sheets we experimentally demonstrated that polarization of blackbody radiation in carbon nanotubes is due to enhanced polarizability of C–C bonds along the tube direction and depolarization effects. Electrical field induced inside the nanotubes in perpendicular direction substantially reduces the external field.

2. Experimental

The highly oriented transparent nanotube sheets were drawn from the sidewall of 300–350 μm tall MWNT forest synthesized by catalytic CVD method [1]. Typical scanning electron microscope (SEM) images of the suspended sheet at increasing magnification

* Corresponding author. Tel.: +1 972 883 6543; fax: +1 972 883 6529.
E-mail address: ali.aliev@utdallas.edu (A.E. Aliev).

are shown in Fig. 1(a), (b). One layer of MWNT sheet is transparent in visible ($85 \pm 5\%$), and has been proposed to be a good conductive transparent electrode for applications in solar cells, light emitting diodes and electrochromic displays [8]. The thickness of free-standing sheet is about $20 \mu\text{m}$ and the density is 0.0015 g/cm^3 . On average, only four of $10 \pm 1 \text{ nm}$ in diameter MWNTs are spaced in the thickness direction. The anisotropy of electrical conductivity along the nanotube alignment versus perpendicular direction is ~ 60 for a densified sheet on the glass substrate [1], and exceeds 100 for a free-standing MWNT sheet.

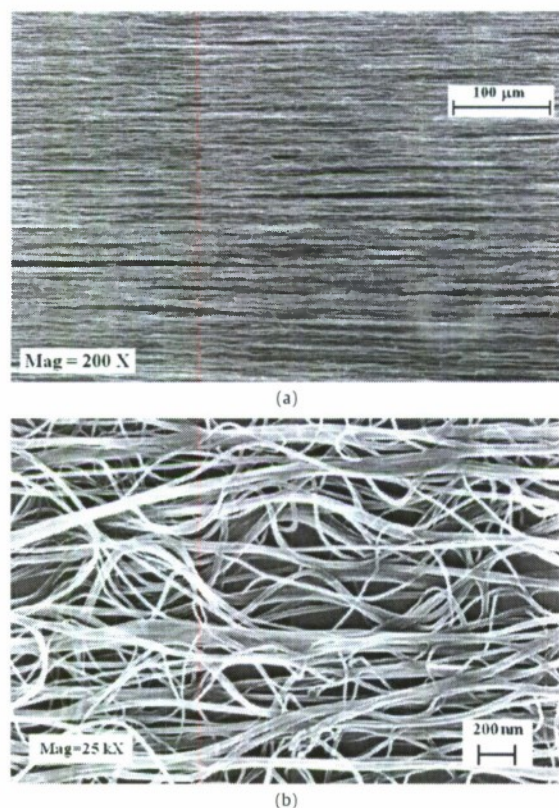


Fig. 1. SEM images of MWNT sheet taken at increasing magnification. Diameter of individual tubes is $10 \pm 1 \text{ nm}$. The average diameter of bundles is about 100–150 nm.

The polarization experiment in multilayered MWNTs was carried out by stacking the sheets on top of each other. To study the light emission from the carbon nanotubes the free-standing MWNT sheet was fixed between two gold covered copper electrodes with silver paste (H-20E) (Fig. 2(a), (b)). The multilayered MWNT sheet comprising 44 layers was prepared from the same MWNT forest by dry-pooling technology [1]. Then the sheet was densified by dipping into ethanol and dried in air (Fig. 2(c), (d)). Surface tension during ethanol evaporation reduces the sheet thickness 360 times. The averaged thickness of 44 layers is $4 \pm 0.4 \mu\text{m}$ with density of $0.8 \pm 0.1 \text{ g/cm}^3$.

All measurements were done under high vacuum of 10^{-6} Torr in glass jar of Advanced Coater 9500 (PAC-1 PELCO). The free-standing MWNT sheets were heated resistively by DC Power Supply 1630 (BK Precision) or Keithley 2425-C 100W Source Meter. The Ni-Cr heater was resistively heated by AC current (60 Hz) using variable autotransformer Powerstat-10A. The blackbody radiation intensity, temperatures and spectra were taken simultaneously by computerized spectrometer SpectraScan PR-650 (PhotoResearch). The spectra were collected through a 2.7X objective MX-75 with 2.5 mm collecting spot in the focal point in the wavelength range 300–800 nm. The scanning electron microscope (SEM) micrographs were taken with a LEO 1530 VP equipped with Energy Dispersive Spectrometer (EDS) for X-ray microanalysis. Raman spectra were taken by polarized Raman microscope (LabRAM HR) working in VV mode.

3. Results and discussion

The spectra of light emitted by both resistively heated multilayered free-standing MWNT sheets (Fig. 3) and indirectly heated 44 layers correspond to the Planck's law of blackbody radiation, confirming the Joule heating mechanism. The intensity of radiation from suspended MWNT sheet was stable and reproducible within $\pm 1\%$ up to 2500 K. No luminescence peaks from sub-band transitions were observed. At MWNTs diameters of 5 nm (inner shell)–10 nm (outer shell) the conductivity of constituent shells is predominantly metallic with finite density of electronic states at Fermi level and negligible contribution of van Hove singularities. The angle dependence of polarization for free-standing MWNT sheet shows pronounced polarization peak of emitted light along the nanotubes alignment. The change of polarized light intensity fitted by $\cos^2 \theta$ (dotted line) is shown in Fig. 4(a), where θ is the angle between the nanotubes alignment direction and polarizer

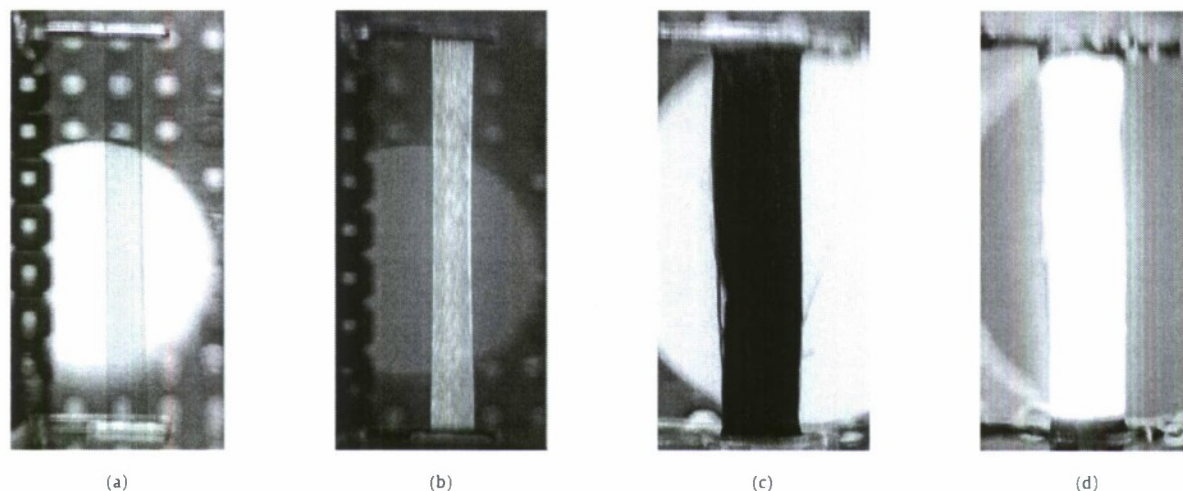


Fig. 2. (a) Suspended MWNT sheet at room temperature, $25 \times 3 \times 0.02 \text{ mm}$. (b) Resistively heated suspended MWNT sheet, $T \sim 1780 \text{ K}$ (color was adjusted by camera). (c) 44 layers of densified free-standing MWNT sheet attached to electrodes. (d) Resistively heated 44 layers, $T \sim 2000 \text{ K}$. (For interpretation of the references to color in this figure legend, the reader is referred to the web version of this Letter.)

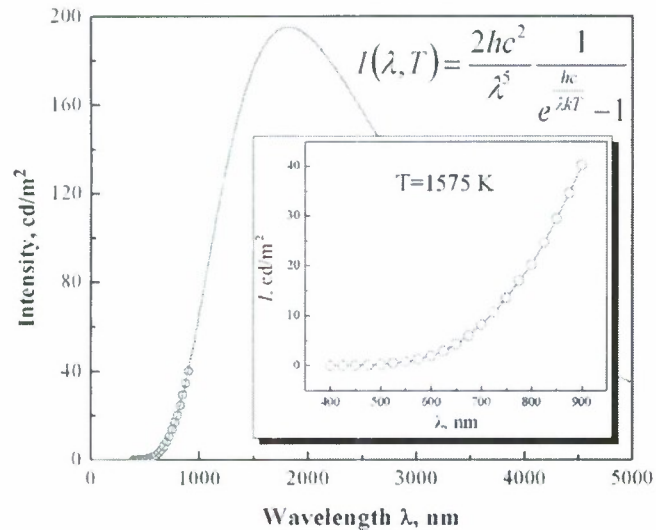


Fig. 3. Blackbody radiation spectra of one layer MWNT sheet ($25 \times 3 \times 0.02 \text{ mm}^3$) taken at $T = 1575 \text{ K}$ in direction normal to the sheet surface. Open (blue) circles are recorded points, and solid (red) line is a Planck spectra fitted for $T = 1575 \text{ K}$. Insert shows the extended plot for experimental data. (For interpretation of the references to color in this figure legend, the reader is referred to the web version of this Letter.)

axis. The degree of linear polarization (DLP) [6] for one suspended MWNT sheet in wide spectral range of 300–900 nm was estimated as

$$P_E = \frac{I_{\perp} - I_{\parallel}}{I_{\perp} + I_{\parallel}} = -0.55, \quad (1)$$

where I_{\perp} and I_{\parallel} are the intensities of emitted light passed through the polarizer being perpendicular and parallel to the nanotubes alignment direction, respectively. DLP does not significantly depend on sheet temperature for the observed temperature range of 900–2500 K. However, it depends from the degree of alignment of nanotubes within the sheet [1] and can be suggested as a simple method to estimate the alignment quality.

One layer of free-standing MWNT sheet has extremely low density of 0.0015 g/cm^3 with a few non-interacting nanotubes spaced in the thickness direction. According to Kirchhoff's law of radiation the ratio between emissivity and absorptivity is constant for a body in thermal equilibrium. Applying this law to obtained experimental results we analyze below the polarization peculiarities of MWNT sheet for absorption (emission) experiments.

The nanotube geometry results in slightly different force constants along the nanotube axis relative to the circumferential direction, where the nanotube curvature reduces the force constant. This anisotropy in the force constant accounts for the frequency difference between the Raman components at 1575 cm^{-1} (attributed to vibrations in the circumferential direction) and at 1584 cm^{-1} (attributed to vibrations along the nanotubes axis) of G-band which is averaged to $1580.8 \pm 0.8 \text{ cm}^{-1}$ of the E_{2g} graphite mode frequency. Because of the small number of allowed k vectors in the circumferential direction, this frequency difference is increased with decreasing nanotube diameter [9]. Taking into account the angular dependence of contribution from tangential modes with A_{1g} , E_{1g} , and E_{2g} symmetry [9], the theoretical predictions for the G-band relative intensities for SWNTs are 1:0.36 for the parallel and per-

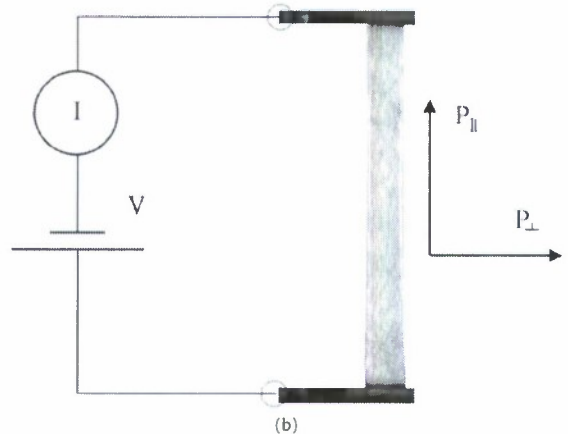
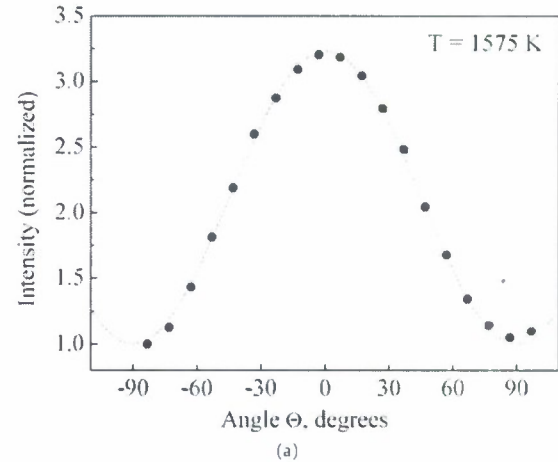


Fig. 4. (a) Normalized intensity of blackbody radiation versus the polarizer orientation at $T = 1575 \text{ K}$. Dotted line is an intensity of polarized light fitted by $\cos^2 \theta$. (b) Schematic diagram of resistively heated MWNT sheet. Parallel polarization P_{\parallel} corresponds to the polarizer direction matched to the direction of nanotubes alignment, $\theta = 0^\circ$.

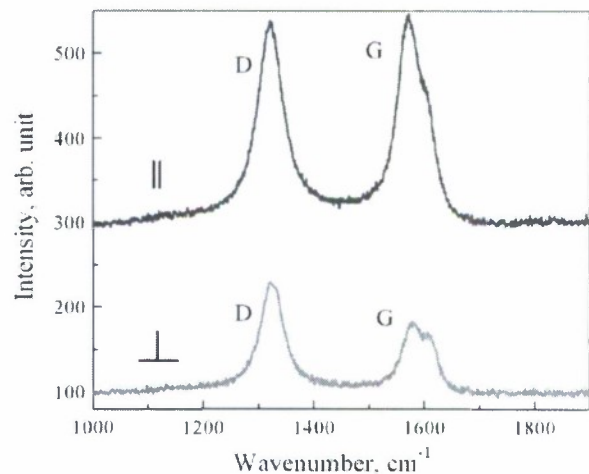


Fig. 5. Polarized Raman spectra for MWNT sheet taken at excitation wavelength of 632.8 nm for polarization along (blue), and perpendicular (red) to the nanotubes alignment. (For interpretation of the references to color in this figure legend, the reader is referred to the web version of this Letter.)

pendicular polarization geometries [10]. Experimentally observed values for aligned MWNT sheet are 1:0.29 (see Fig. 5). However the origin of polarization in our case is different. The optical absorption for the polarization perpendicular to the nanotubes axis is

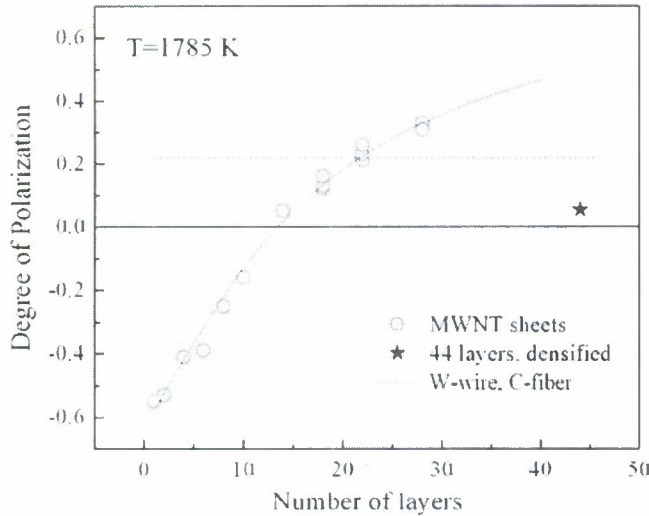


Fig. 6. Degree of linear polarization versus a number of MWNT sheets stacked on each other. Dashed line shows the polarization degree of thin tungsten wire ($D = 12 \mu\text{m}$) and pitch derived carbon fiber (DuPont, E-75, $D = 10 \mu\text{m}$), solid star (green) shows the polarization of 44 layers of densified MWNT sheet. Solid (blue) line is a computer simulation by Eq. (4). (For interpretation of the references to color in this figure legend, the reader is referred to the web version of this Letter.)

suppressed almost completely when the depolarization (antenna) effect is taken into account. The depolarization effect should, however, be relaxed in MWNTs, especially as the diameter increases. On the basis of the depolarization effect one should expect more effective absorption and excitation of resonant Raman scattering for the parallel scattering geometry [11]. In our case the noticeable perpendicular component in Raman spectra (red line in Fig. 5), absorption [1], and radiation is completely due to misalignment of individual nanotubes in MWNT sheets.

The aligned fraction of the nanotubes in MWNT sheet extracted from diffuse X-ray scattering measurements, $AF = 0.72$ [12], is also very consistent with experimentally obtained polarization behavior for Raman G-band peak.

On the other hand, the aligned nanotube assembly can be considered as a stack of thin metal wires. Then the scattering, absorption and emission should be considered as an interaction of light with electron plasma. If the wires are thin enough one will get a strong resonance interaction between the light and the metal plasma at the light frequency for which the dielectric constant of the plasma ϵ is such that $\epsilon = -\epsilon_1$, where ϵ_1 is the dielectric constant for the medium surrounding the wire. For thin silver wire the polarization of absorbed (or emitted) light in visible range was found to be -1 for wire diameter below 100 nm and increased up to $P_E = +0.6$ (polarization perpendicular to the wire direction is dominate) for 10 μm wire [2].

Taking into account the outer diameter of studied MWNT nanotubes of 10 nm (inner shells are totally screened) and the lowest resonance energy of π surface plasmons (SP) of about $\sim 5 \text{ eV}$ ($\sim 250 \text{ nm}$) [7,13,14] one can expect high parallel polarization of absorbed (emitted) light with DLP $P_E = -1$ for ideally aligned individual MWNTs. DLP will increase to positive values when the diameter of individual tubes or bundles is increased. The crossover of polarization, $P_E = 0$, take place for nanotube diameters above 250 nm when the circumferential resonance absorption becomes substantial ($\epsilon = -\epsilon_1$). The further increase of perpendicular polarization is due to the internal refraction in cylindrical structures. Since the aligned MWNTs of 250 nm in diameter are difficult to grow we assembled the MWNT sheet into a multilayered stack. By increasing a number of MWNT layers stacked on each other we increased both the volumetric density and tube–tube interactions.

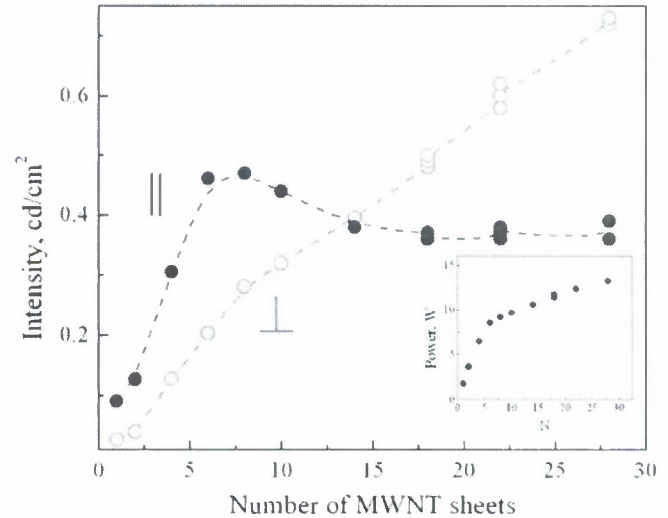


Fig. 7. Intensities of parallel (blue solid circles) and perpendicular (red open circles) polarized light emitted from MWNT sheet with increased number of stacked layers. Inset shows the applied power versus the number of layers. (For interpretation of the references to color in this figure legend, the reader is referred to the web version of this Letter.)

Fig. 6 shows the decrease of polarization degree along the sheet alignment and smooth turn to the perpendicular polarization when the number of sheets are increased.

The ratio of 1:0.29 obtained for parallel and perpendicular intensities of emitted light for one MWNT sheet is decreased with the number of stacked layers, whereas the thickness of whole assembly is changed very little (from 20 to 50 μm for 28 layers). At $N = 6-8$ the slope of both intensities is decreased due to a screening of rear and inner layers (Fig. 7). The further added layers do not contribute directly to the total emission. The front layers absorb the light emitted by inner layers and again reemit this energy. Since we kept the radiation temperature constant at 1785 K the applied power curve changes the slope at that point (see the inset to Fig. 7). The experimentally obtained crossover in DLP takes place at 12–13 layers with further increase up to $+0.33$. The surface plasmon resonance wavelength at crossover corresponds to double increased diameter as compared to initial value of 100–150 nm [15] diameter of bundles in sheet.

Since the DLP behavior of MWNT sheet mainly determined by the ratio $2\pi r/\lambda_{SP}$ [2], where r is the radius of individual nanotubes or bundles and $\lambda_{SP} = 250 \text{ nm}$ is the surface plasmon wavelength, the transmittance of whole stack is a most relevant parameter we can simulate to describe the DLP. The intensities of absorbed (emitted) light for parallel and perpendicular polarizations could be described in term of light absorbed by each next layer as

$$\sum_{i=0}^{n-1} I_p t_p^i = I_p + I_p t_p + I_p t_p^2 + \dots + I_p t_p^{n-1} = I_p \frac{1 - t_p^n}{1 - t_p} \quad (2)$$

$$\sum_{i=0}^{n-1} I_s t_s^i = I_s + I_s t_s + I_s t_s^2 + \dots + I_s t_s^{n-1} = I_s \frac{1 - t_s^n}{1 - t_s} \quad (3)$$

where I_p and I_s are the same as $I_{||}$ and I_{\perp} in Eq. (1), t_p and t_s are the averaged in 300–900 nm region transmission coefficients for parallel and perpendicular directions, and n is number of layers in the stack. Each layer contributes to the total intensity directly or indirectly, by absorption and further reemission. Then the DLP is written as

$$P_E = \frac{\sum_{i=0}^{n-1} I_s t_s^i - \sum_{i=0}^{n-1} I_p t_p^i}{\sum_{i=0}^{n-1} I_s t_s^i + \sum_{i=0}^{n-1} I_p t_p^i} = \frac{\frac{I_s}{I_p} \cdot \frac{1 - t_s^n}{1 - t_s} - \frac{1 - t_p^n}{1 - t_p}}{\frac{I_s}{I_p} \cdot \frac{1 - t_s^n}{1 - t_s} + \frac{1 - t_p^n}{1 - t_p}} \quad (4)$$

perfectly fits the data (see the (blue on-line) solid line in Fig. 6) with $I_s/I_p = 0.27$, $t_s = 0.99$, $t_p = 0.74$. One can see that the perpendicular absorption A is completely suppressed ($A = 1 - t_s = 0.01$), whereas the parallel transmittance t_p is very close to experimentally obtained transmittance of one MWNT layer [1].

The multilayered free-standing MWNT sheet ($11.5 \times 3 \text{ mm}^2$) comprising 44 layers and densified by deeping into ethanol exhibits very weak polarization perpendicular to the nanotubes alignment with $P_E = +0.055 \pm 0.01$. The averaged thickness of 44 layers (each densified layer has thickness 50–100 nm) stacked on each other is $4 \pm 0.4 \text{ }\mu\text{m}$ with density 0.8 g/cm^3 . Note, that degree of alignment of multilayered sheet was the same as the alignment of one layer (withdrawn from the same forest). Such a small DLP in the dense structure of MWNT sheet indicates on a total suppression of the depolarization effect. For comparison we measured the polarization of light emitted by 1.2 mm wide and 2.5 mm long Ni-Cr strip (0.2 mm thick foil) heated resistively by the same way as densified MWNT sheet. Obtained DLP is negligibly small and very similar to dense MWNT sheet. It is worth to note here that polarization measurement in resistively heated pitch-derived carbon fibers (Du-Pont de Nemours, E-75, $D = 10 \text{ }\mu\text{m}$) revealed $P_E = +0.22 \pm 0.01$ which is perpendicular to the fibers orientation. The perfect cylindrical shape of carbon fibers enhances the perpendicular component of polarization due to an internal reflection of light emitted by oscillators located close to the surface of side walls. Almost the same polarization ($P_E = +0.21 \pm 0.01$) was obtained in resistively heated thin tungsten wires (12 μm) (see dot line in Fig. 6).

4. Conclusions

Using MWNT sheets with different number of layers we experimentally demonstrated that polarization of blackbody radiation in carbon nanotubes is due to enhanced polarizability of C–C bonds along the tube direction and depolarization effects in perpendicular direction. For the electric field perpendicular to the tube direction, the induced charges on the nanotube surface produce a depolarizing field inside the nanotubes that largely cancels the external field. This leads to a screened polarization. Our observation of diminishing polarization from dense multilayered MWNT sheet demonstrates that the depolarization effect is due to screening by induced charges and works in separated MWNT sheets, whereas totally disappears in dense structures. The further increase of perpendicular component of emitted light in multilayered structure is

due to the better transmittance of front layers for perpendicular polarized light than for parallel. The contribution of surface plasmons interacting with incident (emitting) light becomes effective when the averaged diameter of bundles exceeds 250–300 nm.

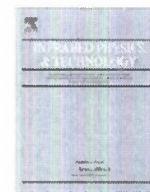
The Raman spectra exhibit higher intensities of G-band peaks along the MWNTs alignment versus perpendicular direction as 1:0.29. We obtained the same polarization ratio for blackbody radiation in visible range, which is consistent with X-ray diffuse scattering observation. The pronounced depolarization effects in all above mentioned cases suggests very simple and effective method to estimate the degree of alignment of carbon nanotubes assemblies by measuring the DLP for absorption or emission.

Acknowledgements

We thank S. Fang for providing us with the MWNT sheets, Prof. R.H. Baughman and Prof. A.A. Zakhidov for encouraging this work and stimulating discussions. The financial support of SPRING Program (Strategic Partnership for Research in Nanotechnology Program, Texas) via AFOSR program is highly appreciated.

References

- [1] M. Zhang, S. Fang, A.A. Zakhidov, S.B. Lee, A.E. Aliev, C.D. Williams, K.R. Atkinson, R.H. Baughman, *Science* 309 (2005) 1215.
- [2] B. Agdur, G. Boling, F. Sellberg, Y. Ohman, *Phys. Rev.* 130 (1963) 996.
- [3] O. Sandus, *Appl. Opt.* 4 (1965) 1634.
- [4] P. Li, K. Jiang, M. Liu, Q. Li, S. Fan, *Appl. Phys. Lett.* 82 (2003) 1763.
- [5] J.D. Jackson, *Classical Electrodynamics*, Wiley, New York, 1975, p. 658.
- [6] M.F. Islam, D.E. Milkie, C.L. Kane, A.G. Yodh, J.M. Kikkawa, *Phys. Rev. Lett.* 93 (2004) 037404.
- [7] Y. Murakami, E. Einarsson, T. Edamura, Sh. Maruyama, *Phys. Rev. Lett.* 94 (2005) 087402.
- [8] M. Zhang, S. Fang, A.E. Aliev, S.B. Lee, A.A. Zakhidov, R.H. Baughman, US patent, US2005041031, 2005.
- [9] A.M. Rao, A. Jorio, M.A. Pimenta, M.S.S. Dantas, R. Saito, G. Dresselhaus, M.S. Dresselhaus, *Phys. Rev. Lett.* 84 (2000) 1820.
- [10] R. Saito, T. Takeya, T. Kimura, G. Dresselhaus, M.S. Dresselhaus, *Phys. Rev. B* 57 (1998) 4145.
- [11] A. Jorio, M.A. Pimenta, A.G. Souza Filho, R. Saito, G. Dresselhaus, M.S. Dresselhaus, *New J. Phys.* 5 (2003) 139.
- [12] Unpublished data provided by J.E. Fischer, P.A. Heiney.
- [13] H. Ago, M.S.P. Shaffer, D.S. Ginger, A.H. Windle, R.H. Friend, *Phys. Rev. B* 61 (2000) 2286.
- [14] A. Seepujak, U. Bangert, A.J. Harvey, *J. Phys.: Conf. Ser.* 26 (2006) 85.
- [15] A.E. Aliev, C. Guthy, M. Zhang, S. Fang, A.A. Zakhidov, J.E. Fischer, R.H. Baughman, *Carbon* 45 (2007) 2880.



Bolometric detector on the basis of single-wall carbon nanotube/polymer composite

Ali E. Aliev *

NanaTech Institute, University of Texas at Dallas, P.O. Box 830688, BE 26, Richardson, TX 75083, USA

ARTICLE INFO

Article history:

Received 11 April 2008

Available online 4 July 2008

PACS:

07.57.Kp

85.35.Kt

Keywords:

Bolometer

Carbon nanotubes

Polymer composite

Thermal conductivity

ABSTRACT

Infrared imaging sensors that operate without cryogenic cooling have the potential to provide the military or civilian users with infrared vision capabilities packaged in a camera of extremely small size, weight and power consumption. We present here the uncooled bolometric sensor on the basis of single-walled carbon nanotubes (SWNTs) polymer composite with enhanced sensitivity. The voltage responsivity of device working at room temperatures exceeds 150 V/W. The absorption coefficient of single-wall carbon nanotubes was increased by involving Forster type energy transfer from polymer film to dispersed SWNT. The temperature gradient of resistivity was substantially improved by chemical functionalization of SWNT.

© 2008 Elsevier B.V. All rights reserved.

1. Introduction

Carbon nanotubes (CNTs) due to their remarkable electrical, thermal, and mechanical properties have attracted a great attention motivated by both basic scientific interest and the possibility of widespread application. A unique property of the CNT is that its electronic structure is essentially one-dimensional and has been a subject of an extensive study [1].

From the application viewpoint there is particular interest in the properties of systems containing randomly distributed or aligned nanotubes. Along with their remarkable electronic properties CNTs combine large surface area, good chemical stability, and significant elastic properties; thus appearing as appropriate candidates for super-capacitors [2], batteries [3], heat exchange systems [4], and actuators [5]. Due to the extremely large aspect ratio the percolation threshold in CNT/polymer composite film is essentially below half of a percent [6]. This makes CNT very useful filler material for various applications: conducting polymer composites, functional material of electronics [7,8], and heat conductors [9,10]. Thin CNT films (50–100 nm) may serve as transparent conducting electrodes for various technological applications as an alternative to ITO. CNT films and bucky-papers (thick mat-like films) are very promising electrode material for solar cell electrodes, organic light emitting diodes, and batteries.

Our recent studies of photoconductivity in SWNT confirm a very weak photoresponse. The SWNT film deposited on glass substrate

by spin-coating technique and then densified by dipping in ethanol shows hardly detectable changes of resistance at low power of excitation light. The spectral features in absorption and photoconductivity match the optical transitions associated with the van Hove singularities. At the same time, extremely low-density and huge surface area of suspended SWNT film having negligible heat capacity makes it very sensitive to electromagnetic radiation. Therefore, very small absorption is needed to heat individual nanotubes to noticeable temperatures. So, the large photoresponse observed for suspended SWNT was recently proposed for sensitive element of an infrared bolometer [11,12]. The temperature dependence of resistance in CNT exhibits exponential decay at low temperatures and very smooth slope at room temperatures. The low temperature coefficient of resistivity of all kind of CNTs grown by different methods is a limiting factor for high performance CNT bolometer.

The variable range hopping (VRH) mechanism of electrical conductivity observed in almost all presently available CNT's is mainly determined by concentration of defects in CNT itself and contact interfaces between single nanotubes. In this paper I am discussing several possible ways to increase the TCR of SWNT by chemical treatment of individual nanotubes dispersed in a polymer matrix. Absorption efficiency of thin SWNT film can be substantially increased by appropriate choice of matrix material providing enhanced energy transfer from polymer to SWNT. In addition, improved thermal conductivity of SWNT/polymer composite film provides a shorter response time of devices.

The main advantages of proposed CNT/polymer composite as a bolometric material are:

* Tel.: +1 972 883 6543; fax: +1 972 883 6529.

E-mail address: Ali.Aliev@utdallas.edu

1. High absorption coefficient in wide electromagnetic wave range, 0.2–20 μm . Emissivity coefficient close to unit (as in graphite).
2. Flexibility of film.
3. Resistive to hard radiation damages.
4. Can work in high magnetic fields.
5. CNT/polymer composite easy to cast and fabricate large surface area matrix-addressable sensors.

2. Experimental

SWNT bucky-paper was fabricated using HiPCO (high pressure carbon oxide) powder (Carbon Nanotechnologies, Inc.) synthesized by high pressure catalytic CVD deposition. The powder was purified from catalytic impurities (Ni, Fe) in strong acid (HNO_3) and ultrasonically dispersed in presence of a surfactant. The SWNT bucky-paper with density 0.33–0.38 g/cm^3 and thin (50–100 nm) film were produced by vacuum filtration and spin-coating techniques. I studied the temperature and Volt–Ampere characteristics of these specimens as a reference material and compared them with SWNT/polymer composite.

SWNT polymer dispersion in polycarbonate (polystyrene) matrix was prepared in Zyvex Inc. as described in [6]. Briefly the homogeneous nanotubes/polymer composite was fabricated using non-covalently functionalized, soluble SWNTs. As-purchased SWNTs were solubilized in chloroform with poly-(phenylene-ethynylene)s (PPE) along with vigorous shaking and/or short bath sonication. The resulting PPE-functionalized SWNT solution was then mixed with a host polymer (polycarbonate or polystyrene) solution in chloroform to produce a homogeneous nanotube/polymer composite solution. The uniform composite film was prepared from this solution on a silicon wafer with a 100 nm thick thermal oxide layer either by drop-casting or by slow speed spin-coating. The sample was then heated to 80–90 $^\circ\text{C}$ to remove residual solvent. Nanotube/polymer composite films with various SWNT loadings from 0.01 to 10 wt% in polystyrene, as well as in polycarbonate, were prepared according to the above procedure. The SWNT loading values for PPE-functionalized SWNT/host polymer composites are based on pristine SWNT material only, and exclude the PPE material.

The temperature dependence of composite resistance and thermal conductivity was measured using physical property measurement system (PPMS, Quantum Design) by four-probe method under excitation current of 10 μA . Gold electrode wires (0.1 mm) were attached to the thin SWNT/polymer strip using epoxy silver paste (H-20E). After annealing at 100 $^\circ\text{C}$ the resistance of silver electrodes did not exceed 0.1 Ω . The measurement was performed in vacuum of 1 mTorr. Volt–Ampere characteristics of composite were studied using electrochemical station, CHI-660A electrochemical Analyzer/Workstation. Infrared reflectance and transmittance spectra were taken using a PerkinElmer AutoIMAGE Microscope combined with PerkinElmer Fourier-transform infrared (FTIR) spectrometer Spectrum GX. The range of the reflection and transmission spectra extends from 1 μm to 16 μm , using a broad-band infrared glowbar source, KBr beamsplitter and liquid-nitrogen-cooled MCT detector. The reflectance and transmittance spectra in visible region were measured in air using a PerkinElmer photo-spectrometer Lambda 900 equipped with Labsphere PELA-1000 integrated sphere. The micrographs of scanning electron microscope (SEM) were taken with a LEO 1500 VP equipped with energy dispersed spectrometer (EDS) for X-ray microanalysis. The elemental analysis of studied SWNT/polymer composite film shows small concentration of residual metallic impurities: 1–2 wt%.

3. Results and discussion

The 17 μm thick film attached to a copper sink (Fig. 1A) exhibits extremely high sensitivity to infrared radiation. The perfect dispersion of SWNT (HiPCO) in polycarbonate polymer obtained by Zyvex Inc. team is shown below in SEM image of 5% composite (Fig. 1B).

3.1. Responsivity

The output voltage of the bolometer operated in constant current mode (CCM) is determined by responsivity which is defined as the change of output voltage for a change in incident power. Neglecting electrothermal effects the responsivity can be written as,

$$S = \frac{dV}{dQ} = 150 \text{ V/W}, \quad (1)$$

where $dV = 1.484 \text{ V}$, is the potential change on the sample measured in chrono-potentiometry mode with constant current of 10 μA , $R_0 = 622 \text{ k}\Omega$ is the initial resistance of the sample and $P = 9.8 \text{ mW}$ is the power of light incident on the sample surface (halogen-tungsten lamp, 15 W). To estimate the power of incident light from the laser source (IQ series laser module, Power Technology Inc., 830 nm, 135 mW) I used calibrated Si detector, UV-100 (Spectra Physics Inc.). At the same time, the energy absorbed by suspended sample can be estimated by comparison of resistance changes caused by incident light with resistance change caused by Joule heating of DC current. The heating power due to the bias current is substantially lower, $P = I^2 R = 0.062 \text{ mW}$.

The obtained value of responsivity at room temperature is much higher than one recently published in Science for suspended SWNT film [12], $S = 20\text{--}30 \text{ V/W}$. Below I analyze the peculiarities of studied SWNT/polymer composite that contributed to enhanced bolometric sensitivity.

3.2. Bolometric performance analysis

Detailed calculations of the transient and steady-state response characteristics of the bolometer have been made in order to determine the peculiarities of a number of different geometries, and to establish their performance limits for certain sets of design parameters. The bolometric heat balance equation for CCM mode can be written as [13]

$$C \frac{dT}{dt} = \eta P + I^2 R(T) - G(T - T_h), \quad (2)$$

where P is the incident radiation power, η is the absorption coefficient of bolometer, I is the constant bias current, G is the thermal conductance to the heat sink, C is the heat capacity of the sensitive element, T_h is the heat sink temperature and $R(T)$ is the temperature dependent sensor resistance. Using Eq. (2) one can calculate the temperature change and compare it with the real signal.

By neglecting thermoelectric heating and heat losses through thermal conductivity of lead wires we can reduce the Eq. (2) to

$$\frac{\Delta R}{R_0} = \frac{\eta \cdot P \cdot dt \cdot \alpha}{C}. \quad (3)$$

One can see that the most significant improvement of bolometer sensitivity could be done by increasing the temperature coefficient of resistivity ($\text{TCR} = \alpha = \Delta R / \Delta T \cdot R_0$) and absorption coefficient η , and reducing the heat capacity, $C = (dQ/dT) \cdot m$ (where m is the mass of suspended part of the film). By incorporation of functionalized SWNT in polymer matrix we can solve simultaneously two problems: increase TCR and η . However, the response time is also increased due to the raise of the total mass of sensitive film.

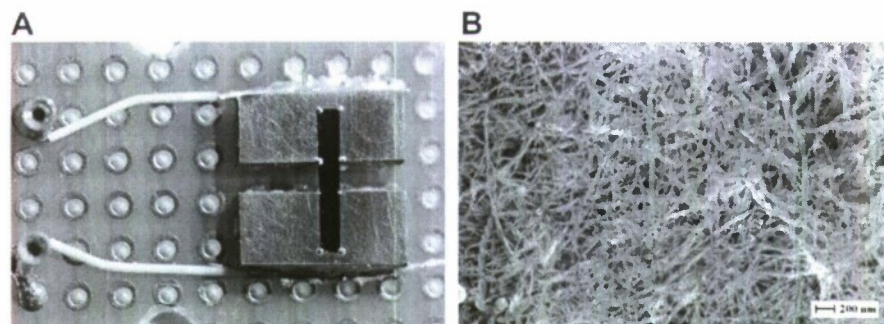


Fig. 1. (A) Seventeen micrometer thin film ($9 \times 1 \text{ mm}^2$) of 5% SWNT/polycarbonate composite attached to two copper bricks ($9 \times 4 \times 2 \text{ mm}^3$) serving as a heat sink. (B) SEM image of the composite (the polymer matrix is invisible under electronic beam).

3.3. Temperature dependence of electrical resistivity

The obtained value of TCR for chemically functionalized SWNT at room temperature, $\alpha = -3 \times 10^{-3} \text{ K}^{-1}$ is much higher than for SWNT bucky-paper or thin SWNT film [12]. The temperature dependence of resistivity of 2% SWNT/polymer composite is shown in Fig. 2. The resistivity of composite was normalized to the volume fraction of SWNT. It is clear that SWNTs embedded into polymeric matrix show higher TCR compared to bare SWNT film. For regular disordered SWNT (HiPCO) film the smooth increase of resistivity toward the low temperatures has been observed. Resistivity increases to three orders of magnitude. The linear behavior of $I-U$ characteristic obtained over wide range of voltages ($I < 20 \mu\text{A}$, $U < 10 \text{ V}$) exhibits Ohmic contacts between nanotubes.

The sharp growth of resistivity for low temperatures is specific for VRH mechanism. The exponent for VRH mechanism depends on the dimensionality of conduction [14]:

$$R = R_0 \exp \left[\left(\frac{T_0}{T} \right)^{1/(D+1)} \right], \quad (4)$$

where R_0 is an independent part of resistivity, D is the dimensionality of electric conductivity and T_0 is the characteristic temperature. In three-dimensional (3D) systems, such behavior of conductivity is known as Mott type hopping mechanism or 3D VRH model, that is often seen in low doped semiconductors, $\ln R \sim T^{-1/4}$. However, in 1D conductors the charge transport could not be independent. In

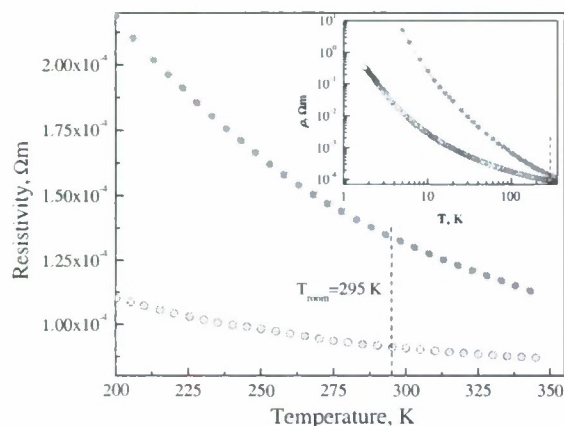


Fig. 2. Temperature dependence of resistivity in SWNT bucky-paper (open circles), and 2% SWNT/Polymer composite (solid circles). Inset shows an extended plot in logarithmic scale.

3D systems the charge flow is diffusive (except superconductors) and can be realized by many pathways. The localized electrons or defects can be bypassed by alternative channels. In 1D system the localized electron or some defect blocks the channel and only way to overcome the defect is jump through the barrier by gaining additional energy or to move the obstacle. Under high concentration of defects the conduction channels of individual nanotube are separated into several sectors with ballistic character of electron transport. Adding or removing the electrons from such area leads to excitation of density of states with quadratic coulomb gap near the Fermi level. Coulomb repulsion in sectors with isolated defects prevents further electron movement. At low temperature this leads to dependence $\ln R \sim T^{-1/2}$ [15]. Eq. (4) shows the possible ways to increase the TCR:

1. Low dimensionality of electron conduction: conductivity 1D is preferable. This requirement also implies the low concentration of SWNT in composite to avoid bundling into 3D systems.
2. High T_0 : T_0 represents here the activation energy of internal barriers and barriers created by tube-tube interconnection. Functionalized nanotubes touch each other through -CH- bonding groups with higher activation barrier for electrons than direct tube-tube contacts.
3. Semiconductor SWNTs with non-linear Volt-Ampere characteristic are more attractive for high TCR. On the other hand, metallic SWNTs have much higher light absorption in IR region.

Current modulation experiments were carried out with 2% SWNT/polycarbonate film with the thickness of $17 \mu\text{m}$ attached to two copper sinks by silver paste (see Fig. 1A). At room temperature, the DC photoresponse to 20 s light pulses (Fig. 3) shows a current modulation of 30%. Estimated power of white light radiation incident on the sample surface was about 10 mW (15 W halogen-tungsten lamp). Modulation intensity does not depend upon applied potential in wide range, 0–10 V.

The noise characterization was performed by biasing a sample at various DC levels and measuring the spectral density of low frequency fluctuations with a HP spectrum analyzer (HP3565B). Narrow strips of 2% SWNT/Polymer composite film ($\sim 40 \text{ k}\Omega$) were voltage biased through a low noise metal-ceramic resistor of $260 \text{ k}\Omega$ using 3 V battery. Low noise preamplifier SR560 was used to measure the current fluctuations. The noise power density measured in the frequency range of $20\text{--}10^4 \text{ Hz}$ is decreased ($1/f$ noise) from 10^{-14} to $10^{-15} \text{ V}^2/\text{Hz}$ which is comparable to the lowest noise level obtained for the MWNT sheet [16], but one order lower than for MWNT and three order for SWNT mats prepared by ordinary filtration method. Chemically functionalized tube-tube interaction strengthened by polymer matrix substantially improves the creep noises specific for weak CNT interconnections.

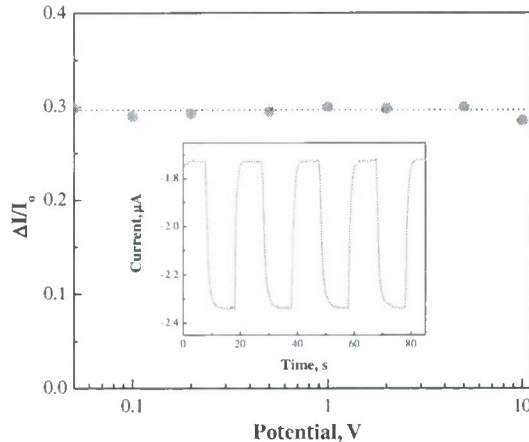


Fig. 3. Current modulation versus applied voltage in 2% SWNT/polycarbonate composite. Inset shows the response time of bolometric cell to 10 mW exposure by white light.

3.4. Thermal conductivity of polycarbonate polymer/SWNT composite

Almost one order enhancement of thermal conductivity was achieved at 4–5% of SWNTs in PC (Fig. 4A). Below is shown the concentration dependence of thermal conductivity of composite measured at 300 K in vacuum ($P = 10^{-7}$ Torr). The thermal conductivity of pure polycarbonate (poly(bisphenol-A-carbonate) $[-OC_6H_4-4C(CH_3)_2C_6H_4-4-OCO-]$) film measured by transient pulse method (PPMS) is very consistent with the data for bulk specimens, 0.19–0.22 W/mK (23 °C). Addition of 0.5% of SWNT with good dispersion almost doubles the thermal conductivity of composite. At concentrations above 4% the thermal conductivity starts to saturate.

SEM images at higher concentrations show agglomeration of SWNT in big chunks with low homogeneity of composite. The thermal conductivity of composite gradually increases in a wide range of temperatures (Fig. 4B) and is very consistent with the concept of phonon propagation in 1D systems. Enhanced thermal conductivity partially decreases the responsivity of bolometric device due to faster heat dissipation to the heat sink. However, the response time is substantially decreased, comparing to the low concentration of SWNT in composite.

For comparison I measured the thermal conductivity of mat-like SWNT bucky-paper. Disordered structure of SWNT paper prepared

by filtration method does not allow to achieve high thermal conductivity, $\lambda = 10\text{--}12$ W/m K. However, the aligned suspended MWNT sheet reveals $\lambda > 50$ W/m K [17].

3.5. Response time

The response time can be characterized by a time constant τ which for a bolometer is given by the equation, $\tau = C/A$, where C is the absorber heat capacity (J/K), and A is the thermal conductance (W/K). The response time of 1% SWNT/polycarbonate composite exceeded 2 s. The 2% SWNT composite exhibits < 1 s response time (measured at half pulse intensity) with substantially higher absorption coefficient. Photoresponse of 17 μm thick 2% SWNT composite shown in inset to Fig. 3 can be improved by further decrease of the film thickness using 4–5% SWNT composite with higher thermal conductivity.

According to Eq. (3), miniaturization of device size by reducing the bolometer surface area shall lead to simultaneous decrease of absorbed energy P and heat capacitance C . The responsivity does not affected by miniaturization. To study the size dependence of responsivity and response time I prepared two samples with different sizes, $13 \times 0.9 \times 0.05$ mm³ and $6.5 \times 0.45 \times 0.05$ mm³. The four times reduced surface area and mass, decrease P and C to the same level. This size reduction did not change the responsivity, either response time. For the response time the obtained result was unexpected. Our previous studies of length dependence of thermal conductivity showed that substantial improvement of response time can be achieved at characteristic length below 0.4 mm, [17]. At higher distances between sink electrodes and given thermal conductivity of SWNT composite the dominated process for dissipation of heat energy is rather intensive blackbody radiation from the surface than the phonon propagation toward the heat sink. Actually, the rate of heat dissipation by blackbody radiation is much faster than by means of phonons. There are two ways to reduce τ , one is a reduction of heat capacity of suspended film by decreasing the thickness of film, and another is reduction of sample dimension below the characteristic size, < 0.4 mm.

3.6. Absorption

Fifty nanometer thick SWNT film absorbs only 10% ($T = 90\%$) of radiation in the wavelength range of 1–10 μm [18]. Transmittance of SWNT/polymer composite film is decreased with the thickness. At some thickness the part of the nanotubes eventually remain in

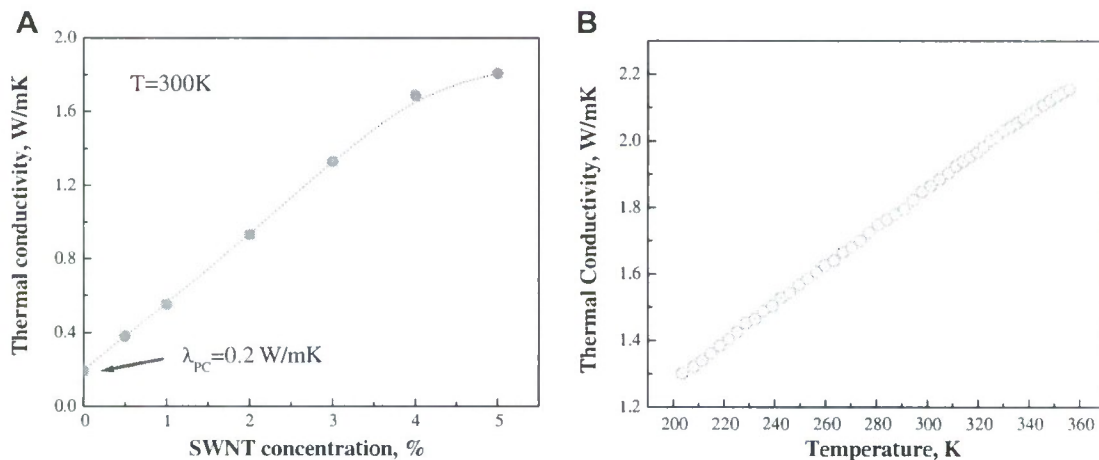


Fig. 4. (A) Concentration dependence of thermal conductivity of polycarbonate/SWNT composite at room temperature. Arrow shows the thermal conductivity of bulk polycarbonate sample. (B) Temperature dependence of thermal conductivity of 5% SWNT/polycarbonate film.

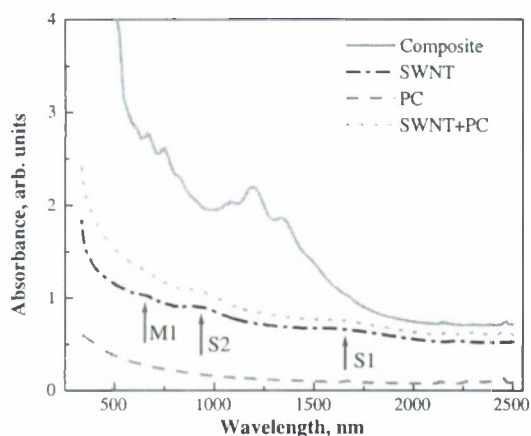


Fig. 5. Absorption spectra of 17 μm thick 2% SWNT/polymer composite shown by solid (red) line. Dashed (green) line is the absorption spectrum of bare 17 μm thick PC polymer. Dashed-dot (black) line is the absorption spectrum of 340 nm thick SWNT film. Dot (red) line is the sum of absorption spectrum of SWNT + PC polymer. Arrows show absorption bands responsible for electron transitions S1, S2, and M1, between van Hove singularities in semiconducting and metallic nanotubes, respectively. (For interpretation of the references to colour in this figure legend, the reader is referred to the web version of this article.)

the shadow of the front layer and do not contribute to the responsivity. What is optimal thickness of SWNT composite? Taking into account only the absorption of SWNT one can estimate the maximal thickness at which the film has low ($T = 10\%$) transmittance, $\sim 1.1 \mu\text{m}$. However, the 17 μm thick 2% SWNT/polymer composite totally absorbs the light ($T < 1\%$) at effective thickness of SWNT component of 340 nm. Note that absorption of the PC polymer at the studied wavelength region is comparably small. Absorption spectra shown above in Fig. 5 revealed some additional mechanism of light absorption inherent to composite. In the composite, dense polymer component absorbs the light uniformly, and transfers it by means of dipole excitation to randomly distributed SWNTs. Thus, absorption cross-section of SWNTs is substantially increased. This type of absorption called Forster resonance energy transfer (FRET) [19,20].

FRET involves the nonradiative transfer of excitation energy from an excited donor (matrix polymer) to a ground-state acceptor (SWNT) brought in close proximity. FRET processes are driven by dipole-dipole interactions and depend on the degree of spectral overlap between donor and acceptor absorption, and on sixth power of the separation distance. The barely perceptible absorption bands labeled S1, S2, and M1 resulting from the electronic transitions between van Hove singularities in SWNT, are shifted towards higher frequencies in the polymer composite and substantially increased (see Fig. 5). Short wavelength absorption shoulder in polymer contributes to the electronic transitions S1, S2, and M1 through FRET.

In conclusion, we have shown that bolometric responsivity and response time of SWNT film can be substantially improved by appropriate functionalization and selection of proper organic matrix. The use of SWNT/polymer composite film instead of SWNT film enormously simplifies the technological processes of manu-

facturing high-density 2D matrix-addressable bolometers for thermal imaging. In SWNT/polymer composite electrical behavior is dominated by functionalized carbon nanotube network, whereas, the absorption cross-section is mostly affected by the oscillator strength of polymer. Despite the increased thermal inertia due to the total rise of the film mass I obtained sixfold enhancement of responsivity by increasing the TCR and absorption of SWNT/polymer composite. The noise power density measured in the frequency range of 20–10⁴ Hz is much lower ($10^{-14} \text{ V}^2/\text{Hz}$) than for SWNT or MWNT mats prepared by ordinary filtration method. Chemically functionalized tube-tube interaction strengthened by polymer matrix substantially improves the creep noises specific for weak CNT interconnections.

The thermal time constant can be further reduced by decreasing the film thickness and choosing low heat capacity organic matrix. Optimization of the room temperature performance of the SWNT-based bolometer may provide a cost-efficient alternative to pyroelectric detectors, vanadium dioxide, and amorphous silicon-based bolometer arrays.

Acknowledgements

The author would like to thank Dr. R. Ramasubramaniam and J. Chen for the samples and fruitful discussions, and Prof. V. M. Agranovich for bringing to my attention recent works on the Furster energy transfer. This work has been partially supported by Texas SPRING program, 2006–2008.

References

- [1] R. Saito, G. Dresselhaus, M.S. Dresselhaus, *Physical Properties of Carbon Nanotubes*, Imperial College Press, London, 1998.
- [2] C. Liu, A.J. Bard, F. Wudl, I. Weitz, J.R. Heath, *Electrochem. Solid-State Lett.* 2 (1999) 577.
- [3] A.S. Claye, J.E. Fisher, C.B. Huffman, A.G. Rinzler, R.E. Smalley, *Electrochem. Soc.* 147 (2000) 2845.
- [4] J. Hone, M.C. Llaguno, M.J. Biercuk, A.T. Johnson, B. Batlogg, Z. Benes, J.E. Fisher, *Appl. Phys. A* 74 (2002) 339–343.
- [5] R.H. Baughman, Ch. Cui, A.A. Zakhidov, Z. Iqbal, J.N. Barisci, G.M. Spinks, G.G. Wallace, A. Mazzoldi, D. De Rossi, A.G. Rinzler, O. Jaschinski, S. Roth, M. Kertesz, *Science* 284 (1999) 1340.
- [6] R. Ramasubramaniam, J. Chen, *Appl. Phys. Lett.* 83 (2003) 2928.
- [7] A.V. Eletskii, *Phys.-Uspekhi (UFN)* 172 (2002) 401.
- [8] A.E. Aliev, P.K. Khabibullaev, H.W. Shin, *Uzbek J. Phys.* 3 (2001) 38.
- [9] S.U.S. Choi, Z.G. Zhang, W.Yu F.E. Lockwood, E.A. Grujke, *Appl. Phys. Lett.* 79 (2001) 2252.
- [10] J. Hone, M.C. Llaguno, M.J. Biercuk, A.T. Johnson, B. Batlogg, Z. Benes, J.E. Fisher, *Appl. Phys. A* 74 (2002) 339.
- [11] M. Zhang, R.H. Baughman, Sh. Fang, A.A. Zakhidov, A.E. Aliev, S.B. Lee, US Patent, US2005041031, 2005.
- [12] M.E. Itkis, F. Borondics, A. Yu, R.C. Haddon, *Science* 312 (2006) 413.
- [13] L.A.L. de Almeida, G.S. Deep, A.M.N. Lima, I.A. Khrebtov, V.G. Malyarov, H. Neff, *Appl. Phys. Lett.* 85 (2004) 3605.
- [14] A.A. Maarouf, C.L. Kane, E.J. Mele, *Phys. Rev. B* 61 (2000) 11156.
- [15] B.I. Shklovskii, A.L. Efros, *Electronic Properties of Doped Semiconductors*, Springer, NY, 1984.
- [16] M. Zhang, Sh. Fang, A.A. Zakhidov, S.B. Lee, A.E. Aliev, Ch.D. Williams, K.R. Atkinson, R.H. Baughman, *Science* 309 (2005) 1215.
- [17] A.E. Aliev, C. Guthy, M. Zhang, Sh. Fang, A.A. Zakhidov, J.E. Fischer, R.H. Baughman, *Carbon* 45 (2007) 2880.
- [18] Zh. Wu, Zh. Chen, Xu Du, J.M. Logan, J. Sippel, M. Nikolou, K. Kamaras, J.R. Reynolds, D.B. Tanner, A.F. Hebard, A.G. Rinzler, *Science* 305 (2004) 1273.
- [19] T. Furster, *Discuss. Faraday Soc.* 27 (1959) 7.
- [20] J.R. Lakowicz, *Principles of Fluorescence Spectroscopy*, second ed., Kluwer Academic, NY, 1999.